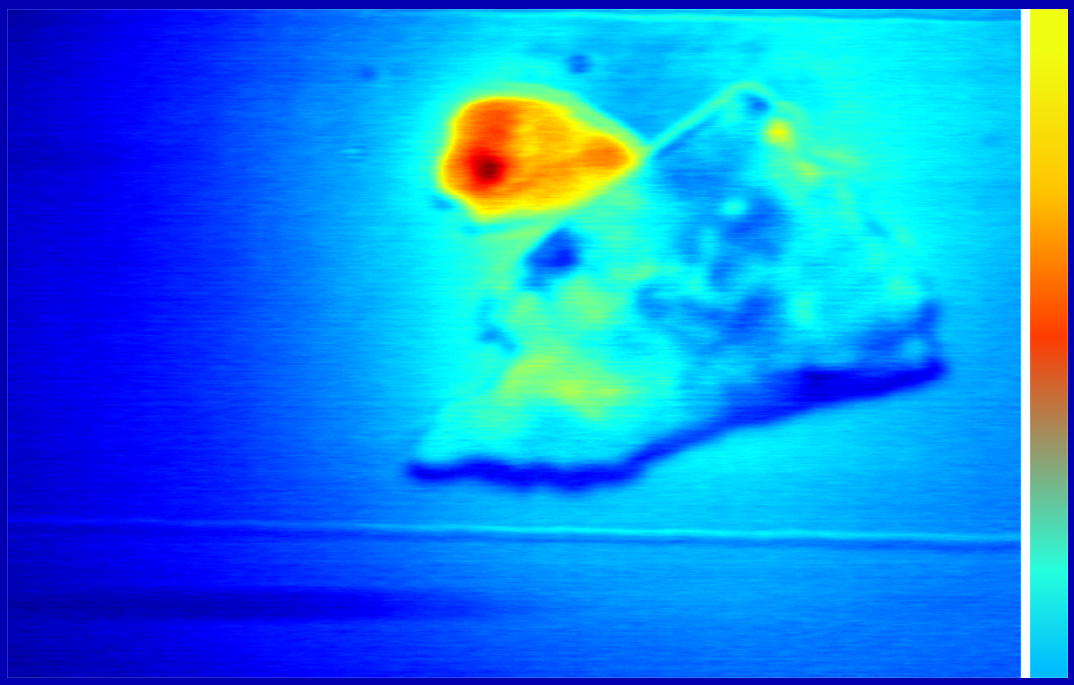
Volume 7, Issue 2, 2021

Journal of Biomedical Photonics & Engineering



Editor-in-Chief:
Valery V. Tuchin

© 2021 J-BPE

doi: 10.18287/JBPE21.07.020001

Journal of Biomedical Photonics & Engineering

by Samara National Research University

Volume 7, Issue 2 (June 2021)

Editor-In-Chief

Valery V. Tuchin - Saratov National Research State University, Russian Federation;
Institute of Precision Mechanics and Control RAS, Russian Federation; a corr.-member of RAS

Deputy Editor-In-Chief

Valery P. Zakharov - Samara National Research University, Russian Federation

Postal address:
39B Lukacheva st., room #301
Samara 443086, Russian Federation

Used Figure from this issue on the Cover

M.H. Aref et al. Characterization of Normal and Malignant Breast Tissues utilizing Hyperspectral Images and Associated Differential Spectrum Algorithm, 020302, Fig. 3c (adapted).

© 2021 J-BPE

Contents

Articles

Topical Gadobutrol Application Causes Fluorescence Intensity Change in RFP-expressing Tumor-Bearing Mice 020301
Natalia I. Kazachkina, Victoria V. Zherdeva, Asiya N. Saydasheva, Irina G. Meerovich, Valery V. Tuchin, Alexander P. Savitsky, and Alexei A. Bogdanov Jr.

Characterization of Normal and Malignant Breast Tissues utilizing Hyperspectral Images and Associated Differential Spectrum Algorithm 020302
Mohamed H. Aref, Abou-Bakr M. Youssef, Ibrahim H. Aboughaleb, and Yasser H. El-Sharkawy

Estimation of Rabbit Pancreas Dispersion Between 400 and 1000 nm 020303
Inês Martins, Hugo Silva, Valery V. Tuchin, and Luís Oliveira

Modeling of 980 nm and 1470 nm Laser Radiation Absorbance Efficiency in the Blood Vessel Depending on the Structure of Titanium–Containing Optothermal Fiber Converter 020304
Tung Thanh Do, Andrey V. Belikov, and Yulia V. Semyashkina

Influence of Activators and Inhibitors on the Collagenase with Collagen Interaction Monitored by Dynamic Light Scattering in Solutions 020305
Irina A. Sergeeva, Anna V. Petrova, Anastasia V. Shlenskaya, and Galina P. Petrova

Optical Signature Analysis of Liver Ablation Stages Exploiting Spatio-Spectral Imaging 020306
Mohamed H. Aref, Ramy Abdlaty, Mohamed Abbass, Ibrahim H. Aboughaleb, Ayman A. Nassar, and Abou-Bakr M. Youssef

Features of the Secondary Structure of BSA – Containing Protein Complexes, Isolated from Milk of High Temperature Processing 020307
Ivan S. Shatalov, Aleksandrina S. Shatalova, Lyudmila V. Plotnikova, and Aleksandr G. Shleikin

Optical Biopsy of Amelanotic Melanoma with Raman and Autofluorescence Spectra Stimulated by 785 nm Laser Excitation 020308
Ivan A. Bratchenko, Yulia A. Khristoforova, Lyudmila A. Bratchenko, Alexander A. Moryatov, Sergey V. Kozlov, Ekaterina G. Borisova, and Valery P. Zakharov

The Effect of Noise in Raman Spectra on the Reconstruction of the Concentration of Amino Acids in the Mixture by Multivariate Curve Resolution (MCR) Analysis 020309
Irina A. Matveeva, Lyudmila A. Bratchenko, Oleg O. Myakinin, Elena N. Tupikova, and Valery P. Zakharov

 © 2021 J-BPE

Topical Gadobutrol Application Causes Fluorescence Intensity Change in RFP-expressing Tumor-Bearing Mice

Natalia I. Kazachkina[1], Victoria V. Zherdeva[1*], Asiya N. Saydasheva[1], Irina G. Meerovich[1], Valery V. Tuchin[2,3,4], Alexander P. Savitsky[1], and Alexei A. Bogdanov Jr.[1,5]

[1] Bach Institute of Biochemistry, Research Center of Biotechnology of the Russian Academy of Sciences. 33 Leninsky Avenue, bld. 2, Moscow 119071, Russian Federation

[2] Research-Educational Institute of Optics and Biophotonics, Saratov State University, 83 Astrakhanskaya str., Saratov 410012, Russian Federation

[3] Interdisciplinary Laboratory of Biophotonics, National Research Tomsk State University, 36 Lenin's Avenue, Tomsk 634050, Russian Federation

[4] Laboratory of Laser Diagnostics of Technical and Living Systems, Institute of Precision Mechanics and Control of the Russian Academy of Sciences, 24 Rabochaya str., Saratov 410028, Russian Federation

[5] Department of Radiology, University of Massachusetts Medical School, Worcester, MA 01655, USA

*** e-mail:** vjerdeva@inbi.ras.ru

Abstract. Optical clearing (OC) allows one to observe tissue structures and metabolic processes occurring in opaque tissues at the depths significantly exceeding the depths that can be reached without OC. Recently, we have shown that gadobutrol is a promising agent for OC of tissues *in vivo*. The aim of this study was to investigate the effect of time-dependence optical clearing caused by gadobutrol on intensity of fluorescent protein constitutively expressed in subcutaneous tumors *in vivo*. The measurements were performed in nu/nu mice bearing HEp-2 tumors expressing the red fluorescent protein TagRFP. Gadobutrol was used directly at concentrations 1.0 M aqueous solution or as a 0.7 M aqueous solution containing 5% dimethyl sulfoxide (DMSO). Gadobutrol was applied topically onto the skin above the tumors for 15 min. Tissue fluorescence was measured by using *in vivo* planar imaging technique. It was shown that the fluorescence intensity of tumors increased by 1.1–1.5 times in different animals under the influence of gadobutrol. The increase in intensity was more pronounced in the case of 0.7 M gadobutrol supplemented with DMSO. Apparently, the observed difference of penetration depths was due to the presence of DMSO in 0.7 M gadobutrol mixture. © 2021 Journal of Biomedical Photonics & Engineering.

Keywords: fluorescence *in vivo* imaging; optical clearing; MRI-contrast agents; DMSO; genetically encoded fluorescent proteins; subcutaneous tumor; nude mice.

Paper #3398 received 28 Dec 2020; revised manuscript received 28 Jan 2021; accepted for publication 29 Jan 2021; published online 27 Mar 2021. doi: 10.18287/JBPE21.07.020301.

1 Introduction

The planar fluorescence imaging method is based on obtaining of fluorescent images using excitation light source at epi-configuration. These methods provide a means for detecting of fluorescent signal in a living animal that reflects specific, mostly disease-related processes, such as the host immune response, inflammation, tumor growth or the presence of pathogens [1–3]. This method was successfully applied for *in vivo* studying of photosensitizers [4–6] or nanoparticles distribution in living animal [7, 8], for studying of various pathological processes using specific targets labeled with different fluorescent probes [2, 9]. In the case of epifluorescence imaging fluorophore molecules

located on the surface or very close to it provide major contribution to the total intensity of fluorescence (FI). The sensitivity limit of planar imaging methods depends on the intensity of autofluorescence of the tissue [1, 2].

Here, the planar fluorescence imaging method was used to study the effectiveness of optical clearing (OC). OC is based on reducing the structural heterogeneity of biological tissue and, as a consequence, strong light scattering, mainly due to the matching of refractive indices between condensed microstructures (cell membranes and organelles, collagen and elastin fibers of the extracellular matrix) and the interstitial fluid of tissues by applying immersion solutions, the so-called optical clearing agents (OCA) [10–14]. The OCA developed for *in vivo* applications should have low toxicity. Thus, it is imperative that components of OCA should be well characterized and their toxicity independently investigated and verified. Among the potential components of OCA, the most promising are the compounds which are already in the clinics and are formulated for human use. In addition, to obtain tissue landmarks that aid in FI signal interpretation it is beneficial to use multimodality approaches that provide anatomical information, e. g. a combination of fluorescence and magnetic resonance imaging (MRI). In the latter case the use of OCA with paramagnetic properties could be beneficial. One of the potential OCA is gadobutrol with optical clearing properties previously proven in experiments involving optical coherent tomography, spectral and fluorescent microscopy [15].

The aim of this work was to further investigate the OC properties of MRI contrast agent gadobutrol, including its combination with a skin permeability enhancer, and to study changes of FI of tumors expressing red fluorescent protein before and after topical application of gadobutrol to perform the optimization of OC time to achieve stable IF.

2 Materials and methods

2.1 Animals and tumor model

All animal studies were performed in accordance with national requirements for the humane treatment of experimental animals. Nu/Nu mice (females, weight 19–21 g) were used in this work (Laboratory animal farm (Shemyakin–Ovchinnikov Institute of Bioorganic Chemistry of the RAS, Pushchino, Russia). Mice were housed in (HEPA)-filter-top cages in sterile barrier cabinet at 26 ºC and 50% humidity; mice received autoclaved certified complete diet and sterile filtered drinking water *ad libitum*. Subcutaneous tumors in mice were obtained by impalnting HEp2-TagRFP human carcinoma cell line constitutively expressing TagRFP marker protein as described earlier [15].

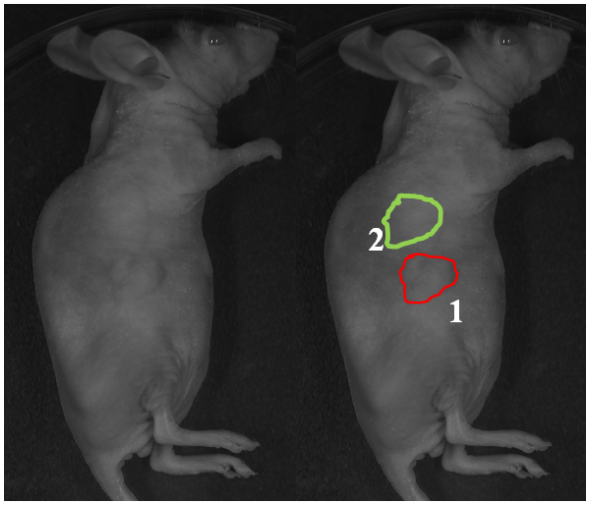
2.2 OC of tissues

Gadobutrol (Gadovist^{tm}, Bayer, Germany) was used as OCA along (at 1.0 M concentration as original formulation), as well as at a concentration of 0.7 M with an addition of 5% DMSO for improving of tissue penetration. Mice were anesthetized with a mixture of tiletamine and zolazepam (“Zoletil”, Virbac Sante Animale, France) at a concentration of 25 mg/ml each and xylazine at a concentration of 20 mg/ml (“Rometar”, Bioveta, a. s., Czech Republic). The mice were anesthetized with an intramuscular injection of 10 µl of a mixture of zoletil-rometar (1:1).

Gadobutrol was applied for 15 min onto the skin above the region of subcutaneous tumor growth and covered with a hygroscopic gauze. Then the gauze was removed and OCA residue was removed with a cotton swab. The OC effect of gadobutrol were estimated by changes in initial fluorescence intensity during 60 minutes after gadobutrol application using *in vivo* fluorescence imaging.

2.3 Equipment and processing of fluorescent images

Fluorescence imaging was obtained by using an iBox^{TM} system (UVP, USA) equipped with a motorized body-positioning elevator and a set of filters for fluorescence excitation and image registration. The unit was equipped an automated BioLite^{TM} light source system, which included a halogen lamp (150 W) and filters for excitation and registration of fluorescence and a cooled CCD camera. The system allowed to make images in white light mode (without optical filters) and fluorescence mode. In this study fluorescence was excited in the wavelength range of 502–547 nm and the registration was carried out in the range of 570–640 nm. The exposure varied from 2 to 15 sec.



(a) (b)

Fig. 1 Images of experimental mouse in “white light” mode (a), with the selected areas (b) of the tumor (1) and skin (2).

Fluorescence image analysis was performed using ImageJ software (NIH, USA). For image processing tumor and skin areas were highlighted (Fig. 1). The skin (background) area was set apart from the area exposed

gadobutrol. The average fluorescence intensities (FI) of tumor and skin were calculated for each mouse with subsequent normalizing of the average FI of tumor to that of skin.

3 Results and discussion

Fluorescence images of mice HEp2-TagRFP tumor are shown in Fig. 2. The unevenness of red fluorescence intensity distribution throughout the tumor can be easily distinguished on these images. There was also a visible increase of FI after the application of gadobutrol, both at 1.0 M (Fig. 1a, b) as well as 0.7 M (Fig. 1c, d) OCA. The combined results of FI measurements in all mice are shown in Tables 1 and 2.

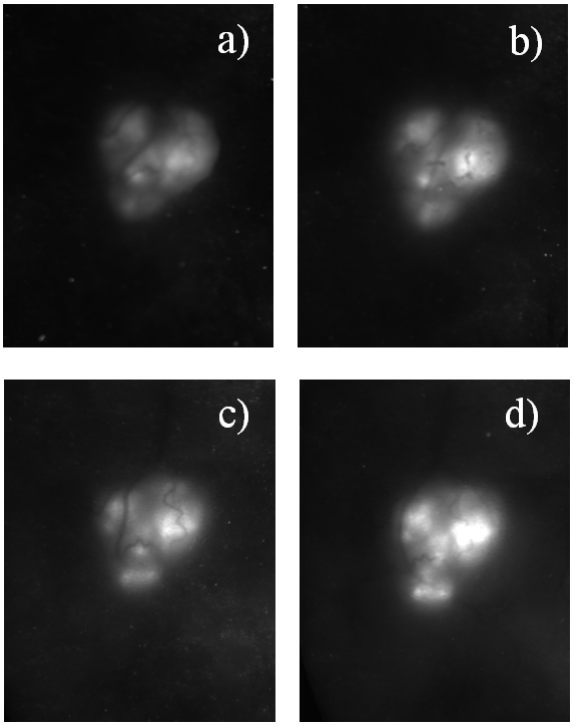


Fig. 2 Fluorescence images of HEp2-TagRFP tumor before (a, c) and 30 min after gadobutrol application (b, d). Exposure to 1.0 M gadobutrol (a, b) and 0.7 M gadobutrol with 5% DMSO added (c, d).

As the tabulated data (Tables 1, 2) show the mean values of FI of the tumor before gadobutrol application showed high levels of variability within the animal group. At the same time, various exposure times had to be used to avoid exceeding the dynamic range of the CCD detector. Under such experimental conditions the comparisons of the non-corrected mean FI values of the tumors and skin areas could not be performed. Thus, in the present study relative values were used to analyze the fluorescence signal intensity changes. Fig. 3 shows the change in FI relative to the initial value of FI (i.e. before OC).

It was shown that the fluorescence intensity of subcutaneous tumors was increased after treating the skin with gadobutrol. However, the dynamics of FI changes was dissimilar in the case of 1.0 M gadobutrol and the OCA containing gadobutrol and DMSO.

Thus, on average, the fluorescence signal in the group of mice treated with 1.0 M gadobutrol increased immediately after the application and then remained nearly unchanged for 1 h. The mice treated with 0.7 M gadobutrol supplemented with 5% DMSO showed a steady increase of FI signal throughout the entire observation period. From the results of data analysis, it was also apparent that the fluorescence intensity of the skin was nearly unchanged. This allowed to use the fluorescence of the non-treated skin area that was not exposed to gadobutrol for FI normalization (Fig. 3).

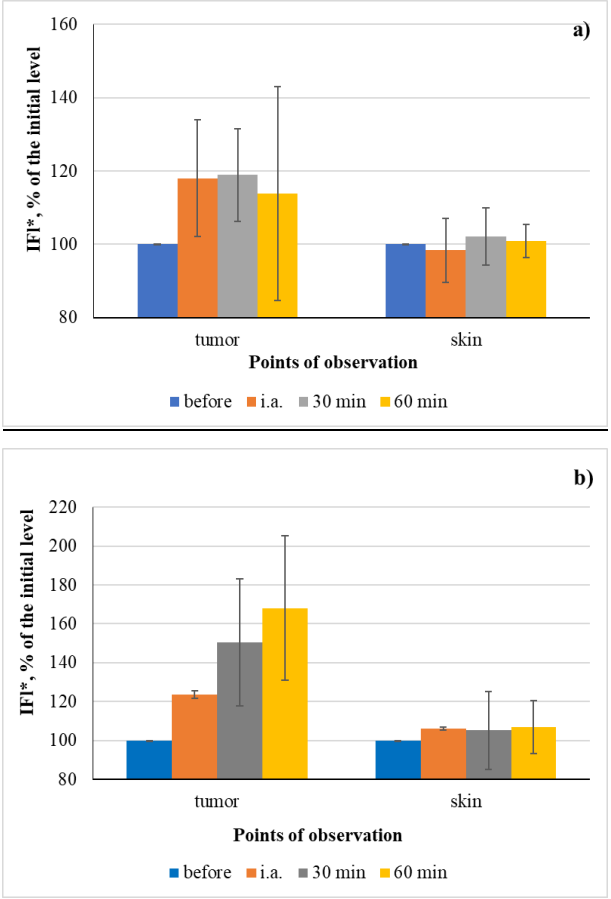


Fig. 3 Fluorescence intensity changes in tumors and skin before and after gadobutrol application. FI after application normalized on initial FI before treating the skin with gadobutrol. Gadobutrol was applied onto the area above the tumor, and the skin area was not exposed to gadobutrol: a) 1.0 M gadobutrol treatment (n = 4); and b) 0.7 M gadobutrol treatment with the addition of 5% DMSO (n = 4, exclude mouse #5 data, see Table 2).

Table 1 Fluorescence intensity of HEp2-TagRFP tumors and the skin of the tumor-bearing mice treated with 1.0 M gadobutrol.

Mouse #	Exposure time, s	Tissue	FI, a. u.			
			Before application	After application		
				Immediately after	30 min	60 min
1	2	Tumor	11995	16696	14875	16296
		Skin	2972	3213	3314	2934
2	2	Tumor	12212	13709	12643	n/d
		Skin	2972	2647	2750	
3	5	Tumor	14728	14896	16961	11895
		Skin	3218	3191	3419	3495
4	2	Tumor	13625	16302	18117	17025
		Skin	2038	2060	2055	2096

n/d – not determined.

Table 2 Fluorescence intensity of HEp2-TagRFP tumors and the skin of the tumor-bearing mice treated with 0.7 M gadobutrol supplemented with 5% DMSO.

Mouse #	Exposure time, s	Tissue	FI, a. u.				
			Before application	After application			
				Immediately after	15 min	30 min	60 min
1	2	Tumor	12505	n/d	17190	23948	24316
		Skin	2132		2208	2781	2763
2	2	Tumor	8790	n/d	12700	11142	n/d
		Skin	2704		2705	2556	
3	3	Tumor	23686	29632	n/d	28809	33588
		Skin	2735	2888		2324	2310
4	5	Tumor	10883	13319	n/d	17576	n/d
		Skin	2094	2237		2324	
5	10-15*	Tumor	24611	22029	n/d	25327	22911
		Skin	5711	4163		4441	4594

n/d – not determined; * – before application the exposure time was 15 s, and 10 s afterwards.

Normalization of tumor FI to skin FI allowed performing mean value comparisons within a set of animals with limited number of observations. The obtained normalized fluorescence (Fn) values are shown in Table 3.

The presented data show that gadobutrol application led to the increase in Fn of the tumors (Table 3, Fig. 4).

Moreover, tumors treated with 0.7 M gadobutrol with the addition of 5% DMSO showed, on average, a distinct tendency to increased Fn in the group compared to the group of animals exposed to 1.0 M gadobutrol, 30 and 60 minutes after the optical clearing agent impact (Fig. 4).

Table 3 The effect of gadobutrol topical application on normalized fluorescence (Fn) values of HEp2-TagRFP tumor fluorescence in various animals.

Mouse #	Fn (FI tumor/FI skin ratio)			
	Before application Fn_0	After application, Fn		
		Immediately after	30 min	60 min
	1.0 M gadobutrol			
1	4.04	5.20	4.49	5.55
2	4.11	5.28	4.60	n/d
3	4.56	4.67	5.0	3.40
4	6.69	7.92	8.82	8.12
Mean*	4.85 ± 1.25	5.77 ± 1.46	5.72 ± 2.08	5.69 ± 2.36
	0.7 M gadobutrol with 5% DMSO added			
1	3.25	n/d	4.36	n/d
2	5.87	n/d	8.61	8.80
3	11.31	13.25	12.39	14.54
4	3.98	4.61	3.75	n/d
5	4.31	5.29	5.70	4.99
Mean*	5.74 ± 3.26	7.72 ± 4.80	6.96 ± 3.57	9.44 ± 4.81

*data shown as mean ±SD; n/d - not determined

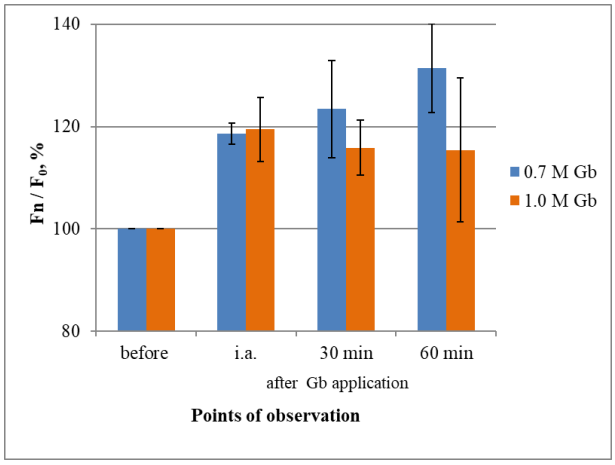


Fig. 4 The changes of HEp2 -TagRFP tumor normalized fluorescence (Fn) after topical application of two different gadobutrol (Gb)-containing solutions on the average for the group: 1.0 M gadobutrol (n = 4), 0.7 M gadobutrol with the addition of 5% DMSO (n = 5); F_0 – initial level of Fn (was taken as 100%) and Fn – after gadobutrol application. Data is shown as M ± SD. i.a. – immediately after application.

However, when considering the effect on each animal separately, it was noted that the dynamics of Fn changes varied in each animal (Fig. 5). Fn increased in most mice immediately after the application of gadobutrol, which facilitated selecting this observation period for further studies using gadobutrol as OCA. At the subsequent periods of observation, a decrease in Fn could be observed but afterwards an increase could be observed again.

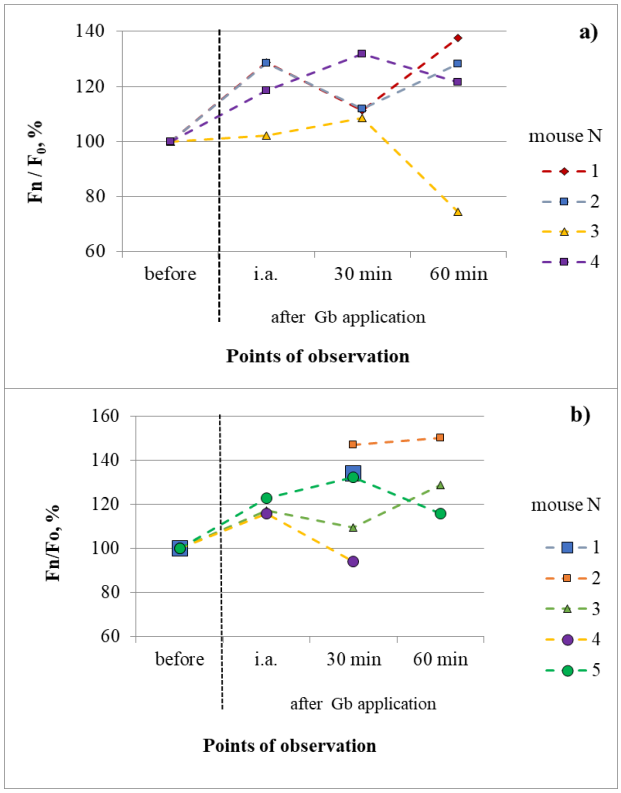


Fig. 5 The changes of the normalized fluorescence (Fn) of the HEp2-TagRFP tumor in individual animals relative to the initial level (Fn/F_0) as a consequence of treating the tumors with: a) 1.0 M gadobutrol, b) 0.7 M gadobutrol with the addition of 5% DMSO; F_0 – initial level of Fn (was taken as 100%) and Fn – after gadobutrol application; i.a. – immediately after application.

The oscillatory pattern of OC effect could be associated with the action of the clearing agent, which sets the water in motion both in the interstitial fluid and in the connective tissue fibers themselves. We hypothesize that the OCA penetrated into the interstitial space and caused a temporary dehydration of collagen fibers, and as a result the refractive index increased in comparison to the pre-OC levels. The resultant scattering of the tissue increased slightly but then the same effect on tissue refraction recurred as a new portion of the agent approached and equalized the refractive index again [16]. In the case of fluorescent tumor, the effects on FI could be even more complicated: a drop-in intensity and a subsequent increase may be associated with the different brightness of the luminous nodes in depth of the tissue, which become more prominent with OC. These effects could result from the heterogeneity of the tumor itself (the data will be published elsewhere, Ref. [17]). Alternatively, as we showed before [18] the FI levels should be measured in various selected areas of the tumor, and not only by integrating the whole tumor volume or individual tumor nodule.

4 Conclusion

Thus, the effect of OC caused by gadobutrol topical application as a potential OCA was investigated at the macroscopic level *in vivo*. There was a profound effect of OC on FI causing an increase of FI of HEp2 tumors expressing red fluorescent TagRFP marker protein**.** The OC effect of gadobutrol was associated with its transdermal penetration into the tissue after it was applied to the skin surface. This effect can be tentatively explained by the observation made in Ref. [17], where it was shown that the T1-weighted MR signal was increased after the application of the gradient echo pulse sequences in the deeper layer of the subcutaneous tissue after the application of gadobutrol/DMSO mixtures. It was also determined that the FI increase in the tumor after gadobutrol topical application persisted for a longer time period if OCA containing 0.7 M gadobutrol was used in combination with the addition of 5% DMSO vs. 1.0 M gadobutrol solution. We associate the mechanism of the observed OC effect of gadobutrol with a high value of its refractive index [15, 19], which is influenced by its high density, molecular structure and the presence of chelated polarizable gadolinium ions. The observed effects bear similarities to those of iodine-containing aromatic compounds which have high refractive indices in solutions and are used as immersion agents in many applications, including biology, mineralogy, and others [19]. This is an assumption requiring separate experimentation, which is beyond the scope of this study. At present, the results obtained allow us to draw the following conclusions:

1) both OCA under study containing gadobutrol cause OC effect when applied to the tumor growth area;

2) the most appropriate observation period is immediately after 15 min application for measuring fluorescence intensity after gadobutrol application;

3) 0.7 M gadobutrol with the addition of 5% DMSO is preferable over 1.0 M gadobutrol as it allows to observe the OC effect for a longer period of time.

Disclosures

All authors declare that there is no conflict of interests in this paper.

Acknowledgements

The work of Valery V. Tuchin was supported by the RFBR grant No. 18-52-16025.

References

1. A. Zelmer, T. H. Ward, "Noninvasive fluorescence imaging of small animals," Journal of microscopy 252(1), 8–15 (2013).
2. N. Stemmer, J. Mehnert, J. Steinbrink, and A. Wunder, "Noninvasive fluorescence imaging in animal models of stroke," Current Medicinal Chemistry 19(28), 4786–4793 (2012).
3. J. P. Miller, C. Egbulefu, J. L. Prior, M. Zhou, and S. Achilefu, "Gradient-Based Algorithm for Determining Tumor Volumes in Small Animals Using Planar Fluorescence Imaging Platform," Tomography 2(1), 17–25 (2016).
4. I. G. Meerovich, N. I. Kazachkina, and A. P. Savitsky, "Investigation of the effect of photosensitizer Tiosense on the tumor model melKor-TurboRFP expressed red fluorescent protein," Russian Journal of General Chemistry 85(1), 274–279 (2015).
5. E. V. Sanarova, A. V. Lantsova, A. P. Polozkova, O. L. Orlova, I. G. Meerovich, L. M. Borisova, M. P. Kiseleva, Z. S. Smirnova, N. Yu. Kul'bachevskaya, O. I. Konyaeva, and N. A. Oborotova, "Effectiveness of liposomal system of delivery of hydrophobic antineoplastic Thiosens photosensitizer," Nanotechnologies in Russia 10(5–6), 492-500 (2015).
6. A. I. Gavrina, M. V. Shirmanova, N. A. Aksenova, D. V. Yuzhakova, L. B. Snopova, A. B. Solovieva, P. S. Timashev, V. V. Dudenkova, and E. V. Zagaynova, "Photodynamic therapy of mouse tumor model using chlorin e6- polyvinyl alcohol complex," Journal of Photochemistry and Photobiology B: Biology 178, 614–622 (2018).
7. Y. Guan, T. Sun, J. Ding, and Z. Xie, "Robust organic nanoparticles for noninvasive long-term fluorescence imaging," Journal of Materials Chemistry B 7(44), 6879–6889 (2019).

8. Y. F. Loginova, Y. F. Loginova, S. V. Dezhurov, V. V. Zherdeva, N. I. Kazachkina, M. S. Wakstein, and A. P. Savitsky, "Biodistribution and stability of CdSe core quantum dots in mouse digestive tract following per os administration: advantages of double polymer/silica coated nanocrystals," Biochemical and Biophysical Research Communications 419(1), 54–59 (2012).
9. F. Stuker, J. Ripoll, and M. Rudin, "Fluorescence Molecular Tomography: Principles and Potential for Pharmaceutical Research," Pharmaceutics 3(2), 229–274 (2011).
10. D. Zhu, K. V. Larin, Q. Luo, and V. V. Tuchin, "Recent progress in tissue optical clearing," Laser & Photonics Reviews 7(5), 732–757 (2013).
11. D. S. Richardson, J. W. Lichtman, "Clarifying tissue clearing," Cell 162(2), 246–257 (2015).
12. P. Matryba, L. Kaczmarek, and J. Gołab, "Advances in ex situ tissue optical clearing," Laser & Photonics Reviews 13(8), 1800292 (2019).
13. I. Costantini, R. Cicchi, L. Silvestri, F. Vanzi, and F. S. Pavone, "In-vivo and ex-vivo optical clearing methods for biological tissues: Review," Biomedical Optics Express 10(10), 5251–5267 (2019).
14. A. Yu. Sdobnov, J. Lademann, M. E. Darvin, and V. V. Tuchin, "Methods for Optical Skin Clearing in Molecular Optical Imaging in Dermatology," Biochemistry 84(Suppl 1), S144–S158 (2019).
15. D. K. Tuchina, I. G. Meerovich, O. A. Sindeeva, V. V. Zherdeva, A. P. Savitsky, A. A. Bogdanov Jr., and V. V. Tuchin, "Magnetic resonance contrast agents in optical clearing: Prospects for multimodal tissue imaging," Journal of Biophotonics 13(11), e201960249 (2020).
16. Q. Xie, N. Zeng, Y. Huang, V. V. Tuchin, and H. Ma, "Study on the tissue clearing process using different agents by Mueller matrix microscope," Biomedical Optics Express 10(7), 3269 (2019).
17. A. A. Bogdanov Jr., N. I. Kazachkina, V. V. Zherdeva, I. G. Meerovich, D. K. Tuchina, I. D. Solovyev, A. P. Savitsky, and V. V. Tuchin, "Magnetic resonance imaging study of diamagnetic and paramagnetic agents for optical clearing of tumor-specific fluorescent signal in vivo," Chapter 25 in Tissue optical clearing: new prospects in optical imaging, D. Zhu, E. Genina, and V. Tuchin (Eds.), CRC Press, Boca Raton, FL (2021) [In press].
18. D. K. Tuchina, I. G. Meerovich, O. A. Sindeeva, V. V. Zherdeva, N. I. Kazachkina, I. D. Solov'ev, A. P. Savitsky, A. A. Bogdanov Jr., and V. V. Tuchin, "Prospects for multimodal imaging of biological tissues using fluorescence imaging," Quantum Electronics 51(2), 104–117 (2021).
19. K. Bai, J. Katz, "On the refractive index of sodium iodide solutions for index matching in PIV," Experiments in Fluids 55, 1704 (2014).

Characterization of Normal and Malignant Breast Tissues utilizing Hyperspectral Images and Associated Differential Spectrum Algorithm

Mohamed H. Aref[1*], Abou-Bakr M. Youssef[2], Ibrahim H. Aboughaleb[1], Yasser H. El-Sharkawy[1]
[1] Biomedical Engineering Department, Military Technical College, Cairo, Egypt
[2] System & Biomedical Engineering Department, Cairo University, Giza, Egypt

*** e-mail:** Mh-aref@ieee.org

Abstract. Breast malignancy is the most pervasive disease and a significant reason for death in women around the world. Recently, Photonic technologies play a vital role in medical applications. This study presents an outline of recent outcomes on the magnitude of breast tissue optical properties. We established an optical system setup utilizing a hyperspectral (HS) camera with poly-chromatic source lights with wavelength (380~1050 nm) for this investigation. Measuring the diffuse reflection (Ṛd) of the investigated *ex vivo* breast sample to select the optimum spectral image to differentiate between the normal and tumor in the near infra-red and visible (NIR–VIS) spectrum. Finally, applying the custom algorithm to increase the image contrast and applying contour delineation of the malignant regions. The experimental analysis indicates key spectroscopic variations between normal tissue and malignant region in range (550~650 nm). Although, after data normalization, there was noticeable variation at three ranges (630–680 nm), (720–770 nm), and (830–880 nm). The calculated standard deviation (Ṣd) between the normal and cancer tissue to validate the selective ranges shows that the highest contrast at wavelength 680 nm. However, the histogram analysis illustrates that the spectral image at 600 nm was higher contrast and wavelength 400 nm was the lowest contrast from the select seven-spectral images (400, 500, 600, 700, 800, 900, 1000 nm) to avoid the processing time of the captured HS 128-frames. The proposed potential method could provide promising results on the investigated breast sample optical properties in the diagnostic applications to assist the pathologist and the surgeon. Where the optimum wavelength at 680 nm for diagnostic applications and the ideal spectral image at 600 nm discriminate between the normal and malignant tissue. © 2021 Journal of Biomedical Photonics & Engineering.

Keywords: breast cancer early detection; hyperspectral imaging system; tissue optical properties; diffuse reflectance; spectral differences algorithm; optical spectroscopy.

Paper #3384 received 30 Oct 2020; revised manuscript received 7 Apr 2021; accepted for publication 12 Apr 2021; published online 6 May 2021. doi: 10.18287/JBPE21.07.020302.

1 Introduction

Breast malignancy is the most predominant disease and a significant reason for death in women overall. Early determination is vital for expanding the survival rate among women with breast malignant growth [1–3]. In male patients, the most leading reason of cancer death is lung cancer. However, in females, breast cancer is mostly the leading cause of mortality [4–6]. More than 8% of women will endure this infection during their lifetime [7]. Breast cancer is a malignant tumor that is

established from cells in the breast with no symptoms in the early stages [8].

Breast-conserving medical procedure stays challenging because of the absence of clinically accessible intraoperative resection edge strategies. Consequently, in up to 37% of women going through a breast-conserving medical procedure, the tumor is found in the resection edge of the resected sample [9–12]. This is a sign of tumor residual kept unintended inside the patient, which spreads the hazards for growing the tumor recurrence and increasing the reheeling time [13]. Consequently, these patients regularly require extra treatment like radiotherapy support or a re-extraction [14]. Right now, a pathologist, who assesses the tissue under a magnifying lens, surveys the resection edge a couple of days after the medical procedure. In that capacity, no immediate input can be given to the specialist during the medical procedure [12, 15].

Conventional diagnosis techniques of histological samples depend on the manual assessment of morphological structures of samples by qualified pathologists. Recently, the utilization of computer-aided skills for improving these systems is a developing pattern to lessen the intra and inter-observer inconstancy [16]. Such innovations are expected to enhance the diagnosis, make it reproducible and quantitative, and reduce time in the assessment of the investigated samples [17, 18].

To decrease the quantity of tumor-positive resection edges, different methods for resection edge appraisal during the breast-conserving medical procedure have been proposed [19–21]. Currently, the available edge assessment methods are frozen section analysis, imprint cytology, specimen radiography, and ultrasound [7, 21–23]. Despite this, none of all these techniques could clinically extensive. With frozen section examination, tissue can be investigated in 30 min with a specificity and sensitivity of 95% and 83%. Although, the main restrictions of this method are the necessity of a qualified pathologist, the possibility of false negatives (FN), and the feasibility of examining the entire resection surface [24, 25].

The hyperspectral imaging (HSI) system is a substitution modality for biological detection and RGB imaging for its ability to segregate between various materials by utilizing both morphological and spectral characteristics [26–28]. This tool has been effectively employed to support the diagnosis of various types of histological samples, for example, blood oxygenation and microcirculation [29–31], brain cancer detection [32, 32], tissue characterization [33–38], and monitoring liver ablation [39–44], and in the field of breast cancer [15, 45–48].

The female human being breast comprises principally glandular, fat, and connective tissue, along with blood and lymphatic vessels, and it contains a few basic mammary glands (lobes), each depleting through a different lactiferous duct [49–52]. Other than blood and lymphatic vessels, the connective tissue (stroma) comprises different stromal cells and the extracellular matrix (ECM) which comprises proteins, water, and polysaccharides [53]. The ECM addresses the platform for the stromal cells as well as passes on biochemical and biophysical signs to cells. breast malignancy development is related to changes in ECM arrangement, with inflammatory cell penetration, and separation of fibroblasts [54]. The spectral differences between the normal breast tissue and the biochemical changes of the malignant tissue which leading to these spectral features could be illustrated in Fig. A1 in the Appendix.

The red and near-infrared (NIR) light source wavelengths provide different propagation in the biological tissues regarding the other visible (VIS) spectrum. Where these sources could reach up to 10 cm thru the tissue and capable of cancer detection. Although, the NIR photons could freely path in the tissue till ~10 cm. However, the corresponding scattering is only 20~40 μm [48]. Additionally, the NIR imaging delivers a high affectability for molecular functions that are relatively near the surface. In any case, because of versatile scattering with different cellular components, NIR source light gets diffuse inside a couple of millimeters of engendering through tissue [55–57]. Finally, the main concern in this experiment was measuring the sample the diffuse reflection (R_d) to identify and characterize the explored breast sample's optical properties regarding its spectral signature, as more clarified in Fig. 1.

In the presented prospective approach, we recognized a system that could offer promising results by investigating the breast sample optical properties for diagnostic applications purposes. Although, optics in the medical sector faced several fluctuations and development depending on the optical properties of the biological tissue. However, optical medical equipment contributes by presenting strategies and making of equipment utilized in the healthcare of different claims to specialties, such as oncology, general surgery, and ophthalmology. Finally, after exploring breast tissue optical properties diffuse reflection (R_d). We could select the optimum wavelength for breast tissue in diagnostic applications to assist the pathologist during the tissue investigation and reduce the time of examination and the surgeon during the breast biopsy and Mastectomy process.

2 Materials and Methods

This experimental investigation was a part of series of consecutive research studies in early breast cancer diagnostic. Where our main objective is to select the lowest and highest contrast spectral image to apply our custom subtraction algorithm and delineate the various tumor regions [45–47].

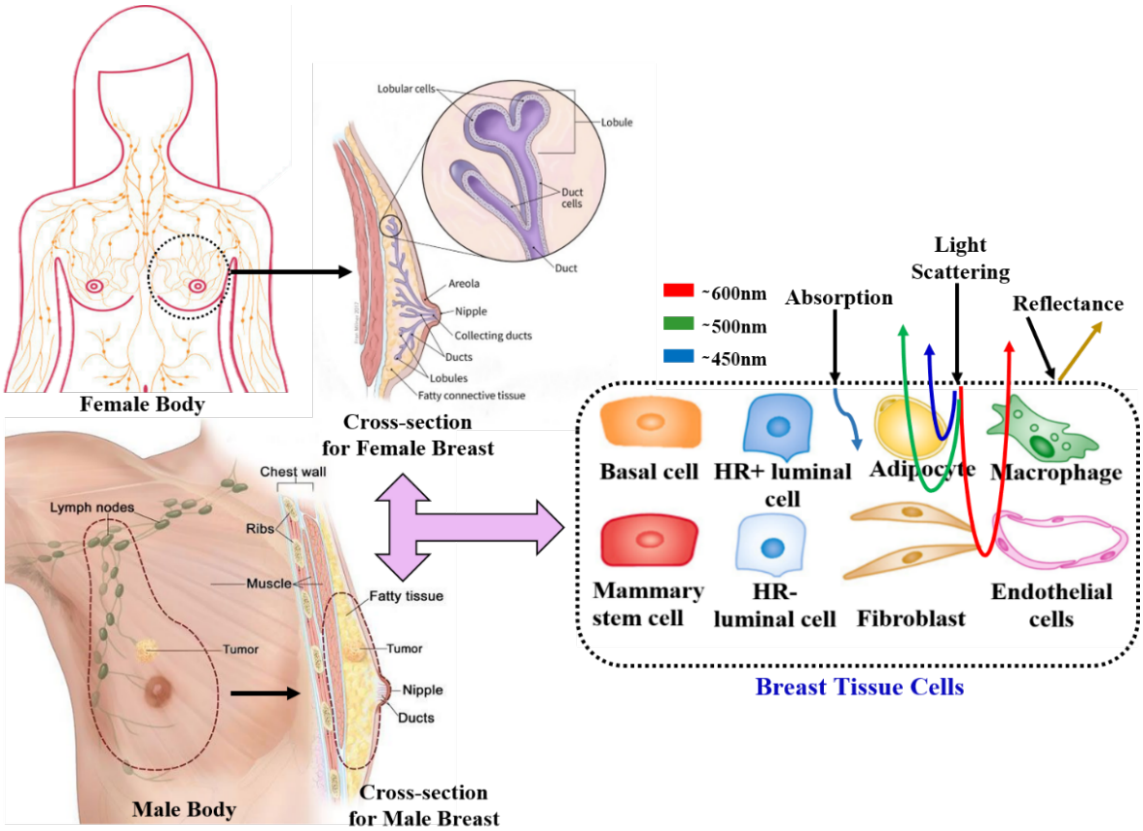


Fig. 1 The Light Interaction (Absorption / Diffuse Reflection / Reflectance) of *ex vivo* Breast Tissue Sample highlighting the Substitution of the breast Tissue Cells and its interaction with the various spectral range.

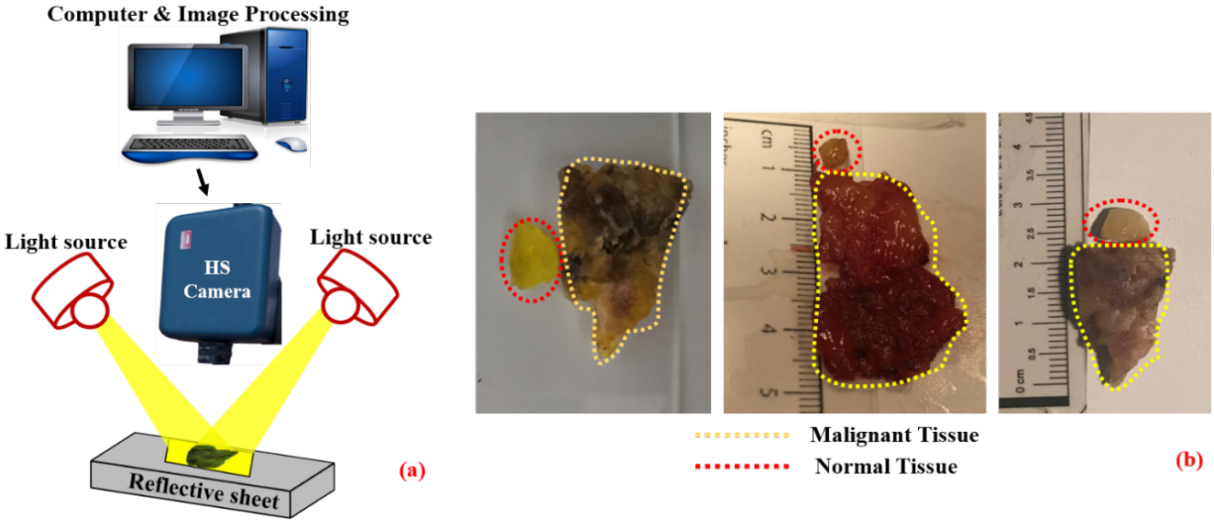


Fig. 2 (a) System Setup Measuring the Optical Properties of the Diffuse Reflection (R_d) of the *ex vivo* Breast Sample; (b) Acquired RGB images for Some Examples of the *ex vivo* Breast Samples Exploited the Investigated Experiments.

2.1 The main framework interconnections protocol could be explained as follows:

- Sample investigation & Tissue characterization.
- HS Image for the *ex vivo* breast sample.
- The measurements for sample diffuse reflection (R_d).
- Selection of the spectral image to differentiate between Tumor and normal regions in the diagnostic applications.
- Applying the custom algorithm to increase the image contrast (image enhancement) and delineation of the tumor regions.

The main framework of the proposed system utilizing hyperspectral HS camera (Surface Optics, SOC710, USA) incorporated with polychromatic source light (Derungs, 150 W, 385~1050 nm, Germany). Fig. 2(a) had been highlighting the schematic diagram for the exploited system to measure the investigated breast sample diffuse reflection (R_d), to discriminate the optimum wavelength for differentiation between the normal and tumor regions in the investigated *ex vivo* breast sample by exploring the optical properties of spectroscopy in the Near and visible (NIR–VIS) spectrum.

2.2 Pathology examination and sample slicing for malignant

In advance of the experimental investigation, the procedure validation was achieved from "Ain Shams University – Faculty of Medicine – Ethics Committee". Ten patients who were encountering Breast cancer development experienced a total Mastectomy process. Subsequently, a careful examination with good evaluation, the breast tumor samples were selected from arbitrary patients, a cancer diagnosis was confirmed to the pathological report which is the ground truth for our investigation. All the patient and the investigated samples necessary data of the presented study was illustrated in Table A1 in the Appendix.

The investigated *ex vivo* breast samples were crudely cut into slices with approximate sizes (2.5 × 3 cm), Sample thickness 4 ~ 6 mm, then transported in icebox fill of deionized saline. The explored sample temperature 25~28 °C at lap temperature 23°C~24 °C. The samples persevered before and after the trails at (–65 ~ –75 °C) inside Lap Refrigerator (ThermoFisher Scientific, ULT2090, USA), as displayed in Fig. 2 (b).

The cancer regions were confirmed to the pathological report which is the ground truth for our investigation. Even though the pathologist could detect the cancerous breast tissues. However, this study aims to build an optical imaging system to assist the pathologist to differentiate between the normal or healthy tissue and the cancer tissue regions to reduce the time of the investigation and increasing the accuracy of the detection. Additionally, to support the surgeon in guidance during the tumor resection in real-time.

2.3 The main theory and system equations

The main block diagram of the system set up to measure the optical properties of the investigated breast samples, measuring the diffuse reflection (R_d) then applying the custom algorithm to increase the image contrast and delineate the tumor region of the samples, which is more identified in Fig. 3.

The transport theory is the main concept for light propagation in the tissue concerning the radiant power of the transferred light in the tissue surface [58, 59]. Where, designating the light propagation in a turbid medium is vital to illustrate optical parameters, radiance, fluence proportion, and flux [34]. The photon scattering function with the power of photons, energy, velocity in the medium, as described in a previous study [45].

Often medical applications involve the interaction of light with the tissue. The amount of light could be expressed as the irradiance E_0, which is realized as the radiant energy flux incident on an element of the surface, divided by the area of the surface. Apart from that incident light is reflected, and another entering the tissue is attenuated by scattering and absorption according to Beer's law, as highlighted in Eqs. (1) and (2).

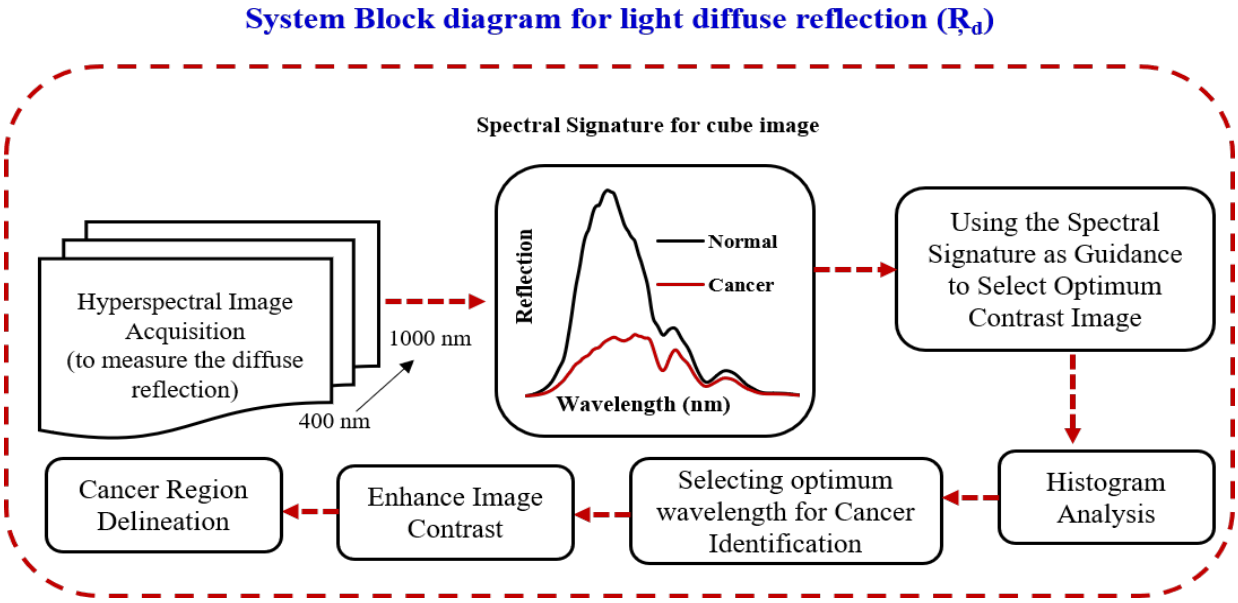


Fig. 3 The Image Processing Protocol for the System Setup to Measure the Optical Properties (Diffuse Reflection (R_d)) for *ex vivo* Breast Tissue Sample.

$$\omega(\text{ḍ}) = \acute{E}_0\,(1 - \text{Ṛ})\left(e^{(-(\mu_a-\mu_s)\text{ḍ})}\right), \quad (1)$$

where (μ_s) is the scattering attenuation, (μ_a) is the absorption attenuation, and $\omega(\text{ḍ})$ is the fluence rate for the un-scattered beam at position ḍ, $\acute{E}_0$ is the irradiance, and Ṛ is the Fresnel surface reflection.

$$\sigma = \frac{1}{(\mu_s+\mu_s)} = \frac{1}{\mu_t}, \quad (2)$$

where (μ_t) *is* the total attenuation coefficient and (σ) is the penetration depth

The light interaction of the light concerning the biological tissues is evaluated regarding the Transmission measurement (Ṭ), diffuse reflection (Ṛ_d), and calculated attenuation absorption (Ạ) [34], as presented in Eqs. (3) and (4).

$$\text{Ṭ} = \frac{\text{Ṭ}s-\text{Ṭ}_0}{\text{Ṭ}st-\text{Ṭ}_0}; \quad (3)$$

$$\text{Ṛ}_\text{d} = \frac{\text{Ṛ}d_s-\text{Ṛ}d_0}{\text{Ṛ}d_{st}-\text{Ṛ}d_0}, \quad (4)$$

where the measured light intensities by diffuse reflectance/transmittance are ($\frac{\text{Ṛ}d_s}{\text{Ṭ}_s}$) and ($\frac{\text{Ṛ}d_{st}}{\text{Ṭ}st}$) with the breast sample and the standard reflecting optical white plate respectively. The $\frac{\text{Ṛ}d_0}{\text{Ṭ}_0}$ demonstrates the captured background light intensity without a sample.

2.4 Spectral planning and Procurement

To capture the required HSI data, we utilized a Hyperspectral camera (Surface Optics, SOC710, USA) with a spectral resolution 4.68 nm corresponding to 600 × 502 pixels for the spectral cluster (the Cube image capturing time = 3.65 sec). The Hyperspectral camera covered overall 128 spectral clusters in range 379~1050 nm. The camera is incorporated with a lens (Schneider, 400~1000 nm, Germany). The exploited source light for the Hyperspectral image scan, polychromatic source light (Derungs, 150 W, 385~1050 nm, Germany). The image processing exploits DADiSP / SE software (DSP Development Co., 6.7 B02, 2020, USA) on a personal Laptop (DELL, Intel Core i7, USA).

An essential step before capturing the investigated breast samples with the Hyperspectral camera, to capture a white (fully reflective) cube image and dark cube image (closing the camera cap) to remove the unnecessary artifacts and background noise [60], as more illustrated in Eq. (5):

$$RF(\vartheta) = \frac{Si(\vartheta)-Di(\vartheta)}{Wi(\vartheta)-Di(\vartheta)} \times 100\%, \quad (5)$$

where $RF(\vartheta)$ is the relative diffuse reflectance of the sample image, $Si(\vartheta)$ is the sample cube image, $Di(\vartheta)$ is the dark cube image (closing the camera cap), and $Wi(\vartheta)$ is the capture a white (fully reflective) cube image.

Even though to cover the spectral range (400 to 1000 nm) we compute 128 frames with 4.68 nm resolution for each investigated breast sample. However, it is time-consuming and needs to make a lot of effort to analyze the 128 images, so from the one-dimensional (1D) signal of investigated breast samples, we optimize the wavelength ranges at which we can differentiate between the normal and the malignant to select the image around this wavelength.

Furthermore, to reduce the time of the image processing instead of the 128 frames, we examine the selection of the spectral image every 100 nm step, starting from 400 nm till 1000 nm. Where, the selected spectral images were (400, 500, 600, 700, 800, 900, 1000 nm), so we can choose the closest result wavelength. Afterward, pertaining statistical analysis (histogram) to select the optimum highest contrast and lowest contrast image. Finally, applying the custom subtraction algorithm to remove the DC background noise, image enhancement, and apply the K-mean segmentation with contour delineation of the variable threshold regions of the tumor regions in the breast sample.

Next, applying the normalization on the selected image to remove the unwanted spectral impact from the polychromatic light. The captured original images various due to the light, the irregular shape of the sample, and temperature variations, spectral images ought to be normalized including pixel normalization, as demonstrated in a previous study [46]. Then, applying the Moving average filter, the arithmetic means filter at kernel value 10 for noise reduction and image enhancement [61], as clarified in Eq. (6):

$$f(x \times y) = \frac{1}{qt} + \sum_{(\acute{r}\times c)\in W}^{\infty} S(\acute{r} \times c), \quad (6)$$

where S is the noisy image, $f(x \times y)$ is the restored image, and $\acute{r}$ and c for the row and column coordinates respectively, within a window W of size $q \times t$ where the process takes place.

Finally, to select the optimum image to distinguish between the normal and malignant regions, we pertaining statistical analysis (histogram), which is corresponding to the bar graph to graphically represents vital information for the spectral over discrete intervals [62–64], as illustrated in Eq. (7):

$$\mathcal{H} = \sum_{i=1}^{n} \mathcal{C}w_i \times fD_i, \quad (7)$$

where the Area of Histogram is ($\mathcal{H}$), the class width is ($\mathcal{C}w$), and the frequency density is (fD).

3 Results

In this section, we going to illustrate the fundamental investigation outcomes. The primary objective of these examinations is to highlight the system capability to discriminate between the normal and malignant tumors of investigated *ex vivo* breast samples utilizing the biological tissue's optical properties.

We established an optical imaging system exploiting a hyperspectral (HS) camera with source light at wavelength range (380~1050 nm), for measurement of breast sample light diffuse reflectance (R_d). To select the optimum wavelength which could be capable to differentiate between the normal and tumor precise regions in the *ex vivo* breast sample by exploring the optical properties spectroscopy in the near and visible (NIR–VIS) spectrum.

The raw data displayed in the graph of Fig. 4(a) signifies the typical spectral values of the measured diffuse reflectance (R_d) from selected points on the malignant and normal regions. Where the discrimination between the malignant and normal regions regarding the intensity versus the wavelength. However, to avoid this problem, the raw data was normalized to neglect the variation of the intensity and focusing on the spectral change to display the spectroscopic point measurements, as demonstrated in Fig. 4(b).

The experiment average outcomes demonstrated that from the raw data signal in Fig. 4 (a) the lowest measured (R_d) at wavelength 400 nm and after data normalization, there was noticeable variation at three ranges (630–680 nm), (720–770 nm), and (830–880 nm). The experiment was repeated on the whole Ten investigated samples to measure the (R_d) of the normal tissue as displayed in the worksheet in Fig. A2 in the Appendix and the magnified image for the combination (Rd) signals of the normal tissue for the Investigated Eight-Samples regards the source light reference, as shown in Fig. A2(i) in the Appendix. Furthermore, the measured (R_d) of the tumor tissue was presented in Fig. A3 in the Appendix and the magnified image for the combination (R_d) signals of the tumor regions for the Investigated Eight-Samples regards the source light reference, as presented in Fig. A2(i) in the Appendix.

Moreover, to validate the selected optimum wavelengths range from the signal of Fig. 4(b), we calculate the Standard Deviation (S_d) between the normal and cancer tissue spectrum signature with spectral step 40 nm, which shows that the highest contrast wavelength at 680 nm, as presented in Table 1.

The Combination of the Measured (R_d) Signals of the normal tissue and the tumor regions for the investigated Ten *ex vivo* breast samples were displayed in Fig. A4 in the Appendix. Moreover, the descriptive analysis of the average signals of the different investigated Ten *ex vivo* breast samples Fig. A4 to highlight the optimum wavelength to differentiate between the Normal tissue and the Tumor regions as illustrated in Table A2 in the appendix. Where Table 1 and Table A2 show that the highest contrast at the wavelength at 680 nm and the lowest contrast at wavelength 400 nm.

To cover the band from 400 to 1000 nm, we calculate 128 frames for each investigated sample with 4.68 nm resolution. However, it's difficult to process the 128 images, so to reduce the time of the image processing, we used the guidance data from the (1–D) signal at Fig. 4(b) and Fig. A4 in the Appendix beside the data from Table 1 and Table A2 in the Appendix. Furthermore, we examine the selection of the spectral image every 100 nm starting from 400 nm till 1000 nm. Then, applying the custom algorithm (Normalization and Moving average filter k = 10) to remove the background noise and enhance the image processing, beside neglecting the intensity effect to focus for the wavelength differentiation between the normal tissue and malignant regions, as shown in Fig. 5. We exploited the histogram analysis to select the optimum spectral image rather than the visual selection, as displayed in Fig. 5(h), Fig. 5(i), and more clarified in Fig. A5 in the Appendix.

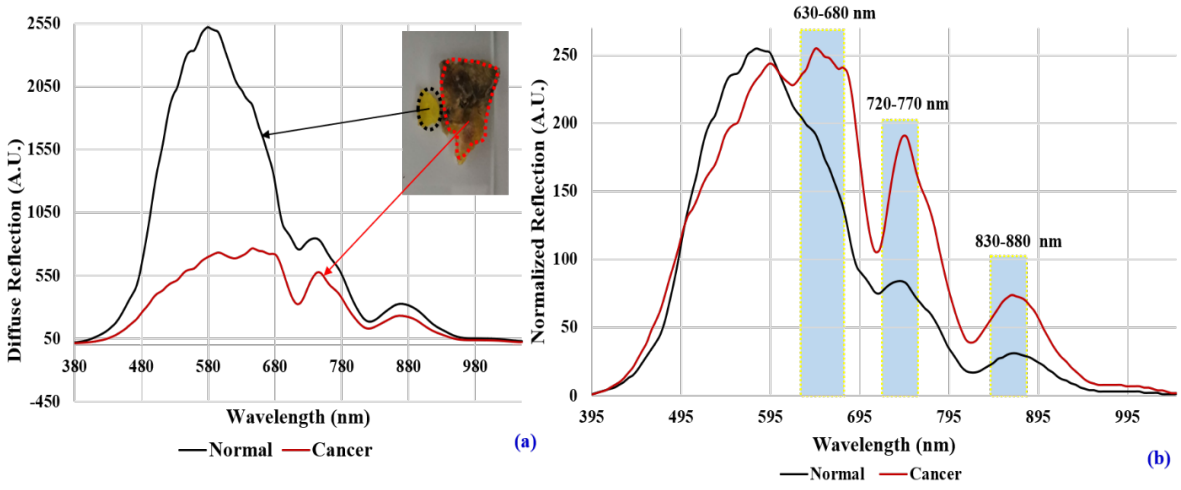


Fig. 4 (a) The raw data of the diffuse reflectance (R_d) measurements of both the normal (black line) and cancer (red line) *ex vivo* breast sample over the whole spectrum range; (b) the diffuse reflectance (R_d) measurements after applying normalization to the raw data to neglect the intensity effect and focus on the wavelength differentiation highlighting the three noticeable ranges (630–680 nm), (720–770 nm), and (830–880 nm).

Table 1 The measured diffuse reflectance (R_d) of the *ex vivo* breast sample of the breast tissue to highlight the highest contrast between the normal and cancer tissue at the various spectrum range.

Wavelength (nm)	**400**	**440**	**480**	**520**	**560**	**600**	**640**
Breast tissue reflection (R_d)	40.2	174.2	695.3	1777.9	2334.9	2420.5	1933.9
Cancer tissue reflection (R_d)	23.3	80.1	270.8	466.9	607.2	727.1	745.8
(S_d) after Normalization	0.001	4.243	12.02	19.09	25.46	2.12	37.48

Wavelength (nm)	**680**	**720**	**760**	**800**	**840**	**880**	**920**
Breast tissue reflection (R_d)	1236.6	783.6	729.8	570.4	241.0	311.6	144.3
Cancer tissue reflection (R_d)	711.9	372.5	499.8	383.2	175.1	221.6	100.2
(S_d) after Normalization	79.903	30.406	65.56	26.16	22.63	28.99	11.31

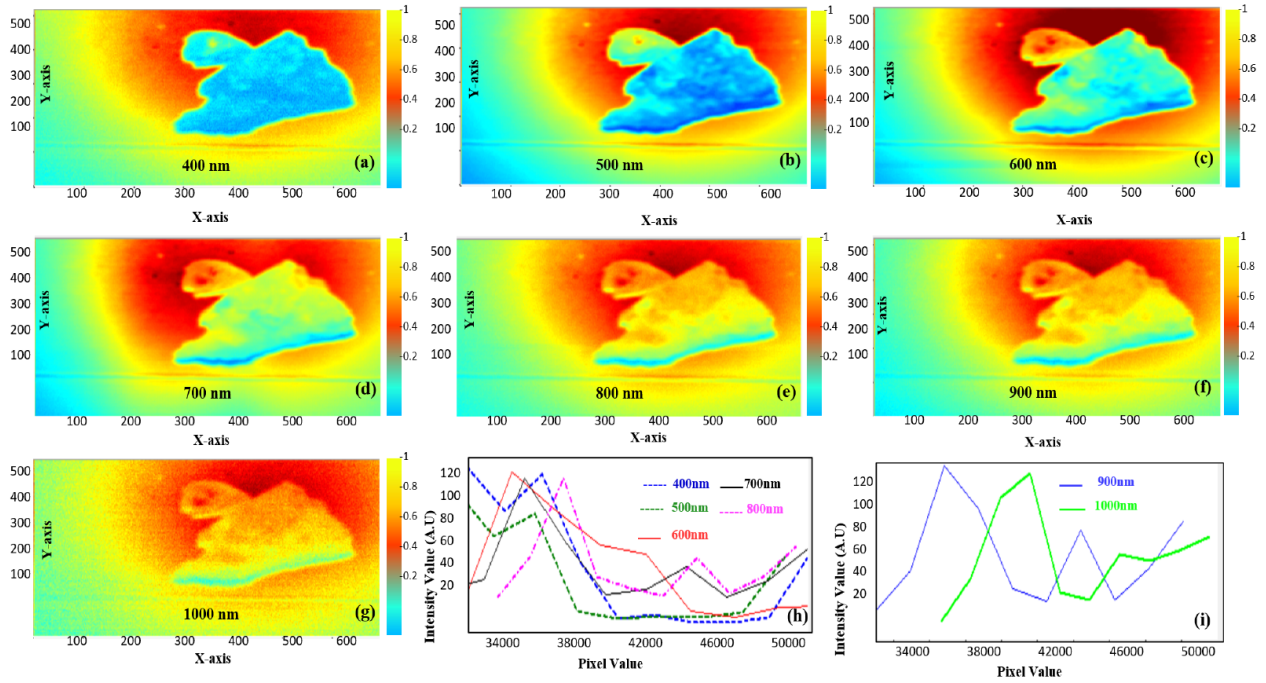


Fig. 5 The hyperspectral image of the investigated breast samples at wavelength range (400~1000 nm); (a) the captured *ex vivo* breast sample image at wavelength 400 nm, (b) wavelength 500 nm, (c) wavelength 600 nm, (d) wavelength 700 nm, (e) wavelength 800 nm, (f) wavelength 900 nm, (g) wavelength 1000 nm, (h) comparing the image contrast at wavelengths (400–800 nm) by the histogram analysis to distinguish between the normal tissue and the malignant regions, (i) the histogram analysis at wavelengths (900–1000 nm).

From the histogram analysis, we could select the optimum spectral image with the highest contrast at the wavelength (600 nm) and the lowest contrast image (400 nm) to apply our custom subtraction algorithm to remove the DC background noise, image enhancement, then apply the K-mean segmentation (K = 8). Finally, the contour delineation of the variable threshold regions of the tumor regions in the breast sample, as illustrated in Fig. 6. For more clarification we apply the algorithm, on the whole, investigated samples are displayed in Fig. A6, Fig. A7, and Fig. A8 in the Appendix.

4 Discussion

There are an escalating interest in enlightening breast malignant identification methods that exploiting clinical imaging devices regarding its efficient therapeutic of breast tumors depending upon its proper and early detection [9]. Essentially, we could identify malignant early before the primary tumor metastasizes [5].

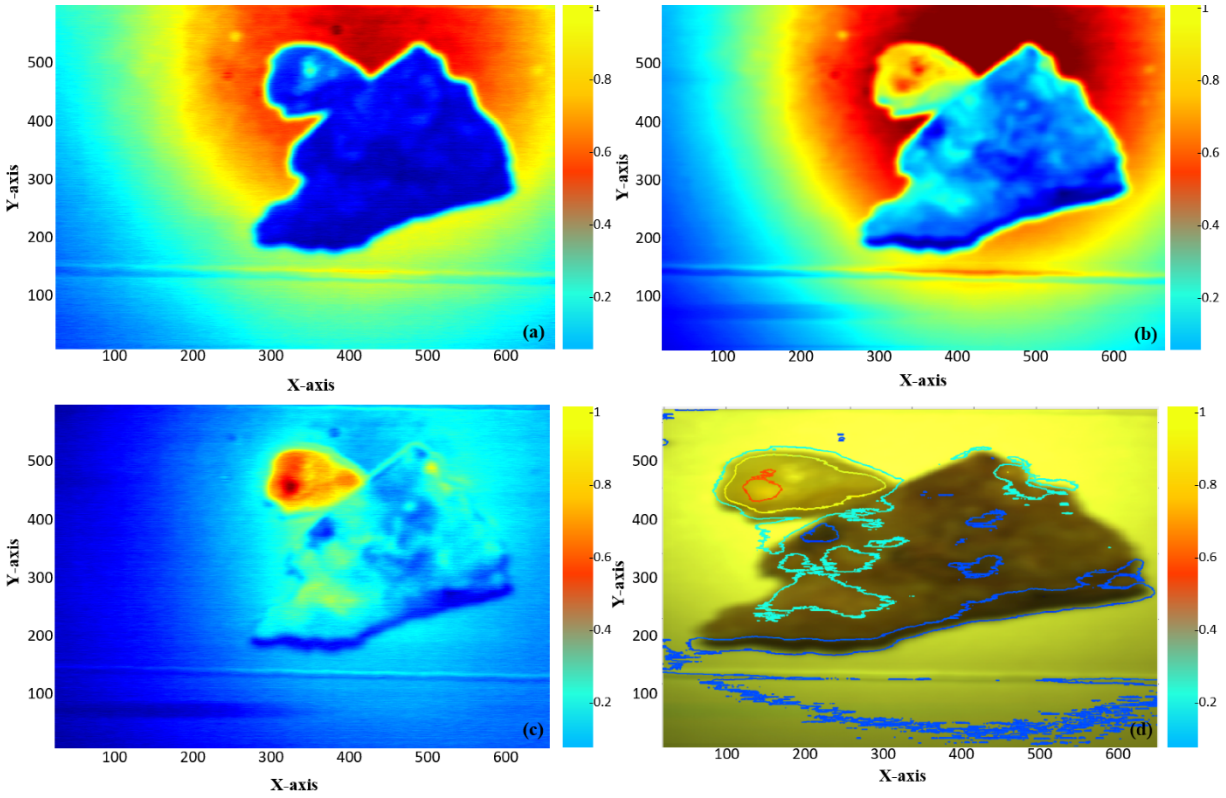


Fig. 6 The investigated *ex vivo* breast sample #1 after applying the image processing, (a) the HS image of the breast sample at wavelength 400 nm, (b) the HS image of the breast sample at wavelength at 600 nm, (c) the spectral difference by subtraction of the HS image at wavelength 600 from the image at wavelength 400 nm to remove the DC background noise, (d) the contour delineation of the tumor variable threshold regions of in the breast sample.

Conventional methods for pathological investigations rely on the manual examination of morphological indicators of the samples by qualified pathologists. Where computer-aided diagnostic (CAD) systems could enhance the results and minimize the time of investigations [16]. Such innovations are planned to improve the diagnosis, make it reproducible and quantitative, and reduce time consumption in the assessment of samples [18].

During recent years, numerous investigations have been executed on the early recognition of malignant growth utilizing noninvasive methods in lieu of customary excisional biopsy. The HSI technology had been exploited in the detection of gastric tumors [65, 66], prostate cancer [67], an integrated endoscopic system with a hyperspectral camera to detect colorectal cancer [68], and breast cancer [45, 47].

We established an optical system setup exploiting a hyperspectral (HS) camera with a range (400~100 nm) with poly-chromatic source lights with wavelength (380~1050 nm), as shown in Fig. 2(a). Measuring the diffuse reflection (R_d) of the ten-investigated *ex vivo* breast sample to select the optimum spectral image to differentiate between the normal and tumor in the near infra-red and visible (NIR–VIS) spectrum.

The raw data of the measured (R_d) for the investigated *ex vivo* breast sample were displayed in Fig. 4(a), which emphasize the differentiation between the normal tissue and cancer region in range (550~650 nm). However, to avoid the variations of the intensity regarding the difference of the tissue optical properties we normalized the signals. To neglect the effect of the intensity and to evaluate the wavelength differentiation of the investigated samples, we normalized the measured initial data and focused on the spectral variations, as displayed in Fig. 4(b). We noticed that the wavelength range (395–495 nm) was almost identical and the variation between the normal and cancer was barely small. Additionally, there was noticeable variation in three ranges (630–680 nm), (720–770 nm), and (830–880 nm).

The experiment was repeated on the whole ten investigated *ex vivo* breast samples to measure the (R_d) of the normal tissue as displayed in the worksheet in Fig. A2 in the Appendix. Although, the worksheet displayed only eight different signals (cannot display more than 9-windows at the same time) in Fig. A2(a) to Fig. A2(h) for sample #1 to sample #8, Consecutively. The magnified image for the combination (R_d) signals of the normal tissue for the investigated eight-samples regards the source light reference was shown in Fig. A2(i) in the Appendix. Furthermore, the measured (R_d) of the tumor tissue was presented in Fig. A3 in the Appendix and the magnified image for the combination (R_d) signals of the tumor regions for the investigated eight-samples regards the source light reference, as presented in Fig. A2(i) in the Appendix.

Moreover, to validate the selected optimum wavelength range from the measured signal of Fig. 4(b),

we calculated the standard deviation ($Ş_d$) between the normal and cancer tissue spectrum signature with spectral step 40 nm, as presented in Table 1. Furthermore, the combination of the measured ($Ŗ_d$) signals regarding the normal tissue and the tumor regions for the investigated ten *ex vivo* breast samples were displayed in Fig. A4 in the Appendix. Additionally, we calculated the descriptive analysis of the average signals from Fig. A4 to highlight the optimum wavelength for differentiation between the normal tissue and the tumor regions as illustrated in Table A2. However, Table 1 and Table A2 show that the highest contrast wavelength for differentiation at 680 nm and the lowest contrast wavelength at 400 nm.

Although to cover the band from 400 to 1000 nm, we calculate 128 frames with 4.68 nm resolution. However, it is difficult and time-consuming to process the 128 images, so to reduce the time of the image processing, we used the guidance data from the (1-D) signal at Fig. 4(b) and Fig. A4 in the Appendix beside the data from Table 1 and Table A2 in the Appendix leading to the selection of the spectral image every 100 nm step, starting from 400 nm till 1000 nm, as noticed from the investigation that 100 nm as a step in the illustrating signal was enough, so we can choose the closest result wavelength, as more clarified in Fig. 5.

After applying the custom algorithm (normalization and moving average filter k = 10) to remove the background noise and enhance the image processing, besides neglecting the intensity effect on the selected spectral images (400, 500, 600, 700, 800, 900, 1000 nm). We noticed visually from Fig. 5, that spectral images at wavelength 600 nm and 700 nm were in higher contrast to identifying the tumor region. However, for more validation, we exploited the histogram analysis to distinguish between the normal tissue and the malignant regions, as shown in Fig. 5(h) and Fig. 5(i) and more illustrated in Fig. A5 in the Manuscript Appendix. Where, from the histogram analysis it identifies that the spectral image at 600 nm was higher in contrast and with minimum noise in the image processing, which provides us with better information to differentiate between normal tissue and tumor regions.

Although after selecting the optimum spectral image from the histogram analysis, we apply the image processing to improve the image contrast. Where, the highest contrast image at a wavelength (600 nm), as shown in Fig. 6(a), and the lowest contrast image at a wavelength (400 nm), as shown in Fig. 6(b). Next, applying the custom subtraction algorithm to remove the DC background noise, as display in Fig. 6(c). Furthermore, applying K-mean segmentation (K=8), and contour delineation for the variable threshold regions of the breast tumor regions, as illustrated in Fig. 6 (d).

Finally, repeating the same previous process on the whole various investigated samples to validate the algorithm reliability and ensure its reproducibility for the given features between the various samples of the same class, as displayed in Fig. A6, Fig. A7, and Fig. A8 in the Appendix.

Although, the worksheets of the investigated sample #2, sample #3, and sample #4 identified the two high contrast images at wavelengths (600 nm and 700 nm) with respect to the lowest contrast image at wavelength 400 nm. However, after enhancing the contrast of the spectral image we noticed that the optimum image in differentiation between the normal tissue and the malignant regions was more identified at wavelength 600 nm, as shown in Fig. A6(e), Fig. A7(e), and Fig. A8(e) in the Appendix. Next, applying the subtraction algorithm on the investigated samples to highlight the contour mapping of the variable threshold regions of the tumors, as displayed in Fig. A6(i), Fig. A7(i), and Fig. A8(i) in the Appendix.

The output result of the custom algorithm on the investigated samples was validated by comparing its results with respect to the pathological report. Where, the investigated RGB image of the *ex vivo* breast sample #1 and sample #3 were displayed in Fig. A9 (a) and Fig. A10(a), respectively in the Appendix. The result of the applied custom algorithm is shown in Fig. A (b) and Fig. A10(b) in the Appendix.

5 Conclusion

The presented approach reveals promising results regards the diagnostic applications of breast cancer to assist the pathologist and in the real-time investigations for assisting the surgeons. Where experiment results clarify that the optimum wavelength at 680 nm for diagnostic applications and the ideal spectral image at 600 nm to discriminate between the normal and malignant tissue. In Future work, we going to update the system hardware like the HS camera and expanding the source light wavelength range. Moreover, we could utilize a Q – switched pulsed laser with a custom optical system (686.9 nm) for breast tumor ablation without normal tissue damage.

Disclosures

The authors stated and declare that No funders for this study. The authors stated and declare that No conflict or competing of interests. All experimental and investigation trails was approved and validated from “Ain Shams University” – Medical College - Ethics Committee. No experimental investigation was performed on individuals within this research study. All the co-authors are agreed for the research study publication. The authors stated and declare that all data is exist and available. The authors stated and declare that all the source codes are available.

References

1. C. Review, "Global, Regional, and National Cancer Incidence, Mortality, Years of Life Lost, Years Lived With Disability, and Disability- Adjusted Life-years for 32 Cancer Groups, 1990 to 2015 A Systematic Analysis for the Global Burden of Disease Study," JAMA Oncology 3(4), 524–548 (2017).
2. F. Bray, J. Ferlay, I. Soerjomataram, R. L. Siegel, L. A. Torre, and A. Jemal, "Global cancer statistics 2018: GLOBOCAN estimates of incidence and mortality worldwide for 36 cancers in 185 countries," CA: A Cancer Journal for Clinicians 68(6) 394–424 (2018).
3. R. L. Siegel, K. D. Miller, and A. Jemal, "Cancer statistics, 2019," CA: A Cancer Journal for Clinicians 69(1), 7–34 (2019).
4. K. Saika, T. Sobue, "Cancer statistics in the world," Gan To Kagaku Ryoho 40, 2475–2480 (2013).
5. R. Siegel, D. Naishadham, and A. Jemal, "Cancer statistics, 2013," CA: A Cancer Journal for Clinicians 63, 11–30 (2013).
6. J. Shan, H.D. Cheng, J. Shan, W. Ju, Y. Guo, and L. Zhang, "Automated breast cancer detection and classification using ultrasound images : A survey Automated breast cancer detection and classification using ultrasound images : A survey," Pattern Recognition 43(1), 299–317 (2010).
7. D. Saravanan, D. Joseph, and S. Vaithyasubramanian, "Effective utilization of image information using data mining technique," in Recent Trends and Advances in Artificial Intelligence and Internet of Things, V. Balas, R. Kumar, R. Srivastava (eds.), Springer, Cham, 207–215 (2020).
8. S. Alrahbi, P. M. Y. Chan, B. C. S. Ho, M. D. W. Seah, J. J. C. Chen, and E. Y. Tan, "Extent of margin involvement, lymphovascular invasion, and extensive intraductal component predict for residual disease after wide local excision for breast cancer," Clinical Breast Cancer 15, 219–226 (2015).
9. A. L. Merrill, S. B. Coopey, R. Tang, M. P. McEvoy, M. C. Specht, K. S. Hughes, M. A. Gadd, and B. L. Smith, "Implications of New Lumpectomy Margin Guidelines for Breast-Conserving Surgery: Changes in Reexcision Rates and Predicted Rates of Residual Tumor," Annals of Surgical Oncology 23, 729–734 (2016).
10. S. Alrahbi, P. M. Y. Chan, B. C. S. Ho, M. D. W. Seah, J. J. C. Chen, and E. Y. Tan, "Extent of margin involvement, lymphovascular invasion, and extensive intraductal component predict for residual disease after wide local excision for breast cancer," Clinical Breast Cancer 15(3), 219–226 (2015).
11. E. Kho, B. Dashtbozorg, L. L. de Boer, K. K. Van de Vijver, H. J. C. M. Sterenborg, and T. J. M. Ruers, "Broadband hyperspectral imaging for breast tumor detection using spectral and spatial information," Biomedical Optics Express 10(9), 4496 (2019).
12. R. G. Pleijhuis, M. Graafland, J. De Vries, J. Bart, J. S. De Jong, and G. M. Van Dam, "Obtaining Adequate Surgical Margins in Breast-Conserving Therapy for Patients with Early-Stage Breast Cancer : Current Modalities and Future Directions," Annals of Surgical Oncology 16, 2717–2730 (2009).
13. E. L. Vos, A. Jager, C. Verhoef, A. C. Voogd, and L. B. Koppert, "Overall survival in patients with a re-excision following breast conserving surgery compared to those without in a large population-based cohort," European Journal of Cancer 51(3), 282–291 (2015).
14. C. D. Runowicz, C. R. Leach, N. L. Henry, K. S. Henry, H. T. Mackey, R. L. Cowens-Alvarado, R. S. Cannady, M. L. Pratt-Chapman, S. B. Edge, and L. A. Jacobs, "American cancer society/American society of clinical oncology breast cancer survivorship care guideline," CA: A Cancer Journal for Clinicians 66(1), 43–73 (2016).
15. S. L. Van Es, "Digital pathology: semper ad meliora," Pathology 51(1), 1–10 (2019).
16. A. Madabhushi, G. Lee, "Image analysis and machine learning in digital pathology: Challenges and opportunities," Medical Image Analysis 33, 170–175 (2016).
17. T. J. Flotte, D. A. Bell, "Anatomical pathology is at a crossroads," Pathology 50(4), 373–374 (2018).
18. J. J. Keating, C. Fisher, R. Batiste, and S. Singhal, "Advances in intraoperative margin assessment for breast cancer," Current Surgery Reports 4(4), 15 (2016).
19. K. Butler-Henderson, A. H. Lee, R. I. Price, and K. Waring, "Intraoperative assessment of margins in breast conserving therapy: A systematic review," Breast 23(2), 112–119 (2014).
20. E. R. St John, R. Al-Khudairi, H. Ashrafian, T. Athanasiou, Z. Takats, D. J. Hadjiminas, A. Darzi, and D. R. Leff, "Diagnostic accuracy of intraoperative techniques for margin assessment in breast cancer surgery," Annals of surgery 265(2), 300–310 (2017).
21. D. P. A. Versteegden, L. G. G. Keizer, L. E. M. Duijm, C. A. P. Wauters, and L. J. A. Strobbe, "Performance characteristics of specimen radiography for margin assessment for ductal carcinoma in situ : a systematic review," Breast Cancer Research and Treatment 166, 669–679 (2017).
22. K. Esbona, Z. Li, and L. G. Wilke, "Intraoperative imprint cytology and frozen section pathology for margin assessment in breast conservation surgery: a systematic review," Annals of surgical oncology 19(10), 3236–3245 (2012).

23. F. K. Althoubaity, A. Merdad, N. Y. Akeel, N. H. Zaidi, and A. O. Sultan, "Frozen Section Analysis of Breast Lumpectomy Margins," Surgical Science 8(6), 269–277 (2017).
24. I. Journal, O. Medical, A. Yilmaz, M. Bayrak, K. Ozerkan, and H. Ozan, "Accuracy of Intraoperative Frozen Section Analysis in Borderline Ovarian Tumor and the Factors Affecting It," International Journal of Medical Science and Clinical Invention 7(9), 7–12 (2020).
25. H. J. C. M. Sterenborg, E. Kho, L. L. de Boer, K. K. van de Vijver, and T. M. Ruers, "Hyperspectral imaging for intraoperative margin assessment during breast cancer surgery," in Asia Communications and Photonics Conference, AF1K-6 (2016).
26. A. Sahu, Hyperspectral Imaging to Discern Malignant and Benign Canine Mammary Tumors, Master Thesis, Temple University, Philadelphia, USA (2012).
27. L. Ma, G. Lu, D. Wang, X. Qin, Z. G. Chen, and B. Fei, "Adaptive deep learning for head and neck cancer detection using hyperspectral imaging," Visual Computing for Industry, Biomedicine, and Art 2(1), 18 (2019).
28. M. H. Fouad Aref, A. A. R. Sharawi, and Y. H. El-Sharkawy, "Delineation of the Arm Blood Vessels Utilizing Hyperspectral Imaging to Assist with Phlebotomy for Exploiting the Cutaneous Tissue Oxygen Concentration," Photodiagnosis and Photodynamic Therapy 33, 102190 (2021).
29. H. Zhao, R. H. Webb, and B. Ortel, "A new approach for noninvasive skin blood imaging in microcirculation," Optics & Laser Technology 34(1), 51–54 (2002).
30. U. Rubins, A. Grabovskis, J. Cimurs, Z. Marcinkevics, and A. Caica, "Hyperspectral evaluation of skin blood oxygen saturation at baseline and during arterial occlusion," Proceedings of SPIE 10685, 106851A (2018).
31. T. Delineation, H. Fabelo, S. Ortega, R. L. Id, D. M. Id, G. M. Callic, E. Ju, D. Bulters, H. B. Id, A. Szolna, J. F. Piñeiro, C. Sosa, A. J. O. Shanahan, S. Bisshopp, D. Ravi, B. R. Kiran, A. Vega, B. Abelardo, G. Yang, and B. Stanciulescu, "An Intraoperative Visualization System Using Hyperspectral Imaging to Aid in Brain," Sensors 18(2), 430 (2018).
32. M. H. Aref, I. H. Aboughaleb, and Y. H. El-Sharkawy, "Tissue characterization utilizing hyperspectral imaging for liver thermal ablation," Photodiagnosis and Photodynamic Therapy 31, 101899 (2020).
33. N. Yavari, Optical spectroscopy for tissue diagnostics and treatment control, Doctoral Thesis, University of Bergen, Norway (2006).
34. J. R. Mourant, J. P. Freyer, A. H. Hielscher, A. A. Eick, D. Shen, and T. M. Johnson, "Mechanisms of light scattering from biological cells relevant to noninvasive optical-tissue diagnostics," Applied Optics 37(16), 3586-3593 (1998).
35. M. Li, Developing a technique for combining light and ultrasound for deep tissue imaging, Master Thesis, Lund University, Sweden (2018).
36. V. Tuchin, "Tissue Optics and Photonics: Light-Tissue Interaction II," Journal of Biomedical Photonics & Engineering 2(3), 030201 (2016).
37. K. G. Wakim, "Physiology of the liver," The American Journal of Medicine 16(2), 256–271 (1954).
38. M. H. Aref, "Biomedical Research and Clinical Reviews," Biomedical Research and Clinical Reviews 1, 1–13 (2020).
39. S. Swierczynski, F. Primavesi, E. Klieser, T. Kiesslich, T. Jäger, R. Illig, D. Neureiter, D. Ofner, and S. Stättner, "382. Thermographic monitoring of radiofrequency and microwave ablation in a perfused porcine liver model," European Journal of Surgical Oncology 40(11), S147 (2014).
40. M. De Landro, M. Barberio, E. Felli, V. Agnus, M. Pizzicannella, M. Diana, and P. Saccomandi, "Hyperspectral image-based analysis of thermal damage in living liver undergoing laser ablation," Proceedings of SPIE 11362, 113620G (2020).
41. R. Sucher, A. Athanasios, H. Köhler, T. Wagner, M. Brunotte, A. Lederer, I. Gockel, and D. Seehofer, "Hyperspectral Imaging (HSI) in anatomic left liver resection," International Journal of Surgery Case Reports 62, 108–111 (2019).
42. M. De Landro, P. Saccomandi, M. Barberio, E. Schena, S. Member, and M. Diana, "Hyperspectral imaging for thermal effect monitoring in in vivo liver during laser ablation Hyperspectral imaging for thermal effect monitoring in in vivo liver during laser ablation," In 2019 41st Annual International Conference of the IEEE Engineering in Medicine and Biology Society, 1851–1854 (2019).
43. M. A. Calin, S. V. Parasca, D. Savastru, and D. Manea, "Hyperspectral imaging in the medical field: present and future," Applied Spectroscopy Reviews 49(6), 435–447 (2014).
44. M. Aref, I. H. Aboughaleb, A.-B. Youssef, and Y. El-Sharkawy, "Novel Approach Exploiting the Hyperspectral Imaging System for Breast Cancer Therapy and Diagnosis," Archives of Breast Cancer 7(4), 189–201 (2020).
45. I. H. Aboughaleb, M. H. Aref, and Y. H. El-Sharkawy, "Photodiagnosis and Photodynamic Therapy Hyperspectral imaging for diagnosis and detection of ex-vivo breast cancer," Photodiagnosis and Photodynamic Therapy 31, 101922 (2020).
46. M. H. Aref, I. H. Aboughaleb, and Y. H. El-Sharkawy, "Custom optical imaging system for ex-vivo breast cancer detection based on spectral signature," Surgical Oncology 35, 547–555 (2020).
47. T. D. O. Sullivan, A. E. Cerussi, D. J. Cuccia, B. J. Tromberg, T. D. O. Sullivan, A. E. Cerussi, D. J. Cuccia, and B. J. Tromberg, "Diffuse optical imaging using spatially and temporally modulated light Diffuse optical imaging using spatially and temporally," Journal of Biomedical Optics 17(7), 071311 (2012).

48. F. Baum, "1 Development, Anatomy, and Physiology of the Mammary Gland," Breast Cancer: Diagnostic Imaging and Therapeutic Guidance, 1–3 (2017).
49. H. Ellis, V. Mahadevan, "Anatomy and physiology of the breast," Surgery (Oxford) 31(1), 11–14 (2013).
50. S. Pandya, R. G. Moore, "Breast development and anatomy," Clinical obstetrics and gynecology 54(1), 91–95(2011).
51. G. Mostafa, L. Cathey, and F. L. Greene (Eds.), Breast Anatomy, in Review of Surgery, Springer, New York, 161–162 (2006).
52. C. Frantz, K. M. Stewart, and V. M. Weaver, "The extracellular matrix at a glance," Journal of Cell Science 123(24) 4195–4200 (2010).
53. T. R. Cox, J. T. Erler, "Remodeling and homeostasis of the extracellular matrix: Implications for fibrotic diseases and cancer," Disease Models and Mechanisms 4(2), 165–178 (2011).
54. R. G. Aswathy, Y. Yoshida, "Near-infrared quantum dots for deep tissue imaging," Analytical and Bioanalytical Chemistry 397, 1417–1435 (2010).
55. C. Bremer, "Fluorescence imaging with near-infrared light : new technological advances that enable in vivo molecular imaging," European Radiology 13, 195–208 (2003).
56. Q. Miao, K. Pu, "Organic Semiconducting Agents for Deep-Tissue Molecular Imaging : Second Near-Infrared Fluorescence," Advanced Materials 30(49), 1801778 (2018).
57. R. J. DiPerna, P. L. Lions, "Ordinary differential equations, transport theory and Sobolev spaces," Inventiones mathematicae 98, 511–547 (1989).
58. K. Rinzema, L. H. P. Murrer, and W. M. Star, "Direct experimental verification of light transport theory in an optical phantom," Journal of the Optical Society of America A 15(8), 2078–2088 (1998).
59. S. S. M. Noor, K. Michael, S. Marshall, and J. Ren, "Hyperspectral image enhancement and mixture deep-learning classification of corneal epithelium injuries," Sensors 17(11), 2644 (2017).
60. V. Kumar, P. Gupta, "Importance of Statistical Measures in Digital Image Processing," International Journal of Emerging Technology and Advanced Engineering 2(8), 56–62 (2012).
61. S. Engineering, J. Zhang, and J. Hu, "Image Segmentation Based on 2D Otsu Method with Histogram Analysis," In 2008 International Conference on Computer Science and Software Engineering 6, 105–108 (2008).
62. M. D. Abràmoff, P. J. Magalhães, and S. J. Ram, "Image processing with ImageJ," Biophotonics International 11(7), 36–42 (2004).
63. O. Holub, S. T. Ferreira, "Quantitative histogram analysis of images," Computer Physics Communications 175(9), 620–623 (2006).
64. H. Akbari, K. Uto, Y. Kosugi, K. Kojima, and N. Tanaka, "Cancer detection using infrared hyperspectral imaging," Cancer Science 102(4), 852–857 (2011).
65. S. Kiyotoki, J. Nishikawa, T. Okamoto, K. Hamabe, M. Saito, A. Goto, Y. Fujita, Y. Hamamoto, Y. Takeuchi, S. Satori, and I. Sakaida, "New method for detection of gastric cancer by hyperspectral imaging: a pilot study," Journal of Biomedical Optics 18(2), 026010 (2013).
66. M. Nathan, A. S. Kabatznik, and A. Mahmood, "Hyperspectral imaging for cancer detection and classification," In 2018 3rd Biennial South African Biomedical Engineering Conference, 1–4 (2018).
67. R. Kumashiro, K. Konishi, T. Chiba, T. Akahoshi, S. Nakamura, M. Murata, M. Tomikawa, T. Matsumoto, Y. Maehara, and M. Hashizume, "Integrated endoscopic system based on optical imaging and hyperspectral data analysis for colorectal cancer detection," Anticancer Research 36(8), 3925–3932 (2016).
68. I. H. Aboughaleb, M. H. Aref, and Y. H. El-Sharkawy, "Hyperspectral imaging for diagnosis and detection of ex-vivo breast cancer," Photodiagnosis and Photodynamic Therapy 31, 101922 (2020).

Appendix: Characterization of Normal and Malignant Breast Tissues utilizing Hyperspectral Images and Associated Differential Spectrum Algorithm

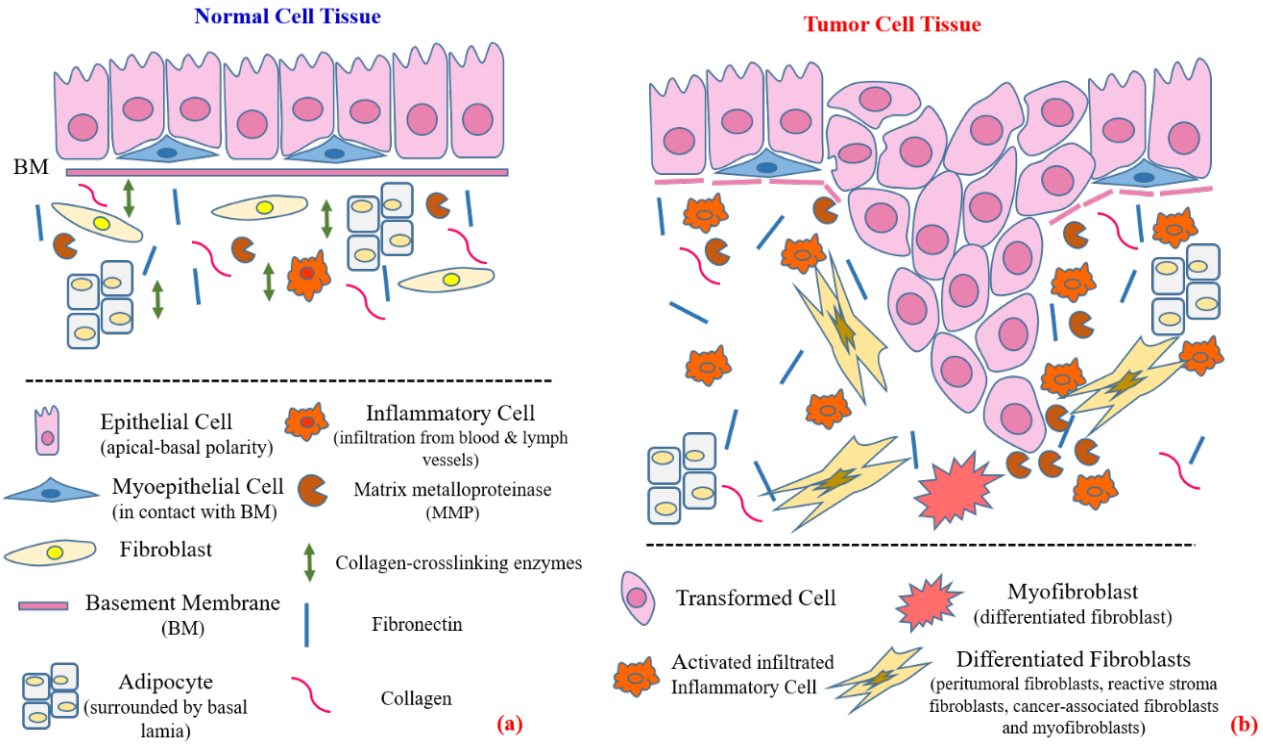


Fig. A1 The function and the structure of the extracellular matrix to highlight the effect of changing tissues in changing the movement of light and its reflections; (a) normal breast cell tissue; (b) tumor breast cell tissue.

Table A1 The patient data for the investigated samples exploited in the presented study.

No	Patient ID	Age (years)	Breast Density	Breast Cancer Type	Pathological Report	Tumor Phase	Score
	Patient#1001	49	Type D	Invasive Ductal Carcinoma (IDC)	Malignant	Phase I (≥4cm in diameter)	Score III
	Patient#1002	53	Type C	Invasive Ductal Carcinoma (IDC)	Malignant	Phase III (>4cm in diameter but confined to the breast)	Score II
	Patient#1003	49	Type D	Invasive Ductal Carcinoma (IDC)	Malignant	Phase II (<4cm in diameter)	Score I
	Patient#1004	54	Type B	Invasive Ductal Carcinoma (IDC)	Malignant	Phase II (<4cm in diameter)	Score II
	Patient#1005	60	Type C	Invasive Ductal Carcinoma (IDC)	Malignant	Phase II (<4cm in diameter)	Score I
	Patient#1006	65	Type D	Invasive Ductal Carcinoma (IDC)	Malignant	Phase II (<4cm in diameter)	Score II
	Patient#1007	46	Type D	Invasive Ductal Carcinoma (IDC)	Malignant	Phase III (>4cm in diameter but confined to the breast)	Score I
	Patient#1008	58	Type D	Invasive Ductal Carcinoma (IDC)	Malignant	Phase II (<3cm in diameter)	Score II
	Patient#1009	50	Type B	Invasive Ductal Carcinoma (IDC)	Malignant	Phase I (<2cm in diameter)	Score I
	Patient#1010	56	Type C	Invasive Ductal Carcinoma (IDC)	Malignant	Phase III (>3cm in diameter but confined to the breast)	Score II

Tumor Score:
Score I – Well differentiated.
Score II – Moderately differentiated.

Tumor Phase:
Phase I – The Breast Cancer is ≤ 2 cm diameter and the Tumor has not spread beyond the breast.
Phase II – The Breast Cancer is 2 ~4 cm diameter or malignant cells have spread to the lymph nodes in the underarm area.
Phase III – The Breast Cancer is widespread identified; however, it is confined to the breast, surrounding tissues.

Breast Density with respect to the "American College of Radiology (ACR):
Type A Fatty Breast.
Type B Scattered Density Breast.
Type C Heterogeneously Density Breast.
Type D Extremely Density Breast.

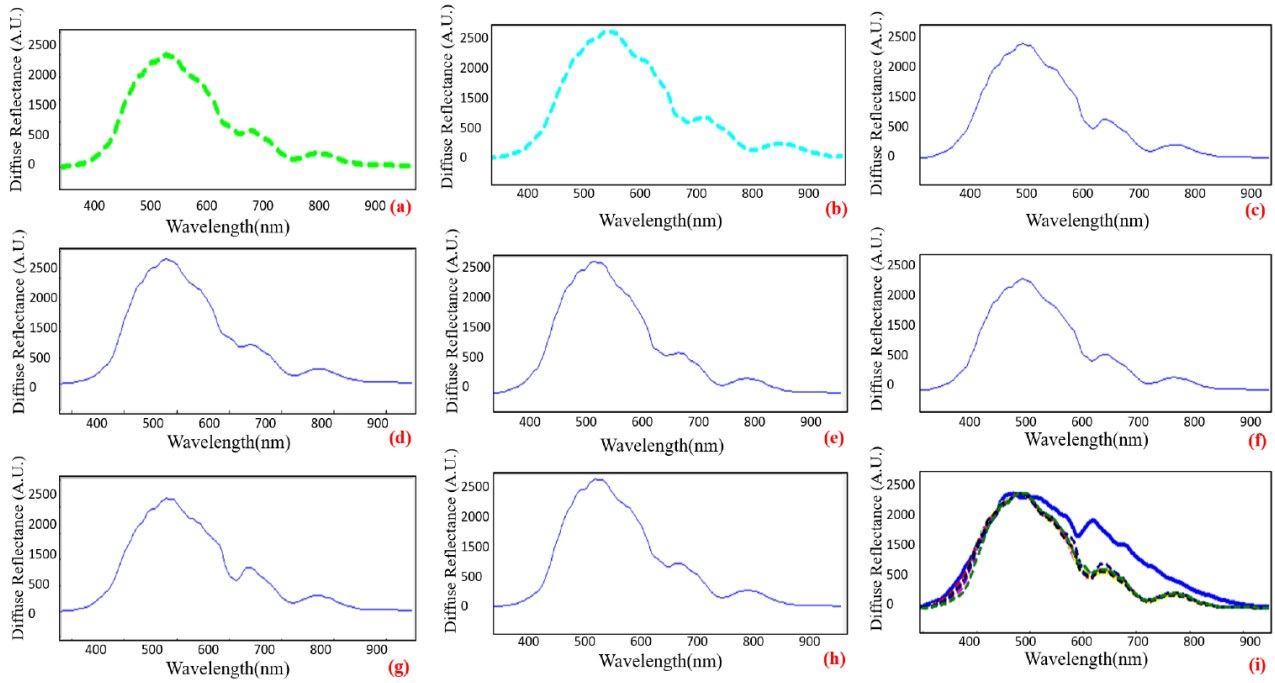


Fig. A2 The Worksheet for the Measured Diffuse Reflection (R_d) of the normal tissue for Different Eight-investigated *ex vivo* breast samples highlighting the system reliability; (a) The measured (R_d) for the normal tissue of Sample #1 , (b) The measured (R_d) for the normal tissue of Sample #2, (c) The measured (R_d) for the normal tissue of Sample #3, (d) The measured (R_d) for the normal tissue of Sample #4, (e) The measured (R_d) for the normal tissue of Sample #5, (f) The measured (R_d) for the normal tissue of Sample #6, (g) The measured (R_d) for the normal tissue of Sample #7, (h) The measured (R_d) for the normal tissue of Sample #8, (i) The combination of the whole signals hilighting the measured (R_d) for the normal tissue of the investigated eight-samples regards the source light reference.

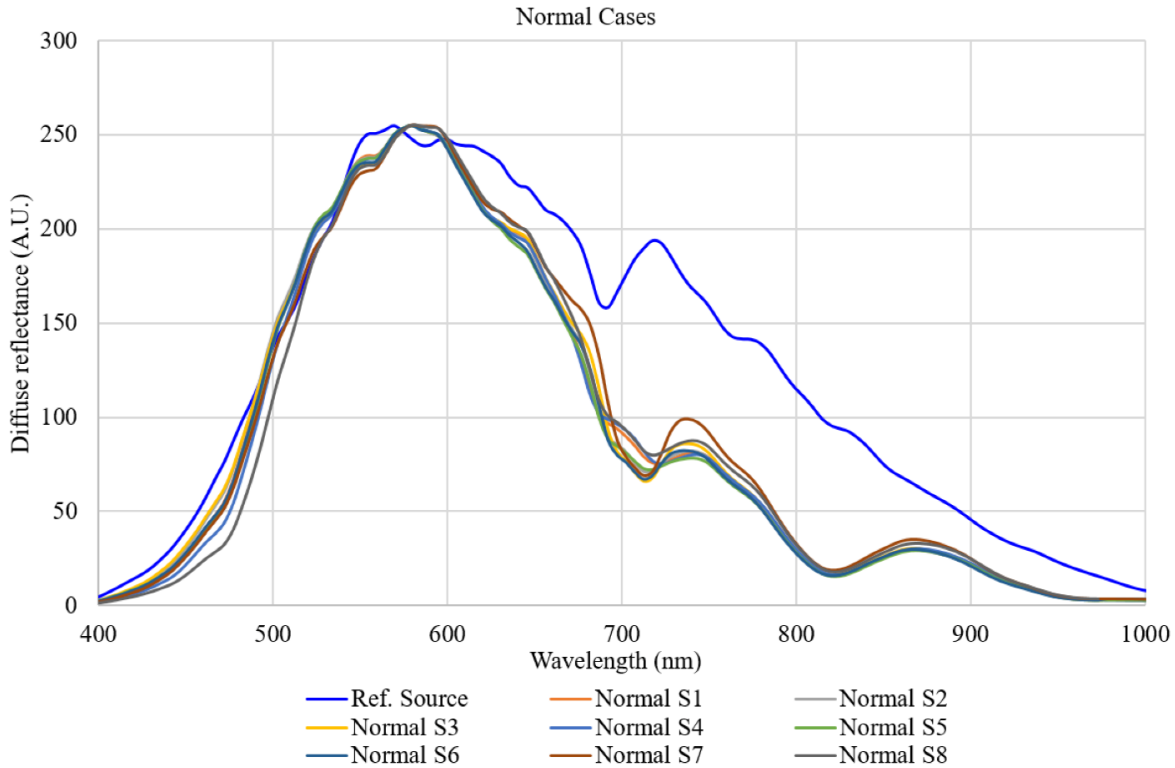


Fig. A2 (i) The magnified image for the combination diffuse reflection (R_d) signals of the normal tissue for the investigated eight-samples regards the source light reference.

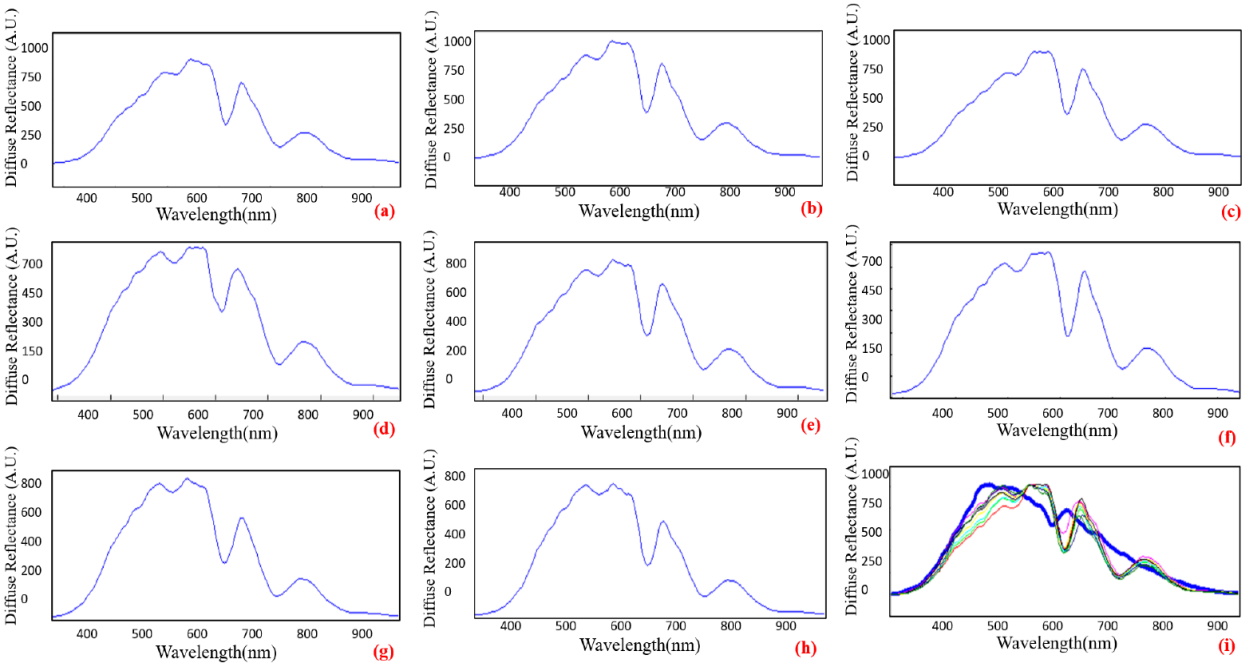


Fig. A3 The worksheet for the measured diffuse reflection (R_d) of the tumor tissue for different eight-investigated *ex vivo* breast samples highlighting the system reliability; (a) the measured (R_d) for the tumor tissue of Sample #1, (b) the measured (R_d) for the tumor tissue of Sample #2, (c) the measured (R_d) for the tumor tissue of Sample #3, (d) the measured (R_d) for the tumor tissue of Sample #4, (e) the measured (R_d) for the tumor tissue of Sample #5, (f) the measured (R_d) for the tumor tissue of Sample #6, (g) the measured (R_d) for the tumor tissue of Sample #7, (h) the measured (R_d) for the tumor tissue of Sample #8, (i) the combination of the whole signals hilighting the measured (R_d) for the tumor tissue of the investigated eight-samples regards the source light reference.

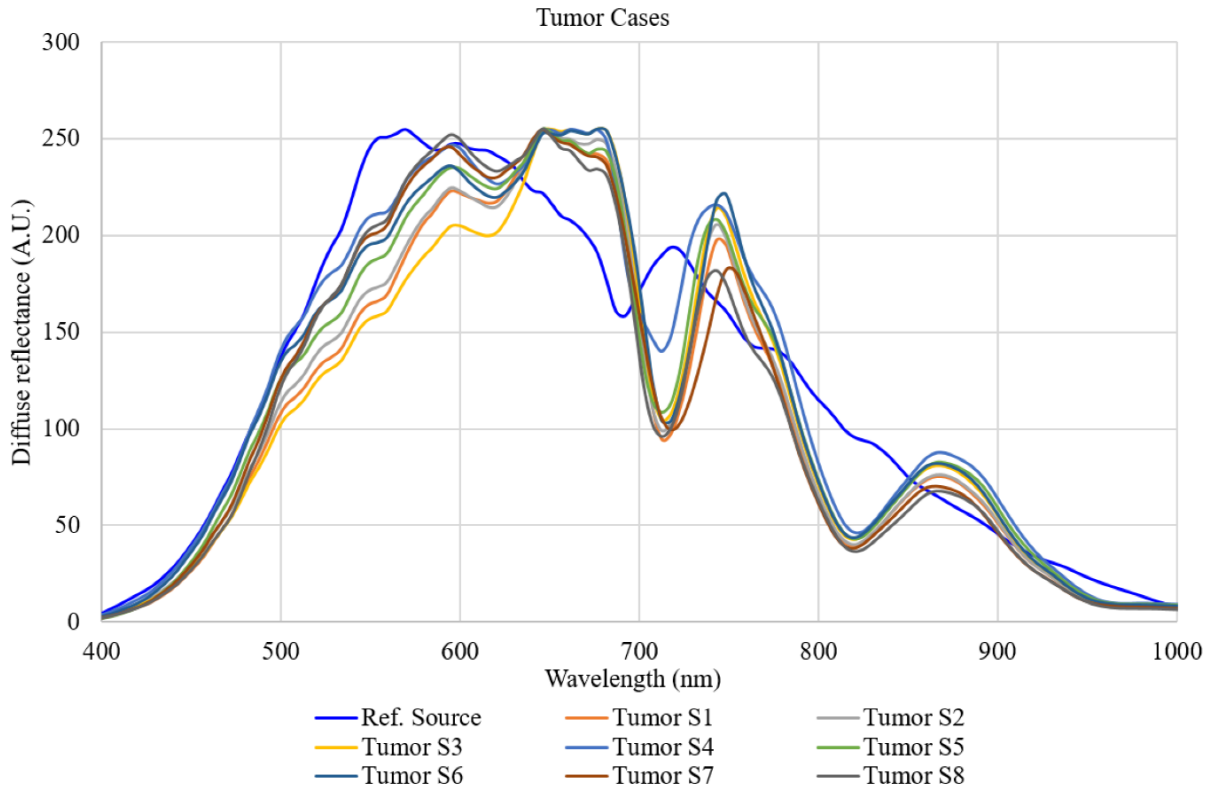


Fig. A3 (i) The magnified image for the combination diffuse reflection (R_d) signals of the tumor tissue for the investigated eight-samples regards the source light reference.

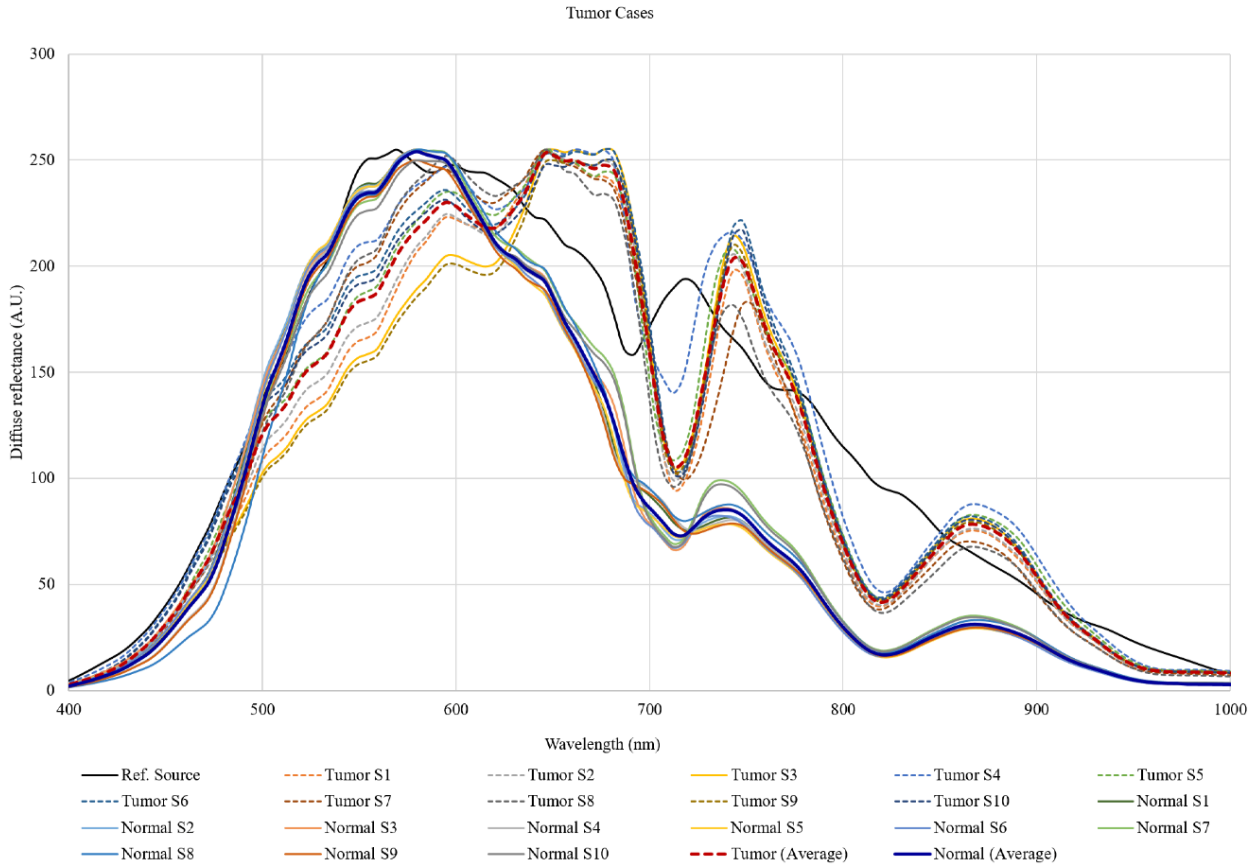


Fig. A4 The combination of the measured diffuse reflection (Rd) signals for the investigated normal tissue regions and the tumor regions of the ten ex-vivo breast samples with respect to the source light reference.

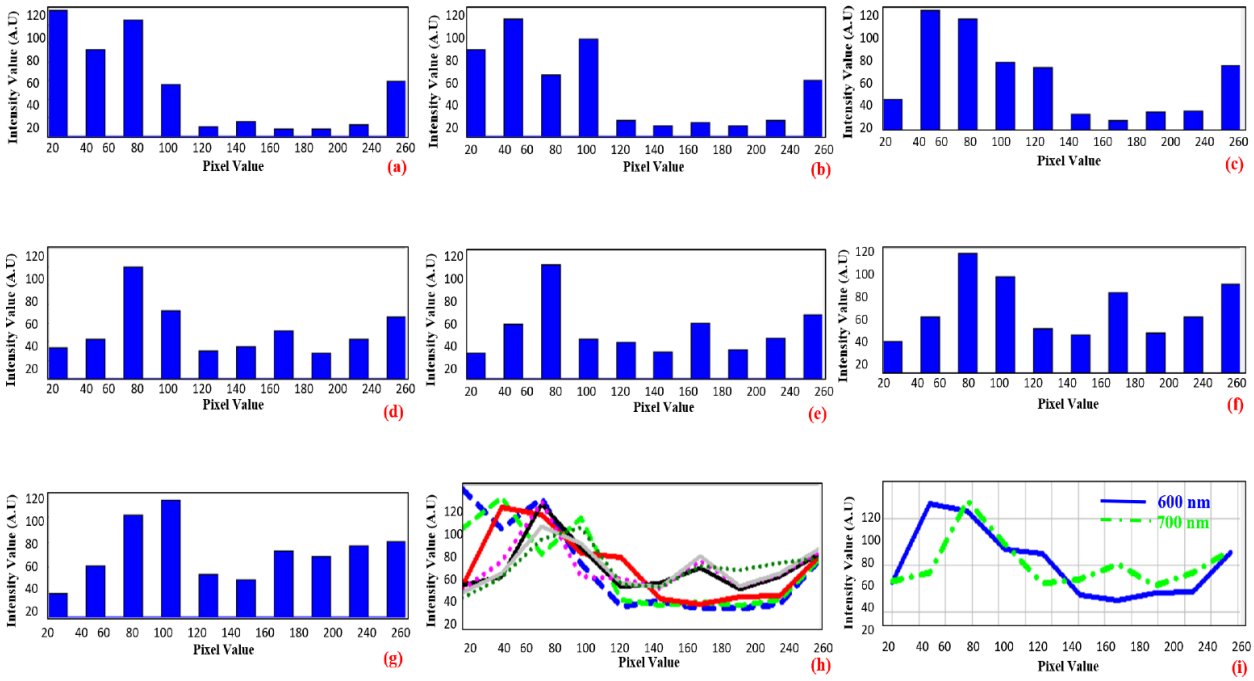


Fig. A5 The histogram of the selected spectral images, (a) spectral image of the investigated sample at wavelength 400 nm, (b) wavelength 500 nm, (c) wavelength 600 nm, (d) wavelength 700 nm, (e) wavelength 800 nm, (f) wavelength 900 nm, (g) wavelength 1000 nm, (h) the histogram analysis of the seven spectral images (400–1000 nm), (i) the histogram analysis of the spectral image at wavelength (600 nm and 700 nm).

Table A2 The descriptive analysis of the average signals of the different investigated ten *ex vivo* breast samples to highlight the optimum wavelength to differentiate between the normal tissue and the tumor regions.

Wavelength	400	440	480	520	560	600	640
Mean	2.6	20.2	80.1	163.5	211.3	235.8	220.5
Standard Error	0.4	2.3	3.6	18.7	23.9	7.6	24.4
Median	2.6	20.2	80.1	163.5	211.3	235.8	220.5
Standard Deviation ($Ş_d$)	0.5	3.2	5.1	26.4	33.8	10.7	34.5
Sample Variance	0.3	10.5	25.8	699.6	1139.4	115.0	1191.7
Range	0.7	4.6	7.2	37.4	47.7	15.2	48.8
Minimum	2.2	17.9	76.6	144.8	187.4	228.2	196.1
Maximum	3.0	22.5	83.7	182.2	235.1	243.3	244.9
Sum	5.2	40.4	160.3	327.0	422.6	471.5	440.9

Wavelength	680	720	760	800	840	880	920
Mean	185.4	99.4	115.4	50.8	40.2	51.5	21.1
Standard Error	59.6	22.7	47.2	20.1	17.5	21.9	8.6
Median	185.4	99.4	115.4	50.8	40.2	51.5	21.1
Standard Deviation ($Ş_d$)	84.3	32.1	66.8	28.4	24.8	31.0	12.2
Sample Variance	7101.5	1027.2	4459.2	807.9	615.2	963.1	147.7
Range	119.2	45.3	94.4	40.2	35.1	43.9	17.2
Minimum	125.8	76.7	68.2	30.7	22.7	29.6	12.5
Maximum	245.0	122.0	162.6	70.9	57.8	73.5	29.7
Sum	370.8	198.8	230.8	101.5	80.5	103.1	42.2

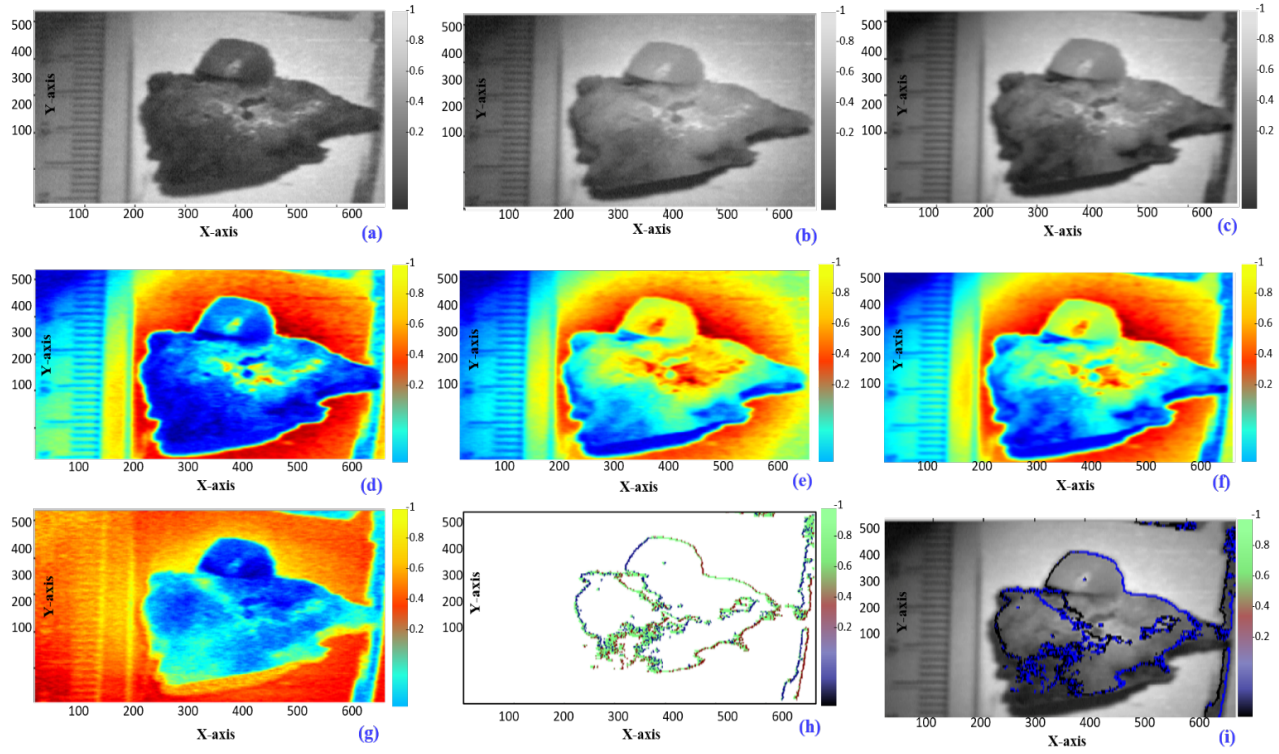


Fig. A6 The worksheet of the investigated *ex vivo* breast Sample #2 to demonstrate the reliability of the applied custom subtraction algorithm to differentiate between the normal tissue and the tumor regions, (a) the *ex vivo* breast sample at wavelength 400 nm, (b) the *ex vivo* breast sample at wavelength 600 nm, (c) the *ex vivo* breast sample at wavelength 700 nm, (d) image enhancement and noise reduction to the scanned to the investigated sample at wavelength 400 nm, (e) image enhancement and noise reduction to the scanned to the investigated sample at wavelength 600 nm, (f) image enhancement and noise reduction to the scanned to the investigated sample at wavelength 700 nm, (g) the subtraction algorithm between the lowest contrast image 400 nm and the highest contrast image 600 nm, (h) the K-mean clustering and the contour mapping of the investigated image, (i) the delineation of the tumor regions applied on the *ex vivo* breast Sample #2.

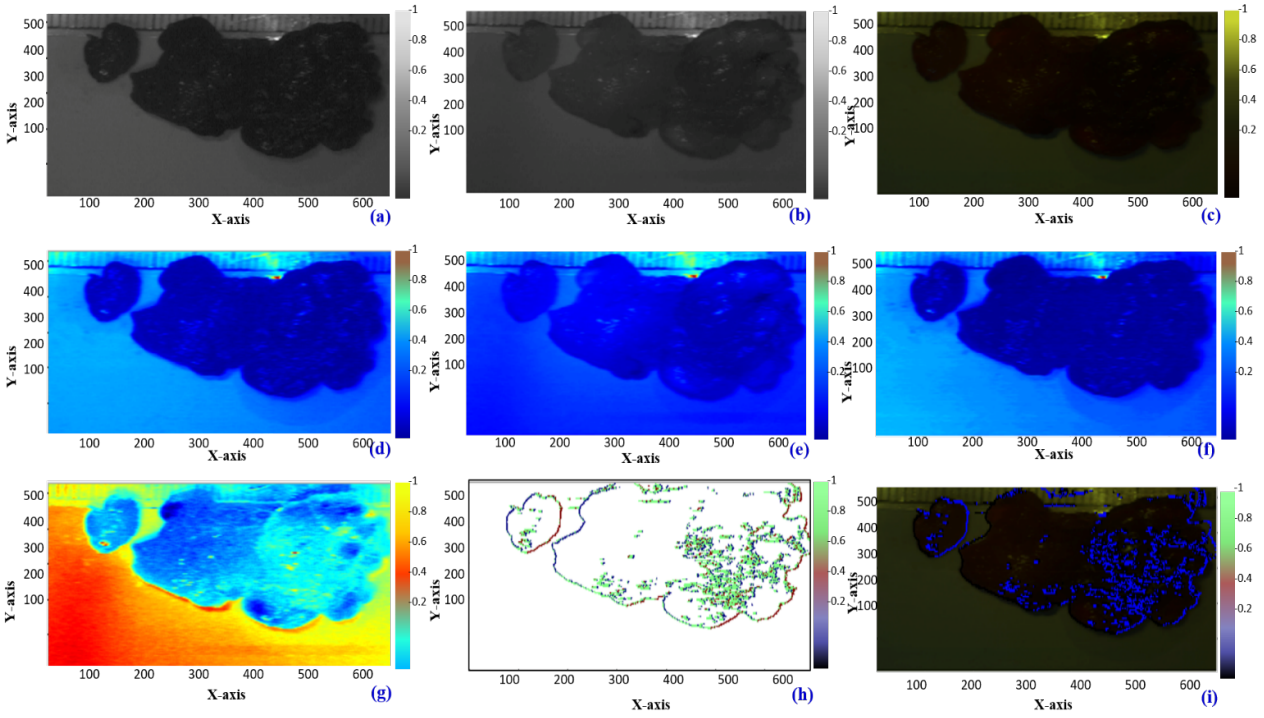


Fig. A7 The worksheet of the investigated *ex vivo* breast sample #3 to demonstrate the reliability of the applied custom subtraction algorithm to differentiate between the normal tissue and the tumor regions, (a) the *ex vivo* breast sample at wavelength 400 nm, (b) the *ex vivo* breast sample at wavelength 600 nm, (c) the *ex vivo* breast sample at wavelength 700 nm, (d) image enhancement and noise reduction to the scanned to the investigated sample at wavelength 400 nm, (e) image enhancement and noise reduction to the scanned to the investigated sample at wavelength 600 nm, (f) image enhancement and noise reduction to the scanned to the investigated sample at wavelength 700 nm, (g) the subtraction algorithm between the lowest contrast image 400 nm and the highest contrast image 600 nm, (h) the K-mean clustering and the contour mapping of the investigated image, (i) the delineation of the tumor regions applied on the *ex vivo* breast Sample #3.

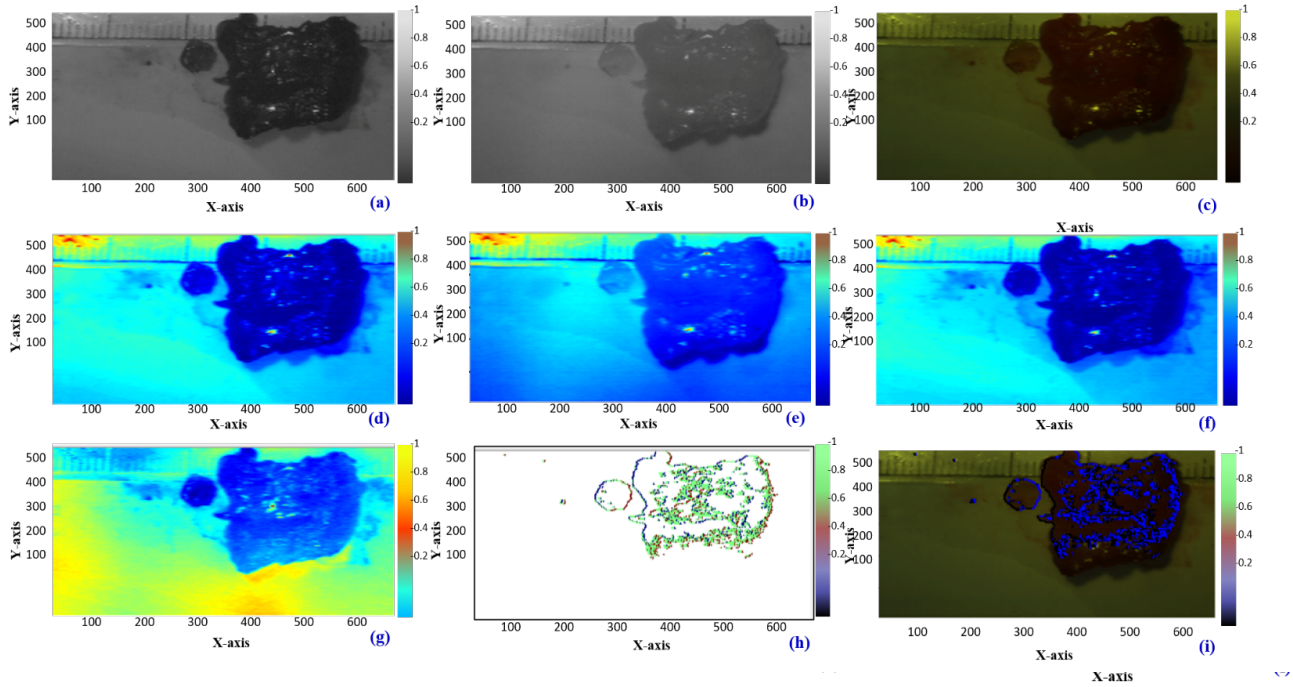


Fig. A8 The worksheet of the investigated *ex vivo* breast Sample #4 to demonstrate the reliability of the applied custom subtraction algorithm to differentiate between the normal tissue and the tumor regions, (a) the *ex vivo* breast sample at wavelength 400 nm, (b) the *ex vivo* breast sample at wavelength 600 nm, (c) the *ex vivo* breast sample at wavelength 700 nm, (d) image enhancement and noise reduction to the scanned to the investigated sample at wavelength 400 nm, (e) image enhancement and noise reduction to the scanned to the investigated sample at wavelength 600 nm, (f) image enhancement and noise reduction to the scanned to the investigated sample at wavelength 700 nm, (g) the subtraction algorithm between the lowest contrast image 400 nm and the highest contrast image 600 nm, (h) the k-mean clustering and the contour mapping of the investigated image, (i) the delineation of the tumor regions applied on the *ex vivo* breast Sample #4.

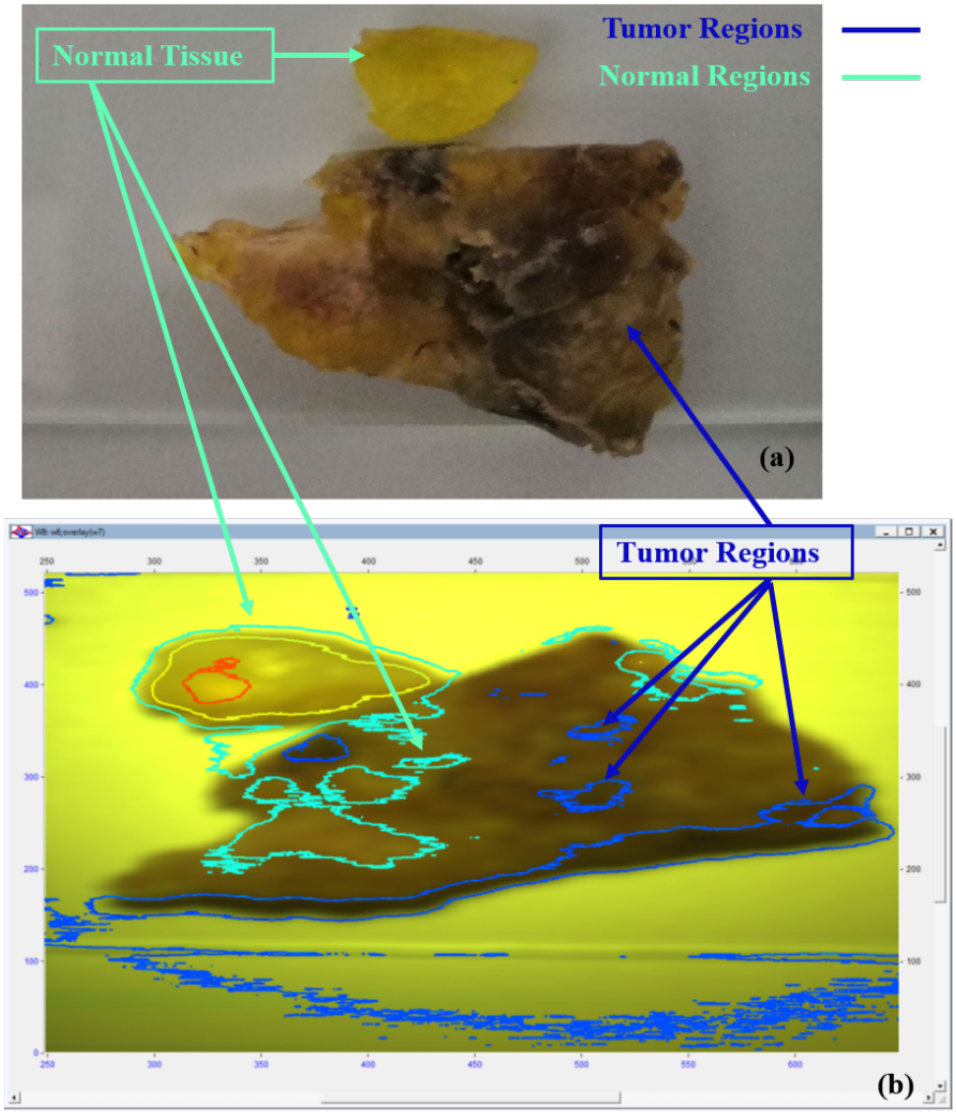


Fig. A9 (a) The investigated RGB image of the *ex vivo* breast Sample #1, (b) the hyperspectral scan image regions after applying the custom algorithm to highlight and contour mapping the normal regions and the various tumor regions.

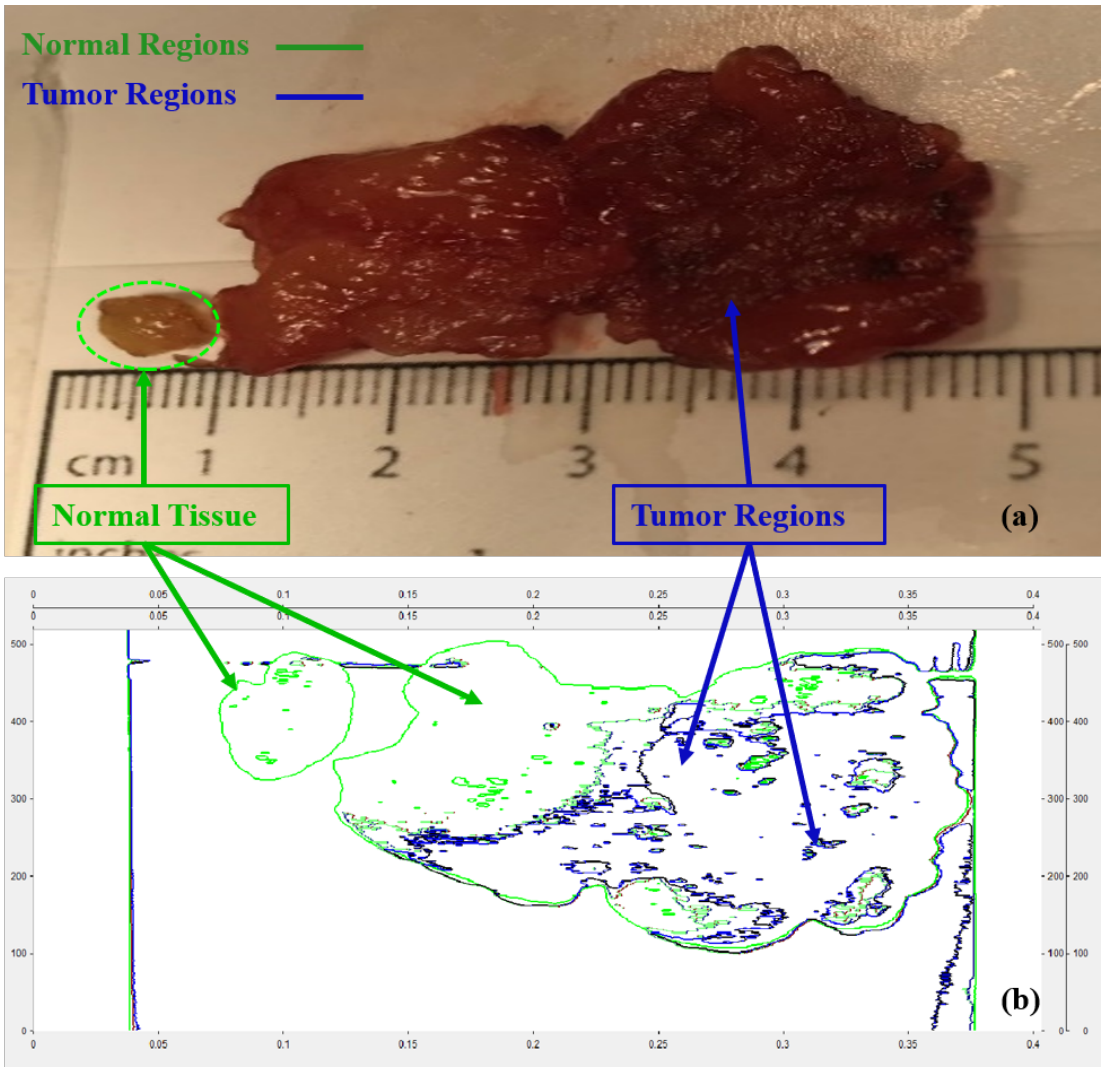


Fig. A10 (a) The investigated RGB image of the *ex vivo* breast Sample #3, (b) the contour mapping of the hyperspectral scan image after applying the custom algorithm to highlight the normal regions and the various tumor regions.

Estimation of Rabbit Pancreas Dispersion Between 400 and 1000 nm

Inês Martins[1,2], Hugo Silva[1,2], Valery V. Tuchin[3,4,5], and Luís Oliveira[1,2*]

[1] Physics Department, School of Engineering, Polytechnic Institute of Porto,
Rua Dr. António Bernardino de Almeida 431, 4249-015 Porto, Portugal

[2] Center of Innovation in Engineering and Industrial Technology, ISEP, Rua Dr. António Bernardino de Almeida 431, 4249-015 Porto, Portugal

[3] Science Medical Center, Saratov State University, 83 Astrakhanskaya str.,
Saratov 410012, Russian Federation

[4] Interdisciplinary Laboratory of Biophotonics, National Research Tomsk State University, 36 Lenin's av.,
Tomsk 634050, Russian Federation

[5] Laboratory of Laser Diagnostics of Technical and Living Systems, Precision Mechanics and Control Institute of the Russian Academy of Sciences, 24 Rabochaya str., Saratov 410028, Russian Federation

*** e-mail:** lmo@isep.ipp.pt

Abstract. Current biophotonics methods cover the entire optical spectrum from the deep ultraviolet to the terahertz. To optimize such methods for diagnostic and therapeutic applications, the need to obtain the wideband dispersion of tissues is high. The pancreas is a very important organ in the human body, since it produces insulin and its malfunction may induce diabetes. A reduced number of biophotonics publications regarding the pancreas is available, meaning that studies to determine its optical properties and their variation during optical clearing treatments are necessary. Considering this fact, we used the total internal reflection method to measure the refractive index of the rabbit pancreas for wavelengths between 400 and 850 nm. The experimental results allowed to calculate the pancreas dispersion with the Cauchy, Conrady and Cornu equations. It was observed that all those equations provided good data fitting in the spectral range of the measurements, but differences were observed outside these limits. Considering the wavelength of 633 nm, the mean value from the three dispersions was 1.3521, while the one published for porcine pancreas is 1.3517. The dispersion calculated with the Conrady equation does not present a fast decreasing behavior for shorter wavelengths as the ones calculated with the Cauchy and Cornu equations, but comparing these curves with a dispersion for a tissue-like material, all seem to have good agreement. © 2021 Journal of Biomedical Photonics & Engineering.

Keywords: pancreas tissue; refractive index; total internal reflection; tissue dispersion.

Paper #3409 received 13 Mar 2021; revised manuscript received 8 Apr 2021; accepted for publication 12 Apr 2021; published online 8 May 2021. doi: 10.18287/JBPE21.07.020303.

1 Introduction

Among the various optical properties of biological tissues, the refractive index (RI) is one of the most important and fundamental, since it can be used for many biophotonics applications. If, from one hand, the RI can be a practical measurement to mark pathologies [1–3], it is needed, on the other hand, to estimate the other optical properties through inverse simulations [4], to correct optical coherence tomography (OCT) or microscopy

images [5–7] and to optimize light tissue interactions in diagnostic or treatment procedures [8–10].

Clinical applications of light can be made at various wavelengths within a very wide spectral range that goes from the deep ultraviolet (UV) to the terahertz (THz) [11]. Consequently, the determination of tissue's dispersions for a broad range of wavelengths is of great interest.

The evaluation of tissues' dispersions is also of great interest for the application of optical clearing (OC) treatments, since the exchange of interstitial tissue water by an optical clearing agent (OCA) induces RI variations that will be responsible for the light scattering decrease and consequent increase in tissue transparency [12]. For such particular application, the knowledge of the tissue dispersion and of the dispersions of its components is highly important [13, 14].

While in the THz range, direct RI measurement of biological tissues and OCAs for a wide spectral range is possible [15, 16], in the ultraviolet-near infrared (UV–NIR) range such methodology is not possible, and dispersion calculations must be made from discrete measurements [4, 17–19]. There are some distinct methods to measure the RI of biological samples at discrete wavelengths, such as the ones based on interferometer or ellipsometer setups [20], but the most commonly used nowadays are the ones that use multi-wavelength refractometers [18] or the total internal reflection setup to be used with various lasers at different wavelengths [21]. Other techniques to measure the RI of biological tissues and the importance of these measurements for optical diagnosis have also been recently described [22]. Although the multi-wavelength refractometers provide results with better precision, the setup based on the total internal reflection method can be easily implemented in any optics laboratory at a reduced cost. Another benefit of this method is that additional wavelengths can be selected for measurement, provided that lasers are available at those wavelengths. The total internal reflection was first proposed by Li and Xie in 1996 to measure the RI of biological tissues [21], and it has been widely used since then to measure the RI and estimate the correspondent dispersions for various tissues, such as human normal and pathological colorectal tissues [23, 24], human normal and pathological liver tissues [19, 25], porcine skin [26], or human skin [27]. An improvement to this setup was presented by Deng et al in 2015 [28], which allows a fast determination of the continuous wavelength dependence of the biological materials' RI for a limited spectral range. Such setup, uses a broad-band xenon lamp and a spectrometer to perform measurements [29], making it beneficial for a fast dispersion calculation, but it uses more expensive instrumentation.

Pancreas is an organ that plays an important role in human and animal physiology. It is responsible for the production of insulin that prevents the occurrence of diabetes [30]. Pancreatic cancer, on the other hand, although rare, has presented an increasing number of cases over the years [31]. Due to the lack of early-diagnostic and treatment procedures, the pancreatic cancer is highly lethal. Although some reviews on treatment methods for this pathology have been carried out, the results have been disappointing [32]. Pancreatic ductal adenocarcinoma (PDAC) is the type of cancer with the most lethal malignancies in humans, where a huge percentage of the patients presents an advanced stage and a life expectancy less than 1 year after diagnosis. This problem is largely due to the low number of immunotherapy and drug approaches that target driver mutations [33]. An identification of the risk factors and an early diagnosis are very important to improve overall survival. There are some risk factors that have been reported, like the pancreatic duct dilation, chronic pancreatitis, pancreatic cyst, intraductal papillary mucinous neoplasia (IPMN), and the deterioration of diabetes mellitus [34]. In comparison to other cancers, pancreatic cancer has a wide range of metastatic diseases, like carcinomas at the time of diagnosis, from localized 1–2 cm primary tumors to diffuse carcinomatosis within and outside the abdomen [35].

Regarding biophotonics, pancreas is one of the biological organs that is less studied. From the few optical studies on pancreas, there is one regarding OCT imaging of pancreas with needles for in-depth image acquisition [36], and another that suggests the potential of tissue optical spectroscopy to characterize the human pre-cancerous neoplasms in human pancreatic tissues [37]. A third study has been reported [38], showing the visible spectra for the measured fluorescence and for the estimated absorption and reduced scattering coefficients from human pancreatic tissues (normal, adenocarcinoma and pancreatitis) for comparison.

More recently, two other pancreas-related papers have been published. These papers [39, 40], report on studies about blood microcirculation and blood flow monitoring in rat pancreas with alloxan diabetes by laser speckle contrast imaging, and show that the disease development in animals induces changes in the microcirculatory system response to the application of optical clearing solutions.

The improvement of such techniques or the development of new optical approaches for pancreas imaging or spectroscopy, with particular interest in the early pancreatic cancer detection, can be achieved with the help of OC treatments. To proceed with the study of pancreas tissues under OC treatments, it is necessary to evaluate its optical properties, especially its RI for a wide spectral range. Only after obtaining such data, the variations induced by OC treatments can be truly evaluated.

Regarding the evaluation of the RI of pancreas, only two studies have been published so far. One presents the RI of porcine pancreas for 632.8 nm at 20 ± 2 °C [41] and the other presents the calculated dispersion for human pancreas at 25 °C between 450 and 1550 nm [42].

In the present study, we measured the RI of rabbit pancreas tissues at wavelengths in the visible and NIR and calculated the corresponding dispersion for this

spectral range. The methodology used in this study is described in Section 2, and the obtained results and discussion are presented in Section 3.

2 Materials and methods

In order to measure the refractive index of the pancreas, at different wavelengths, and calculate its dispersion, the total internal reflection method was used [23, 24]. The sample preparation, experimental methodology and dispersion calculation are described in the following subsections.

2.1 Tissue samples

The pancreas of three recently sacrificed rabbits were dissected and frozen for 24 h. Fig. 1 shows one of those pancreas.

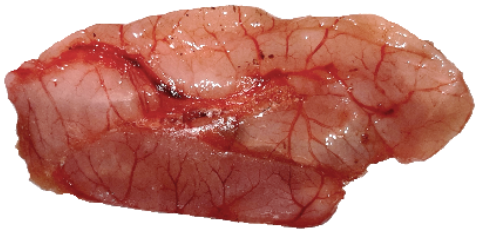


Fig. 1 One of the rabbit pancreas used in the RI measurements during thawing at room temperature.

One tissue sample with 1 cm × 1 cm × 3 mm was taken from each of the three rabbit pancreas, while they were still frozen. All the samples were prepared with a thickness of 3 mm and completely flat and uniform surfaces to perfectly adhere to the prism surface, without creating air bubbles in-between. These samples were kept in saline for 10 min and then were cleaned to remove outside remains of the solution.

2.2 Measurement procedure

Each sample was submitted to measurements with different lasers to obtain the pancreas RI at discrete wavelengths in the visible and NIR range.

The lasers used in this study had emission wavelengths at 401.4, 534.6, 626.6, 782.1, 820.8, and 850.7 nm. All these lasers are laser diodes from Edmund Optics, with the exception of the 534.6 nm and 626.6 nm lasers. The 534.6 nm laser is from Kvant (Slovakia) and the 626.6 nm laser is from Pasco (USA). The emitting power of all lasers was 5 mW or less and their emitting wavelengths were verified with a spectrometer from Avantes™.

For a particular set of measurements with a particular tissue sample and a particular laser, the tissue sample was placed in perfect contact with the base of the prism in the internal reflection setup (see Fig. 2).

A laser emitting at a particular wavelength entered the prism by another surface, where by refraction, was redirected to the prism/tissue interface. A reflected beam at this interface exited the prism through the third interface, where a detector (laser power sensor from Coherent with spectral range from 0.15 μm to 11 μm) connected to an electrical voltmeter (from Wavetek Meterman) was placed to collect the signal.

The prism was placed over a rotating stage (constructed in our lab – see Fig. 2), which allowed to vary the angle of incidence of the beam over the setup. As the incidence angle varied, the detector was also rotated to detect the reflected beam at each angular position.

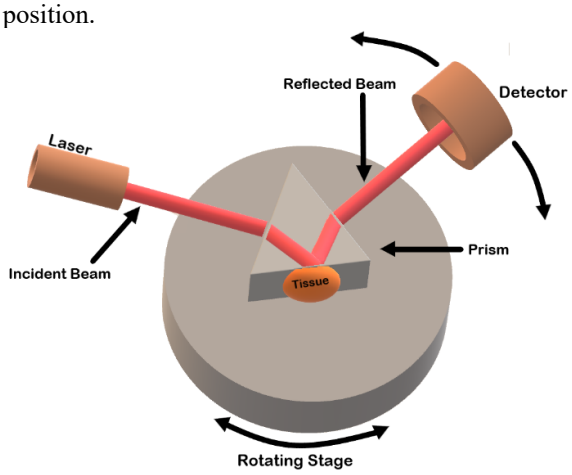


Fig. 2 Total internal reflection setup for RI measurements.

The dispersion prism used in these measurements is a SCHOTT N-SF11 prism acquired from Edmund Optics, with a wavelength dependence for its RI as presented in Fig. 3.

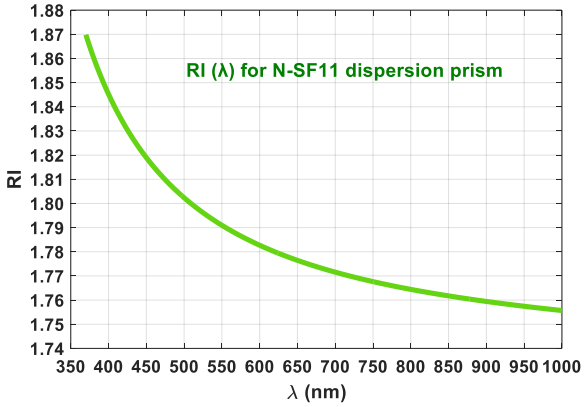


Fig. 3 Refractive index as a function of wavelength for the N-SF11 dispersion prism.

The curve presented in Fig. 3 is described by the Sellmeier equation [43], at 20 °C:

$$n^2 - 1 = \frac{K_1\lambda^2}{\lambda^2 - L_1} + \frac{K_2\lambda^2}{\lambda^2 - L_2} + \frac{K_3\lambda^2}{\lambda^2 - L_3}, \qquad (1)$$

where the Sellmeier coefficients have the following values for the SCHOTT N-SF11 glass: $K_1 = 1.7376$, $K_2 = 0.3137$, $K_3 = 1.8988$, $L_1 = 0.0132$, $L_2 = 0.0623$, and

$L_3 = 155.2363$. According to Ref. [43], since λ is represented in μm in Eq. (1), K_1, K_2 and K_3 are dimensionless coefficients, without units, while L_1, L_2 and L_3 are represented in μm^2.

Three sets of measurements were performed for each laser, one per tissue sample. In each individual study, temperature was kept constant at 20 °C, and the following measuring procedure was performed:

1. The sample was placed in perfect contact with the prism base (see Fig. 2).
2. Illumination of the setup was made with the laser beam through one side of the prism.
3. The reflected beam was collected with a photocell, connected to a voltmeter to read the electrical potential.
4. This measuring procedure was repeated for several incidence angles (α) between the incident laser beam and the normal to the air/prism interface. The angular resolution for these measurements was 1°.

Such procedure was repeated for the other lasers. The collected data from each set of measurements needed to be submitted to calculations to obtain the RI of pancreas at the wavelengths of the lasers used. The following sub-section describes these calculations.

2.3 RI calculations

Considering Fig. 2, and since the incident and reflected angles for the beam can only be measured outside the prism, at the prism/air interfaces, the Snell-Descartes equation needed to be used to convert the angle of the incident (or reflected) beam as measured outside the prism (α) to the incident (or reflected) angle at the prism/tissue interface (θ) [44]:

$$\theta = \beta - \arcsin\left[\frac{1}{n_{prism}} \times \sin(\alpha)\right], \tag{2}$$

with β representing the internal angle of the prism (60° in our case) and n_{prism} representing the RI of the prism at the wavelength of the laser in use (see Fig. 3).

Considering the electrical potential measurements and the corresponding angles at the prism/tissue interface, as obtained with Eq. (2), a reflectance curve was calculated as [25]:

$$R(\theta) = \frac{V(\theta) - V_{noise}}{V_{laser} - V_{noise}}, \tag{3}$$

with the potential measured at angle θ represented by $V(\theta)$, the potential measured with background light represented by V_{noise} and the potential measured directly from the laser represented by V_{laser}.

Once the reflectance curve was calculated with Eq. (3), the critical angle of reflection (θ_c) needed to be obtained from it. To identify such angle from the curve, its first derivative was first calculated. Such calculation was made according to [25]:

$$deriv(\theta) = \frac{R(\theta_i) - R(\theta_{i-1})}{\theta_i - \theta_{i-1}}, \tag{4}$$

where θ_i and θ_{i-1} are the consecutive angles of measurement and $R(\theta_i)$ and $R(\theta_{i-1})$ are the corresponding reflectance at those angles. As previously observed in other studies [23, 24], those derivatives will present a strong peak, whose central angle identifies the critical angle for each set of measurements.

By representing the curve for the first derivative, the value of θ_c was identified and then used in Eq. (5) to calculate the RI of the pancreas (n_{tissue}) at the laser wavelength [7]:

$$n_{tissue}(\lambda) = n_{prism}(\lambda) \times \sin(\theta_c). \tag{5}$$

Since three sets of measurements were performed with a particular laser, mean and standard deviation values for n_{tissue} provide higher accuracy and describe data dispersion between samples [7, 25].

Such calculation procedure was performed for each laser used in the RI measurements, so that the mean n_{tissue} values can be fitted with appropriate curves to obtain pancreas dispersion.

According to literature [2, 3, 7, 12, 18, 23–25, 27, 42], the most common dispersion equations to fit discrete RI data from biological tissues are the Cauchy (Eq. (6)), the Conrady (Eq. (7)) and the Cornu (Eq. (8)) equations [7, 25]:

$$n_{tissue}(\lambda) = A + \frac{B}{\lambda^2} + \frac{C}{\lambda^4}, \tag{6}$$

$$n_{tissue}(\lambda) = A + \frac{B}{\lambda} + \frac{C}{\lambda^{3.5}}, \tag{7}$$

$$n_{tissue}(\lambda) = A + \frac{B}{(\lambda - C)}, \tag{8}$$

where A, B and C are the Cauchy, Conrady, or Cornu parameters, that are obtained during the fitting of the experimental data.

All these curves were tested to fit the experimental RI data obtained for pancreas. Such data fittings were made using the Curve Fitting Tool (CFTOOL) of MATLAB™.

The results obtained and their discussion are presented next.

3 Results and discussion

After performing all experimental measurements, we started by calculating the reflectance curves for each set of measurements with each laser. Those reflectance curves, as calculated with Eq. (3), are presented in Fig. 4.

Using Eq. (4), we calculated the first derivative of the reflectance curves presented in Fig. 4 to obtain the values of θ_c. Those curves are presented in Fig. 5 for the measurements with each laser.

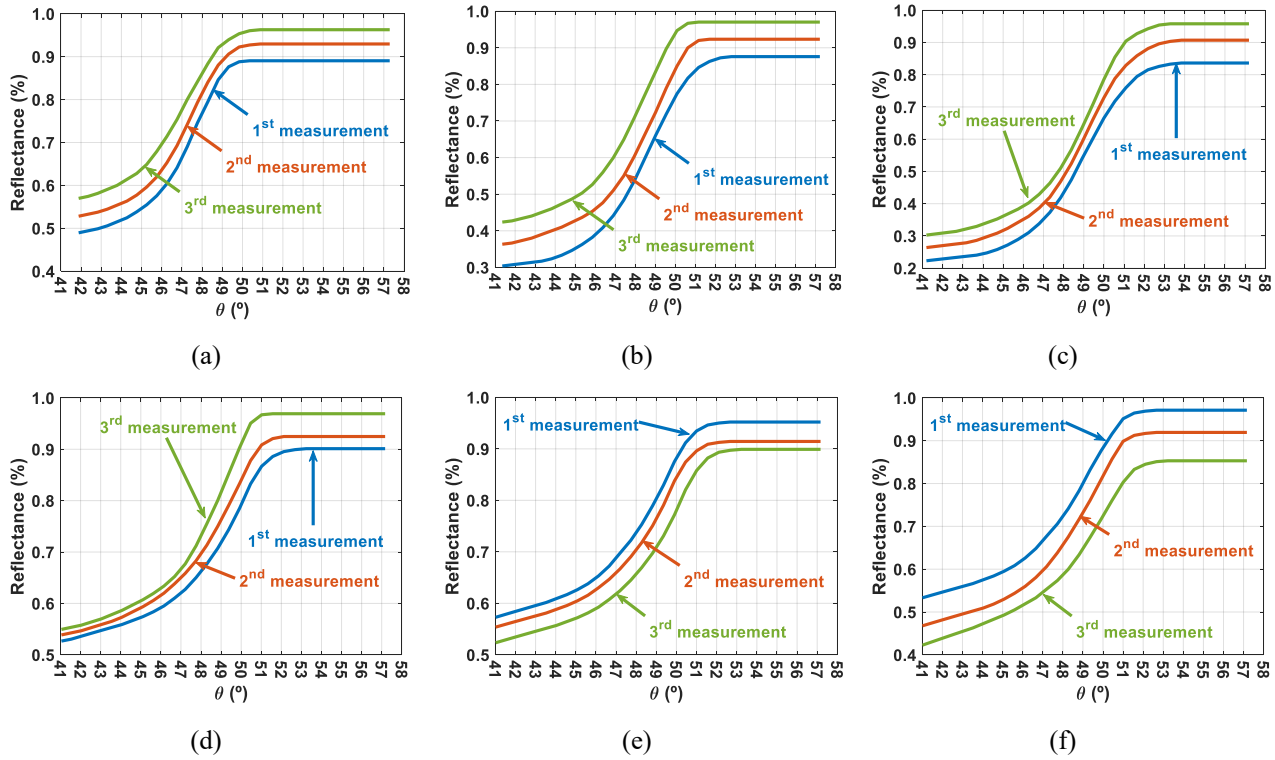


Fig. 4 Reflectance curves for the studies with the: 401.4 nm (a), 534.6 nm (b), 626.6 nm (c), 782.1 nm (d), 820.8 nm (e) and 850.7 nm (f) lasers.

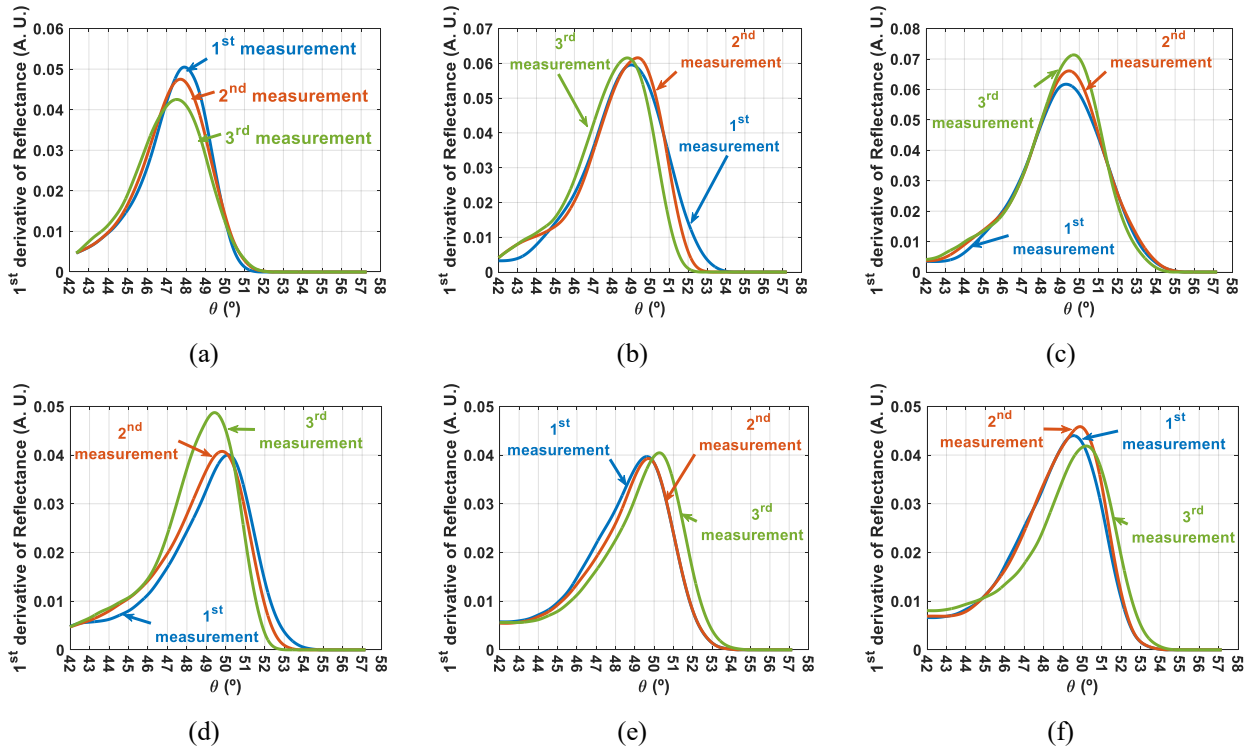


Fig. 5 First derivative of the reflectance curves for the studies with the: 401.4 nm (a), 534.6 nm (b), 626.6 nm (c), 782.1 nm (d), 820.8 nm (e) and 850.7 nm (f) lasers.

The values of θ_c as obtained from the graphs in Fig. 5 are presented in Table 1.

Using the θ_c values presented in Table 1 in Eq. (5), we calculated the corresponding n_{tissue} values. Those values, the mean and SD for each laser wavelength are presented in Table 2.

Using the CFTOOL in MATLAB, we fitted the mean RI values in Table 2 with the Eqs. (6), (7) and (8) for comparison. Fig. 6 presents such calculated dispersions for the spectral range of the experimental measurements (401–851 nm), along with some data for pancreas RI as collected from literature [41, 42].

Table 1 θ_c values obtained from the graphs in Fig. 5.

	θ_c (deg) per measurement		
Laser	**1st**	**2nd**	**3rd**
401.4 nm	47.9	47.7	47.5
534.6 nm	49.0	49.3	48.8
626.6 nm	49.3	49.5	49.7
782.1 nm	50.1	49.8	49.4
820.8 nm	49.6	49.7	50.3
850.7 nm	49.5	49.9	50.2

Table 2 Calculated n_{tissue} data for each laser wavelength.

	n_{tissue}				
λ (nm)	**1st**	**2nd**	**3rd**	**Mean**	**SD**
401.4	1.3688	1.3643	1.3604	1.3645	0.0042
534.6	1.3542	1.3612	1.3499	1.3551	0.0057
626.6	1.3491	1.3521	1.3572	1.3528	0.0041
782.1	1.3411	1.3489	1.3552	1.3484	0.0071
820.8	1.3429	1.3447	1.3560	1.3479	0.0071
850.7	1.3409	1.3474	1.3537	1.3473	0.0064

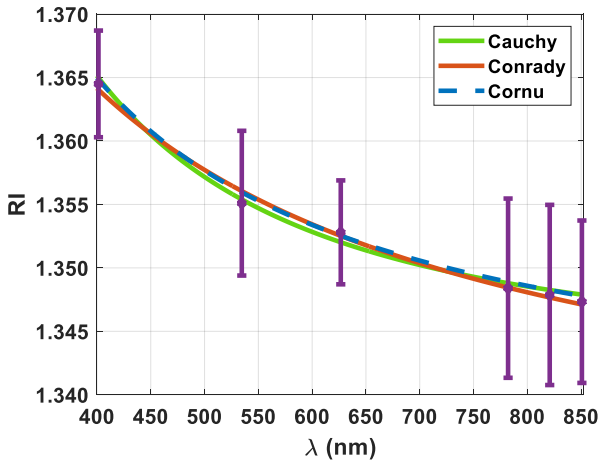


Fig. 6 Mean n_{tissue} data and calculated dispersions.

Fig. 6 shows that all curves provide good fitting of our experimental data for this range. All the calculated curves fall within the SD bars for each laser wavelength. Such SD bars present higher values for the longer wavelengths, already inside the NIR, a fact that is correlated with the visual difficulty in the alignment of invisible laser beams during measurements.

The calculated equations that describe the dispersions represented in Fig. 6 were the following:

$$n_{tissue}(\lambda) = 1.343 + \frac{3542}{\lambda^2} + \frac{0.1576}{\lambda^4} \quad \text{(Cauchy)}, \tag{9}$$

$$n_{tissue}(\lambda) = 1.332 + \frac{12.86}{\lambda} + \frac{0.1576}{\lambda^{3.5}} \quad \text{(Conrady)}, \tag{10}$$

$$n_{tissue}(\lambda) = 1.337 + \frac{7.915}{(\lambda - 117)} \quad \text{(Cornu)}. \tag{11}$$

The R-square values obtained in these fittings were: 0.994 (Cauchy and Conrady) and 0.997 (Cornu).

Comparing the data in these curves with data in literature, we see that the rabbit pancreas has a similar RI to the one from porcine pancreas at 633 nm – 1.3521 for rabbit (our study) and 1.3517 for porcine (Ref. [41]). Since the two results were obtained at 20 °C, their similarity makes perfect sense. Comparing our data with the human pancreas dispersion published in Ref. [42], which was calculated with only the first two terms in Eq. (6), our values within the visible–NIR range are higher, but we need to consider the difference in temperatures between studies.

As indicated in the introduction, the knowledge of tissue dispersion from the deep-UV to the infrared is highly important for a wide range of applications. Due to this interest, we extended the calculated dispersions to the spectral range between 200 and 1000 nm and looked in literature to find dispersions of tissues or tissue-like materials for comparison.

The only data for tissue or tissue-like dispersion that we could find for that spectral range, corresponds to histologic rat liver sections, which were initially fixed in Bouin's, Zenker's or Carnoy's fluid, then embedded and cut in paraffin and later deparaffinized in xylene [45]. Xylene is known as an OCA, and is also known to be toxic [46], meaning that the histologic preparation of those samples have altered the native dispersion of the liver sections. These changes are due to two processes. First, by embedding the liver samples in paraffin, a dehydration of the samples occurs, leading to an increase of the entire dispersion. Second, by deparaffinizing the samples in xylene leads to a RI matching mechanism, which further increases the sample's dispersion, in particular in the deep-UV, where the RI of proteins is bigger.

Although these changes occurred in the liver's dispersion, the contributions of collagen, DNA and hemoglobin to that dispersion remained unchanged, meaning that it is still the better approximation available in literature for the spectral range of interest. Retrieving that dispersion from Ref. [45], we modified its scale factor and baseline to match our experimental results for normally hydrated soft tissue (the complete rat liver

dispersion was multiplied by 0.34 and then we added 0.83 to it). By multiplying by 0.34, we reversed the dehydration and RI matching effects in a certain extent. Different values were tried in this rescaling process, but the ones indicated above were the ones that provided the best match to our experimental data.

To have a wide-band view, such rescaled dispersion and the calculated dispersions for the rabbit pancreas are presented in Fig. 7 for comparison.

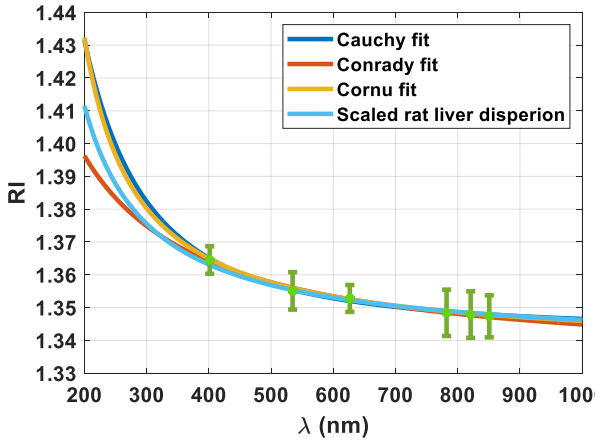


Fig. 7 Various dispersions for comparison.

Analyzing the various curves in Fig. 7, we see that the adjusted dispersion from rat histologic sections is also a good fit to our experimental data between 401 and 851 nm. It is also contained within the SD bars of our experimental data. For longer wavelengths, such adjusted dispersion is in better agreement with the Cauchy and Cornu dispersions, while in the deep-UV it falls almost in the middle of the calculated Conrady and the Cauchy/Cornu dispersions. Such positioning of the rescaled rat liver dispersion in-between the Conrady and the Cauchy/Cornu dispersions may be related to the RI matching of proteins, which was not completely reversed by our mathematical arrangement.

This means that, considering the UV-range, where major differences are observed, we cannot be sure which of the calculated dispersions for the pancreas is the more precise. They all may have equal probability to describe the pancreas dispersion in this range. To be sure, further studies are necessary. One possible approximation to get accurate dispersion for pancreas in the UV range is to obtain the spectrum of the absorption coefficient of pancreas and then through Kramers-Kronig (K-K) relations, calculate the real part of the RI [47].

Such procedure has been used in other studies [19, 47, 48], and in addition it provides more information, since spectral signatures of the pancreas can be seen in the dispersion after the calculation with the K–K relations. The calculated dispersions, as described by Eqs. (9), (10), and (11) do not show such spectral signatures due to the fact that they were obtained from measurements at discrete wavelengths. To obtain the pancreas dispersion between 200 and 1000 nm through K-K relations, the absorption coefficient spectrum ($\mu_a(\lambda)$) in that range must be obtained from spectral measurements. Then, the imaginary part of the RI ($\kappa(\lambda)$) of the pancreas can be calculated from $\mu_a(\lambda)$ [47]:

$$\kappa(\lambda)=\frac{\lambda}{4\pi}\mu_a(\lambda). \tag{12}$$

After calculating $\kappa(\lambda)$, the real part of pancreas RI ($n_{\text{tissue}}(\lambda)$) can be calculated through the following K-K relation [47,48]:

$$n_{tissue}(\lambda)=1+\frac{2}{\pi}\int_0^{\infty}\frac{\lambda}{\Lambda}\times\frac{\lambda}{\Lambda^2-\lambda^2}\kappa(\lambda)\,d\Lambda, \tag{13}$$

with Λ representing the integrating variable and λ representing a fixed wavelength that can be tuned for better vertical adjustment of the calculated dispersion to the one obtained from discrete data. In previous studies that we have made for other tissues [4, 13, 14, 19], we observed that by tuning λ, a better vertical alignment was obtained between the dispersion that results from calculations with Eqs. (12) and (13) and the dispersion that was calculated from discrete RI measurements.

This better adjustment is obtained if some dispersion, even for a shorter spectral range, such as the one obtained from discrete measurements through the total internal reflectance is available [4, 13].

Returning to the calculated dispersions for pancreas, as presented in Fig. 6 and described by Eqs. (9), (10), and (11), and considering only the wavelength range between 401 and 851, they all provide a good fit of our experimental data.

4 Conclusion

The RI values of rabbit pancreas were obtained from measurements acquired with the total internal reflection setup.

Three dispersion curves were calculated using the most common equations to fit discrete RI data from biological tissues: the Cauchy, the Conrady and the Cornu equations. All these curves fit the experimental data well in the visible-NIR range, but in the UV range, the curves calculated with the Cauchy and the Cornu equations present a faster decrease with wavelength than the one calculated with the Conrady equation. Such difference motivates further studies to inquire which of these curves provides an accurate fitting for the pancreas dispersion in the UV range.

For visible wavelengths, our data fits well with published data for porcine pancreas, although a single value for 633 nm is available in literature. A comparison with data in literature for human pancreas shows some significant differences, which are probably related to the difference in temperatures used in both studies.

After calculating the three dispersion curves that fit our data, it is our plan to continue this research with rabbit pancreas by perform spectral measurements to estimate the wavelength dependence of the optical properties of this tissue from the deep-UV to the NIR. In

those estimations, we will use the $\mu_a(\lambda)$ of the pancreas to calculate real dispersion through the K-K relations. We will use that dispersion to compare with the ones obtained in this study to check which one is the best. After such selection is made, we intend to use the selected pancreas dispersion in further studies that involve OC treatments.

Disclosures

All authors declare that there is no conflict of interests in this paper.

Acknowledgements

This research was supported by the Portuguese grant FCT-UIDB/04730/2020. VVT was supported by RFBR grant 18-52-16025.

References

1. Z. Wang, K. Tangella, A. Balla and G. Popescu, "Tissue refractive index as a marker of disease," Journal of Biomedical Optics 16(11), 116017 (2011).
2. P. Giannios, K. G. Toutouzas, M. Matiatou, K. Stasinos, M. M. Konstadoulakis, G. C. Zografos, and K. Moutzouris, "Visible to near-infrared refractive properties of freshly-excised human-liver tissues: marking hepatic malignancies," Scientific Reports 6, 27910 (2016).
3. P. Giannios, S. Koutsoumpos, K. G. Toutouzas, M. Matiatou, G. C. Zografos, and K. Moutzouris, "Complex refractive index of normal and malignant human colorectal tissue in the visible and near-infrared," Journal of Biophotonics 10(2), 303–310 (2017).
4. S. Carvalho, I. Carneiro, R. Henrique, V. Tuchin, and L. Oliveira, "Lipofuscin-type pigment as a marker of colorectal cancer," Electronics 9(11), 1805 (2020).
5. F. Carpignano, G. Rigamonti, G. Mazzani, and S. Merlo, "Low-coherence reflectometry for refractive index measurements of cells in micro-capillaries," Sensors 16(10), 1670 (2016).
6. Z. Turani, E. Fatemizadeh, Q. Xu, S. Daveluy, D. Mehregan, and M. R. N. Avanaki, "Refractive índex correction in optical coherence tomography images of multilayer tissues," Journal of Biomedical Optics 23(7), 070501 (2018).
7. E. N. Lazareva, L. Oliveira, I. Yu. Yanina, N. V. Chernomyrdin, G. R. Musina, D. K. Tuchina, A. N. Bashkatov, K. I. Zaytsev, and V. V. Tuchin, "Refractive index measurements of tissue and blood and OCAS in a wide spectral range" in Tissue optical clearing: new prospects in optical imaging, D. Zhu, E. Genina, and V. Tuchin (Eds), CRC Press, Boca Raton, USA, to be published.
8. A. R. Knuettel, M. Boehlau-Godau, "Spatially confined and temporally resolved refractive index and scattering evaluation in human skin performed with optical coherence tomography," Journal of Biomedical Optics 5(1), 83–92 (2000).
9. J.-C. Lai, Z.-H. Li, and A.-Z. He, "Influence of complex refractive index on diffuse reflection of biological tissues," Chinese Physics Letters 22(2), 332–334 (2005).
10. A. K. Dunn, Light scattering properties of cells, PhD dissertation, University of Texas at Austin, Texas, USA (1997).
11. L. M. Oliveira, K. I. Zaytsev, and V. V. Tuchin, "Improved biomedical imaging over a wide spectral range from UV to THz towards multimodality," Proceedings SPIE 11585, 1158503 (2020).
12. L. M. C. Oliveira, V. V. Tuchin, The Optical Clearing Method: A New Tool for Clinical Practice and Biomedical Engineering, Springer, Cham, Switzerland (2019). ISBN: 978-3-030-33055-2.
13. N. Gomes, V. V. Tuchin, and L. M. Oliveira, "UV-NIR efficiency of the refractive index matching mechanism on colorectal muscle during treatment with different glycerol osmolarities," Journal of Biomedical Photonics & Engineering 6(2), 020307 (2020).
14. N. Gomes, V. V. Tuchin, and L. M. Oliveira, "Refractive index matching efficiency in colorectal mucosa treated with glycerol," IEEE Journal of Selected Topics in Quantum Electronics 27(4), 7200808 (2021).
15. O. A. Smolyanskaya, N. V. Chernomyrdin, A. A. Konovko, K. I. Zaytsev, I. A. Ozheredov, O. P. Cherkasova, M. M. Nazarov, J.-P. Guillet, S. A. Kozlov, Yu. V. Kistnev, J.-L. Coutaz, P. Mounaix, V. L. Vaks, J.-H. Son, H. Cheon, V. P. Wallace, Yu. Feldman, I. Popov, A. N. Yaroslavsky, A. P. Shkurinov, and V. V. Tuchin, "Terahertz biophotonics as a tool for studies of dielectric and spectral properties of biological tissues and liquids," Progress in Quantum Electronics 62, 1–77 (2018).
16. K. I. Zaytsev, A. A. Gavdush, N. V. Chernomyrdin, and A. O. Yurchenko, "Highly accurate in vivo Terahertz spectroscopy of healthy skin: Variation of refractive index and absorption coefficient along the human body," IEEE Transactions on Terahertz Science and Technology 5(5), 817–827 (2015).
17. I. Carneiro, S. Carvalho, R. Henrique, L. Oliveira, and V. V. Tuchin, "Measuring optical properties of human liver between 400 1000 nm," Quantum Electronics 49(1), 13–19 (2019).
18. I. Yu. Yanina, E. N. Lazareva, and V. V. Tuchin, "Refractive index of adipose tissue and lipid droplet measured in wide spectral and temperature ranges," Applied Optics 57(17), 4839 (2018).

19. I. Carneiro, S. Carvalho, R. Henrique, L. Oliveira, and V. V. Tuchin, "Measurement of optical properties of normal and pathological human liver tissue from deep-UV to NIR," Proceedings SPIE 11363, 113630G (2020).
20. R. Khan, B. Gul, S. Khan, H. Nisar, and I. Ahmad, "Refractive index of biological tissues: Review, measurement techniques and applications," Photodiagnosis and Photodynamic Therapy 33, 102192 (2021).
21. H. Li, S. Xie, "Measurement method of the refractive index of biotissue by total internal reflection," Applied Optics 35, 1793–1975 (1996).
22. A. N. Bashkatov, K. V. Berezin, K. N. Dvoretskiy, M. L. Chernavina, E. A. Genina, V. D. Genin, V. I. Kochubey, E. N. Lazareva, A. B. Pravdin, M. E. Shvachkina, P. A. Timoshina, A. K. Tuchina, D. D. Yakovlev, D. A. Yakovlev, I. Yu. Yanina, O. S. Zhernovaya, and V. V. Tuchin, "Measurement of tissue optical properties in the context of tissue optical clearing," Journal of Biomedical Optics 23(9), 091416 (2018).
23. I. Carneiro, S. Carvalho, R. Henrique, L. Oliveira, and V. V. Tuchin "Water content and scatterers dispersion evaluation in colorectal tissues," Journal of Biomedical Photonics & Engineering 3(4), 040301 (2017).
24. S. Carvalho, N. Gueiral, E. Nogueira, R. Henrique, L. Oliveira, and V. V. Tuchin, "Wavelength dependence of the refractive index of human colorectal tissues: comparison between healthy mucosa and cancer," Journal of Biomedical Photonics & Engineering 2(4), 040307 (2016).
25. I. Carneiro, S. Carvalho, R. Henrique, L. Oliveira, and V. V. Tuchin, "Simple multimodal optical technique for evaluation of free/bound water and dispersion of human liver tissue," Journal of Biomedical Optics 22(12), 125002 (2017).
26. H. Ding, J. Q. Lu, K. M. Jacobs, and X.-H. Hu, "Determination of refractive indices of porcine skin tissues and intralipid at eight wavelengths between 325 and 1557 nm," Journal of Optical Society of America A 22(6), 1151–1157 (2005).
27. H. Ding, J. Q. Lu, W. A. Wooden P. J. Kragel, and X.-H. Hu, "Refractive indices of human skin tissue at eight wavelengths and estimated dispersion relations between 300 and 1600 nm," Physics in Medicine and Biology 51(6), 1479–1489 (2006).
28. J. Wang, Z. Deng, X. Wang, Q. Ye, W. Zhou, J. Mei, C. Zhang, and J. Tian, "Measurement of the refractive index of hemoglobin solutions for a continuous spectral region," Biomedical Optics Express 6(7), 2536–2541 (2015).
29. Z. Deng, J. Wang, Q. Ye, T. Sun, W.-Y. Zhou, J. Mei, C. Zhang, and J. Tian, "Determination of continuous complex refractive index dispersion of biotissue based on internal reflection," Journal of Biomedical Optics 21(1), 015003 (2016).
30. B. Lewis, J. Mao, "Development of the pancreas and related structures," in The Pancreas: An Integrated Textbook of Basic Science, Medicine and Surgery, 3rd Ed., H. G. Beger, A. L. Warshaw, R. H. Hruban, M. W. Brüchler, M. M. Lerch, J. P. Neoptolemos,T. Shimosegawa, and D. C. Whitcomb (Eds.), Wiley-Blackwell, Hoboken, New Jersey, USA (2018).
31. A. P. Klein, "Pancreatic cancer: a growing burden," The Lancet 4(12), 895–896 (2019).
32. S. Mohammed, G. van Buren 2nd, and W. E. Fisher, "Pancreatic cancer: advances in treatment," World Journal of Gastroenterology 20(28), 9354–9360 (2014).
33. D. P. Ryan, T. S. Hong, and N. Bardeesy, "Pancreatic adenocarcinoma," New England Journal of Medicine 371(11), 1039–1049 (2014).
34. K. Yamaguchi, T. Okusaka, K. Shimizu, J. Furuse, Y. Ito, K. Hanada, T. Shimosegawa, and K. Okazaki, "Clinical practice guidelines for pancreatic cancer 2016 from the pancreas society: A synopsis," Pancreas 46(5), 595–604 (2017).
35. I. D. Fleming, J. S. Cooper, D. E. Henson, R. V. P. Hutter. B. J. Kennedy, G. P. Murphy, B. O'Sullivan, L. H. Sobin, and J. W. Yarbro (Eds.), American Joint Committee for Cancer: Cancer Staging Manual, Whiting Press, Chicago, USA (1978).
36. J. H. Hwang, M. J. Cobb, M. B. Kimmey, and X. Li, "Optical coherence tomography imaging of the pancreas: a needle-based approach," Clinical Gastroenterology and Hepatology 3(7 Suppl 1), S49–S52 (2005).
37. S. Y. Lee, W. R. Lloyd, M. Chandra, R. H. Wilson, B. McKenna, D. Simeone, J. Scheiman, and M. A. Mycek, "Characterizing human pancreatic cancer using quantitative tissue optical spectroscopy," Biomedical Optics Express 4(12), 2828 (2013).
38. R. H. Wilson, M. Chandra, J. Scheiman, D. Simeone, B. McKenna, J. Purdy, and M.-A. Mycek, "Optical spectroscopy detects histological hallmarks of pancreatic cancer," Optics Express 17(20), 17502–17516 (2009).
39. P. A. Timoshina, A. B. Bucharskaya, D. A. Alexandrov, and V. V. Tuchin, "Study of blood microcirculation of pancreas in rats with alloxan diabetes by Laser Speckle Contrast Imaging," Journal of Biomedical Photonics & Engineering 3(1), 020301 (2017).
40. O. A. Smolyanskaya, E. N. Lazareva, S. S. Nalegaev, N. V. Petrov, K. I. Zaytsev, P. A. Timoshina, D. K. Tuchina, Ya. G. Toropova, O. V. Kornyushin, A. Yu. Babenko, J.-P. Guillet, and V. V. Tuchin, "Multimodal Optical Diagnostics of Glycated Biological Tissues," Biochemistry (Moscow) 84, 124–143 (2019).
41. J.-C. Lai, Y.-Y. Zhang, A.-H. Li, H.-J. Jiang, and A.-Z. He, "Complex refractive index measurement of biological tissues by attenuated total reflection ellipsometry," Applied Optics 49(16), 3235–3238 (2010).

42. M. Matiatou, P. Giannios, S. Koutsoumpos, K. G. Toutouzas, G. C. Zografos, and K. Moutzouris, "Data on the refractive index of freshly-excised human tissues in the visible and near-infrared spectral range," Results in Physics 22, 103833 (2021).
43. Refractive Index Database (accessed 7 February 2021) [https://refractiveindex.info/].
44. Q. W. Song, C.-Yu Ku, C. Zhang, R. B. Gross, R. R. Birge, and R. Michalak, "Modified critical angle method for measuring the refractive index of bio-optical materials and its application to bacteriorhodopsin," Journal of the Optical Society of America B 12(5), 797–803 (1995).
45. M. T. Jansen, "On the refractive index of histological tissue sections in visible and in ultraviolet light," Experimental Cell Research 15(1), 239–242 (1958).
46. N. Alwahaibi, S. Aljaradi, and H. Alazri, "Alternative to xylene as a clearing agent in histopathology," Journal Laboratory Physicians 10(2), 189–193 (2018).
47. O. Sydoruk, O. Zhernovaya, V. V. Tuchin, and A. Douplik, "Refractive index of solutions of human hemoglobin from the near-infrared to the ultraviolet range: Kramers-Kronig analysis," Journal of Biomedical Optics 17(11), 115002 (2012).
48. J. Gienger, H. Groβ, J. Neukammer, and M. Bär, "Determining the refractive index of human hemoglobin solutions by Kramers-Kronig relations with an improved absorption model," Applied Optics 55(31), 8951–8961 (2016).

Modeling of 980 nm and 1470 nm Laser Radiation Absorbance Efficiency in the Blood Vessel Depending on the Structure of Titanium–Containing Optothermal Fiber Converter

Do Thanh Tung, Andrey V. Belikov, and Yulia V. Semyashkina*
ITMO University, 49 Kronverksky av., Saint Petersburg 197101, Russian Federation

* **e-mail:** yvsemyashkina@mail.ru

Abstract. Using quartz fiber with titanium-containing optothermal fiber converter (TOTFC) is promising in endovenous laser coagulation (EVLA) for the treatment of varicose veins. This study aims to research the variation in the optical properties of TOTFC as its microstructure changes under the condition that TiO_2 spheres inside converter are arranged in such a way that the Mie theory approximation can be applied. The absorbance efficiency of laser energy with 980 nm and 1470 nm wavelengths for TOTFC has been calculated. Optical multidimensional simulation for the EVLA process was developed and calculated. The optimal ranges of microstructure's parameters for TOTFC in the EVLA process were discussed. © 2021 Journal of Biomedical Photonics & Engineering.

Keywords: titanium; optical fiber; varicose vein; blood; optical properties; converter.

Paper #3399 received 31 Dec 2020; revised manuscript received 10 May 2021; accepted for publication 14 May 2021; published online 20 May 2021. doi: 10.18287/JBPE21.07.020304.

1 Introduction

Optothermal fiber converter (OTFC) generated on the distal end of the quartz fiber combined with a laser source has shown advantages for medical surgeries [1]. The use of such converters makes it possible to efficiently process (coagulate, cut, evaporate, etc.) soft biological tissues at different laser wavelengths of laser radiation [2]. Researchers have also confirmed the OTFC is highly effective in the treatment of soft tissue [3, 4]. One of their recent prospects is used in the treatment of varicose veins by endovasal laser coagulation (EVLA) method.

Widely known for treating varicose veins, EVLA uses a puncture in the vein and inserts quartz fiber into the vein. After the laser source is turned on at the suitable wavelength, the fiber is pulled at a speed of several mm/s [5]. Laser radiation with different wavelengths including 980 nm and 1470 nm is used for endovasal laser coagulation [6, 7]. Of course, an anesthetic is injected during the procedure to avoid causing pain to the patient. As a result of laser radiation interactions, the vein vessel wall is heated up to 80 °C and above, that leads to collagen fiber deformation, coagulation, and collapse of the vein [8]. When clear quartz fiber is used, a carbon layer is formed at the tip due to carbonized blood and can be heated to 1200 °C [9, 10]. The high temperature of the tip will easily lead to damage on the vein wall vessel, at the same time, the tip of the fiber is often deformed and broken down. One promising solution to overcome is to use the OTFC on the distal end of optical fiber.

Many types of converters have been fabricated for effective transformation of laser radiation to the heat [11, 12]. Among them, there is the titanium-containing optothermal fiber converter (TOTFC), which is created using of original technology based on 3-stage process. Fabrication technology and structure of TOTFC are described in detail in studies [11, 13] with the microstructure is made up of homogeneous TiO_2 spheres immersed in silica medium. TOTFC shows its good advantages and more suits to other materials in the EVLA process. Using quartz fiber optics with TOTFC makes it easy to control the input parameters in EVLA to help the temperature on the vessel wall reach 80 °C and minimize damage [13–15]. TOTFC has a spherical shape with a smooth surface that makes it easy to put quartz fiber with converter inside blood vessels without causing damage.

Besides, TOTFC is resistant to deformation when laser-heated, as it is capable of being heated up to 2700 °C in air without being destroyed [11]. TOTFC has a strong mechanical connection with optical fiber [11]. Unfortunately, the correlation between the microstructure of TOTFC and its optical properties, as well as the influence of this microstructure to the absorption in converter and in blood vessel of laser radiation with 980 nm and 1470 nm wavelengths of lasers widely used in EVLA has not been studied [7, 10, 15, 16]. We believe that wavelength for EVLA will be a wavelength for which the absorption in the converter will be maximum. On the one hand, this will reduce the power of the laser source necessary for the converter to reach the specified temperature (enough for EVLA), and, on the other hand, it will reduce the risk of unwanted radiation exposure to the vessel wall because laser radiation is not absorbed in the converter, that will lead to an increase in the efficiency and safety of the procedure.

The aim of this study is to find out and evaluate the dependence of TOTFC's optical parameters and light absorbance efficiency at 980 nm and 1470 nm wavelengths on microstructure of converter when the distribution of the TiO_2 spheres inside the converter allows one to apply an approximation of the Mie theory, evaluate the possibility to appear of radiation on the inner vessel wall surface for these two wavelengths in the EVLA procedure and determine the possible optimal for EVLA at 980 nm and 1470 nm wavelengths the parameters of microstructures of TOTFC.

2 Materials and methods

The TOTFC fabrication technology is described in detail in the studies [11, 13]. As the result of fabrication according to this technology, TOTFC is composed of titanium dioxide (TiO_2) spheres with a constant diameter of 1.2 μm and surrounded by silica (SiO_2), forming cubes of equal size (Fig. 1a). The converter has a strong mechanical connection to a quartz fiber of 440 μm diameter.

The volume fraction of spheres in medium (k) characterizes changes in the microstructure of TOTFC is defined by formula:

$$k = \frac{V_{TiO_2}}{V_{cube}} = \frac{\pi d_{sph}^{\ 3}}{6e^3} \qquad (1)$$

where d_{sph} – the diameter of the TiO_2 sphere (constant and equals 1.2 μm), e is a side dimension of the cube.

The microstructure of TOTFC will change if the value k changes, the volume of silica will decrease as k increases. Examples of the microstructures of TOTFC for different values of k are shown in Fig. 1b. When $k = 0$, at this time TOTFC will be completely quartz.

Mie scattering theory is the scattering theory of electromagnetic waves by homogeneous spheres used to calculate the optical properties of materials or substances containing particles in many cases, and its approximation has been confirmed by experimental measurement [17, 18]. Even the particles are not necessarily spherical as in the study [19], and they are not perfectly uniformly arranged in the medium, or in other words, the distance between particles is different. Likewise, TOTFC was generated with homogeneous TiO_2 spheres that were relatively uniformly distributed in silica medium. The ratio of the volume of TiO_2 to silica is one of the standards in TOTFC fabrication. As mentioned above about the structure of TOTFC, by dividing TOTFC's volume by the number of TiO_2 particles, it is easy to find out the structure of a silica cube containing a single TiO_2 sphere embedded within it (as shown in the Fig. 1b).

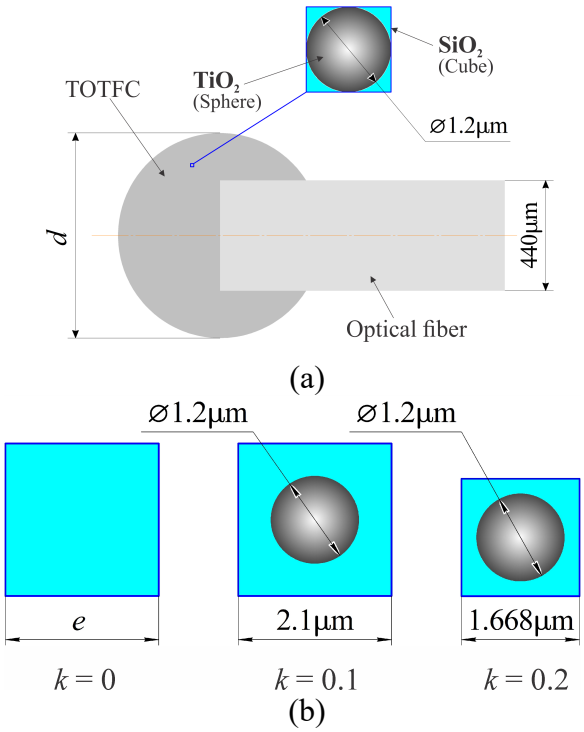


Fig. 1 Structural model of TOTFC (a) and illustration of microstructural changes for various volume fraction of spheres (k) in TOTFC (b).

Since the sphere's diameter (d_{sph} = 1.2 μm) has a value approximately equal to the wavelengths of laser radiation (980 nm and 1470 nm), therefore, to calculate the absorption, scattering, and anisotropy coefficients of TOTFC, we consider using Mie scattering theory [20, 21].

It is well known that scattering by small spheres is well predicted by Mie theory when a sphere is isolated or the distance between the spheres is large enough [22, 23]. This particular kind of scattering is called independent scattering. In this case, intensity scattered by sparse particles can be considered without regard to the phase of the scattered wave. Therefore, it is possible to study scattering by a small particle that is not affected by other particles [24, 25]. Contrary, when the particles are close enough together, the kind of scattering is called dependent scattering, then investigating the scattering for

the spheres cannot ignore the interaction between them, especially the scattering angle [26–28].

According to study [29], using a discrete dipole approximation has shown the criterion for independent scattering when the following condition are met:

$$\frac{h}{a} \geq \frac{2}{x}, \tag{2}$$

where h – distance between the particles (surface to surface), a – radius of each sphere, x – sphere size parameter is defined as:

$$x = \frac{2\pi a}{\lambda}. \tag{3}$$

Thus, for $\lambda = 980$ nm the independent scattering approximation is satisfied at $k \leq 0.26$, and for $\lambda = 1470$ nm the independent scattering approximation is satisfied at $k \leq 0.2$. A task about independent scattering particles has also been theoretically calculated and experimentally carried out in Ref. [30] up to a volume particle concentration of 0.227, although the wavelength of the incident rays is 1.5 times greater than the diameter of particles. The computation of the electromagnetic waves transferred under dependent scattering condition when k is outside the above ranges is complex, and it is out of the scope of this paper. Following Liou in Ref. [24], a complementary theory of Mie scattering has been developed for a sample of spherical particles under independent scattering condition. Whereby, when the minimum radius of particles a_1 is asymptotic to the maximum radius a_2, the scattering phase matrix for a sample of particles is equal to the scattering phase matrix for an isolated particle. In other words, when the radius of all spheres is similar, the scattering intensity of a sample of particles can be calculated by predicting for an isolating sphere. Therefore, with the above description of the TOTFC microstructure, Mie scattering theory can be applied if $k \leq 0.26$ for $\lambda = 980$ nm and $k \leq 0.2$ for $\lambda = 1470$ nm.

According to the formula given in studies [20, 21, 32], TOTFC's optical properties are defined by:

$$\mu_s = \frac{1}{4}\pi d_{sph}^2 Q_{abs}, \tag{4}$$

$$\mu_s = \frac{1}{4}\pi d_{sph}^2 Q_{sca}, \tag{5}$$

$$Q_{ext} = Q_{sca} + Q_{abs}, \tag{6}$$

where μ_a, μ_s – the absorption and scattering coefficients of TOTFC, respectively. Q_{sca} – the scattering efficiency follows from the integration of the scattered power over all directions, and Q_{ext} – the extinction efficiency follows from the Extinction Theorem, leading to:

$$Q_{sca} = \frac{2}{\alpha^2}\sum_{n=1}^{\infty}(2n+1)\left(|a_n|^2 + |b_n|^2\right), \tag{7}$$

$$Q_{ext} = \frac{2}{\alpha^2}\sum_{n=1}^{\infty}(2n+1)\,\mathrm{Re}\left(a_n + b_n\right), \tag{8}$$

note that:

$$\alpha = \frac{\pi m d_{sph}}{\lambda}, \tag{9}$$

where m is the refractive indices of the host medium (here is silica), a_n and b_n are Mie coefficients, function $\mathrm{Re}(a_n + b_n)$ represents the real part of the argument.

Based on the previously defined volume fractions of titanium dioxide k, together with the library of refractive index constants of TiO_2 and SiO_2 [31], we can calculate the refractive index of TOTFC depending on the value k. Then, using the tools of program "MATLAB" (MathWorks, USA) [32] and with the help of Scott Prahl given in Ref. [33], the absorption, scattering, and anisotropy coefficients of TOTFC were determined.

In the EVLA process, the temperature interacts to the blood vessel wall is mainly due to the absorbed laser radiation at TOTFC and heating it up. To calculate the TOTFC's light absorbance efficiency (A), a simulation model of the EVLA procedure is created in environment 3-dimensional space configuration "TracePro® Expert-7.0.1 Release" ("Lambda Research Corporation", USA), shown in Fig. 2.

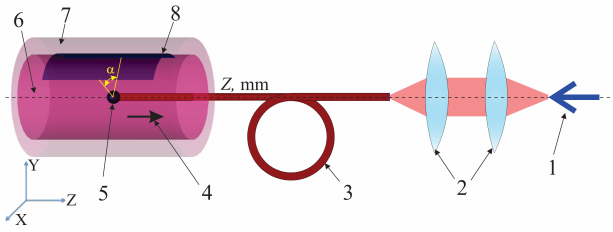


Fig. 2 EVLA procedure model; 1 – laser source; 2 – lenses; 3 – quartz optical fiber; 4 – the direction of movement of fiber and TOTFC; 5 – TOTFC; 6 – blood; 7 – vein wall; 8 – the detector plane which totally absorbs light and located on the inner wall of the vein and limited by an angle α.

Optical modeling was performed by Monte Carlo simulations of radiative transfer. Laser sources radiation continuously with tracing of 10000 rays, the numerical aperture NA = 0.22. After passing through two focusing lenses, the focused beam passes through a quartz optical fiber 3 m in length. The TOTFC is located at the distal end of the fiber and it is centrally located in a blood vessel 5 mm in inner diameter. The physical parameters of the

vein, quartz fiber and titanium-containing optothermal fiber converter required to construct an optical model were taken in [15, 34, 35] and are represented in Table 1.

Table 1. Physical parameters for laser source, quartz fiber, vein and TOTFC.

Laser source	Optical power	20 W
	Divergence	0.22
Quartz fiber	NA	0.22
	Diameter (core)	0.4 mm
	Diameter (cladding)	0.44 mm
	Length	3 m
	Refractive index (core)	1.457
	Refractive index (cladding)	1.44
Vein	Inner diameter	5 mm
Vein wall	Thickness	1 mm
TOTFC	Thickness/Diameter	0.7 mm/ 0.78 mm

Here, we define TOTFC's diameter as 780 μm, which is similar to the actual dimensions has been fabricated in the study [13]. But during modeling we will change the diameter of TOTFC. The optical parameters of the vein wall and blood for 980 nm and 1470 nm wavelengths are given in studies [6, 36–39], these are shown in Table 2.

Table 2. Optical parameters for vein wall and blood at 980 nm and 1470 nm.

Wavelength [nm]		980	1470
Vein wall	Absorption coefficient [mm^{-1}]	0.22	2.01
	Scattering coefficient [mm^{-1}]	14.8	31
	Anisotropy factor	0.96	0.95
Blood	Absorption coefficient [mm^{-1}]	0.29	2.33
	Scattering coefficient [mm^{-1}]	46.7	27.78
	Anisotropy factor	0.9763	0.9562

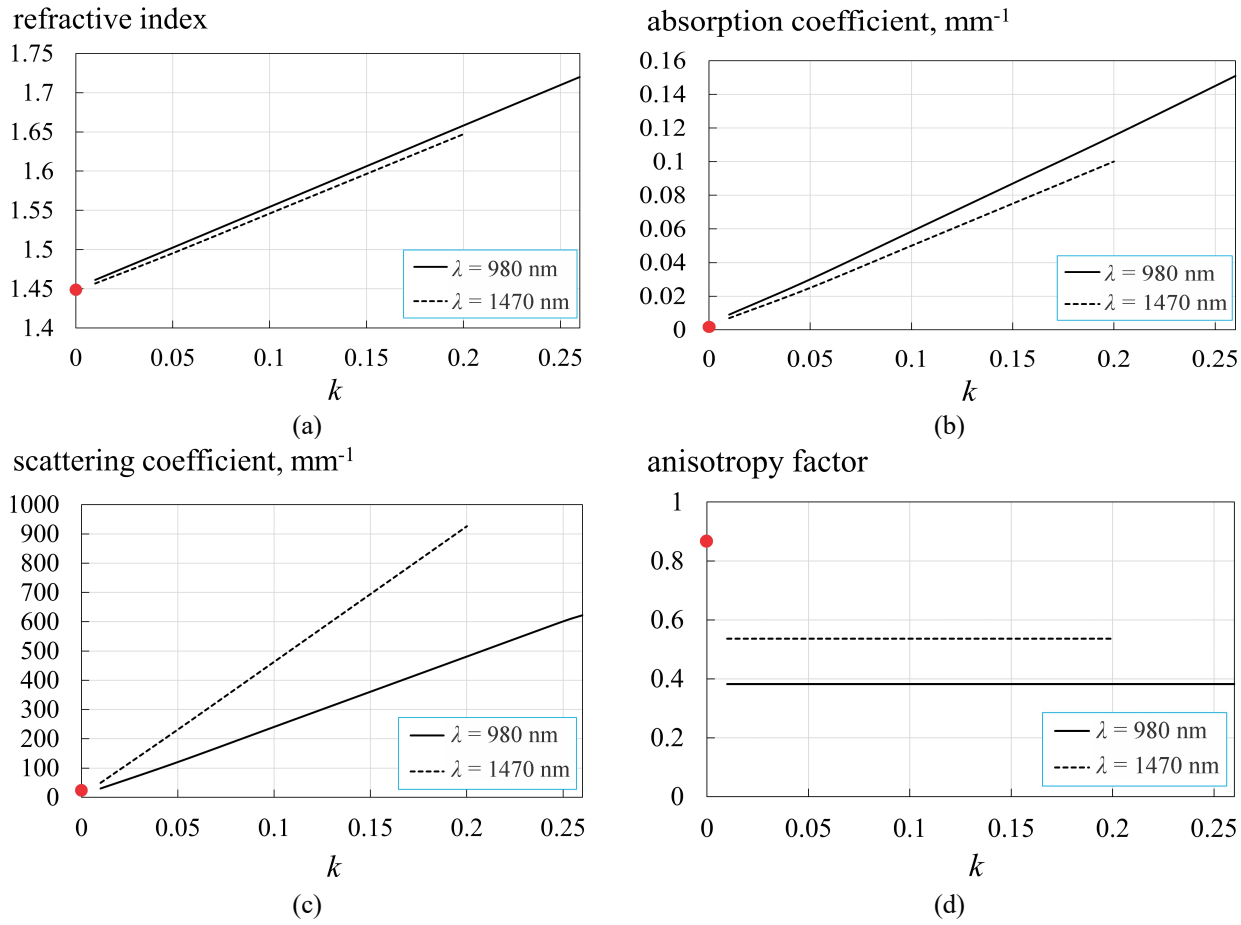


Fig. 3 Dependence of the refractive index (a), absorption coefficient (b), scattering coefficient (c) and anisotropy factor (d) on the volume fraction k of TiO_2 in TOTFC.

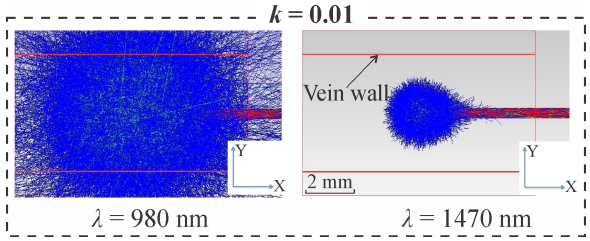
3 Results and Discussion

The change of the microstructure in TOTFC as the volume fraction k of TiO_2 shown in Eq. (1) will significantly change the optical properties of TOTFC. Fig. 3 shows the influence of the value k on the optical properties of TOTFC.

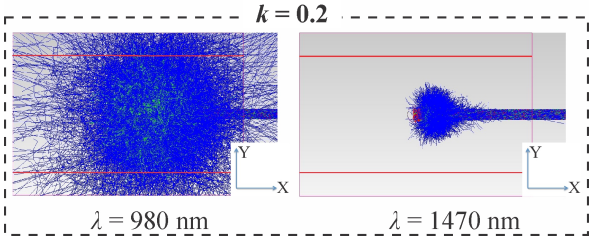
Investigate the k ranging from 0.01 to 0.2 for $\lambda = 1470$ nm and from 0.01 to 0.26 for $\lambda = 980$ nm. At a value of $k = 0$, meaning that there is no TiO_2 sphere in the silica cube (see Fig. 1b), in this case, the optical properties of TOTFC are the optical properties of silica (SiO2). In Fig. 3, at $k = 0$, the red spots showing the refractive index, absorption, scattering coefficient, and anisotropy factor of SiO_2 were confirmed in Refs. [31, 40, 41]. It can be seen that when k changes there is not much difference in the refractive index of TOTFC between 980 nm and 1470 nm wavelengths. They both increase linearly with the increasing of the value k. For the refractive index of SiO_2 corresponding to $k = 0$, the red point in this case belongs to the graph line showing the computation certainty (see Fig. 3a). Similar to the dependence of the absorption and scattering coefficient on the volume fraction of TiO_2 (see Fig. 3b, c). The absorption coefficient of silica is very small, equal to 10^{-6} mm^{-1} [40]. The scattering coefficient of silica ranges from 14.6 to 20.2 mm^{-1} [41]. The absorption and scattering coefficients of TOTFC increased as the volume fraction k of TiO_2 increased, because at this time, the number of TiO_2 spheres in the TOTFC would increase, increasing optical absorption and scattering. The absorption coefficient of TOTFC increased with increasing k, but in general, for both wavelengths these values are very small, less than 0.15 mm^{-1}. The scattering coefficient of TOTFC increased strongly with increasing k, with maximum values of 620 mm^{-1} for 980 nm and 930 mm^{-1} for 1470 nm wavelength. The anisotropy factor of TOTFC is unchanged when k is changed, and it only depends on the laser wavelength (see Fig. 3d). This can be explained because the size of the TiO_2 spheres is unchanged. In Fig. 3d, at $k = 0$, the red point represents the magnitude of the anisotropy factor of SiO_2 is equal to 0.88, which was experimented on in research [41]. Comparison between wavelengths 980 nm and 1470 nm show that the scattering coefficient and anisotropy factor of TOTFC for 1470 nm wavelength is the magnitude higher. The anisotropy factor of TOTFC $g = 0.3815$ for 980 nm and $g = 0.5360$ for 1470 nm wavelength.

The diagrams of the absorption and scattering coefficients of TOTFC increased linearly as the volume fraction k increased, consistent with a similar experimental measurement in the study [30]. In there, experiments were measured for the Intralipid with diffused soybean oil particles. In Ref. [30], the scattering coefficient increases non-linearly as k increases close to the maximum value, possibly due to the influence of dependent scattering. A proof of this can be seen in Ref. [28] when the relative between the independent and the dependent scattering is shown. The anisotropy factor g has also been measured in Ref. [30], with a slight decrease as the volume fraction k increased; however, the error of this measurement was so much, up to 8%.

It is generally accepted that during endovasal laser coagulation, optical influence assessment, and further, the distribution of temperature onto the vein wall is crucial [36–38]. According to this, after calculating the optical properties of TOTFC, using "TracePro® Expert-7.0.1 Release" the ray tracing for 980 nm and 1470 nm laser radiation in the blood vessel was done. In Fig. 4, the path of rays through TOTFC placed in the blood vessel for the volume fraction $k = 0.01$ and $k = 0.2$ were obtained.



(a)



(b)

Fig. 4 Path of rays through TOTFC placed in the blood vessel for the volume fraction $k = 0.01$ (a) and $k = 0.2$ (b) into the YZ plane (X = 0).

As seen in Fig. 4, the distribution of rays leaving the TOTFC for $k = 0.01$ is different with $k = 0.2$ at the same wavelength. This is probably because the absorption and scattering coefficients of TOTFC are gradually increasing as the value k increases (see Fig. 3b, c). Wherein, the change is significant as the laser wavelength changes. It can be observed that laser radiation for 980 nm reaches the vein wall. While laser radiation for 1470 nm is concentrated mostly near the converter, and cannot reach the vein wall, even at all values of k. This can be explained by the fact that the absorption coefficient of blood for 1470 nm is many times of the magnitude larger than that for 980 nm wavelength (see Table 2).

To evaluate the magnitude of 980 nm radiation intensity impacting the blood vessel walls, we used a detector plane which totally absorbs light and located on the inner wall of the vein and limited by an angle $\alpha = 90^{\circ}$ with along Z-axis length equal to 7 mm (see Fig. 2). The distal end of fiber with TOTFC is placed in the position

where the coordinate Z = 0. Fig. 5 shows the radiation intensity distribution on the inner vessel wall surface with $k = 0.01$ and $k = 0.26$ (if laser power equals 20 W).

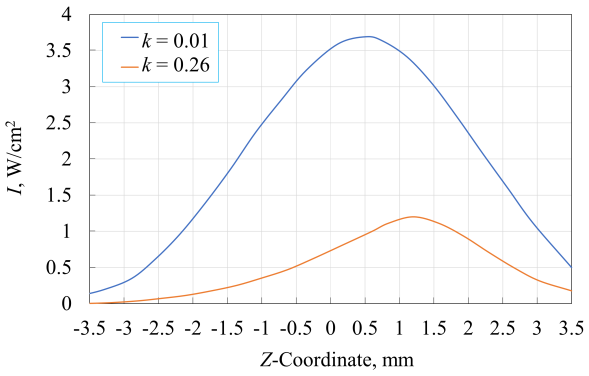


Fig. 5 The distribution of the 980 nm laser radiation intensity (I) on the inner vein wall surface along Z-coordinate with $k = 0.01$ and $k = 0.26$.

The dependence of average 980 nm laser radiation intensity on the inner vessel wall surface on k was determined. It can be seen that the radiation intensity distribution on the inner vein wall surface reaches peak magnitude at a point in the opposite direction to the incident rays. At $k = 0.26$, this peak has a coordinate farther from the TOTFC's center (Z = 0) as compared with $k = 0.01$. This may be due to the increase in the scattering coefficient of TOTFC as the value k increases (see Fig. 3c). The average of laser radiation intensity on the inner vessel wall surface reaches magnitude $I = 3.70$ W/cm^2 for $k = 0.01$ and $I = 1.25$ W/cm^2 for $k = 0.26$. As can be seen, a larger value k will reduce the intensity of radiation on the inner vein wall surface, thereby reducing the risk of unwanted radiation exposure to the vessel wall by laser radiation.

The dependences of TOTFC's light absorbance efficiency (A) and transmission (T) on k and diameter of converter (d) for wavelengths of 980 nm and 1470 nm are shown in Fig. 6.

In general, the TOTFC with volume fraction $k = 0.26$ and $d = 0.78$ mm is optimal with the light absorbance efficiency A of over 83% (see Fig. 6a). However, for TOTFC at $k = 0.15$ we also demonstrated the ability to absorb radiation well with 80% for 980 nm and 82% for 1470 nm wavelength. Using TOTFC at $k = 0.2$, we examined its A and T when the diameter of the TOTFC d was changed (see Fig. 6b).

The transmission is calculated directly by measuring the percentage of the power received around the TOTFC by using a totally absorbing spherical detector. Besides, a detector plane is also placed in front of the source to measure the percentage reflectance of the TOTFC. Then, after subtracting 4% of the Fresnel loss energy at the fiber's input, the radiation is absorbed in quartz fiber, which is 0.3% for 3 m in length [13, 34], from there the rest is the TOTFC's light absorbance efficiency. In accordance with Ref. [40, 42], the transmittance of silica quartz is about 92% for the wavelength range from 0.4 μm to 2 μm for 1 m length, plus the radiation loss due to reflection implies that the absorption of the silica is close to zero. These correspond to the red and blue spots shown in Fig. 6a.

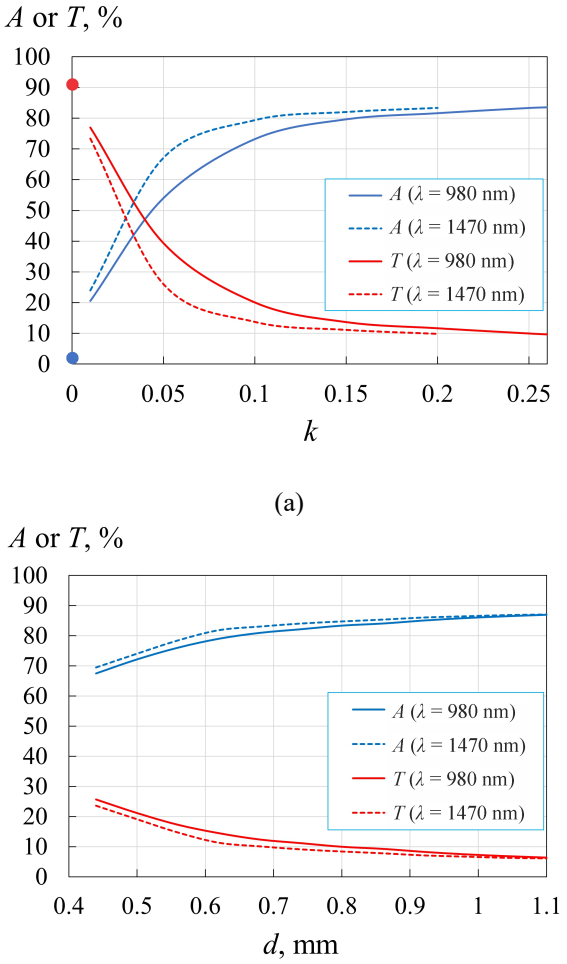


Fig. 6 Dependence of TOTFC's light absorbance efficiency (A) and transmission (T) on the volume fraction k with $d = 0.78$ mm (a) and diameter of converter d with $k = 0.2$ (b) for wavelengths 980 nm and 1470 nm.

It can also be seen that the transmittance of TOTFC (red line) decreases rapidly in the k range from 0.01 to 0.1, then slowly decreases until $k = 0.26$. It is synonymous with that, TOTFC's light absorbance efficiency increases rapidly when k is from 0.01 to 0.1 and reaches maximum magnitude at $k = 0.26$. Apparently, the presence of TiO_2 spheres greatly increased TOTFC's ability to absorb radiation.

In addition, the TOTFC's light absorbance efficiency for 980 nm is the magnitude lower than that for 1470 nm wavelength in the k range of 0.01 to 0.15 and is almost equals when $k > 0.15$. At the value $k = 0.22$, the magnitude of TOTFC's light absorbance efficiency is equal to 83.2% for 980 nm wavelength, agreement with the results in Ref. [13, 15].

Since the diameter of the quartz optic fiber is 0.44 mm, so the minimum diameter of TOTFC is 0.44 mm. Fig. 6b shows the TOTFC's light absorbance efficiency and transmission as the diameter of TOTFC increases from 0.44 mm to 1.1 mm for both wavelengths. TOTFC's light absorbance efficiency increase but gradually slow as the TOTFC's diameter increases. The opposite happens with the transmission. Obviously, when the diameter of the TOTFC increases, it will lead to an increase in its volume, that makes the radiation absorption efficiency of TOTFC to increase.

In summary, the increased diameter of the TOTFC will increase the radiation absorption efficiency and decrease the radiation intensity on the inner vessel wall surface. TOTFC's light absorbance efficiency will be 80% higher when its diameter is greater than 0.67 mm. Therefore, the TOTFC structure with k from range $0.15 \div 0.26$ and $d > 0.67$ mm demonstrates the high enough absorbance efficiency. It should be noted that the diameter d is limited from above by the size of the vein and cannot exceed its inner diameter.

4 Conclusion

The optical properties of TOTFC with different volume fraction k of TiO_2 at wavelengths of 980 nm and 1470 nm of lasers widely used in EVLA are considered when the TiO_2 spheres are sparse enough for the Mie theory approximation application. The optical properties of TOTFC at these wavelengths changed significantly as the microscopic structure of TOTFC changed. The radiation absorption efficiency of TOTFC increases with increasing the volume fraction k up to 0.26 for 980 nm and up to 0.2 for 1470 nm. The results are confirmed based on the known optical properties of silica (SiO_2) and a measurement experiment with independent scattering particles [30]. TOTFC's absorbance efficiency of laser radiation has been calculated. It was clearly evident from the calculated results that absorbance efficiency increased as diameter of converter increased. As a result of optical calculations, radiation intensity distributions on the inner vessel wall surface were investigated. The results also showed that for 1470 nm wavelength, radiation could not reach the vein wall, that is positive as it increases the efficiency and safety of EVLA. The possible optimal for EVLA, microstructures of TOTFC with $0.15 \le k \le 0.26$ for 980 nm and $0.15 \le k \le 0.2$ for 1470 nm wavelengths, and diameter $d > 0.67$ mm because of these ranges of volume fraction and diameter of converter observe the high enough absorbance efficiency of laser radiation for TOTFC (more than 80%). The results of this study will be used in the subsequent thermophysical modeling of laser heating of a vein and can be useful in the development of new laser devices for EVLA.

Disclosures

All authors declare that there is no conflict of interests in this paper.

Acknowledgements

The authors are grateful to ITMO University (Saint Petersburg, Russia) for providing equipment and support to this study. This work was carried out within the framework of the program for improving the competitiveness of ITMO University among the world's leading research and educational centers for 2013–2020 ("5 in 100" program, grant 08-08).

References

1. A. V. Skripnik, "Opto-thermal fiber converter of laser radiation," Journal of instrument engineering 9(56), 37–42 (2013).
2. R. M. Verdaasdonk, C. F. P. Van Swol, "Laser light delivery systems for medical applications," Physics in Medicine and Biology 42, 869–894 (1997).
3. A. V. Belikov, A. V. Skrypnik, and K. V. Shatilova, "Comparison of diode laser in soft tissue surgery using continuous wave and pulsed modes in vitro," Frontiers of Optoelectronics 8(2), 212–219 (2015).
4. A. V. Belikov, A. V. Skrypnik, and V. Y. Kurnyshev, "Modeling of structure and properties of thermo-optical converters for laser surgery," Proceedings of SPIE 9917, 99170G (2015).
5. Yu. L. Shevchenko, K. V. Mazaishvili, and Yu. M. Stoiko, Laser Surgery for Varicose Vein Disease, Borges, Moscow (2010) [in Russian]. ISBN: 978-5-9902607-1-9.
6. A. A. Poluektova, W. S. J. Malskat, M. J. C. van Gemert, M. E. Vuylsteke, C. M. A. Bruijninckx, H. A. Martino Neumann, and C. W. M. van der Geld, "Some controversies in endovenous laser ablation of varicose veins addressed by optical-thermal mathematical modeling," Lasers in Medical Science 29(2), 441–452 (2014).
7. R. R. Van Den Bos, P. W. M.van Ruijven, C. W. M. van der Geld, M. J. C. van Gemert, H. A. M. Neumann, and T. Nijstena, "Endovenous simulated laser experiments at 940 nm and 1470 nm suggest wavelength-independent temperature profiles," European Journal of Vascular and Endovascular Surgery 44(1), 77–81 (2012).
8. E. V. Shaydakov, E. A. Iluhin, Endovascular methods in the treatment of varicose veins, Diton-Art, Saint Petersburg (2016).
9. Yu. L. Shevchenko, Yu. M. Stoyko, K. V. Mazayshvili, and T. V. Khlevtova, "The mechanism of endovenous laser obliteration: a new look," Phlebology 5(1), 46–50 (2011) [in Russian]. ISBN: 978-5-905048-97-5.

10. M. Amzayyb, R. R. van den Bos, V. M. Kodach, D. M. de Bruin, T. Nijsten, H. A. M. Neumann, and M. J. C. van Gemert, "Carbonized blood deposited on fibres during 810, 940 and 1,470 nm endovenous laser ablation: thickness and absorption by optical coherence tomography," Lasers in Medical Science 25(3), 439–447 (2010).
11. A. V. Belikov, A. V. Skrypnik, "Laser heating dynamics and glow spectra of carbon-, titanium- and erbium-containing optothermal fibre converters for laser medicine," Quantum Electronics 47(7), 669−674 (2017).
12. A. V. Belikov, A. V. Skrypnik, "Soft tissue cutting efficiency by 980 nm laser with carbon-, erbium-, and titanium-doped optothermal fiber converters," Lasers in Surgery and Medicine 51(2), 185−200 (2019).
13. A. V. Belikov, A. V. Skrypnik, and I. S. Salogubova, "Optical and thermal modeling of Ti-doped optothermal fiber converter for laser surgery," Proceedings of SPIE 11065, 1106514 (2019).
14. A. V. Belikov, T. Do, and Yu. V. Semyashkina, "Laser heating numerical simulation of titanium-containing optothermal fiber converter and vein wall during endovasal laser coagulation," Scientific and Technical Journal of Information Technologies, Mechanics and Optics 20(4), 485–493 (2020).
15. A. V. Belikov, T. Do Thanh, A. V. Skrypnik, and Y. V. Semyashkina, "Modeling of optothermal fiber converters interaction with vein during endovenous laser coagulation," Proceedings of SPIE 11457, 114571L (2020).
16. M. Vuylsteke, J. V. Dorpe, J. Roelens, Th. D. Bo, and S. Mordon, "Endovenous laser treatment: a morphological study in an animal model," Phlebology 24(4), 166–175 (2009).
17. T. Wriedt, "Mie theory: a review," The Mie Theory 169, 53–71 (2012).
18. J. M. Steinke, A. P. Shepherd, "Comparison of Mie theory and the light scattering of red blood cells," Applied Optics 27(19), 4027–4033 (1988).
19. P. K. Jain, K. S. Lee, I. H. El-Sayed, and M. A. El-Sayed, "Calculated absorption and scattering properties of gold nanoparticles of different size, shape, and composition: applications in biological imaging and biomedicine," The journal of physical chemistry B 110(14), 7238–7248 (2006).
20. W. C. Mundy, J. A. Roux, and A. M. Smith, "Mie scattering by spheres in an absorbing medium," JOSA 64(12), 1593–1597 (1974).
21. Q. Fu, W. Sun, "Mie theory for light scattering by a spherical particle in an absorbing medium," Applied Optics 40(9), 1354–1361 (2001).
22. C. F. Bohren, D. R. Huffman, Absorption and scattering of light by small particles, Wiley, New York, USA (1983).
23. H. C. van de Hulst, Light scattering by small particles, Dover Publications, New York, USA (1981).
24. K. N. Liou, "A complementary theory of light scattering by homogeneous spheres," Applied Mathematics and Computation 3(4), 331–358 (1977).
25. M. I. Mishchenko, J. W. Hovenier, and L. D. Travis (Eds.), "Concepts, terms, notation," Chapter 1 in Light Scattering by Nonspherical Particles, 3–27 (2000).
26. J. D. Cartigny, Y. Yamada and C. L. Tien, "Radiative Transfer With Dependent Scattering by Particles: Part 1–Theoretical Investigation," Journal of Heat Transfer 108(3), 608–661 (1986).
27. L. X. Ma, J. Y.Tan, J. M. Zhao, F. Q. Wang, and C. A. Wang, "Multiple and dependent scattering by densely packed discrete spheres: Comparison of radiative transfer and Maxwell theory," Journal of Quantitative Spectroscopy and Radiative Transfer 187, 255–266 (2017).
28. G. Göbel, J. Kuhn, and J. Fricke, "Dependent scattering effects in latexsphere suspensions and scattering powders," Waves in Random Media 5(4), 413–426 (2006).
29. Z̆. Ivezić, M. P. Mengüç, "An investigation of dependent/independent scattering regimes using a discrete dipole approximation," International Journal of Heat and Mass Transfer 39(4), 811–822 (1996).
30. G. Zaccanti, S. Del Bianco, and F. Martelli, "Measurements of optical properties of high-density media," Applied Optics 42(19), 4023–4030 (2003).
31. Refractive index database (accessed 1 December 2020). [https://refractiveindex.info/?shelf=main&book=TiO2&page=Devore-o].
32. C. Mätzler, MATLAB functions for Mie scattering and absorption, version 2, Bern, Switzerland (2002).
33. S. Prahl, Mie Scattering Calculator (accessed 1 December 2020). [https://omlc.org/calc/mie_calc.html].
34. Buffered Fiber Optics, Edmund Optics (accessed 1 December 2020). [http://www.edmundoptics.com/optics/fiber-optics/buffered-fiber-optics/2456].
35. E. Péry, W. C. P. M. Blondel, J. Didelon, A. Leroux, and F. Guillemin, "Simultaneous characterization of optical and rheological properties of carotid arteries via bimodal spectroscopy: Experimental and simulation results," IEEE Transactions on Biomedical Engineering 56(5), 4760278, 1267–1276 (2009).
36. M. Hirokawa, T. Ogawa, H. Sugawara, S. Shokoku, and S. Sato, "Comparison of 1470 nm laser and radial 2ring fiber with 980 nm laser and bare-tip fiber in endovenous laser ablation of saphenous varicose veins: a multicenter, prospective, randomized, non-blind study," Annals of Vascular Diseases 8(4), 282–289 (2015).
37. P. W. van Ruijven, A. A. Poluektova, M. J. C. van Gemert, H. A. M. Neumann, T. Nijsten, and C. W. M. van der Geld, "Optical-thermal mathematical model for endovenous laser ablation of varicose veins," Lasers in Medical Science 29, 431–439 (2014).
38. S. Nozoea, N. Honda, K. Ishii, and K. Awazu, "Quantitative analysis of endovenous laser ablation based on human vein optical properties," Proceedings of SPIE-OSA Biomedical Optics, 80921J (2011).

39. N. Bosschaart, G. J. Edelman, M. C. G. Aalders, T. G. van Leeuwen, and D. J. Faber "A literature review and novel theoretical approach on the optical properties of whole blood," Lasers in Medical Science 29, 453–479 (2014).
40. "Silica Glass (SiO_2)," Crystran (accessed 1 December 2020). [https://www.crystran.co.uk/optical-materials/silica-glass-sio2].
41. K. Fujiwara, T. Maruyama, S. Nakamura, K. Nitta, and O. Matoba, "Measurement of scattering coefficient in PMMA with SiO2 particles by optical coherence tomography," 17th Microoptics Conference (MOC' 11), 1–2 (2011).
42. Technical Note: Optical Materials, Newport Corporation (accessed 1 December 2020). [https://www.newport.com/n/optical-materials].

Influence of Activators and Inhibitors on the Collagenase with Collagen Interaction Monitored by Dynamic Light Scattering in Solutions

Irina A. Sergeeva, Anna V. Petrova*, Anastasia V. Shlenskaya, and Galina P. Petrova
Chair of Molecular Processes and Extreme Matter States, Faculty of Physics, Lomonosov Moscow State University, GSP–1, 1–2 Leninskie Gory, Moscow 119991, Russian Federation

*** e-mail:** av.sukneva@physics.msu.ru

Abstract. Real–time digestion of type I collagen molecules by bacterial collagenase from Clostridium histolyticum has been monitored using Dynamic Light Scattering method. Time dependencies for translation diffusion coefficient (D_t) and hydrodynamic radius (R_H) on were obtained for pure "collagen + collagenase" Tris–HCl buffer solution at different temperatures and for solutions with added $CaCl_2$, $ZnCl_2$ and $MgCl_2$ and EDTA. It was shown that digestion of type I collagen molecules by bacterial collagenase is the first-order reaction. Reaction rate coefficients were calculated. © 2021 Journal of Biomedical Photonics & Engineering.

Keywords: dynamic light scattering; type I collagen; translation diffusion coefficient; collagenase from Clostridium histolyticum; first-order reaction; activators; inhibitors; reaction rate coefficient.

Paper #3405 received 29 Jan 2021; revised manuscript received 1 May 2021; accepted for publication 13 May 2021; published online 2 Jun 2021. doi: 10.18287/JBPE21.07.020305.

1 Introduction

Enzyme-based drugs are commonly used in different fields of modern medicine: in surgery, gynecology, otolaryngology, ophthalmology, as well as in dermatology and cosmetology. Bacterial collagenase (for example, from *Clostridium histolyticum*) is one of them. The main collagenase feature is its ability to digest key protein of the animal extracellular matrix – collagen [1].

Violation of the collagen catabolism leads to fibrosis of organs and tissues. Increasing of collagen degradation rate occurs in case of autoimmune diseases (rheumatoid arthritis, lupus, etc.) because of excess collagenase synthesis as a result of immune response [2].

Clostridium histolyticum collagenases G and H (ColG and ColH) can easily digest collagens, regardless of their types and sizes [3]. It breaks down multiple bonds in collagen triple helixes as well as peptide bonds [4].

Bacterial collagenase from *Clostridium histolyticum* is extensively used as a clinical tool in the nonsurgical treatment of Dupuytren's disease [4, 5] in eye's diseases treatment, for enzymatic debridement, for accelerated resorption of catgut sutures.

Structural changes of collagen fibrils caused by collagenase are well studied by microscopy, and the degradation rate of protein is determined [6, 7]. Results obtained with microscopy clearly demonstrate the process of collagen fibers digestion and allow one to evaluate the rate of collagen fibril diameter changing. However, these results do not agree well with the results obtained in conditions close to physiological [6, 7].

Optical methods, like Dynamic Light Scattering (DLS), enable us to investigate collagen and collagenase molecules solutions in conditions close to physiological. By changing the solution's parameters (pH, temperature, solvent type) and adding of collagenase activators and inhibitors we can simulate the processes in living organisms. In our work, we studied the influence of temperature, activators ($CaCl_2$ and $ZnCl_2$) and inhibitors ($MgCl_2$ and EDTA) on collagenase activity. Since collagen by collagenase digestion in solutions takes on average 60 min, DLS enables us to monitor the dynamics of this process in real time [8].

2 Materials

2.1 Collagen

Collagen is the key component of extracellular matrix, making up from 25% to 35% of the whole-body protein

content. Although different types of collagen exist, they all are composed of molecules containing three polypeptide chains arranged in a triple helical conformation [6].

Over 90% of the collagen in the human body is type I collagen. It is a component of skin, bone, tendon and other fibrous connective tissues [9]. Molecular mass of collagen is approximately 300 kDa, average length of molecule is 300 nm [10].

In normal healthy tissues collagen molecules are resistant to most proteases attacks. Only specialized enzymes like collagenases can attack the collagen molecule.

2.2 Collagenase

There are two types of collagenase: tissue and bacterial. Tissue collagenases split collagen in its native triple helical conformation at a specific site, yielding fragments representing 3/4 and 1/4 lengths of the collagen molecule. After fragmentation the pieces tend to uncoil into random polypeptides and are more susceptible to attack by other protease [11].

Bacterial collagenases attack many sites along the helix. Collagenases from *Clostridium histolyticum* degrades the helical regions in native collagen preferentially at the X-Gly bond in the sequence Pro-X-Gly-Pro where X is most frequently a neutral amino acid [12]. This bond in synthetic peptide substrates may also be split. Bacterial collagenase cleaves the peptide bond of collagen in more than 200 places [11].

Molecular mass of collagenase is 79 kDa. Hydrodynamic radius is 4 nm according to the data obtained by dynamic light scattering method [5].

2.3 Enzymes activators and inhibitors

Enzyme activators are molecules or ions that bind to enzymes and increase their activity. Collagenases from *Clostridium histolyticum* are activated by ions Ca^{2+}, Zn^{2+} [13, 14]. Calcium ions support the conformation of the enzyme which is required for binding to the protein peptide chain. This conformation makes the active site available for the reaction. Zn^{2+} ions also are activators of collagenase, but its effect on the enzyme activity is much lower than that of Ca^{2+}. Zn^{2+} ions are located in the active site of the enzyme. Enzyme inhibitors are molecules that binds to an enzyme and decreases its activity. Collagenases from *Clostridium histolyticum* are inhibited by ions Mg^{2+}, EDTA, 1,10-phenanthroline, dipyridyl disulfide, 8-hydroxyquinoline [15, 16].

3 Experimental method

3.1 Dynamic Light Scattering

The DLS method enables one to determine the translation diffusion coefficient of particles in solutions by analyzing characteristic time of scattered light intensity fluctuations [17].

Translation diffusion coefficient of the particles is proportional to the decay rate of light scattering intensity fluctuations. The decay rate is obtained from the time-dependent correlation function of the scattered light intensity.

In the case of poly-dispersed solution where the particle sizes are different, the spectrum of the photocurrent is a continuous set (integral) of Lorentz curves with different half-widths. Consequently, to find the size distribution of particles (diffusion coefficients), it is necessary to solve the inverse spectral problem in the form of an integral equation with a Lorentzian kernel:

$$g^{(2)}(t) = \left[g^{(1)}(t) \right]^2 + 1 + \zeta(t), \tag{1}$$

$$g^{(1)}(t) = \int_0^\infty P(\Gamma) e^{-\Gamma t} \partial\Gamma, \tag{2}$$

where $g^{(1)}(t)$ – is the normalized autocorrelation function of the signal, $\zeta(t)$ – is the error associated with the stochastic nature of the signal itself [17]. If we neglect the influence of constant experimental noise $\zeta(t)$, Eq. (1) (Siegert relation) will allow us to calculate $g^{(1)}(t)$ in terms of $g^{(2)}(t)$, accumulated by the correlator during the experiment.

Integral Eq. (2) forms the basic principle of data processing in the photon correlation spectroscopy technique. This equation for $P(\Gamma)$ is a Fredholm integral first-order equation, known in mathematics as an ill-posed problem, that is a problem with a fundamentally absent algorithm for finding an exact solution. In this regard, various approximate solution methods are being developed, many of which give very good results.

In the experiments, the results were processed using the ***DYNALS*** software, in which the search for an approximate solution (4) is carried out using the regularization method of A. N. Tikhonov for integral equations [18].

Γ can calculated as described below:

$$\begin{aligned} \Gamma &= D_t q^2, \\ q &= \frac{4\pi n}{\lambda} \sin\frac{\theta}{2}, \\ D_t &= \frac{kT}{6\pi\eta R_H}, \end{aligned} \tag{3}$$

where D_t is the translation diffusion coefficient, q is the scattering vector, n is the refraction index, λ is the scattered light wave length, θ is the scattering angle, k is the Boltzmann constant, η is the dynamic viscosity of the solvent, T is the absolute temperature of the solution and R_H is the hydrodynamic radius.

3.2 Samples preparation

Collagen solutions were prepared by dissolving collagen type I from calf skin produced by Sigma Aldrich in 10 mM Tris-HCl (pH 7.5) buffer. Bacterial collagenase

from *Clostridium histolyticum* type IA by Sigma Aldrich was added in collagen solution. Concentration of collagen was 0.1 mg/ml, concentration of collagenase was 0.2 mg/ml (i.e 8 molecules of collagenase per 1 molecule of collagen).

As activators we have used salts $CaCl_2$, $ZnCl_2$ and as inhibitors – salt $MgCl_2$ and EDTA. Ionic strengths were 0.03 mol/L in all solutions.

The samples were processed in the ultrasonic bath with the frequency 3 kHz during 1 min.

Experiments have been carried out using the photon-correlation spectrometer Photocor-Complex with diode laser (wavelength of 647 nm, power 25 mW) [19]. Photocor-Complex spectrometer is equipped with built-in thermostat which allows one to control sample temperature.

4 Results and Discussions

4.1 Temperature dependencies

Using the DLS method we have experimentally obtained translation diffusion coefficient (D_t) on time dependencies of scattering particles in "collagen + collagenase" Tris-HCl buffer solution at different temperatures (Fig. 1).

The uniform increase in the mobility of scattering particles over time was observed at 22 °C and 30 °C. The maximum growth of D_t (and speed) is observed during the first 30 min, then the increase is not so rapid. At 40 °C average mobility of scattered particles is increasing threefold during first 30 min and then D_t on time dependence reaches saturation.

Since $T = 40$ °C is not optimal for collagen (protein can denature), all further experiments were carried out at T=30 °C (as the most optimal temperature).

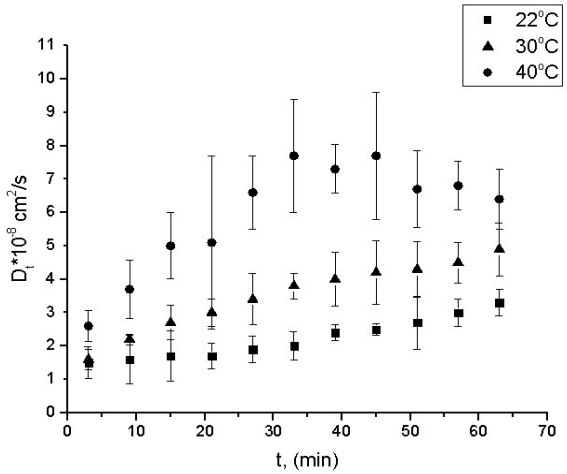


Fig. 1 Time dependencies of translation diffusion coefficient (D_t) on of scattering particles in "collagen + collagenase" Tris-HCl buffer solution at different temperatures.

Using the DYNALS package of programs evaluated values of hydrodynamic radius R_H has been calculated from D_t and then $\ln R_H(t)$ dependencies were obtained (Fig. 2).

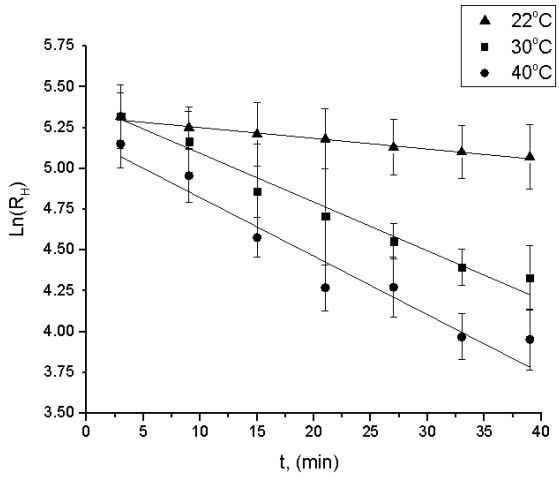


Fig. 2 The $\ln R_H$ dependencies on time at different temperatures, where R_H is hydrodynamic radius of scattering particles in "collagen + collagenase" Tris-HCl buffer solution.

In the first approximation, we can assume that concentration of collagen molecules in solution linearly depends on radius. In this case concentration of collagen molecules (C) exponentially decreases with time. Such character of $C(t)$ dependence corresponds to the first-order reaction [20].

The equations describing first-order reaction kinetics are given below. C_0 is initial concentration, k_1 is the reaction rate coefficient in units 1/time.

$$\ln C = \ln C_0 - k_1 \tau, \tag{6}$$

$$k_1 = -\tan\alpha. \tag{7}$$

Plotting $\ln(C)$ with respect to time for a first-order gives us a straight line with the slope of the line equal to $-k_1$ (Fig. 2).

In the Table 1 values of k_1 (min^{-1}) for different temperatures are presented. STD k_1 was calculated using a graphing program based on the least squares method.

Table 1 Values of k_1 (min^{-1}).

Temperature, °C	k_1	STD k_1
22	0.012	0.001
30	0.031	0.003
40	0.054	0.003

The highest value of k_1 corresponds to 40 °C. However, this temperature is not optimal for collagen. With prolonged thermal action protein may denaturate, which happened at 90th min of the experiment.

4.2 "Collagen + collagenase" solutions with activators $CaCl_2$ and $ZnCl_2$

We have selected the following scheme for investigations of "collagen + collagenase" solutions with activators and inhibitors: experimentally obtain translation diffusion coefficient on time $D_t(t)$ dependence, evaluate values of hydrodynamic radius R_H from D_t, plot $\ln R_H(t)$ dependencies.

The $\ln R_H(t)$ dependencies for pure "collagen + collagenase" Tris-HCl buffer solution and in solutions with added $CaCl_2$ and $ZnCl_2$ are presented in Fig. 3. Calculated values of k_1 (min^{-1}) are presented in Table 2.

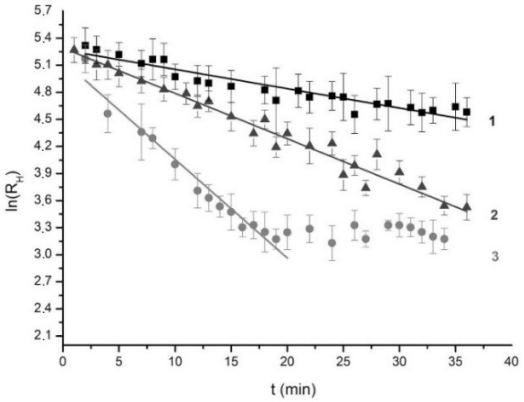


Fig. 3 The $\ln R_H$ time dependencies, where R_H is hydrodynamic radius of scattering particles, in pure "collagen + collagenase" Tris-HCl buffer solution (1) and with added $ZnCl_2$ (2) and $CaCl_2$ (3), T = 30 °C.

Bacterial collagenase initially contains Zn^{2+} and Ca^{2+} ions. Zn^{2+} is responsible for the activation of amide group and Ca^{2+} for the formation of tertiary structure [21].

When $ZnCl_2$ is added to "collagen + collagenase" Tris-HCl buffer solution, Zn^{2+} ions may occupy calcium positions in collagenase, but due to the difference in ionic radii ($r_{ion}(Ca^{2+})$ = 114 pm, $r_{ion}(Zn^{2+})$ = 88 pm) the effect of activity centers formation is not fully achieved (Fig. 3, curve 2).

When $CaCl_2$ is added to "collagen + collagenase" Tris-HCl buffer solution Ca^{2+} ions occupy all available positions in collagenase and form maximum number of active centers (Fig. 3, curve 3).

Also, for the solution with $CaCl_2$ added $\ln R_H(t)$ dependence becomes non-linear after 20 min (Fig. 3, curve 3). We suppose that it corresponds to further digestion of collagen molecule's pieces by bacterial collagenase. Unlike tissue collagenase which splits collagen in its native triple-helical conformation at a specific site, bacterial collagenase is able also to attack and degrade collagen molecule's fragments [11].

4.3 "Collagen + collagenase" solutions with inhibitor EDTA

To investigate inhibitor influence on collagen by collagenase digestion, we have added EDTA to "collagen + collagenase" Tris-HCl buffer solution. During first 30 min D_t value was changed from $(1.5 \pm 0.2) \times 10^{-8}$ cm^2/s to $(2.1 \pm 0.3) \times 10^{-8}$ cm^2/s, and during next 30 min from $(2.1 \pm 0.3) \times 10^{-8}$ cm^2/s to $(2.6 \pm 0.4) \times 10^{-8}$ cm^2/s.

At 64th minute $CaCl_2$ as an activator was added to "collagen + collagenase + EDTA" solution. In half an hour after that D_t value changed from $(2.6 \pm 0.4) \times 10^{-8}$ cm^2/s to $(10.0 \pm 1.2) \times 10^{-8}$ cm^2/s, and in 1 h to $(13.0 \pm 2.1) \times 10^{-8}$ cm^2/s (Fig. 4)

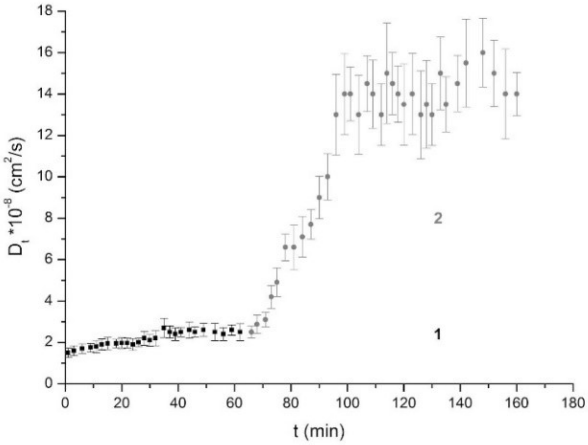


Fig. 4 Translation diffusion coefficient (D_t) on time dependencies of scattering particles in "collagen + collagenase" Tris-HCl buffer solution with added EDTA (1) and EDTA with $CaCl_2$ (2), T = 30 °C.

Corresponding hydrodynamic radius R_H values were calculated and $\ln R_H(t)$ dependencies were obtained for pure "collagen + collagenase" Tris-HCl buffer solution and for solutions with added EDTA and EDTA + $CaCl_2$ (Fig. 5). Values of k_1 (min^{-1}) are presented in Table 2.

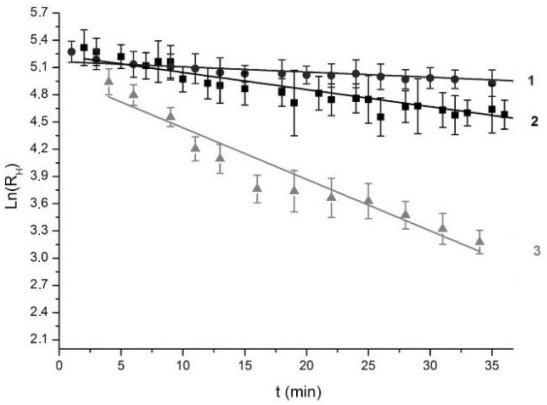


Fig. 5 The $\ln R_h$ time dependencies, where R_h is hydrodynamic radius of scattering particles, in pure "collagen + collagenase" Tris-HCl buffer solution (2) and with added EDTA (1) and EDTA with $CaCl_2$ (3), T = 30 °C.

EDTA molecules bind with calcium ions in solution and block calcium ions access to all available places in collagenase. So collagen by collagenase digestion slows down (Figs. 5, 6). When we add $CaCl_2$ to

"collagen + collagenase + EDTA" solution, amount of Ca^{2+} ions recovers and collagenase activity restores.

4.4 "Collagen + collagenase" solutions with inhibitor $MgCl_2$

The same way we have investigated $MgCl_2$ influence on collagen by collagenase digestion. $D_t(t)$ and $\ln R_H(t)$ dependencies were obtained (Figs. 6, 7).

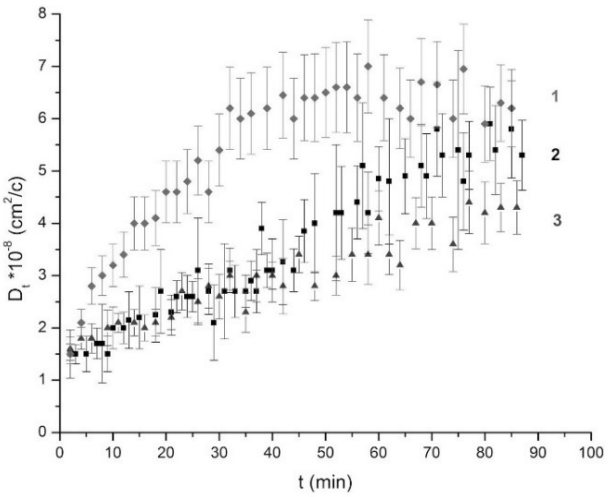


Fig. 6 The time dependencies of translation diffusion coefficient (D_t) of scattering particles in "collagen + collagenase" Tris-HCl buffer solution (2) with added $MgCl_2$ (3) and with added $MgCl_2$ and $CaCl_2$ (1), T = 30 °C.

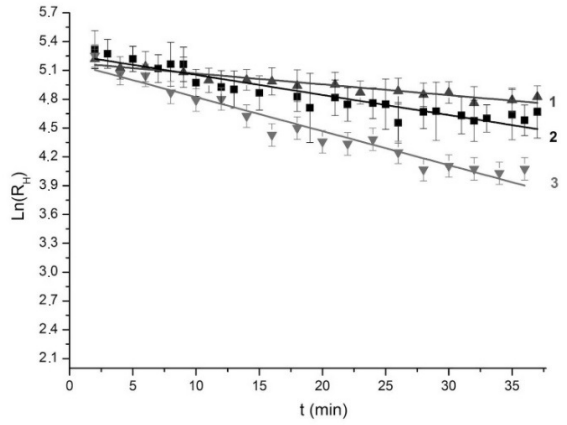


Fig. 7 The $\ln R_h$ time dependencies, where R_h is hydrodynamic radius of scattering particles, in pure "collagen + collagenase" Tris-HCl buffer solution (2) added $MgCl_2$ (1) and $MgCl_2$ with $CaCl_2$ (3), T = 30 °C.

According to the Pearson acid base concept Ca^{2+} and Mg^{2+} are hard Lewis acids and Zn^{2+} is intermediate Lewis acid [22].

When $MgCl_2$ is added to "collagen + collagenase" Tris-HCl buffer solution magnesium mainly aims to replace the zinc in collagenase due to close values of the ionic radii: $r_{ion}(Mg^{2+})$ = 6 pm, $r_{ion}(Zn^{2+})$ = 88 pm. However, Mg^{2+} is hard Lewis acid and it decreases the activity of the amide group in enzyme. This fact leads to the inhibition of protein destruction process (Fig. 3, 5). Calculated values of k_1 (min^{-1}) are presented in Table 2.

When we add $CaCl_2$ to "collagen + collagenase + $MgCl_2$" solution, collagenase activity partially restores but initial value is not achieved.

5 Conclusions

Presented results allow one to draw a conclusion that digestion of type I collagen molecules by bacterial collagenase is the first-order reaction. Corresponding values of k_1 (min^{-1}) calculated for solutions with activators and inhibitors are given in Table 2.

Table 2 Values of k_1 (min^{-1}).

Solution	k_1	STD k_1
Collagen + Collagenase	0.023	0.002
Collagen + Collagenase + $ZnCl_2$	0.051	0.004
Collagen + Collagenase + $CaCl_2$	0.104	0.008
Collagen + Collagenase + $MgCl_2$	0.011	0.001
Collagen + Collagenase + EDTA	0.006	0.001
Collagen + Collagenase + $MgCl_2$ + $CaCl_2$	0.035	0.003
Collagen + Collagenase + EDTA + $CaCl_2$	0.057	0.004

It was found that the most efficient activator of collagen type I digestion by collagenase is Ca^{2+} and the most efficient inhibitor is EDTA.

It was shown that influence of EDTA and $MgCl_2$ on collagen type I digestion by collagenase may be reduced by adding $CaCl_2$ to the solution. Ca^{2+} ions restore collagenase activity.

The obtained results demonstrate that Dynamic Light Scattering method can be used for first-order reaction rate coefficient k_1 determination. The key advantage of Dynamic Light Scattering based k_1 measurement is the possibility of real-time digestion monitoring. By variating temperature, solution formula and collagen-collagenase ratio different physiological states can be simulated for *in vitro* investigation.

Disclosures

All authors declare that there is no conflict of interests in this paper.

Acknowledgements

The authors would like to thank Dr. Nataliya E. Borisova from Department of Radiochemistry, Chemical Faculty, Lomonosov Moscow State University for the opinion of an expert and for providing $ZnCl_2$ and $MgCl_2$.

This research has been supported by the Interdisciplinary Scientific and Educational School of Moscow University «Photonic and Quantum Technologies. Digital Medicine».

References

1. R. Bauer, K. Janowska, K. Taylor, B. Jordan, S. Gann, T. Janowski, E. C. Latimer, O. Matsushita, and J. Sakon, "Structures of three polycystic kidney disease-like domains from Clostridium histolyticum collagenases ColG and ColH," Acta Crystallographica Section D: Biological Crystallography 71(3), 565–577 (2015).
2. I. Mandl, "Collagenases and elastases," in Advances in Enzymology and Related Areas of Molecular Biology 23, F. F. Nord (Eds.), Interscience Publishers, New York, 163–264 (1961).
3. Collagenase from Clostridium histolyticum, Merck KGaA, (accessed 01 May 2021). [https://www.sigmaaldrich.com/catalog/product/sigma/c9891].
4. S. Müller-Herrmann, T. Scheibel, "Enzymatic degradation of films, particles, and nonwoven meshes made of a recombinant spider silk protein," ACS Biomaterials Science & Engineering 1(4), 247–259 (2017).
5. J. Nanchahal, K.S. Midwood, "Treatment for dupuytren's disease," Isis Innovation Limited 8(2), 22–23 (2015).
6. M. F. Paige, A. C. Lin, and M. C. Goh, "Real-time enzymatic biodegradation of collagen fibrils monitored by atomic force microscopy," International Biodeterioration & Biodegradation 50(1), 1–10 (2002).
7. S. K. Mallya, K. A. Mookhtiar, and H. E. Van Wart, "Kinetics of hydrolysis of type I, II, and III collagens by the class I and II Clostridium histolyticum collagenases," Journal of Protein Chemistry 11(1), 99–107 (1992).
8. A. V. Petrova, I. A. Sergeeva, G. P. Petrova, and A. V. Mitrofanova, "The Features of Interaction of Collagen and Collagenase Molecules in the Presence of Chromium and Calcium Ions in Solutions by Dynamic Light Scattering," Moscow University Physics Bulletin 75(6), 611–617 (2020).
9. R. Ritchie, W. Yang, and M. Meyers, "Structural Architectures with Toughening Mechanisms in Nature: A Review of the Materials Science of Type-I Collagenous Materials," Progress in Materials Science 103, 425–483 (2019).
10. K. Wu, W. Liu, and G. Li, "The aggregation behavior of native collagen in dilute solution studied by intrinsic fluorescence and external probing," Spectrochimica Acta Part A: Molecular and Biomolecular Spectroscopy 102, 186–193 (2012).
11. Worthington Tissue Dissociation Guide, Worthington Biochemical Corporation, (accessed 01 May 2021). [http://www.worthington-biochem.com/tissuedissociation/collagenase.html].
12. N. Ohbayashi, N. Yamagata, M. Goto, K. Watanabe, Y. Yamagata, and K. Murayama, "Enhancement of the Structural Stability of Full-Length Clostridial Collagenase by Calcium Ions," Applied and Enviromental Microbiology 78, 5839–5844 (2012).
13. J. J. Wilson, O. Matsushita, A. Okabe, and J. Sakon, "A Bacterial Collagen-binding Domain with Novel Calcium-binding Motif Controls Domain Orientation," The EMBO Journal 22(8), 1743–52 (2003).
14. E. L. Angleton, H. E. Van Wart, "Preparation and Reconstitution with Divalent Metal Ions of Class I and Class II Clostridium histolyticum apocollagenases," Biochemistry 27(19), 7406–7412 (1988).
15. S. Seifter, P. M. Gallop, LeRoy Klein, and E. Meilman, "Studies on Collagen: II. Properties of Purified Collagenase and Its Inhibition," Journal of Biological Chemistry 234(1), 285-293 (1959).
16. P. Seglen, "Preparation of isolated rat liver cells," Methods in Cell Biology 13, 29-83 (1976).
17. H. Z. Cummins, E. R. Paik (Eds.), Photon Correlation and Light Beating Spectroscopy, Springer Science and Business Media, New York (1974). ISBN: 978-1-4615-8906-8.
18. [http://www.softscientific.com/science/WhitePapers/dynals1/dynals100.htm].
19. Multi-angle particle size analyzer Photocor Complex, Photocor Instrument, (accessed 01 May 2021). [http://www.photocor.com/dls-instrument].
20. P. Atkins, J. Paula, Physical Chemistry, 8-th ed., W. H. Freeman and Company, Gordonsville, USA (2006).
21. U. Eckhard, E. Schönauer, D. Nüss, and H. Brandstetter, "Structure of collagenase G reveals a chew-and-digest mechanism of bacterial collagenolysis," Nature Structural & Molecular Biology 18(10), 1109–1115 (2011).
22. G. P. Robert, R. G. Pearson, "Absolute Hardness: Companion Parameter to Absolute Electronegativity," Journal of the American Chemical Society 105(26), 7512–7516 (1983).

Optical Signature Analysis of Liver Ablation Stages Exploiting Spatio-Spectral Imaging

Mohamed H. Aref[1*], Ramy Abdlaty[1], Mohamed Abbass[1], Ibrahim H. Aboughaleb[2], Ayman A. Nassar[2], and Abou-Bakr M. Youssef[3]

[1] Biomedical Engineering Department, Military Technical College, Cairo, Egypt
[2] Biomedical Engineering Researcher, Egyptian armed forces, Cairo, Egypt
[3] System & Biomedical Engineering Department, Cairo University, Giza, Egypt

*** e-mail:** Mh-aref@ieee.org

Abstract. *Background and Objective:* Thermal ablation modalities such as Radiofrequency ablation (RFA) / Microwave ablation (MWA) are deliberately used for marginally invasive tumor removal by escalating tissue temperature. For precise tumor extinguish, thermal ablation outcomes need routine monitoring for tissue necrosis in a challenging research task. The study aims to exploit hyperspectral imaging (HSI) to evaluate the impact of the liver tissue ablation. *Materials and Methods*: RFA with temperature range (≥80 °C) was accomplished on the *ex vivo* animal liver and evaluated using a spectral camera (400~1000 nm). The spectral signatures were extracted from the HSI data after the following processing steps: capturing three spectral data cubes for each liver sample with total 7-samples (before ablation, after ablation, and after ablation with sample slicing) using an HSI optical configuration. The custom HSI processing comprises "Top-hat and Bottom-hat transform" combined with "watershed transform" image segmentation to increase the intensity for a region of interest (ROI) of the investigated tissue, linking spectral and spatial data. Additionally, statistical analysis for HSI data was performed to exclusively select the best spectral band that discriminates between the normal, thermally-damaged, and ablated liver regions. *Results:* The variation of the optical parameters for the investigated liver samples provides variable interaction with the light diffuse reflection (R_d) over the spectrum range (400~1000 nm). Where, the extracting spectral information of the various tissue zones from the induced RFA linked to the hemoglobin, methemoglobin, and water permits variations. The generated spectral image after image enhancement utilizing "Top-hat and Bottom-hat transform" followed by "watershed segmentation", showed high contrast between normal and thermal regions at a wavelength (600 nm). However, the wavelength (900 nm) shows a high variance between the normal and ablated regions. Finally, delineation of the thermal and ablated regions on the complemented enhanced image. *Conclusion*: HSI is considered a promising optical noninvasive technique for monitoring the RFA toward enhancing the ablation-based treatment for liver tumor outcomes. © 2021 Journal of Biomedical Photonics & Engineering.

Keywords: liver cancer; hyperspectral imaging; radiofrequency ablation; thermal damage; top-hat and bottom-hat transform; watershed segmentation.

Paper #3412 received 29 Mar 2021; revised manuscript received 19 Jun 2021; accepted for publication 21 Jun 2021; published online 29 Jun 2021. doi: 10.18287/JBPE21.07.020306.

1 Introduction

The liver is the biggest organ regarding the human organs and exemplifies about 3~5% of its weight in grown-ups. The growing knowledge of the liver anatomy assists in developing novel surgical techniques that are mainly used in treating both primary and secondary liver lesions [1]. There are several causes of liver inflammation, such as (drug- venomousness, hepatitis A, hepatitis B, liver alcoholic disease, and nonalcoholic steatohepatitis) [2].

Hepatocellular carcinoma (HCC) is the significant recurrent crucial tumor of the liver [3]. HCC is ranked the 4th in tumor repetition frequency and the 3rd in death by malignancy worldwide [4]. HCC is the most widely recognized liver cancer with more or less three-quarters of the diagnosed cases [5]. Over 600,000 liver patients pass away by HCC annually. Seeking the causes for the liver malignancy is a challenging task for both clinical and pharmaceutical research teams [6]. Egypt witnessed a noticeable augmentation of HCC patients who were earlier diagnosed with other liver diseases regarding the other countries in the same region [7].

The early diagnosis of HCC enables the request of primary stage therapies that considerably increases the potential for patients survival [8]. Liver transplantation, if available, is the highest survival option for HCC patients treatment [9–11]. The availability of liver transplantation is restrained by the availability of donors and the financial abundance beside complying with the Milan criteria [12].

The fusion of the significance of minimum invasive diagnosis and therapeutic methods is an approach for elevating the proficiency of the modern surgical techniques [13]. Although, the resection of cancers in neurosurgery with regular restorative strategies are generally depends on the experience of neurosurgeons during the open operation [14]. However, for liver-tumor therapy, careful resection is a very common technique [15]. The third therapeutic option is suitable for primary stage HCC patients with the non-cirrhotic liver is hepatic resection [16]. Minimal invasive thermal ablation modality has proved to be a vital treatment choice when achievable [17].

The minimal invasive thermal ablation techniques such as: radio-frequency ablation (RFA) [18], laser thermal ablation (LTA) [19, 20], microwave ablation (MWA) [21, 22], high-intensity focused ultrasound (HIFU) [23], and bulk thermal ablation (BTA) [24, 25]. All the aforementioned techniques represent significant result therapy for unresectable essential and secondary liver tumors [18, 26, 27]. The main role of all the thermal ablation techniques is to gradually increase the temperature in the investigated sample (≥60 °C) to deliver a necrotic condition for tumor cells.

Recently, various studies informed the incorporation of few imaging techniques for the purpose of monitoring the ablation of the liver`s tumors. Where, the diffuse reflectance spectroscopy (DRS) is utilized to assess RFA of 8 investigated samples of liver tumor with high accuracy (97~99%) to discriminate between the predicted thermal damage and the histology report [17]. Moreover, another study exploiting the computed tomography (CT) with MWA to investigate three ex-vivo porcine samples with a thermal procedure (100 W, 4.5 min), the results demonstrate ablation region ($4.1 \pm 0.2 \times 5.6 \pm 0.2$) [28]. Additionally, Magnetic Resonance Imaging for Thermometry (MRIT) is recently counted as the gold-standard in measuring the tumor necrosis by thermal ablation [29].

HSI is else called imaging spectroscopy, which declares the innovation of integration typical imaging and spectroscopy modalities to secure both spatial and spectral data of an item [30–32]. Although imaging spectroscopy has been accessible as a far off detecting innovation since the 1980s [33, 34]. Up to this point, spectral imaging has regularly just been accessible to a constraint number of researchers and experts because of the significant expenses of building spectral cameras and the complexity of processing spectral extracted data related to multiple bands [35–39].

HSI is an expanding imaging technique to divergent fields of science including the medical field such as monitoring of thermal ablation.-M. Landro et. al. present a study in assessing the laser ablation in the porcine *in vivo* liver [40] and monitoring laser-induced thermal damage in gastric mucosa [41]. There are also Skin Erythema and Pigmentation [42], Breast cancer identification from the pathological tissues [43–46]. Furthermore, a research on brain tissue was capable to identify glioblastoma (GB) with sensitivity 88% and specificity 77% [47, 48]. Moreover, the diffuse reflectance measurements to indicate the hemoglobin oxygenated and deoxygenated condition [49–51].

The incident light interrelates with the liver tissue regarding its optical properties (type/size/density/color) to provide several optical properties as example (Transmission, Absorption, and Diffuse Reflectance) [52, 53]. As a result of these properties, it can be recognizing and characterized the investigated samples in a certain band by their spectral signature, as more clarified in Fig. A1 in the appendix.

This study was performed in the form of successive series of investigation trials to highlight HSI capability to monitor RFA [54–56]. M. H. Aref et al. have showed in previous study that the HSI could be discriminate the surface thermal removals upon on the investigated 10 samples of the *ex vivo* bovine liver at ideal spectral picture (720 ± 18.92 nm) [55]. Additionally, investigate both the side penetration and surface of RFA [54]. Moreover, successfully distinguish and delineate with cross-correlation algorithm the thermal damage in *ex vivo* liver samples [56]. However, the HSI strategy offers a particular spectral picture over the spectrum range as it gathers latitudinal and spectral data for under investigation samples [8, 57–58].

In the presented study, we aimed to build up an optical imaging system to measure the diffuse reflectance (R_d) exploiting the hyperspectral (HS) camera to identify and characterize the spectral signature of the thermal and

ablated regions in *ex vivo* liver samples. Applying image processing incorporates contrast enhancement to the raw data uitilizing "Top-hat and Bottom-hat transform" combined with "watershed transform" image segmentation to increase the intensity of the region of interest (ROI) for the investigated tissue. Moreover, delineation of the thermal and ablated regions on the complemented enhanced image to provide a vital information for assisting the surgeon in monitoring the thermal ablation outcomes.

2 Materials and Methods

The captured image data with the HSI system, image progression in advance, and subsequently thermal ablation, contrast enhancement to the original image using "Top-hat and Bottom-hat transform" combined with "watershed transform" image segmentation algorithm as channels to highlight the thermal and ablated regions in the scan image cubes by the HS camera. The capturing time for each image is about 6~10 sec and calculation time is <15 sec using MATLAB software (The MathWorks, Natick, MA, USA, 2019) on a computer with processor Intel Core i7 @1.8 GHz with a 16 GB RAM.

2.1 The prospective approach interconnections protocol and procedures

- Sample preparation & Tissue characterization.
- Hyperspectral (HS) scan Images for the *ex vivo* liver samples.
- The measurements for sample diffuse reflection (R_d).
- The statistical Calculation of the optical properties for validation.
- Selecting the optimum spectral image with high contrast between normal, thermal, and ablation.
- Applying the Custom clustering algorithms.
- Delineation of the ablation and thermal effect regions of the enhancement image.

2.2 Investigated sample slicing and preparation

Before proceeding to the experimental investigation, the sample collection procedure was approved by Ain Shams university – faculty of medicine – ethics committee. A total of seven different samples of bovine liver tissue achieved from a fresh slaughtered cow which was attained from a local abattoir in Egypt, then transported in an icebox to the laboratory. The investigated *ex vivo* liver samples were crudely cut into slices with approximate sizes (~10 × 8 cm), Sample thickness 23~36 mm. The investigated samples were preserved in an evacuated bags in the freezer at temperature ≤ –65 °C, and picked out and added in a neutral buffered saline before the RFA experiments with enough time [55]. The inspected lap trails at temperature 23 ~ 24 °C, and the explored sample temperature 25 ~28 °C, observed with a multimeter (Fluke, 289, USA), as shown in Fig. 1 and the additional investigated samples had been displayed in Fig. A2 in the Appendix.

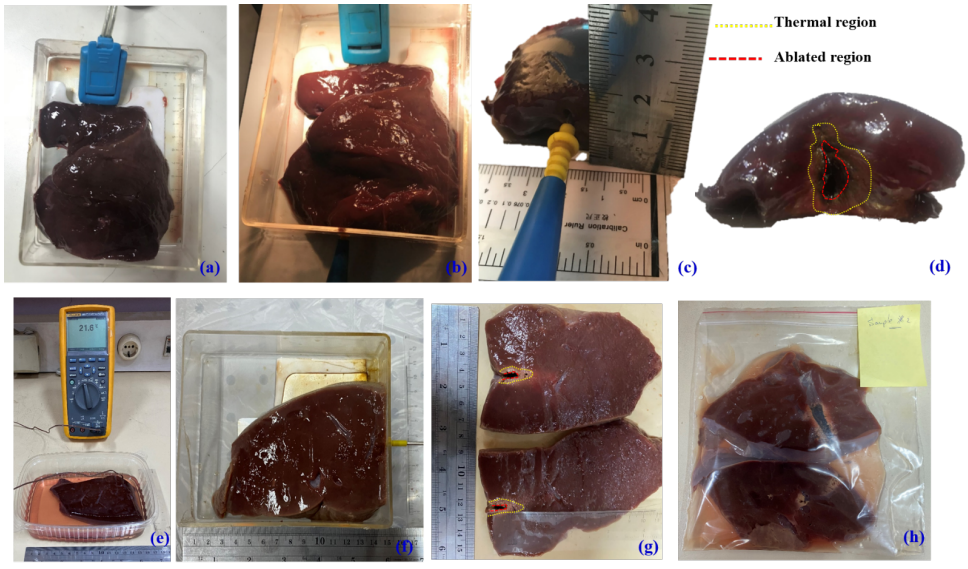


Fig. 1 The investigated *ex vivo* liver samples; (a) the liver Sample #1 before ablation, (b) the liver Sample #1 after ablation in the plastic tray of the experiment and with the RF probe, (c) the illustration for the active blade of the RF tip inserted in the investigated liver Sample #1; (c) the liver Sample #1 after the ablation trail highlighting the affected ablation region in Red dotted lines and thermal regions in yellow dotted lines, (e) the investigated liver Sample #4 before ablation inserted in neutral buffered saline and observed with a multimeter (Fluke, 289, USA), (f) the investigated liver Sample #4 after ablation in the experimental plastic tray and with the RF tip inserted , (g) the investigated liver Sample #4 after ablation and slicing to compare the actual ablated region with scientific expert, (h) the sliced liver Sample #4 after ablation and wrapped in the vacuumed bags and tissue storage solution prepared to be sent to the pathological lap.

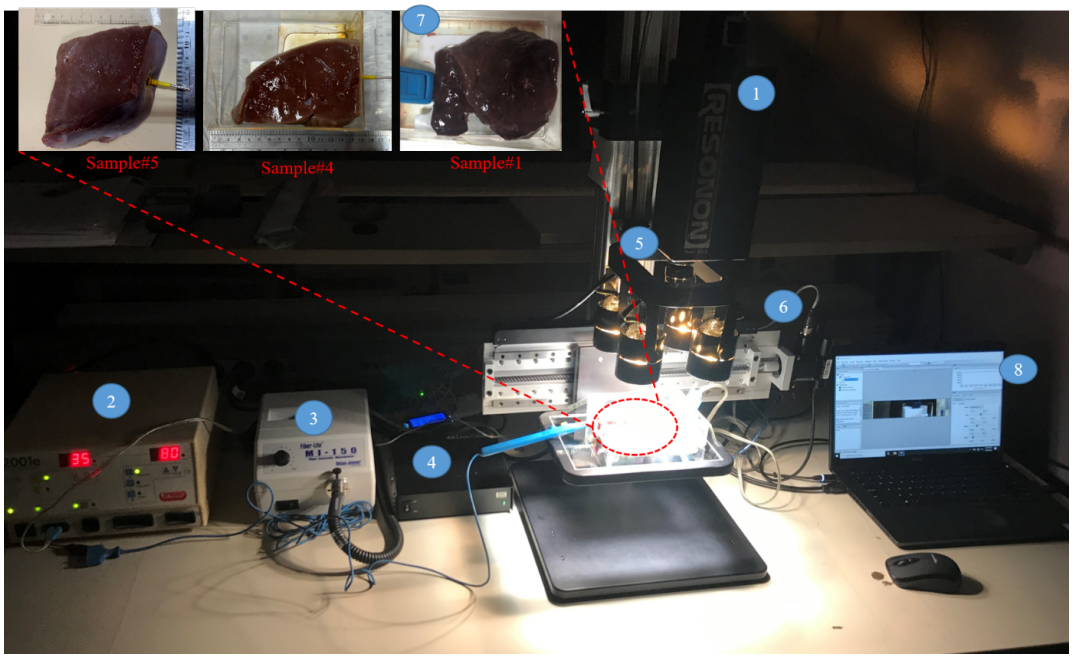


Fig. 2 Hyperspectral optical imaging system for measuring the light diffuse reflectance (R_d) of the investigated *ex vivo* tissue samples; (1) hyperspectral camera (Resonon, Pika XC2, USA); (2) electrosurgical generator (Premier; 2001e, France); (3) the source light for the transmission measurement trails (Fiber-lite, MI-150, USA); (4) the power supply controller for the light source (Mean Well, ENP360-12, Taiwan) of diffuse reflection (R_d) measurement trails; (5) the 4-halogen lamps (4 × 35 W halogen lamps) at wavelength range (380~1050 nm); (6) the linear translation stage; (7) the investigated *ex vivo* liver samples; (8) the computer and image software processing and analysis.

The experiment was performed with Radiofrequency (RF) Generator (Premier; 2001e, France) to generate the necessary thermal ablation in the liver tissue. The power protocol was as following (25~50 W, 1~5 min, Continues). The affected ablation region in the sample was around ~10 × ~8 mm. Furthermore, all the image processing of the captured HS cube was less than 5 min during the thermal elaboration. The complete data of the investigated tissue with the power protocol for each sample experiment, had been illustrated in Table A1 in the Appendix.

2.3 Optical imaging system and experimental trail

The active blade of the RF generator was positioned in the center of the investigated sample. Where terminal was embedded around 1.5 ~ 2 cm into the liver sample, and RF power was applied for 2 ~ 5 min. Following data procurement, markers were embedded into the imaging plane on the two sides of the electrode, and the ablation was cut through this plane and captured with the commercial CCD camera for data recording. After the RFA the samples is sliced in the coronal plane from the RF tip insertion and had been manually measured and prepared to be sent to the pathology evaluation (pathology is the ground truth to validate the tissue necrosis and thermal effect).

To capture the necessary HSI data, we exploited hyperspectral camera (Resonon, Pika XC2, USA) with spectral resolution equal to 1.3 nm, bit depth of 12 bits, maximum frame rate equal to 165 fps, spatial channels = 1600, and 462 spectral channels. The camera is incorporated with a lens (Schneider, 6 mm, CNG 2.1/6- 0901, Range 400 : 1000 nm, Germany). The utilized light assembly for the HSI data capturing is a configuration of a polychromatic source light controller (Mean Well, ENP360-12, Taiwan) with a light source (4 × 35 W tungsten halogen lamps) at wavelength range (380 ~ 1050 nm). The prospective approach and its experimental setups aimed to measure the light diffuse reflectance (R_d) for an *ex vivo* tissue sample, by exploring the optical properties spectroscopy in the near-infrared and visible (NIR-VIS) spectrum, as shown in Fig. 2.

2.4 Hyperspectral Image Conquering

HSI sensors produce a three-dimensional (3D) information structure, called HS cube, where the spatial data is contained in the initial two measurements, while the third measurement incorporates the spectral data [59, 60]. In a hyperspectral picture, every pixel has an arrangement of reflectance in various spectral frequencies that can show the spectral outline of that pixel [48].

Three individual arrangements of hyperspectral pictures were gotten for each explored liver sample. Line-scan images were captured for exposure times of 6 sec at 1.3 nm intervals, and corresponding to 1600 × 600 pixels per spectral band (3.6 sec for each cube image). The hyperspectral images were composed of a total of 447 spectral bands in the range from

approximately 379 to 1050 nm, incorporated with a lens with Visible and Near-infrared range (VNIR) range (400 to 1000 nm).

2.5 Basic Concepts and Fundamentals of Clustering Algorithms

The cluster is commonly handled as a gathering of an item's which were "identical" between them just as "divergent" to an item's having a place with the further clusters [61]. Clustering algorithms are as follows:

1. Exclusive-clustering.
2. Overlapping-clustering.
3. Hierarchical-clustering.
4. Probabilistic-clustering.

In this study, we used one of the capturing is frequently applied clustering and segmentation algorithms:

- K-mean clustering.
- Watershed transform / Segmentation.
- Fuzzy C-means clustering.

2.5.1 K-means Clustering

The K-means clustering is the simplest unsupervised learning algorithm that is capable to solve the distinguished clustering issues. K-means algorithm is prevalent in rapid decision making approach for its simplicity, adequacy as well as being moderate although it had a steady presentation across various issues [54, 62, 63] Despite the way that the time inconvenience was direct to the information size, customary k-implies is so far not admirably compelling to manage a web-scale data [61]. The strategy follows a basic as well as a simple approach to characterize a given data set via a specific number of clusters settled an earlier [64].

2.5.2 Watershed transform / Segmentation

The watershed transform is a structural essential tool for image segmentation [65]. It is established on a mathematical structure for segmenting the data of interest. It was initially represented by L. Vincent and Soille in the image segmentation field then extended rapidly in recent years [66, 67]. It is touchy to weak edges and is appropriate for getting one-pixel associated and closed contours with accurate area [68, 69]. Conventional watershed segmentation is sensitive to noise and can prompt critical over-segmentation. Along these lines, numerous analysts have proposed different strategies ceaselessly for improving the technique including developing a preprocessing step for calculating the distance transform for a binary picture before watershed transformation [67, 70].

2.5.3 Fuzzy C-means clustering

Fuzzy C-means (FCM) strategy is considered as a significant high beneficial because it isolates a lot of information from one single picture unlike to other hard-segmentation methods [71]. In FCM clustering technique, the image pixel was assigned to the fuzzy clusters instead of a label [72]. FCM empowers pixel to have a spot with different clusters through changing degrees of part transport function, dissimilar to a hard-clustering system that powerfully designates the pixel to just a single class. The FCM Algorithm is the technique for clustering at which it concurs a solitary purpose of a content having a place with two or more clusters [73].

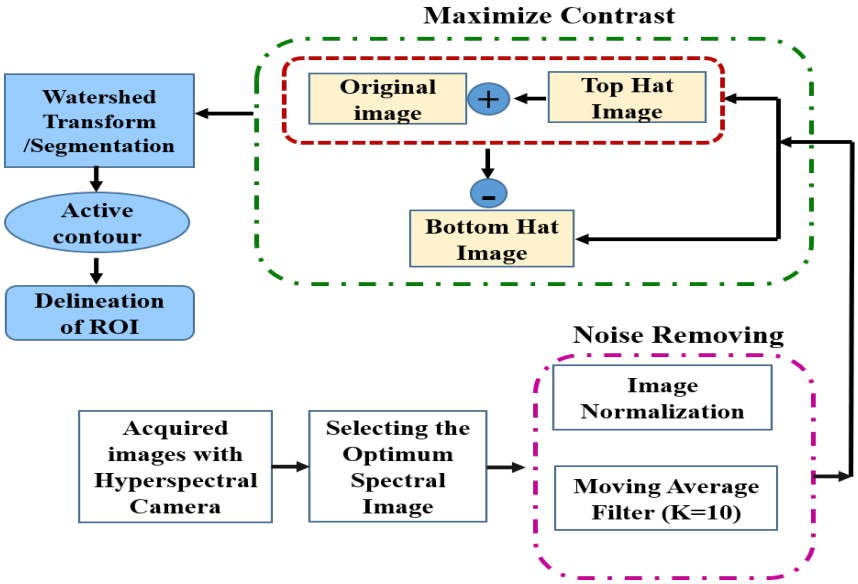


Fig. 3 The basic block diagram of the custom algorithm for image analysis and preprocessing after selecting the optimum spectral image of the investigated liver sample tissue.

2.6 The Image Analysis and Preprocessing

The image analysis and preprocessing step mainly incorporates the Moving average filter and normalization for the acquired HSI to remove the background noise. Moving average filter (K = 10) is exploited to banish the noise influences. For image enhancement, we exploit a common methodology using "Top-hat and Bottom-hat transform". Next, utilizing the "watershed transform" for image segmentation to increase the ROI of the investigated liver tissue samples. Moreover, delineation of the thermal and ablated regions on the complemented enhanced image to discriminate the distinct regions, as explained in the block diagram in Fig. 3.

A basic advance in HSI imaging, before image procurement, is a level field correction for data standardization. A white equalization and dim current measurements were utilized to gain relative reflectance from the sample [60]. The dark cube was captured by closing the HS camera lens with its cap to avoid any incidence light to the sensor. Information from a dark image and white balance estimations were utilized to correct the deliberate material image. The fundamental reason for this amendment is to wipe out artifacts and noise impacts on the sample tissue, as more clarified in Eq. (1):

$$RF(\theta) = \frac{Im(\theta) - Id(\theta)}{Iw(\theta) - Id(\theta)} \times 100\%, \quad (1)$$

where $RF(\theta)$ is the qualified reflectance of the sample image, $Im(\theta)$ is the caught image, $Id(\theta)$ is the dark scanned image with a closing lens, and $Iw(\theta)$ is the acquired whiteboard image.

Employing the normalization on the acquired image to remove the polychromatic light noise. The originally captured images numerous due to the incident light, the asymmetrical shape of the investigated sample, and temperature deviations, spectral images have to be normalized comprising pixel normalization, as demonstrated in Eq. (2).

$$I_{new} = (I_{previous} - min_{previous}) \times \times \frac{max_{new} - min_{new}}{max_{previous} - min_{previous}} + min_{new}. \quad (2)$$

Even though, Normalization adjusts an m-dimensional grayscale subsequent image $I_{previous}$:{A} with intensity evaluations in the range ($min_{previous}$) to the extreme ($max_{previous}$) into a new image I_{new}:{A} with intensity rates in the least range (min_{new}) to the extreme (max_{new}).Then, utilizing the Moving average filter, the filter at kernel value = 10 for noise elimination and image improvement [74], as clarified in Eq. (3).

$$f(x \times y) = \frac{1}{qt} + \sum_{(r \times c) \in W}^{\infty} S(r \times c), \quad (3)$$

where S is the noisy picture, $f(x \times y)$ is the restored picture, and r and c for the row and column coordinates correspondingly, within a window W of size qt where the procedure takes place.

To maximize the image contrast, we utilized Top-hat and Bottom-hat Transform for image contrast enhancement.

- **The top-hat transform** could be illustrated as the difference between the original image and the opening image. Where the opening image is a collection of spotlight parts that fit a precise structuring element.
- **The bottom-hat transform** could be illustrated as the difference between the closing of the original image and the original image. The closing of an image is the collection of background parts of an image that fit a precise structuring element.

Although in image contrast enhancement, the bottom-hat image represents the gaps between the targets of interest. To maximize the contrast between the targets and the gaps that separate them from each other, the "bottom-hat" image is subtracted from the "original + top-hat" image.

Since "watershed transform" distinguishes intensity "valleys" of the acquired image. We utilized the (*imcomplement*) function on the contrast-enhanced image to convert our targets of interest to intensity valleys. We discriminate all the intensity valleys under a certain threshold with the (*imextendedmin*) function. The outcome of this function is a binary image. Where the location is more important than the region size of the image. To confine the selected valleys extracted by the function (*imextendedmin*) we utilized another function called (*imimposemin*) changing the valley`s pixel value to "0". However, all the discrete regions contain the minimum values will be detected by the "watershed transform".

Finally, the reflectance spectra of the pixels made out of thermal ablated tissue surface were isolated and used to figure a typical reflectance extend to delineate the thermal levels in the investigated liver sample. The delineation contours were finally displayed on the complemented enhanced image in red and blue for ablation and thermally affected areas, respectively.

3 Results

Regarding the system interconnections protocol and process, beginning from hyperspectral image scanning for the investigated liver sample and image enhancement to measure the (R_d) of the various regions of the investigated sample, we could differentiate between these regions regarding the wavelength variations. each pixel in the investigated liver tissue has a relative reflectance for the wavelength variations. The experimental setup was evaluated and verified with respect to the pathological report.

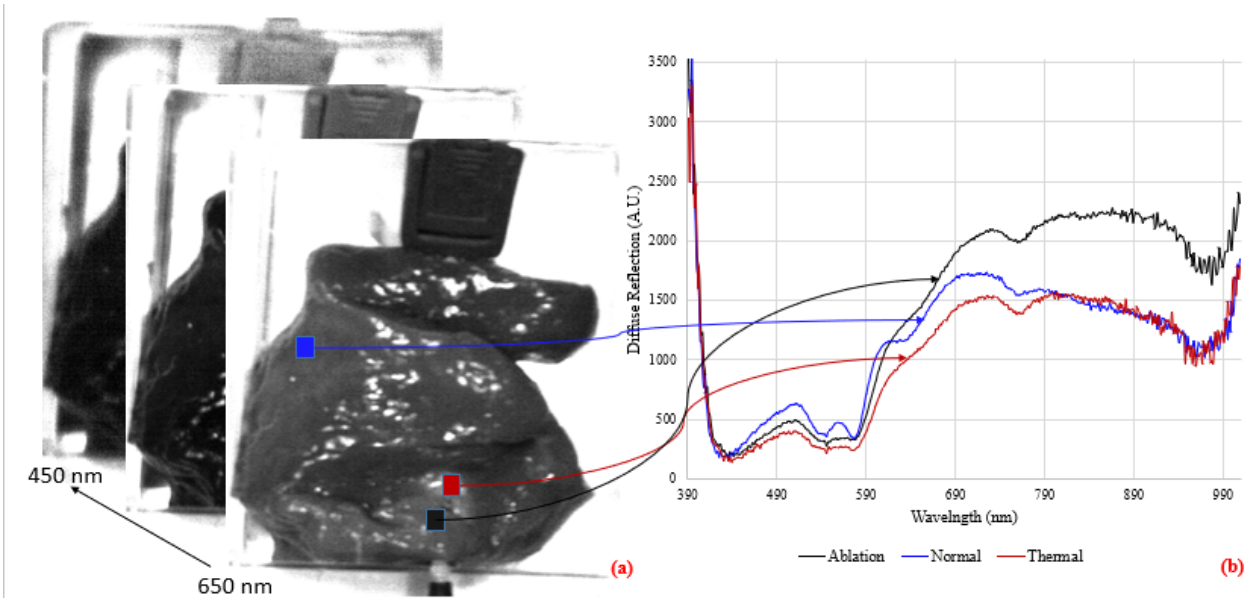


Fig. 4 (a) The scanned Hyperspectral (HS) image of the investigated Liver Tissue Sample#1 highlighting the measured diffuse reflection (R_d) regions over the spectral range (400~1000 nm); (b) the blue pixel demonstrate the (R_d) of the normal tissue not affected with the thermal region where it's presented in the graph by the blue solid line; the red pixel representing the thermal regions and plotted in the graph with the red solid line, additionally the black pixel represent the ablated region with a black solid line in the graph.

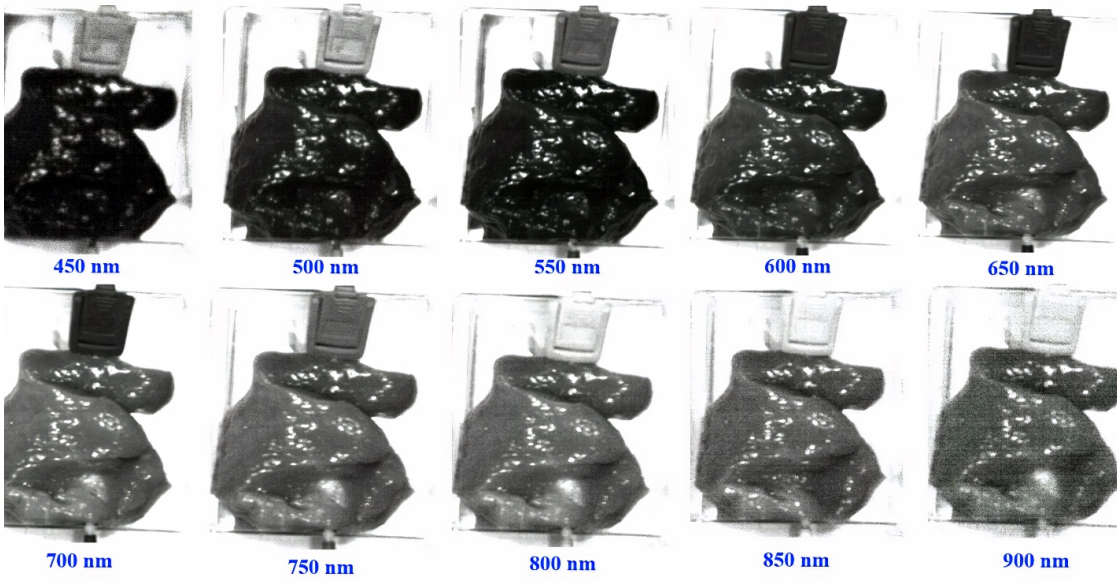


Fig. 5 The scanned HS images of the investigated *ex vivo* liver Sample #1 after ablation from 450 nm till 900 nm with 50 nm resolution, where we could visually see the differentiation of the Ablation and thermal effect regions on the various HS images in the spectral range.

The reflectance spectrum signature of each pixel generated from the thermal and ablated regions of a liver tissue surface was separated and used to compute a normal reflectance range. The degree and level of thermal effect to the tissue could be highlighted according to the spectrum wavelength to distinguish the selective regions (ablated, thermal manipulated, and normal tissues). The spectral reflectance signatures were measured and evaluated from the mean of the three different regions on the investigated liver tissue sample, as illustrated in Fig. 4(a).

The deliberate optical spectrum of the investigated liver sample over the wavelength spectrum 400~1000 nm. The experiment was exploited utilizing *ex vivo* bovine liver tissue, where captured HSI is scanned and segmented, selecting specific regions to measure the optical properties of the ablation region and another region around it for measuring the thermal consequence to the normal tissue, as shown in the pixel identification in Fig. 4(a).

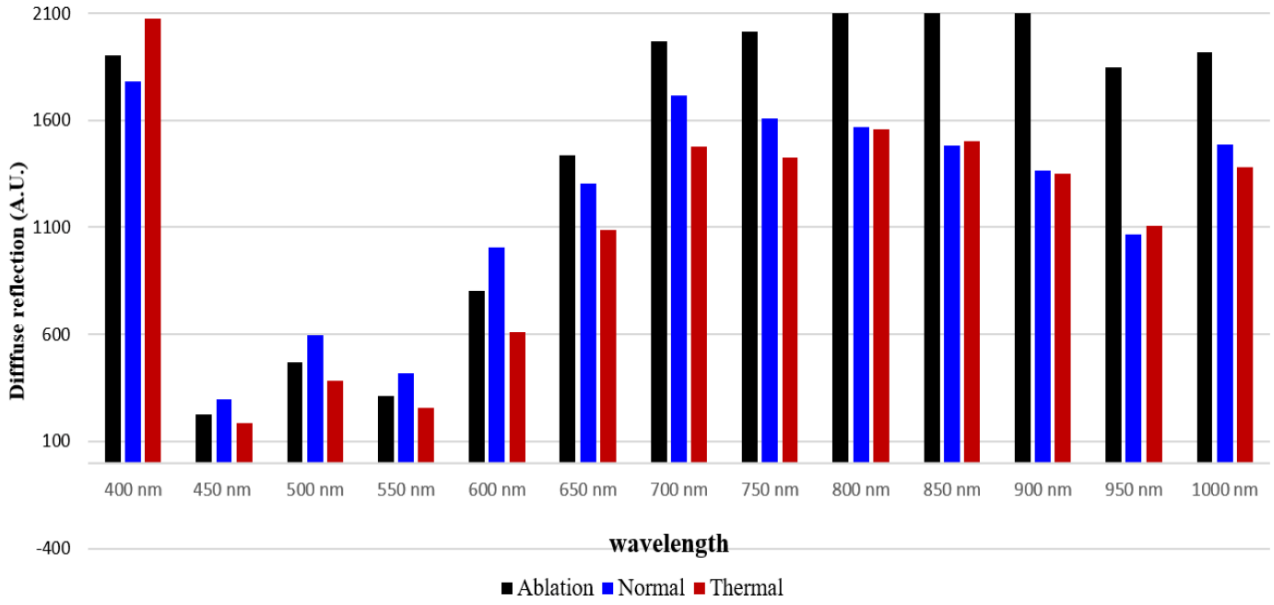


Fig. 6 The bar plot which highlighted the contrast between each region (normal, thermal, and ablated) districts in the investigated *ex vivo* Liver Sample #1.

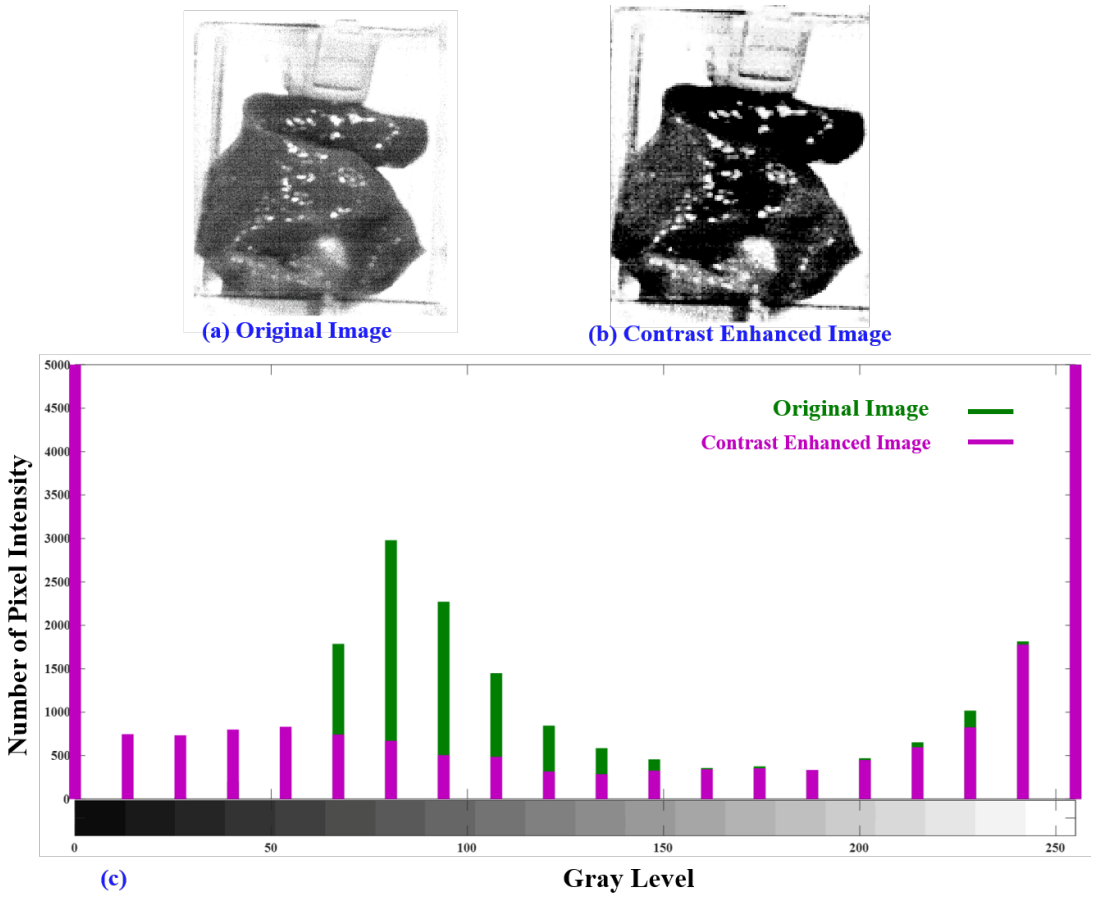


Fig. 7 (a) The original image at wavelength 900 nm of the investigated liver tissue Sample #1 before image contrast enhancement; (b) the enhanced image contrast utilizing the Top-hat and Bottom-hat transforms; (c) the histogram which reveals the contrast of the original image with the green bars and the enhanced image contrast with the purple bars.

The measured diffuse reflectance (R_d) of the selected regions (normal, thermal, and ablated) were plotted in the graph illustrating the distinction shift of the wavelength between the normal tissue and ablated signature, as demonstrated in Fig. 4(b). The blue pixel demonstrates the diffuse reflection (R_d) of the normal tissue which is

not affected with the thermal region where it is presented in the graph by the blue solid line; the red pixel representing the thermal regions and plotted in the graph with the red solid line, additionally the black pixel represent the ablated region with a black solid line in the graph.

To avoid the time-consuming of the 447 spectral images of the investigated sample, we select the Ten images of the investigated sample after ablation over the spectrum (400~1000 nm) with 50 nm resolution. We noticed visually that to differentiate between the normal and the thermal region was more identified in the spectrum (550~650 nm). However, to segregate between the normal and the ablated regions was highlighted in the wavelength (850~950 nm), as liver Sample #1 illustrated in Fig. 5, liver Sample #4 in Fig. A3, and liver Sample #5 in Fig. A4 at the Appendix.

The bar chart highlighted the contrast between the investigated *ex vivo* liver sample regions (normal, thermal, and ablated). The wavelength (600 nm) shows high contrast between the normal and the thermal regions. On the other hand, at wavelength (900 nm) represents high contrast between the normal and the ablated regions, although discriminate between the thermal and ablated regions, as more clarified in Fig. 6.

Selecting the optimum spectral image (900 nm) from the bar plot of Fig. 6, which could discriminate between (normal / ablated) regions, additionally between (thermal / ablated) regions to the original image utilized with the custom processing algorithm to increase the image contrast then image clustering.

To validate the increment of the image contrast we utilize the Histogram chart. The original image of the investigated liver tissue at spectral wavelenght (900 nm), is presented in Fig. 7(a) that is drawn in the histogram chart with green bars. Then, the enhanced image displayed in Fig. 7(b) was clearly highlighted the stretch of the histogram bars drawn in purple, as illustrated in Fig. 7(c). Furthermore, we apply the same procedure on the additional experimental investigation liver tissue samples, where Sample #4 and Sample #5 after ablation and slicing had been displayed in Fig. A5 and Fig. A6, respectively in the Appendix.

Fig. 8 represents the custom algorithm processing, where the selected optimum spectral image (900 nm) as the original image. Which could discriminate between (normal / ablated) and additionally between (thermal / ablated) regions, as displayed in Fig. 8(a). Increasing the image contrast utilizing the "Top-hat Transform" and "Bottom-hat Transform", as shown in Fig. 8(b) and Fig. 8(c), respectively. The image outcome in the Fig. 8(d) is the high contrast image. Next, this high contrast image with the "Watershed segmentation", as shown in Fig. 8(e) was used. Finally, there are the delineation of the ablation region in red contour and the thermally affected region in blue contour, as displayed in Fig. 8(f). Moreover, to validate the custom algorithm processing, we apply the same steps on the additional experimental investigation liver tissue samples, where Sample #4 and Sample #5 after ablation and slicing had been displayed in Fig. A7 and Fig. A8, respectively in the Appendix.

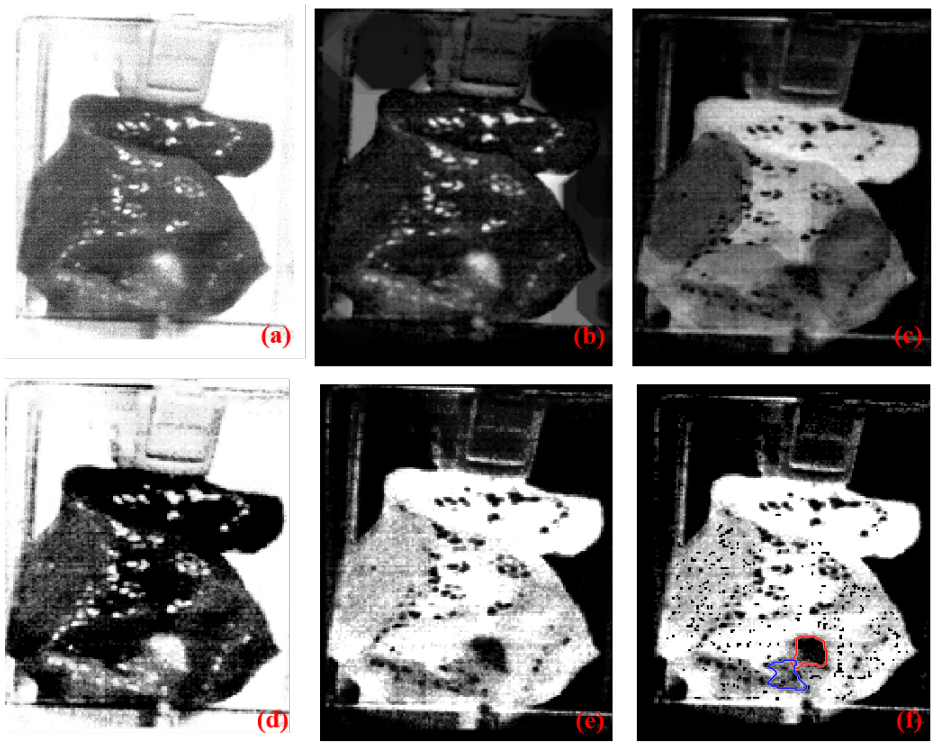


Fig. 8 The investigated liver tissue Sample #1; (a) the acquired hyperspectral image at 900 nm; (b) the image contrast enhancement after top-hat transforms; (c) the image contrast enhancement after bottom-hat transforms; (d) the enhanced contrast image; (e) the final complement enhancement image; (f) the delineation contour for the ablation and thermally affected region in red and blue, respectively.

4 Discussion

The non-invasive thermal ablation such as (RFA, MWA, and Laser Ablation) is the leading therapeutic equipment for un-resection liver tumors. The thermal observation with the well-chosen image-guided system is vital to achieving a fruitful removal of tumors with the least possible thermal damage of liver tissues [75–78].

The presented approach setup utilizing HS camera aims to measure the diffuse reflectance ($\hat{R}_d$) of the selected regions (normal, thermal, and ablated) for the investigated *ex vivo* liver Sample #1. The scanned HS image cube over the spectral range (400~1000 nm) shows a different spectral signature for each region, as displayed in Fig. 4.

To reduce the time of image processing for the investigated cube, we select from the 447 spectral channel, ten images in the wavelength range (450 ~ 900 nm) with 50 nm resolution. Although, from visual inspection, it was clear that the wavelength range (550 ~ 650 nm) was highly identifying between the normal and the thermal region. However, wavelength (850 ~ 950 nm) highlights more the contrast between the normal and ablated regions, as liver Sample #1 illustrated in Fig. 5, liver Sample #4 in Fig. A3, and liver Sample #5 in Fig. A4 at the Appendix.

Demonstrating these results by utilizing the histogram in the appearance of a bar graph to highlight the contrast between the investigated *ex vivo* liver sample regions (normal, thermal, and ablated). Wavelength (600 nm) represents a high contrast between the normal and the thermal regions. Contrariwise, at a wavelength (900 nm) represents high contrast between the normal and the ablated regions, as shown in Fig. 6.

Next, to verify the experimental results we exploited the statistical analysis of the measured diffuse reflectance ($\hat{R}_d$) for the investigated samples. Which, demonstrates a high sample variance ($\hat{S}_v$) between normal and thermal regions at a wavelength (600 nm). However, the wavelength (900 nm) shows a high variance between both the normal / ablated and ablated / thermal regions, as represented in Table 1.

Selecting the optimum spectral image (900 nm) which could discriminate between (normal / ablated) regions, additionally between (thermal / ablated) regions to the original image utilized with the custom processing algorithm to increase the image contrast then image clustering.

To verify the enhancement of the image contrast we utilize the histogram chart, as shown in Fig. 7. The original image of the investigated liver tissue at spectral image (900 nm), is presented in Fig. 7(a) that is was drawn in the histogram chart with green bars. The enhanced image displayed in Fig. 7(b) was clearly highlighted the stretch of the histogram bars drawn in purple, as illustrated in Fig. 7(c). Furthermore, for more validation to the algorithm steps, we apply the same procedure on the additional experimental investigation liver tissue samples, where Sample #4 and Sample #5 after ablation and slicing had been displayed in Fig. A5 and Fig. A6, respectively in the Appendix.

The optimum spectral image at (900 nm) was selected and processed by the custom algorithm, to discriminate mainly between (Normal / Ablated), then classify (Thermal / Ablated) regions. To enhance the image contrast, we exploited the "Top-hat Transform" and "Bottom-hat Transform", as shown in Fig. 8(b) and Fig. 8(c), respectively. The outcome improved image, as presented in Fig. 8(d) was processed utilizing the "Watershed segmentation", as shown in Fig. 8(e). Furthermore, the delineation of the ablation and thermally affected regions were displayed in Fig. 8(f) and identified with red and blue contours, respectively. Finally, for more validation to the algorithm process, we repeat the experimental investigation on additional liver samples, as shown in Fig. A7 and Fig. A8 in the Appendix, for sample #4 and sample #5, respectively.

5 Conclusion

In brief, the represented approach reveals the hyperspectral camera capabilities to provide precise information for surgeons by early delineation to the detected thermal effects to avoid overheating ablation. This overheating may lead to cell necrosis due to the inaccuracy of the exploratory modality used, or the lack of experience. Hyperspectral imaging is a prevailing tool in perception the thermal ablation with the least time, however, it cost too much in regards to the commercial CCD camera and it can't work progressively as the spectral cube consumes more time for image analysis over the 447 frames and image processing. To reduce the time expenses for HSI data processing we were able to identify a spectral band, centered at 600 nm, to discriminate between the normal and the thermally ablated regions Moreover, at the spectral band centered at 900 nm a high contrast was achieved between the normal and the ablated regions. Therefore, it would be possible in the future work to provide direct feedback on the resection edges to the specialist during surgery. Along these lines, the subsequent stage is to approve the procedure as an edge evaluation method during liver tumor surgery.

Disclosures

The authors declare and state that the work was affirmed by the Ethics Committee of Ain Shams university – Faculty of Medicine, Cairo, Egypt. We confirm that this work is original and has not been published elsewhere nor is it currently under consideration for publication elsewhere. The authors declare and state that they have all the research data and all the materials are available. The authors declare and state that they have no competing interests. The authors declare that there are no funders neither no one had any role in the design of the study; in the collection, analyses, or interpretation of data; in the writing of the manuscript, or in the decision

to publish the results. The authors declare and stated that they have not Acknowledgements.

References

1. S. Morini, G. Carpino, S. Carotti, and E. Gaudio, "Anatomy and Embryology of the Liver," Chapter in Liver Diseases, F. Radu-Ionita, N. T. Pyrsopoulos, M. Jinga, I. C. Tintoiu, Z. Sun, and E. Bontas (Eds.), Springer International Publishing, Cham, 3–16 (2020).
2. M. W. Robinson, C. Harmon, and C. O. Farrelly, "Liver immunology and its role in in fl ammation and homeostasis," Cellular & Molecular Immunology 13, 267–276 (2016).
3. C. Review, "Global, Regional, and National Cancer Incidence, Mortality, Years of Life Lost, Years Lived With Disability, and Disability- Adjusted Life-years for 32 Cancer Groups, 1990 to 2015 A Systematic Analysis for the Global Burden of Disease Study," JAMA Oncology 3(4), 524–548 (2017).
4. J. Ferlay, H. R. Shin, F. Bray, D. Forman, C. Mathers, and D. M. Parkin, "Estimates of worldwide burden of cancer in 2008: GLOBOCAN 2008," International Journal of Cancer 127(12), 2893–2917 (2010).
5. Y. F. Liaw, "Antiviral therapy of chronic hepatitis B: Opportunities and challenges in Asia," Journal of Hepatology 51(2), 403–410 (2009).
6. P. Ferenci, M. Fried, D. Labrecque, J. Bruix, M. Sherman, M. Omata, J. Heathcote, T. Piratsivuth, M. Kew, J. A. Otegbayo, S. S. Zheng, S. Sarin, S. S. Hamid, S. B. Modawi, W. Fleig, S. Fedail, A. Thomson, A. Khan, P. Malfertheiner, G. Lau, F. J. Carillo, J. Krabshuis, and A. Le Mair, "Hepatocellular carcinoma (HCC): A global perspective," Journal of Clinical Gastroenterology 44(4) 239–245 (2010).
7. S. Abd-Elsalam, N. Elwan, H. Soliman, D. Ziada, W. Elkhalawany, M. Salama, N. Hawash, M. Arafa, R. Badawi, and W. M. Shehata, "Epidemiology of liver cancer in Nile delta over a decade: A single-center study," South Asian Journal of Cancer 7(1), 24 (2018).
8. T. Hennedige, S. K. Venkatesh, "Imaging of hepatocellular carcinoma: diagnosis, staging and treatment monitoring," Cancer Imaging 12(3), 530 (2012).
9. T. Longerich, K. Breuhahn, and P. Schirmacher, "Molecular pathology of liver tumors," in Molecular Surgical Pathology, L. Cheng, J. Eble (Eds), Springer, New York, NY, 43–63 (2013). ISBN: 978-1-4614-4899-0.
10. J. Ferlay, I. Soerjomataram, R. Dikshit, S. Eser, C. Mathers, M. Rebelo, D.M. Parkin, D. Forman, and F. Bray, "Cancer incidence and mortality worldwide: sources, methods and major patterns in GLOBOCAN 2012," International Journal of Cancer 136(5), E359–E386 (2015).
11. W. M. Rashed, M. A. M. Kandeil, M. O. Mahmoud, and S. Ezzat, "Hepatocellular Carcinoma (HCC) in Egypt: A comprehensive overview," Journal of the Egyptian National Cancer Institute 32(1), 1–11 (2020).
12. M. J. Englesbe, S. P. Patel, K. He, R. J. Lynch, D. E. Schaubel, C. Harbaugh, S. A. Holcombe, S. C. Wang, D. L. Segev, and C. J. Sonnenday, "Sarcopenia and mortality after liver transplantation," Journal of the American College of Surgeons 211(2), 271–278 (2010).
13. H. Liao, "Integrated diagnostic and therapeutic techniques: Toward an intelligent medical system," Computerized Medical Imaging and Graphics:The Official Journal of the Computerized Medical Imaging Society 38(5), 421 (2014).
14. N. Sanai, M.-Y. Polley, M. W. McDermott, A. T. Parsa, and M. S. Berger, "An extent of resection threshold for newly diagnosed glioblastomas," Journal of Neurosurgery 115, 3–8 (2011).
15. B. K. P. Goh, J.-Y. Teo, C.-Y. Chan, S.-Y. Lee, P.-C. Cheow, P. K. H. Chow, L. L. P. J. Ooi, and A. Y. F. Chung, "Evolution of laparoscopic liver resection at Singapore General Hospital: a nine-year experience of 195 consecutive resections," Singapore Medical Journal 58(12), 708 (2017).
16. A. Forner, M. Gilabert, J. Bruix, and J. L. Raoul, "Treatment of intermediate-stage hepatocellular carcinoma," Nature Reviews Clinical Oncology 11, 525–535 (2014).
17. E. Tanis, J. W. Spliethoff, D. J. Evers, and G. C. Langhout, "Real-time in vivo assessment of radiofrequency ablation of human colorectal liver metastases using diffuse reflectance spectroscopy," European Journal of Surgical Oncology 42(2), 251–259 (2020).
18. T. Livraghi, H. Mäkisalo, and P. Line, "Treatment options in hepatocellular carcinoma today," Scandinavian Journal of Surgery 100(1), 22–29 (2011).
19. S. G. Nour, "MRI-Guided Laser Ablation of Liver Tumors," in Primary and Metastatic Liver Tumors, K. Cardona, S. Maithel (Eds), Springer, Cham, 323–332 (2018).
20. G. Giuseppe, D. Costanzo, C. Hospital, and M. Guarracino, Image-guided Laser Ablation, Springer, Cham (2020). ISBN: 978-3-030-21747-1.
21. C. L. Brace, Microwave tissue ablation: Biophysics, technology, and applications, Critical Reviews in Biomedical Engineering 38(1), 65–78 (2010).
22. B. Imene, B. Farid, and B. Khaoula, "CT-guided microwave liver tumors ablation and automatic adjustment of frequency," Averroes European Medical Journal 2(1), (2018).

23. J. Macdonell, N. Patel, S. Rubino, G. Ghoshal, G. Fischer, E.C. Burdette, R. Hwang, and J. G. Pilitsis, "Magnetic resonance–guided interstitial high-intensity focused ultrasound for brain tumor ablation," 44(2), 1–6 (2018).
24. H. Zhi-Yu, L. Ping, Y. Xiao-Ling, C. Zhi-Gang, L. Fang-Yi, and Y. Jie, "A clinical study of thermal monitoring techniques of ultrasound-guided microwave ablation for hepatocellular carcinoma in high-risk locations," Scientific Reports 7, 41246 (2017).
25. H. Takahashi, M. Akyuz, E. Aksoy, K. Karabulut, and Eren Berber, "Local recurrence after laparoscopic radiofrequency ablation of malignant liver tumors : Results of a contemporary series," Journal of Surgical Oncology 115(7), 830–834 (2017).
26. T. R. Fosnight, F. M. Hooi, R. D. Keil, A. P. Ross, S. Subramanian, T. G. Akinyi, J. K. Killin, P. G. Barthe, S. M. Rudich, S. A. Ahmad, M. B. Rao, and T. G. Mast, "Echo decorrelation imaging of rabbit liver and VX2 tumor during in vivo ultrasound ablation," Ultrasound in Medicine & Biology 43(1), 176–186 (2017).
27. T. J. Vogl, A. Dommermuth, B. Heinle, N.-E. A. Nour-Eldin, T. Lehnert, K. Eichler, S. Zangos, W. O. Bechstein, and N. N. N. Naguib, "Colorectal Cancer Liver Metastases: Long-Term Survival and Progression-Free Survival After Thermal Ablation Using Magnetic Resonance–Guided Laser-Induced Interstitial Thermotherapy in 594 Patients Analysis of Prognostic Factors," Investigative Radiology 49(1), 48–56 (2014).
28. J. Paul, T. J. Vogl, and A. Chacko, "Dual energy computed tomography thermometry during hepatic microwave ablation in an ex-vivo porcine model," Physica Medica 31(7), 683–691 (2015).
29. M. De Landro, J. Ianniello, M. Yon, A. Wolf, B. Quesson, E. Schena, and P. Saccomandi, "Fiber bragg grating sensors for performance evaluation of fast magnetic resonance thermometry on synthetic phantom," Sensors 20(22), 1–17 (2020).
30. L. Feng, S. Zhu, F. Liu, Y. He, Y. Bao, and C. Zhang, "Hyperspectral imaging for seed quality and safety inspection: A review," Plant Methods 15, 91 (2019).
31. P. Martín-Mateos, F. U. Khan, and O. E. Bonilla-Manrique, "Direct hyperspectral dual-comb imaging," Optica 7(3), 199–202 (2020).
32. R. Abdlaty, Q. Fang, "Acousto-optic tunable filter-based hyperspectral imaging system characterization," SPIE Proceeding 10870, 108700Y (2019).
33. M. A. Calin, A. C. Calin, and D. N. Nicolae, "Application of airborne and spaceborne hyperspectral imaging techniques for atmospheric research: past, present, and future," Applied Spectroscopy Reviews 56(4), 1–35 (2020).
34. G. Polder, A. Gowen, The hype in spectral imaging, Journal of Spectral Imaging 9, (2020).
35. D. Inamdar, M. Kalacska, G. Leblanc, and J. P. Arroyo-Mora, "Characterizing and mitigating sensor generated spatial correlations in airborne hyperspectral imaging data," Remote Sensing 12(4), 641 (2020).
36. X. Jin, H. Memon, W. Tian, Q. Yin, X. Zhan, and C. Zhu, "Spectral characterization and discrimination of synthetic fibers with near-infrared hyperspectral imaging system," Applied Optics 56(12), 3570–3576 (2017).
37. E. Bonah, X. Huang, J. H. Aheto, and R. Osae, "Application of hyperspectral imaging as a nondestructive technique for foodborne pathogen detection and characterization," Foodborne Pathogens and Disease 16(10), 712–722 (2019).
38. M. L. Pieper, D. Manolakis, E. Truslow, T. W. Cooley, M. Brueggeman, J. Jacobson, and A. Weisner, "Performance limitations of temperature–emissivity separation techniques in long-wave infrared hyperspectral imaging applications," Optical Engineering 56(8), 81804 (2017).
39. J. Deal, S. Mayes, C. Browning, S. Hill, P. Rider, C. Boudreaux, T. C. Rich, and S. J. Leavesley, "Identifying molecular contributors to autofluorescence of neoplastic and normal colon sections using excitation-scanning hyperspectral imaging," Journal of Biomedical Optics 24(2), 021207 (2018).
40. M. De Landro, I.E. García-Molina, M. Barberio, E. Felli, V. Agnus, M. Pizzicannella, M. Diana, E. Zappa, and P. Saccomandi, "Hyperspectral Imagery for Assessing Laser-Induced Thermal State Change in Liver," Sensors 21(2), 643 (2021).
41. M. De Landro, M. Barberio, E. Felli, V. Agnus, M. Pizzicannella, M. DIana, and P. Saccomandi, "Hyperspectral imaging system for monitoring laser-induced thermal damage in gastric mucosa," In 2020 IEEE International Symposium on Medical Measurements and Applications (MeMeA), 1–6 (2020).
42. R. Abdlaty, J. Haywar, T. Farrell, and Q. Fang, "Skin Erythema and Pigmentation Optical Assessment Techniques," Photodiagnosis and Photodynamic Therapy 33, 102127 (2020).
43. M. H. Aref, I. H. Aboughaleb, and Y. H. El-Sharkawy, "Custom optical imaging system for ex-vivo breast cancer detection based on spectral signature," Surgical Oncology 35, 547–555 (2020).
44. M. H. Aref, A. M. Youssef, I. H. Aboughaleb, and Y. H. El-sharkawy, "Characterization of Normal and Malignant Breast Tissues utilizing Hyperspectral Images and Associated Differential Spectrum Algorithm," Journal of Biomedical Photonics & Engineering 7(2), 020302 (2021).
45. I. H. Aboughaleb, M. H. Aref, and Y. H. El-Sharkawy, "Hyperspectral imaging for diagnosis and detection of ex-vivo breast cancer," Photodiagnosis and Photodynamic Therapy 31, 101922 (2020).
46. M. Aref, I. H. Aboughaleb, A.-B. Youssef, and Y. El-Sharkawy, "Novel Approach Exploiting the Hyperspectral Imaging System for Breast Cancer Therapy and Diagnosis," Archives of Breast Cancer 7(4), 189–201 (2020).

47. S. Ortega, M. Halicek, H. Fabelo, R. Camacho, M. d. l. L. Plaza, F. Godtliebsen, G. M. Callicó, and B. Fei, "Hyperspectral Imaging for the Detection of Glioblastoma Tumor Cells in H&E Slides Using Convolutional Neural Networks," Sensors 20, 1911 (2020).
48. H. Fabelo, S. Ortega, R. Lazcano, D. Madroñal, G. M. Callicó, E. Juárez, R. Salvador, D. Bulters, H. Bulstrode, A. Szolna, J. F. Piñeiro, C. Sosa, A. J. O'Shanahan, S. Bisshopp, M. Hernández, J. Morera, D. Ravi, B. R. Kiran, A. Vega, A. Báez-Quevedo, G.-Z. Yang, B. Stanciulescu, and R. Sarmiento, "An Intraoperative Visualization System Using Hyperspectral Imaging to Aid in Brain," Sensors 18(2), 430 (2018).
49. M. H. Fouad Aref, A. A. R. Sharawi, and Y. H. El-Sharkawy, "Delineation of the Arm Blood Vessels Utilizing Hyperspectral Imaging to Assist with Phlebotomy for Exploiting the Cutaneous Tissue Oxygen Concentration," Photodiagnosis and Photodynamic Therapy 33, 102190 (2021).
50. P.-C. Chen, W.-C. Lin, "Spectral-profile-based algorithm for hemoglobin oxygen saturation determination from diffuse reflectance spectra," Biomedical Optics Express 2(5), 1082–1096 (2011).
51. M. W. Wukitsch, "Pulse oximetry: Historical review and Ohmeda functional analysis," International Journal of Clinical Monitoring and Computing 4, 161–166 (1987).
52. V. Tuchin, "Tissue Optics and Photonics: Light-Tissue Interaction II," Journal of Biomedical Photonics & Engineering 2(3), 030201 (2016).
53. V. V Tuchin, "Tissue Optics and Photonics: Biological Tissue Structures," Journal of Biomedical Photonics & Engineering 1(1), 3–21 (2015).
54. M. H. Aref, "Biomedical Research and Clinical Reviews," Biomedical Research and Clinical Reviews 1, 1–13 (2020).
55. M. H. Aref, I. H. Aboughaleb, and Y. H. El-sharkawy, "Photodiagnosis and Photodynamic Therapy Tissue characterization utilizing hyperspectral imaging for liver thermal ablation," Photodiagnosis and Photodynamic Therapy 31, 101899 (2020).
56. M. H. Aref, I. H. Aboughaleb, A.-B. M. Youssef, and Y. H. El-Sharkawy, "Hyperspectral image-based analysis of thermal damage for ex-vivo bovine liver utilizing radiofrequency ablation," Surgical Oncology 38, 101564 (2021).
57. A. Robles-Kelly, C. P. Huynh (Eds.), Imaging Spectroscopy for Scene Analysis, Springer, London (2013). ISBN: 978-1-4471-4652-0.
58. J. M. Bioucas-Dias, A. Plaza, G. Camps-Valls, P. Scheunders, N. Nasrabadi, and J. Chanussot, "Hyperspectral remote sensing data analysis and future challenges," IEEE Geoscience and remote sensing magazine 1(2), 6–36 (2013).
59. T. Adão, J. Hruška, L. Pádua, J. Bessa, E. Peres, R. Morais, and J. J. Sousa, "Hyperspectral imaging: A review on UAV-based sensors, data processing and applications for agriculture and forestry," Remote Sensing 9(11), 1110 (2017).
60. S. S. M. Noor, K. Michael, S. Marshall, and J. Ren, "Hyperspectral image enhancement and mixture deep-learning classification of corneal epithelium injuries," Sensors 17(11), 2644 (2017).
61. N. Dhanachandra, K. Manglem, and Y. J. Chanu, "Image Segmentation Using K-means Clustering Algorithm and Subtractive Clustering Algorithm," Procedia Computer Science 54, 764–771 (2015).
62. A. Janßen, P. Wan, "k-means clustering of extremes," Electronic Journal of Statistics 14(1), 1211–1233 (2020)
63. A. Badawi, M. Bilal, "High-level synthesis of online k-means clustering hardware for a real-time image processing pipeline," Journal of Imaging 5(3), 38 (2019).
64. A. Gulhane, P. L. Paikrao, and D. S. Chaudhari, "A Review of Image Data Clustering Techniques," International Journal of Soft Computing and Engineering 2(1), 212-215 (2019).
65. M. A. Hamdi, "Modified Algorithm marker-controlled watershed transform for Image segmentation Based on Curvelet Threshold," Canadian Journal on Image Processing and Computer Vision 2(8), 88–91 (2008).
66. S. Derivaux, G. Forestier, C. Wemmert, and S. Lefèvre, "Supervised image segmentation using watershed transform, fuzzy classification and evolutionary computation," Pattern Recognition Letters 31(15), 2364–2374 (2010).
67. Y. Zhao, J. Liu, H. Li, and G. Li, "Improved Watershed Algorithm for Dowels Image Segmentation," In 2008 7th World Congress on Intelligent Control and Automation, 7644–7648 (2008).
68. X. Fengying, J. Zhiguo, and Z. Fugen, "Immune cell image segmentation based on mathematical morphology," Journal of Image and Graphics 7(11), 1119–1122 (2002).
69. H. P. Ng, S. H. Ong, K. W. C. Foong, P. S. Goh, and W. L. Nowinski, "Medical Image Segmentation Using K-Means Clustering and Improved Watershed Algorithm," 2006 IEEE Southwest Symposium on Image Analysis and Interpretation, 61–65 (2006).
70. S. Liu, L. Zeng, B. Liu, and Y. Fang, "Separating Algorithm for Overlapping Granule Images," Computer Engineering 28(2), 198–199 (2002).
71. X. Yang, S. Zhan, D. Xie, H. Zhao, and T. Kurihara, "Hierarchical prostate MRI segmentation via level set clustering with shape prior," Neurocomputing 257, 154–163 (2017).
72. J. C. Dunn, "A fuzzy relative of the ISODATA process and its use in detecting compact well-separated clusters," Journal of Cybernetics 3(3), 32–57 (1973).
73. C. Kalyani, K. Ramudu, and G. R. Reddy, "A review on optimized k-means and FCM clustering techniques for biomedical image segmentation using level set formulation," Biomedical Research 29(20), 3660–3668 (2018).

74. V. Kumar, P. Gupta, "Importance of Statistical Measures in Digital Image Processing," International Journal of Emerging Technology and Advanced Engineering 2(8), 56–62 (2012).
75. H. Wu, L. R. Wilkins, N. P. Ziats, J. R. Haaga, and A. A. Exner, "Real-time monitoring of radiofrequency ablation and postablation assessment: Accuracy of contrast-enhanced US in experimental Rat liver model," Radiology 270(1), 107–116 (2014).
76. P. Wiggermann, K. Brünn, J. Rennert, M. Loss, H. Wobser, A. G. Schreyer, C. Stroszczynski, and E. M. Jung, "Monitoring during hepatic radiofrequency ablation (RFA): Comparison of real-time ultrasound elastography (RTE) and contrast-enhanced ultrasound (CEUS): First clinical results of 25 patients," Ultraschall in der Medizin-European Journal of Ultrasound 34(06), 590–594 (2013).
77. Y. Z. Zhang, T. Xu, H. Y. Gong, C. Y. Li, X. H. Ye, H. J. Lin, M. P. Shen, Y. Duan, T. Yang, and X. H. Wu, "Application of high-resolution ultrasound, real-time elastography, and contrast-enhanced ultrasound in differentiating solid thyroid nodules," Medicine 95(45), e5329 (2016).
78. S. Swierczynski, F. Primavesi, E. Klieser, T. Kiesslich, T. Jäger, R. Illig, D. Neureiter, D. Ofner, and S. Stättner, "382. Thermographic monitoring of radiofrequency and microwave ablation in a perfused porcine liver model," European Journal of Surgical Oncology 40(11), S147 (2014).

 doi: 10.18287/JBPE21.07.020306A

Appendix: Optical Signature Analysis of Liver Ablation Stages Exploiting Spatio-Spectral Imaging

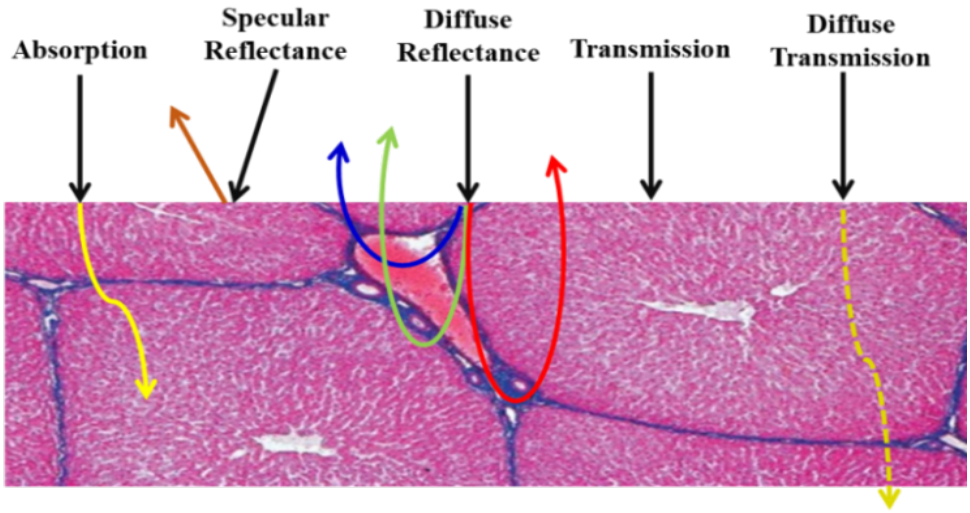


Fig. A1 Demonstration for the *ex vivo* Liver Tissue from a bovin for the optical properties (transmission, reflection, absorption, and scattering) over the various spectrum ranges.

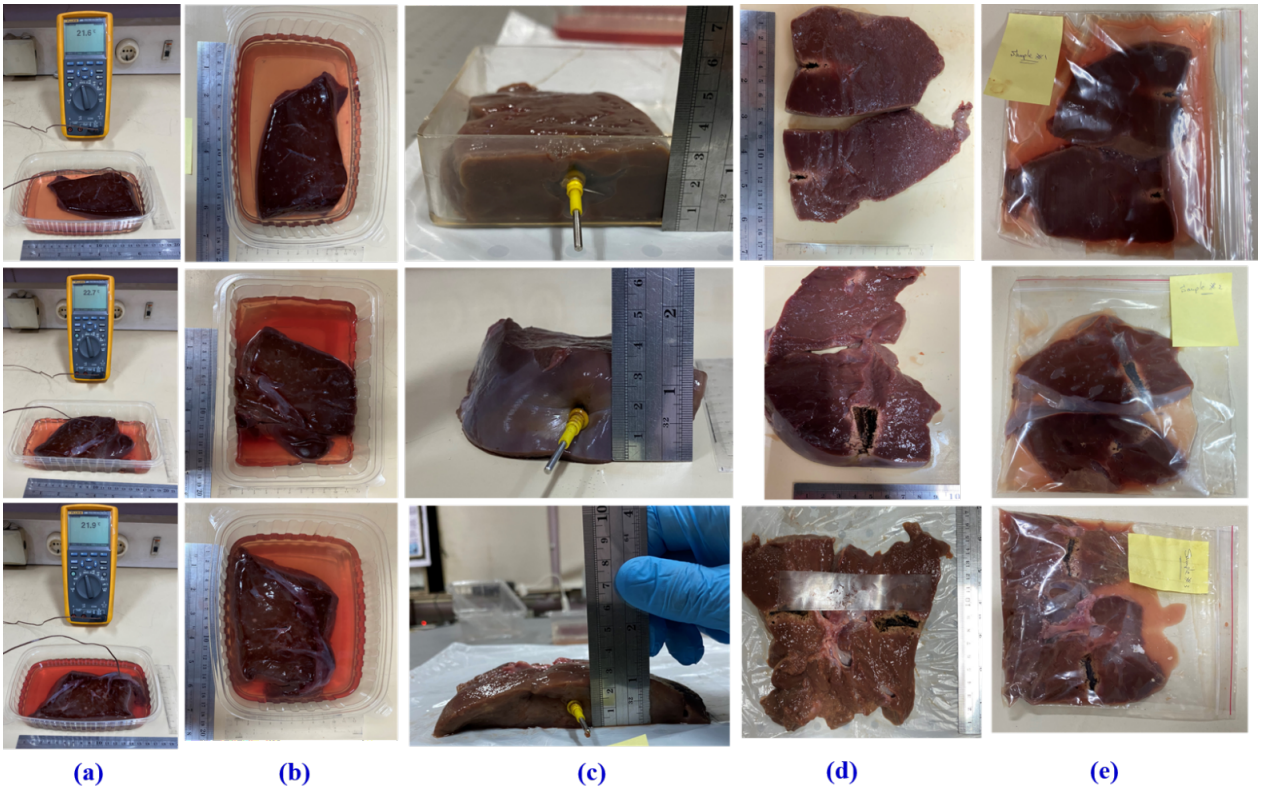


Fig. A2 (From Up to Down) The investigated liver Sample #5, liver Sample #6, and liver Sample #7; (a) the investigated liver sample before ablation inserted in neutral buffered saline and observed with a multimeter (Fluke, 289, USA), (b) the investigated liver sample inserted in the neutral buffered saline for tissue size recording, (c) the investigated liver sample after ablation in the experimental plastic tray with the active RF tip inserted in the sample, (d) the investigated liver sample after ablation and slicing to compare the actual ablated region and recording the size by scientific expert, (e) the sliced liver Sample #2 after ablation and wrapped in the vacuumed bags and tissue storage solution prepared to be sent to the pathological lap.

Table A1 The experimental data of the investigated liver tissue samples with the power protocol and duration for each experiment and the actual measured of the ablation region after sample slicing.

No.	Liver Sample Identification	Sample Size L×W, cm	Tissue Thickness h, cm	Position of RF Tip, cm	RF generator Power, W	Time of Ablation, min	Size of Ablation L×W, cm
1	Sample #1	10.1×9.5	2.8	1.5	35	2.5	1.9×0.7
2	Sample #2	9.1×10.5	2.3	1.5	35	4	2.1×0.8
3	Sample #3	11.1×10.2	2.7	1.5	30	5	3.1×1.3
4	Sample #4	15.1× 9.5	3.1	2	25	2	1.1×0.41
5	Sample #5	16×10.6	3.6	1.5	40	2.3	4×1.2
6	Sample #6	17×9	2.5	1.5	50	3.5	4.7×1.3
7	Sample #7	9.2×9.5	2.3	1.5	35	2	2.1×0.8

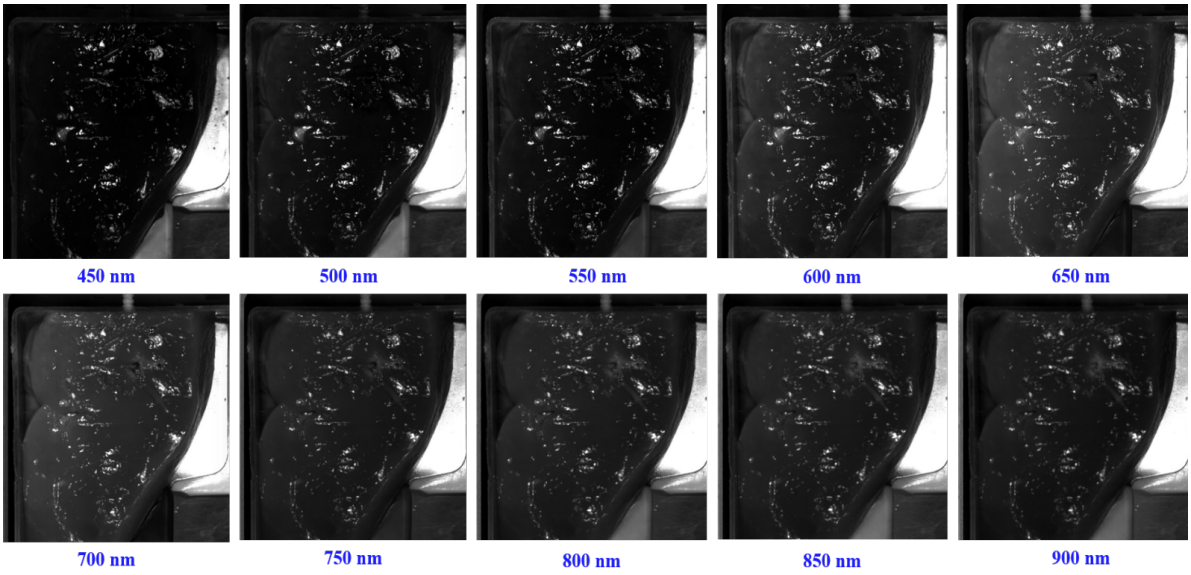


Fig. A3 The scanned HS images of the investigated *ex vivo* liver Sample #4 after ablation from 450 nm till 900 nm with 50 nm resolution, where we could visually see the differentiation of the ablation and thermal effect regions on the various HS images in the spectral range.

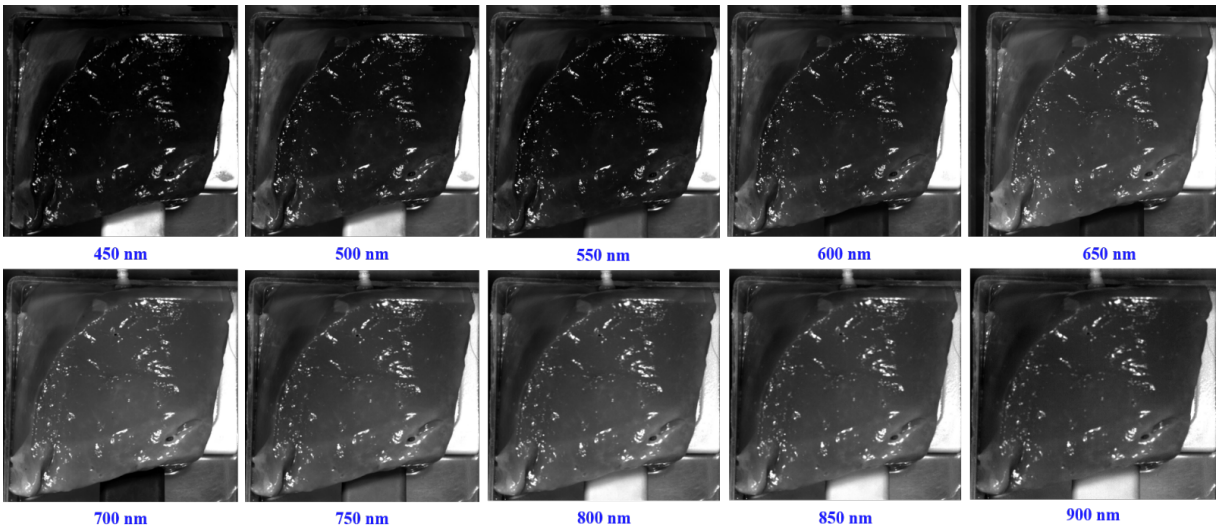


Fig. A4 The scanned HS images of the investigated *ex vivo* liver Sample #5 after ablation from 450 nm till 900 nm with 50 nm resolution, where we could visually see the differentiation of the ablation and thermal effect regions on the various HS images in the spectral range.

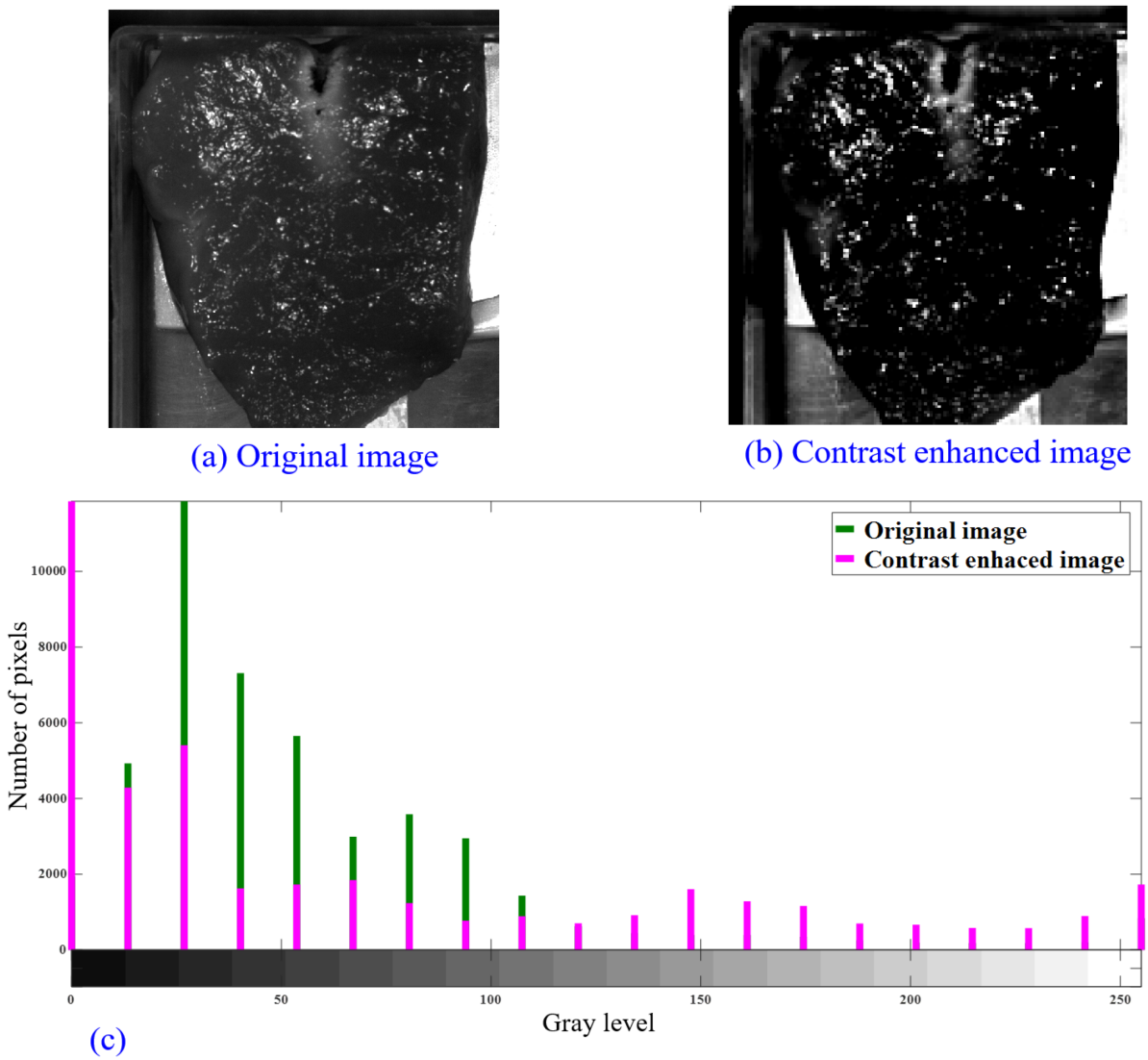


Fig. A5 The original image at wavelength 900 nm of the investigated Liver tissue Sample #4 after ablation and slicing but before image contrast enhancement; (b) the enhanced image contrast utilizing the "Top-hat and Bottom-hat transforms"; (c) the histogram which weveals the contrast of the original image with the green bars and the enhanced image contrast with the purple bars.

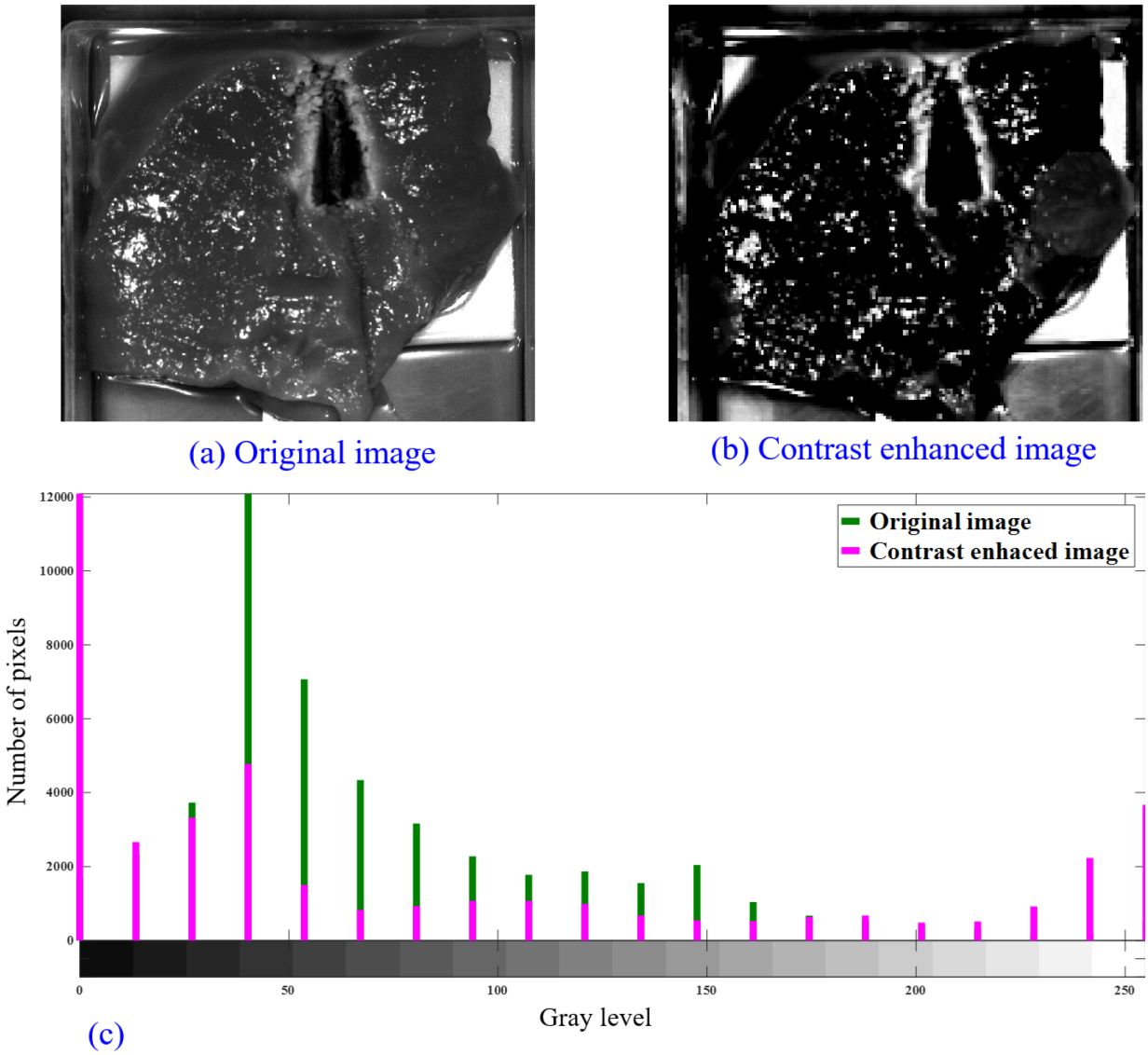


Fig. A6 The original image at wavelength 900 nm of the investigated liver tissue Sample#5 after ablation and slicing but before image contrast enhancement; (b) the enhanced image contrast utilizing the "Top-hat and Bottom-hat transforms"; (c) the histogram which reveals the contrast of the original image with the green bars and the enhanced image contrast with the purple bars.

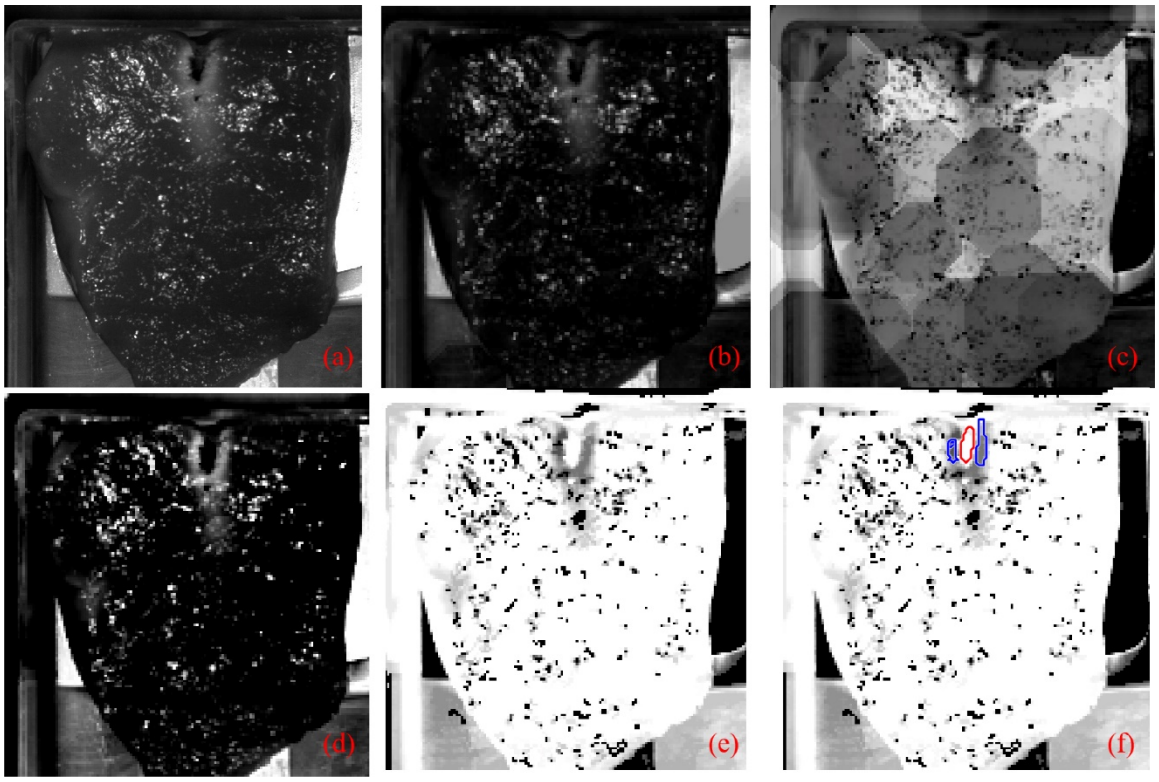


Fig. A7 The investigated liver tissue Sample #4 after thermal ablation and slicing; (a) the acquired hyperspectral image at 900 nm; (b) the image contrast enhancement after top-hat transforms; (c) the image contrast enhancement after bottom-hat transforms; (d) the enhanced contrast image; (e) the final complement enhancement image; (f) the delineation contour for the ablation and thermally affected region in red and blue, respectively.

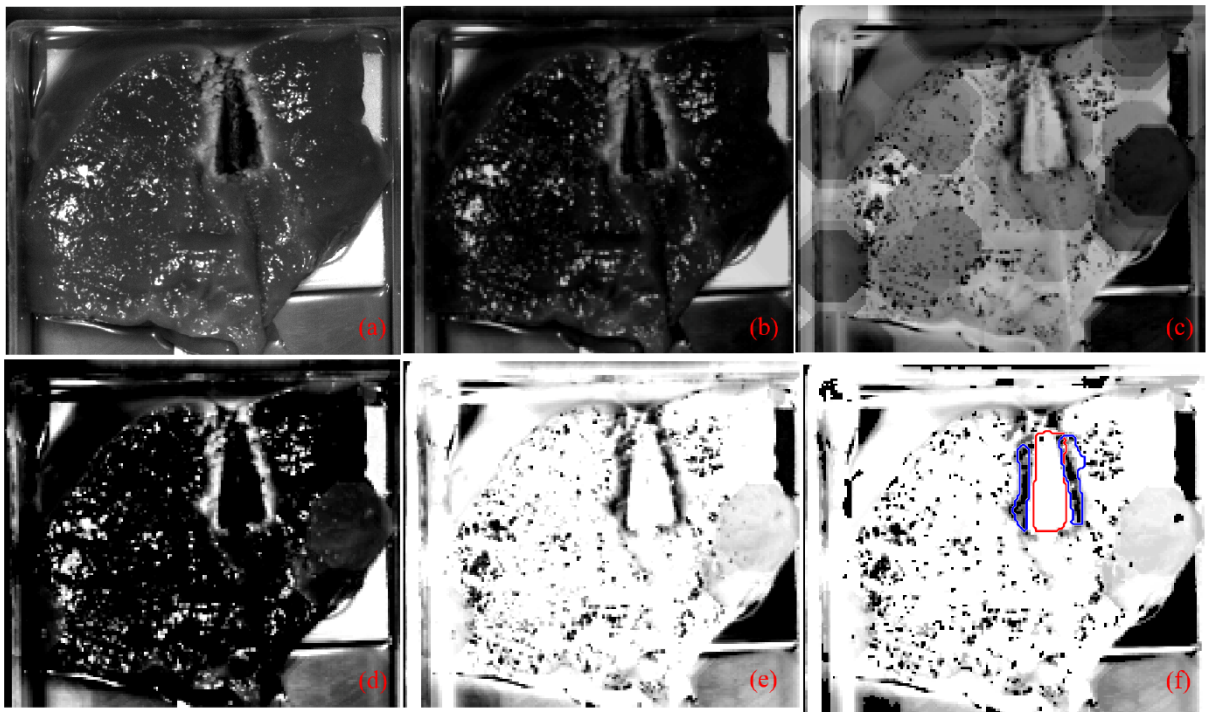


Fig. A8 The investigated liver tissue Sample#5 after thermal ablation and slicing; (a) the acquired hyperspectral image at 900 nm; (b) the image contrast enhancement after top-hat transforms; (c) the image contrast enhancement after bottom-hat transforms; (d) the enhanced contrast image; (e) the final complement enhancement image; (f) the delineation contour for the ablation and thermally affected region in red and blue, respectively.

A stable light source is very important to achieve usable measurement information, also to ensure measurement repeatability, and affecting the accuracy of the HS camera. We aimed to measure the light diffuse reflectance (R_d) for an *ex-vivo* liver tissue samples, by exploring the optical properties spectroscopy in the near-infrared and visible (NIR-VIS) spectrum. Where, the utilized light assembly for our hyperspectral imaging (HSI) system, a power supply controller for the source light (Mean Well, ENP360-12, Taiwan) with a polychromatic light source (4 × 35 W tungsten halogen lamps) at wavelength range (380~1050 nm), as shown in Figure A9.

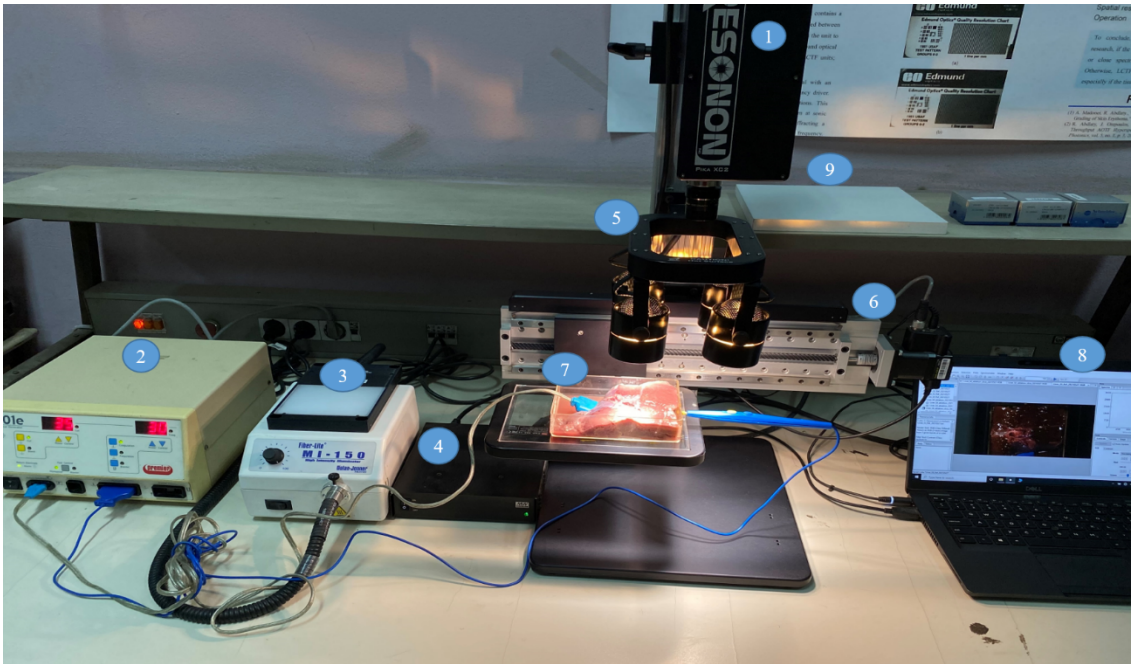


Fig. A9 Hyperspectral Optical Imaging system for measuring the light diffuse reflectance (R_d) of the investigated *ex-vivo* tissue samples; (1) Hyperspectral camera (Resonon, Pika XC2, USA); (2) Electrosurgical Generator (Premier; 2001e, France); (3) The Source light for the transmission measurement trials (Fiber-lite, MI-150, USA); (4) The power supply controller for the light source (Mean Well, ENP360-12, Taiwan) of diffuse reflection (R_d) measurement trails; (5) The 4-Halogen lamps (4 × 35 W halogen lamps) at wavelength range (380~1050 nm); (6) the linear translation stage; (7) The investigated *ex-vivo* liver sample; (8) The computer and Image Software Processing and Analysis, (9) white tile with high reflectance (Avian Technologies, FWT-99-300R058, UK).

The tungsten halogen incandescent lamps are thermal radiators. Where, light is generated by heating a solid body up to a high temperature, as temperature increase leading to more luminous light, and inversely for the wavelength (The melting point of tungsten (3383 °C) does not allow the peak to be shifted into the visible, about 20% of the total radiation is given off as “light”, about 0.3% in the UV region, and the remaining majority as heat) [1].

This type of lamps, generates a continuous distribution of light across the visible spectrum, although most of the energy emitted by these lamps is dissipated as heat in the infrared (IR) wavelengths. Due to their relatively weak emission in the ultraviolet portion of the spectrum, tungsten-halogen lamps are not as useful as arc lamps and lasers for examining specimens that must be illuminated with wavelengths below 400 nm [2], as illustrated in Figure A10.

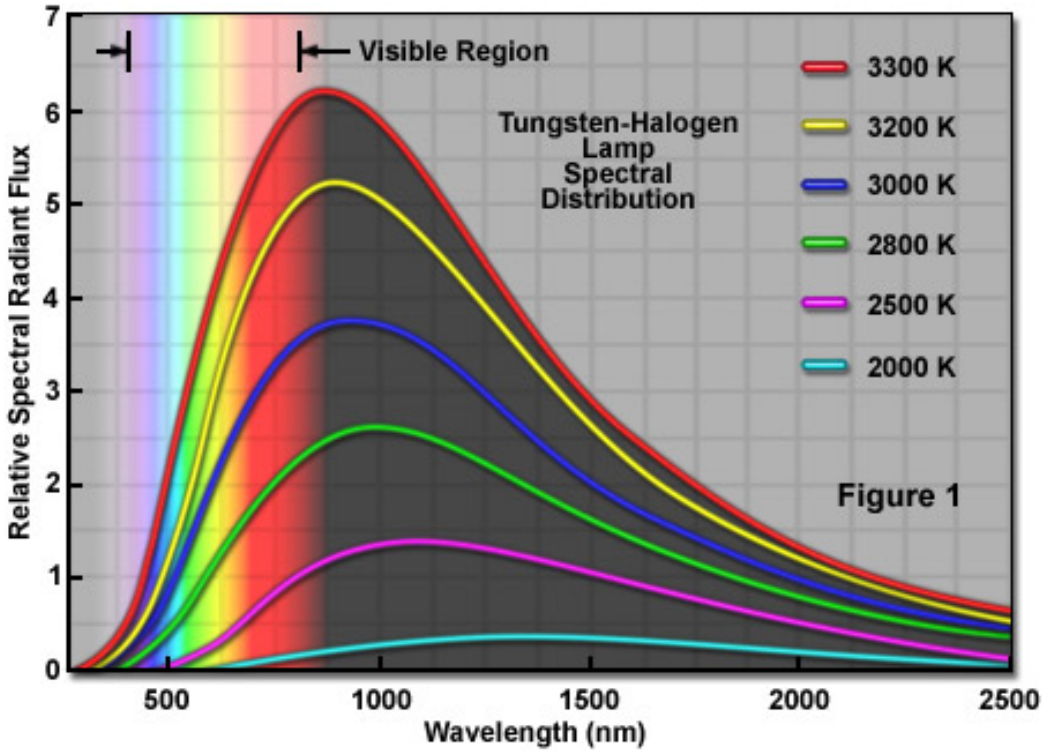


Fig. A10 The spectral distribution of the tungsten halogen incandescent lamps illustrates as temperature increase leading to more luminous light and shorter wavelength and the heat dissipation in the direction of the infrared (IR) wavelengths.

Furthermore, during the warm-up time, tungsten halogen light sources normally alter their spectral power distribution and release considerable amount of energy by way of heat, IR. Throughout this warm-up period, an increasing amount of IR promotes changes in the spectral power distribution and results may differ when measurements are taken during this time. Hence, it is recommended that the light source is allowed to stabilize for about 3-5 minutes [3]. In the presented study we maintain a considerable time about ~3 minutes (warming in advance of the investigation sample capturing), and not to exceed the reasonable warming time to avoid the heat effect on the investigated samples.

Additionally, in the NIR and VIS region, if the wavelength is longer, its signal/noise ratio would be relatively better for measurements. Such types of light sources are ideal for reflective and transmissive measurements in the VIS-NIR's longer wavelengths [2,3]. As in our investigation, we aim to measure the light (R_d), that's why we chose this specifically HS camera model (Resonon, Pika XC2, USA) with spectral range (400-1000 nm), as displayed in Figure A11.

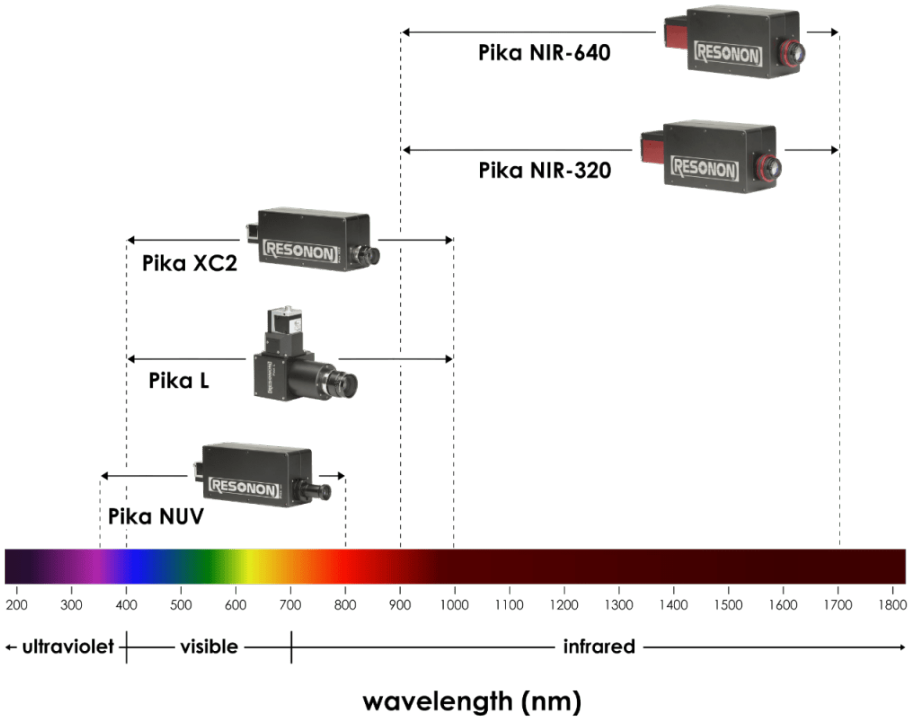


Fig. A11 The different models of the Resonon HS camera identifying the various spectrum wavelength.

Finally, at the startup of each investigation, and before capturing the investigated samples, we measure the light diffuse reflectance (Ṛd) of the highly reflectance white board (Avian Technologies, FWT-99-300R058, UK) to be our reference, as indicated with No# 1 in Figure A9.

References

[1] J.. Coaton, Halogen light sources Operating tungsten halogen lamps Halogen light sources Operating tungsten halogen lamps, 9(1) (1977) 25–30.
[2] A. Ożarowski, National High Magnetic Field Laboratory, Florida State University, 1800 E, Paul Dirac Drive, Tallahassee, Florida. 32310 (n.d.).
[3] A. V Arecchi, R.J. Koshel, T. Messadi, Field guide to illumination, in: SPIE, 2007.

Features of the Secondary Structure of BSA – Containing Protein Complexes, Isolated from Milk of High Temperature Processing

Ivan S. Shatalov[1*], Aleksandrina S. Shatalova[1], Lyudmila V. Plotnikova[2], and Aleksandr G. Shleikin[3]

[1] Faculty of Food Biotechnologies and Engineering, Saint Petersburg National Research University of Information Technologies, Mechanics and Optics, 49A Kronverksky Pr., Saint Petersburg 197101, Russia

[2] Department of Physics, Saint Petersburg State University, 13B Universitetskaya Emb., Saint Petersburg 199034, Russia

[3] Research and Educational Center of Chemical Engineering and Biotechnology, Saint Petersburg National Research University of Information Technologies, Mechanics and Optics, 49A Kronverksky Pr., Saint Petersburg 197101, Russia

*** e-mail:** shataloff.iv@gmail.com

Abstract. Present paper describes features of the component composition in the secondary structure of BSA–containing protein complexes isolated from ultra-pasteurized (UHT), sterilized (SHT) and powdered (DRY) milk. We have found β – sheets to present in all complexes investigated. However, the smallest number of such components have been revealed in samples derived from sterilized milk with less β – sheets in 1621–1626 cm^{-1} region. The composition study of the complexes originated from UHT milk has shown random coils to be the rarest in them. When considering the structure of the complexes isolated from powdered milk, the α – 3_{10} – helices were more characteristic for such samples, then the α – helix. Moreover, during spray–drying, the number of random structures increase with a simultaneous decrease in the number of β – sheets, whereas in UHT – and SHT – processing the number of random structures is inversely proportional to the number of α – helices. © 2021 Journal of Biomedical Photonics & Engineering.

Keywords: milk protein complexes; heat treatment; BSA; secondary structure.

Paper #3413 received 12 Apr 2021; accepted for publication 3 Jun 2021; published online 30 Jun 2021. doi: 10.18287/JBPE21.07.020307.

1 Introduction

Due to its high nutritive value, milk is a useful and popular food product worldwide. Therefore, the development of preservation methods along with the means to maximize its nutritional value is a trend in the food industry. Today, main technological approaches are based on high temperature treatment aimed at removing pathogenic microflora. Table 1 shows the main temperature diapasons of heat treatments, which are currently used for long–term milk preservation.

Milk proteins undergo certain changes of their conformation under technological conditions. However, the rate and nature of alterations vary drastically and depend not only on the chemical composition, but also on the structural organization of a protein globule.

Table 1 General Milk Processing Parameters.

Type of the Heat–Treatment	Heating Temperature, °C	Incubation time, sec
UHT	~135 –143	0.4–4 [1]
SHT	~115 – 120	900–1200 [1]
Spray drying	~150 – 200	Few sec. [1–3]

Milk proteins undergo certain changes of their conformation under technological conditions. However, the rate and nature of alterations vary drastically and depend not only on the chemical composition, but also on the structural organization of a protein globule.

Whey proteins are the most thermolabile. Because of the different component composition of the secondary structure, the presence of SS/SH – groups and bonds and the presence of metal ions, thermal stability decreases in the series α – actalbumin > β – lactoglobulin > BSA [4–6].

Among whey proteins BSA is one of the least thermally stable, denaturing irreversibly already at 57 – 59 ºC. However, the conformational changes occurring twice: at 57 ºC and 75 ºC [7]. In its native state this protein contain no β – sheets but mainly α – helices [8], It loses them together with β–turns at 57 °C, while at temperatures above 70 ºC irreversible intramolecular β – sheets are formed [7]. Since this protein contains free thiol group at Cys34, which is hidden inside the hydrophobic pocket in native globule, but exhibited at denaturation [6], SS/SH – exchange reactions are also an important factor in the formation of aggregates which includes this protein. On the other hand, BSA also forms protein complexes due to hydrophobic interactions with its surface. During the treatment with the temperatures higher than thermal denaturation, BSA is assumed to convert into a molten globule (MG), MG1. With further increase in temperature, MG1 slowly turns into MG2 – the structure with a more hydrophobic surface [9], which makes protein highly reactive [10]. Therefore, the aggregation of BSA proceeds mainly via two mechanisms: 1 – through the reactions of thiol–disulfide exchange, and 2 – hydrophobic interaction.

The more heat–resistant whey protein milk is β – lactoglobulin. Although aggregating is mostly the result of SS/SH–exchange reactions, this process is mediated by a change of the secondary structure. Each individual globule mainly consists of anti–parallel β – sheets formed by eight β – chains wrapped around the molecule and forming a hydrophobic pocket, flanked by an α – helix from its outer surface [11]. Separate β – chains are connected with two disulfide bridges: Cys66 – Cys160 and Cys106 – Cys119. Cys121 possessing free SH – group is hidden inside the hydrophobic pocket under the α – helix [12, 13]. Partially irreversible denaturation of this protein occurs at 58–60 ºC and mainly affects the α – helix. Irreversible denaturation occurs at 63 ºC and results in critical decrease in the β – sheets content, followed by the exposure of hidden SH– group and the initiation of SS/SH polymerization reactions of β – lactoglobulin [14, 15]. At this state β – lactoglobulin is highly reactive and aggregates with milk proteins including BSA both via SS/SH–exchange and hydrophobic interaction [16].

Possessing Ca^{2+} ion, α – lactalbumin reversibly denatures up to 95 ºC [17]. Native α – lactalbumin consists of two α – helical domains, including four α – helices and three α – 3_{10} – helices, as well as β – sheet areas that include antiparallel β – sheet and α – 3_{10} – helix. Although this protein does not contain free thiol groups, during heat-treatment it can form aggregates through thiol-disulfide exchange reactions with other milk proteins, possessing available free-SH – group (e.g denaturated BSA) [18]. These authors also reported the formation of hydrophobically stabilized aggregates of α – lactalbumin and BSA during heating.

BSA is also known to form protein complexes with caseins, mainly with κ – casein and to a lesser extent αS2 – casein, formed via SS/SH–reactions [19–21]. In αS2 – and κ – casein mainly random coil, unordered structures, β – sheets and β – turns exist, but very little or no α – helices. The formation of the latter structures is distorted due to the high content of non–polar amino acids (35–40%), mainly proline [22, 23]. All caseins are phosphorylated in a various degree. Possessing of hydrophobic and hydrophilic regions together with the flexible structure, caseins are also capable of creating non-covalent intermolecular interactions [24–26].

This paper discusses the conformational features of protein complexes formed during various technological treatments of milk. Since BSA is one of the most thermolabile and reactive milk protein, the protein complexes containing it are the objects for this study.

2 Materials and Methods

Commercially available samples of spray–dried (N = 9), UHT (N = 12) and SHT (N = 8) milk produced in Russia, Belarus and Finland were used for investigation. The fat content in samples was 25 ± 5 g/L.

2.1 Milk samples preparation before the analysis

Dry milk samples were reconstituted with distilled water (1 : 10), followed by the supp1ementation with 1 g/L preservative (5 – bromo – 5 nitro – 1.3 – dioxin, "Bronidox"). After that the samples were left for incubation overnight at +4 ºC for complete solubilization. The prepared samples were of 26 g/L in fat content.

The preservative was also added to all samples of SHT and UHT milk.

All samples were centrifuged at 23'500 g during 50 min to exclude the lipids and insoluble aggregates. After that the supernatants were filtered through the Whatman 4 filter. The filtered solutions were used for affinity chromatography purification.

2.2 Affinity chromatography

Milk samples were applied to monoclonal anti-BSA antibody (clone X69, XEMA) coupled to NH2 – Agarose through Diels-Alder cycloaddition using TCO-NHS and tet-NHS pre-activation of antibody and resin (Click Chemistry Tools). Unbound

matter was washed out with 0.1 mol/L Tris, pH 7.2. 0.4 mol/L $MgCl_2$ in 0.1 mol/L Tris, pH 7.2 was used to elute BSA complexes.

2.3 Sample preparation for electrophoretic analysis

For further electrophoretic study the eluates were intensively dialyzed in two steps. The first dialysis was performed against 0.1 mol/L Tris buffer pH 7.2 containing 5 mmol/L Na–EDTA using Vivaspin Turbo 4 50 MWCO at 1200 g for 20 min to reach the final sample: buffer ratio 1 : 1600. The samples then were dialyzed against 0.1 mol/L phosphate buffer, pH 7.2. All buffers contained 0.5 g/L NaN_3 as a preservative.

2.4 Determination of protein concentration

To obtain the samples of equal protein concentration we used the Pierce BCA kit (Thermo Scientific) with BSA as the standard.

2.5 Gel electrophoresis

SDS–PAGE in reducing (with 2ME) conditions was performed according to according to Laemmli method in a mini–chamber (BioRad). Briefly, the 120 g/L polyacrylamide gel was used. Buffer solution used for electrophoresis contained Tris–glycine, pH 8.3, containing 1 g/L sodium dodecyl sulfate (SDS). The 0.06 mol/L Tris–HCl buffer, containing 1 g/L SDS, glycerol and bromophenol blue, pH 6.8 was used as a sample buffer. Samples containing 1 mg/ml total protein were applied to the gel in a volume of 20 µl well. Electrophoresis was carried out for 2 h at a current of 30 mA. The starting voltage was 40 mV, which was increased to 150 mV after the sample entered the upper gel. After the front of the samples reached the middle of the gel the voltage was increased to 210 mV. After the run was complete, the gels were fixed in 500 ml/L ethanol for 30 min, after that they were washed three times with deionized water. The gel was stained with Coomassie brilliant blue G250. To decrease background the stained gels were washed with 100 g/L acetic acid overnight with constant agitation at 400 rpm.

2.6 MALDI-TOF

Protein bands were cut from the gel for MALDI-TOF analysis. The procedure was conducted at the Institute of Biomedical Chemistry, Moscow. All reagents were purchased at Sigma-Aldrich (Moscow, Russia).

The procedure was described previously [27]. Briefly, the gel cuts were washed twice with 50% acetonitrile solution in 0.1–M NH4HCO3 for 20 min at 37 °C followed by dehydration with acetonitrile for 5 min. The tryptic digestion was performed with 5 µL of enzyme in 0.1–M NH4HCO3 for 4 h at 37 °C with subsequent peptide extraction with 0.7% TFA. The extracts obtained were analyzed using MALDI-TOF mass spectrometry.

To obtain mass spectra of digests MALDI-TOF/TOF mass-spectrometer (Ultrafle II, Bruker Daltonics, Germany) equipped with an Nd : YAG laser in the reflector mode was used. The measurement of monoisotopic [MH+] ions was conducted in the 700 – 4500 m/z range with a tolerance of 70 ppm. The lift mode was used to obtain fragment ion spectra. The accuracy of fragment ion mass peak measurements was within 1 Da.

Spectral data analysis was performed via FlexAnalysis 3.3 software (Bruker Daltonics, Germany). To identify individual proteins MASCOT search software. Reliably identified proteins had the scores of > 82 ($p < 0.05$) with the use of "peptide fingerprint" option and > 55 ($p < 0.05$) with the use of "ion score" option. The search was conducted in National Center for Biotechnology Information (NCBI) databases or EST (expressed sequence tag) plant database or both.

2.7 FT–IR spectroscopy

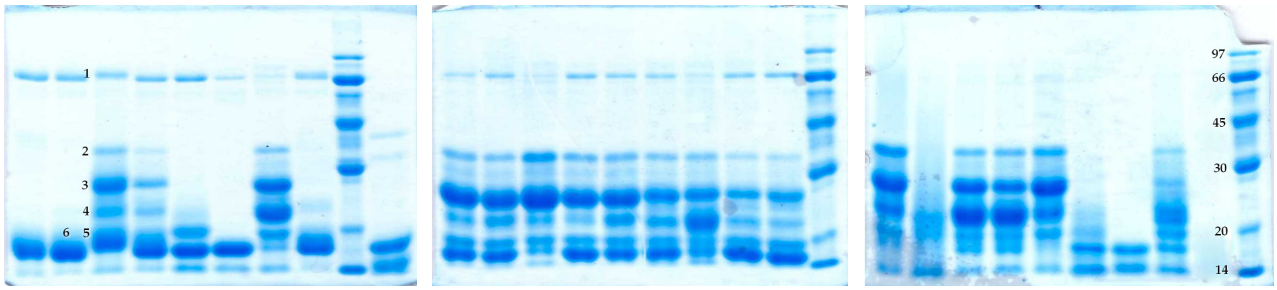
To record the absorption spectra in the mid–IR range, a Tensor 37 Fourier spectrometer (Bruker, Germany) was used in combination with an ATR–instrument based on a ZnSe crystal. The ATR spectra were corrected automatically using the software provided (Opus Software). The spectra of each sample were recorded with a resolution of 2 cm^{-1} and averaged over 256 accumulations. From the obtained absorption spectra, we subtracted the spectrum of the buffer solution (0.1 mol/L phosphate buffer, pH 7.2 + 0.5 g/L NaN_3), selecting the subtraction coefficient in such a way as to achieve a smooth baseline in the region of 2000–1800 cm^{-1} [28]. The protein concentration in the samples was at least 5 mg/ml.

The obtained spectrum at this site was smoothed by 15 points using the Savitzky–Golay algorithm. Second derivative allowing us to determine the hidden absorption peaks, we used it to transform the spectrum according to Gauss.

2.8 Data processing

ATR–FTIR spectrograms were processed with Origin Lab 2016.

Statistical processing of the results obtained and data plotting were performed using RStudio with the packages "ggplot", "ggpubr", "scales". In boxplots,



(a) (b) (c)

Fig. 1 Electrophoretic study of the BSA–complexes from: (a) DRY–, (b) UHT–, (c) SHT–milk: 1 – BSA; 2 – α – S1 – casein (dimer); 3 – beta casein, precursor; 4 – beta casein; 5 – κ – casein; 6 – β – lactoglobulin (monomer). Molecular weight marker (vertical): 97, 66, 45, 30, 20, 14 kDa. The composition of each band observed was performed via MALDI – TOF.

Table 2 The contingency of bands presence at a given Amide 1 region.

Treatment type	Absorption at the region (cm^{-1})	
	N observations	N total – N observations

the values being higher than 4×IQR (interquartile range) were treated as outliers.

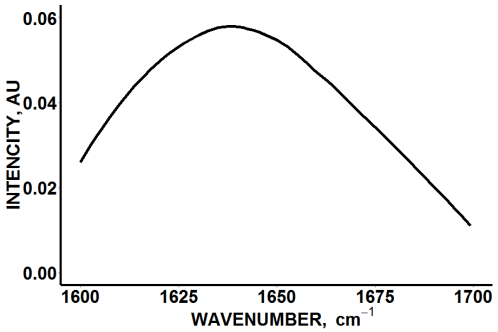
To perform Barnard's exact test, the "Exact" package was used. The structure of contingency tables to be analyzed with Barnard's exact test is described in Table 2.

3 Results

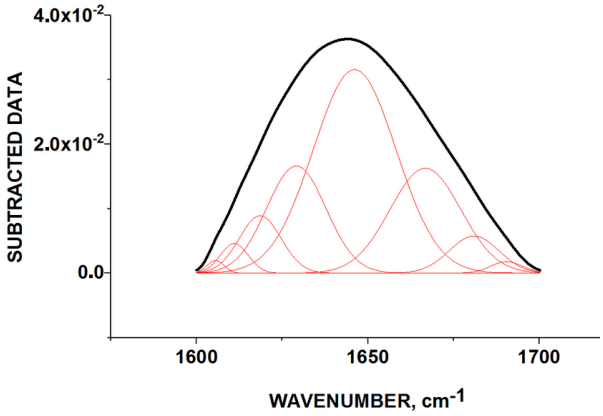
3.1 BSA-containing protein complexes from SHT–milk showed lowest content of β – sheets

To investigate the qualitative composition of the BSA–containing protein complexes from milk we have performed electrophoretic analysis, the results of which showed not only the presence of BSA, but also other proteins that are the usual constituents of milk (Fig. 1), and their content in the complexes varied in samples depending on the source. The most homogeneous in composition were the complexes from UHT–milk.

To study the secondary structure, the Amide I region, located at the 1700–1600 cm^{-1}, was investigated. At this region "stretching" vibrations of peptide bonds C = O (approximately 80%) and –NH (about 20%) occur. The frequency of absorption and extraction of this band in this area depend on the origin of hydrogen bonds between –CO and –NH, making this area extremely sensitive to conformational changes of the protein molecule [29]. Quantitative study of this area initially assumes that it can be represented as a linear sum of several fundamental structural components: α – helices, β – sheets, random structures, etc. It is worth noting that the intensity of individual component absorption in the Amide I region is quite low, and individual peaks overlaps. Thus, under such conditions it is impossible to draw a certain conclusion about the quantitative and qualitative structural profile of the sample investigated. To overcome this problem various methods of signal amplification are used. In this paper we used the second derivative of the resulting spectrum, which allowed us to find hidden absorption peaks.



(a)



(b)

Fig. 2 (a) A typical FT–IR spectrogram of the Amide I region of protein complexes isolated from milk; (b) the result of decomposition of the Amide I region into subcomponents.

Fig. 2 shows typical diagram of the FT–IR–spectroscopy of the Amide I region of the protein complexes investigated. Fig. 2(a) illustrates that the absorption peak is centered around 1640 cm^{-1}, which was noticed for all samples regardless of the processing source. In this area both β – sheets and random coils are absorbed.

In order to further interpret the results obtained and clarify the component composition of the spectrograms obtained we found the second derivative for each spectrum (Fig. 2b).

From its wavenumber each peak attributes to a specific structure, i.e. α – helix, β – sheets, random coils, since each of the secondary structure has its own vibration. As Amide I is the sum of all the individual structures, it is also possible to reveal the contribution of a particular structure to the total absorption. This allowed us to conclude on the quantitative composition for the secondary structure of the samples studied. In this paper, the wavenumbers are correlated with a specific structure as shown in Table 3.

Table 3 The main spectral bands characteristic for the secondary structures

Secondary structure	Wavenumber, cm^{-1}	Reference
β – sheet	1620 – 1639	[29–31]
α – helix	1650 – 1660	[32]
Random coil	1640 – 1650	[29–31]
α – 3_{10} – helix	1660 – 1666	[33]
β – turn and β – loop	1667 – 1688	[30]
Intermolecular β – sheet	1615 – 1620	[34–36]
	1690 – 1695	[36]

Fig. 3 shows the heat map of the absorption peaks prevalence at the Amid I region for BSA–containing protein complexes isolated from milk of various processing temperatures.

As can be seen, the areas of β – sheets absorbance 1614–1620, 1627–1639, 1678–1695 cm^{-1} were observed in all of the complexes studied. On the other hand, the presence of absorption peaks in the areas of 1621–1626, 1640–1650, 1651–1658, and 1660– 1664 cm^{-1} varies depending on the milk treatment used. To investigate the significance of the differences observed at these regions we compiled sets of contingency tables. These tables were analyzed using the Barnard's exact test, which is similar to Fisher's exact test, but with greater power analyzing 2 × 2 contingency tables with a small number of observations [37]. The results of the Barnard's exact test are shown in Table 4.

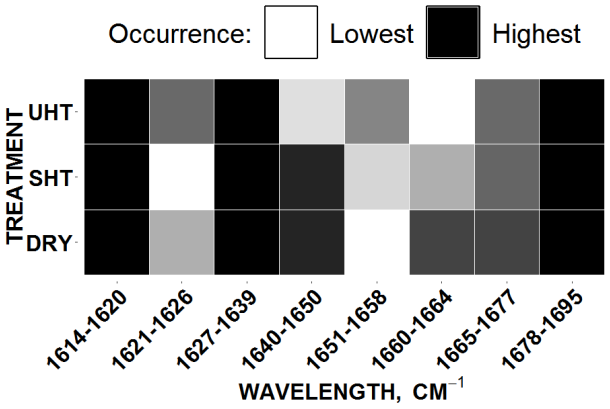


Fig. 3 Occurrence frequency of absorption peaks of the Amide I region in the BSA–containing protein complexes isolated from milk of various heat treatments. The higher the density (black color) is, the more frequent the occurrence.

Table 4 Comparison of the structure occurrence at the given Amide I region in the samples depending on the treatment applied

Range, cm^{-1}	Treatment type comparison	N observations	N total	P–value (Barnard' test)
1621–1626	UHT vs SHT	8 vs 1	12 vs 8	0.023
	UHT vs DRY	8 vs 4	12 vs 9	0.356
1640–1650	UHT vs SHT	4 vs 7	12 vs 8	0.023
	UHT vs DRY	4 vs 8	12 vs 9	0.012
1660–1664	UHT vs SHT	3 vs 3	12 vs 8	0.603
	UHT vs DRY	3 vs 7	12 vs 9	0.021

At all the regions considered the absorption peaks of BSA–containing complexes from dry and sterilized milk the significant differences in their abundance were not found. In addition, when analyzing the frequency of peak occurrence at the region of 1651–1658 cm^{-1} all the complexes showed no significant differences between each group. On the other hand, when analyzing the area of 1640–1650 cm^{-1}, in which oscillations of random structures are observed, the lowest abundance of such structures was found in the complexes originated from UHT–milk, while such structures were shown to present in all complexes from sterilized and dried milk. At the region of 1660–1664 cm^{-1}, where $\alpha - 3_{10}$ – helices are usually observed, when comparing complexes from dry and UHT milk for the latter these structures were statistically less common.

The analysis of 1621–1626 cm^{-1} region showed the smallest presence of absorption peaks for complexes isolated from sterilized milk. Absorption in this area is also associated with the presence of intermolecular β – sheets of unfolded protein components formed during heat treatment [38]. According to Ref. [39], absorption at this site is characteristic of intermolecular amyloid–like structural components.

Considering the heat map analysis, it can be concluded that although the absorption profiles were distributed similarly, there is a number of significant differences between the samples of the complexes resulting from different processing. The displacement towards the higher wave numbers of the structural profile in protein complexes isolated from dry milk was the most common characteristic among all the samples studied. Generally, the density distribution of wavenumbers in this profile was shifted to the right, which is clearly noticeable when analyzing the region of α – helices (1651–1658 cm^{-1}). These samples had the highest density of $\alpha - 3_{10}$ – helices located at 1660–1664 cm^{-1} region, which indicates a trend to the "α – helices → $\alpha - 3_{10}$ – helices" shift in them. Being typical for certain milk proteins, for example, α – lactalbumin [40], the presence of $\alpha - 3_{10}$ – helices in this case can be attributed to the result of denaturation changes taking place in the milk proteins during drying.

Comparing samples originated from UHT– and SHT–milk it is noticeable that both groups had little differences at the region of α – helices, however, the greatest variety in the presence of such structures are found at the region of random coil. Such structures we shown to be more typical for samples from sterilized milk. The same observation for this region was also valid for the samples isolated from dry milk, where the presence of random structures was characteristic in all the considered cases. It can be concluded that the formation of random coil was not typical for the UHT processing, in which the high–temperature effect is of short duration.

3.2 Random coil was the prevalent structure for all types of BSA–complexes

The quantitative analysis of the secondary structure components in the samples under consideration showed their uneven distribution (Fig. 4). The components with vibrations in the range of 1642–1660 cm^{-1} were shown to have the greatest contribution, which was also observed in the original spectrograms. Both random coil and α – helix vibrate in this region.

To evaluate the ratio of the contribution of each secondary structure and the level of its significance, Fig. 4 shows the quantitative structural compositions in the studied protein complexes originated from milk of various heat treatments. In the complexes investigated, the contribution scatter of the random coil to the secondary structure of protein aggregates originated from dry milk was the widest among both the type of processing applied and the contributions of other structures under consideration (Table 5).

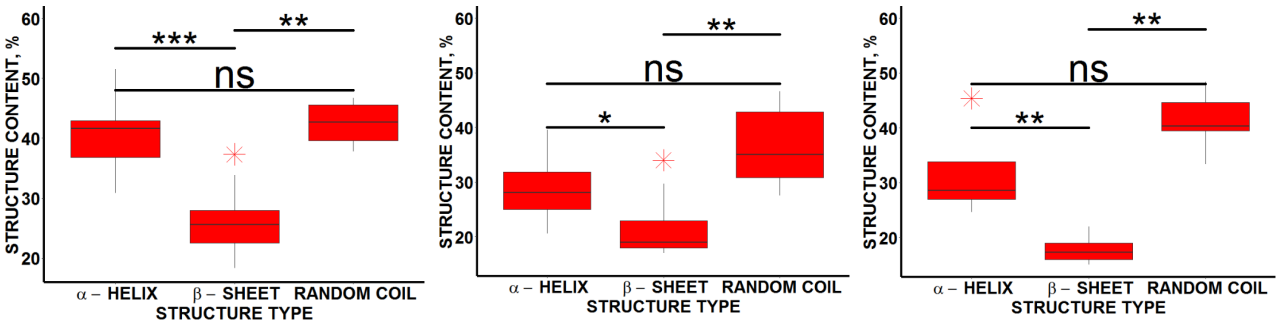


Fig. 4 Quantitative distribution of structural components in samples of complexes isolated from milk of various technological processing: (a) UHT–milk, (b) SHT–milk, (c) spray–dried milk. Red asterisk denotes outliers, Black indicates Mann–Whitney test significance levels: "ns" – $p > 0.05$; "*"– $p \le 0.05$; "**" – $p \le 0.01$; "***" – $p \le 0.001$; "****" – $p \le 0.0001$.

All complexes investigated were shown to have the greatest number of random structures, the smallest – β – sheets ($p = 0.0045$) in their overall secondary structure. When considering complexes formed in UHT–milk, the difference in the content of β – sheets and α – helices is most pronounced ($p = 0.001$). The content of the latter in such complexes was high (about 40 ± 6.4%), and their distribution in the samples was rather narrow. Quantitatively, in all cases studied the content of β – sheets was significantly smaller than the content of random structures ($p = 0.004$).

The secondary structures in complexes from sterilized milk were distributed similarly to the ones of UHT–milk. β – sheet content was smaller with respect to both random coil ($p = 0.001$) and α – helices ($p = 0.004$).

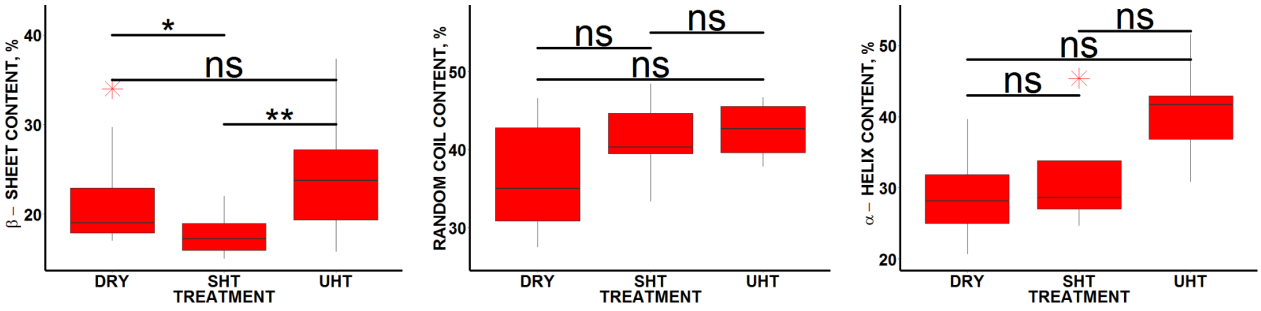
The number of random coils in all the complexes studied was at the level of 37–43% and was not statistically different with respect to the treatment used, but the widest variation in quantity of such structures was found in the complexes isolated from dry milk, as noted above. This observation can be explained by the wider variety of temperature regimes used for the milk spray–drying implementation, leading to a higher variation of denaturation degree in milk proteins, which reflects in the secondary structure. Table 5 shows the β – sheets possessed the least quantitative contribution into the secondary structure components of all the samples studied, being less than 30%. Depending on the source of the complexes, they were distributed according to the principle of SHT ≤ DRY ≤ UHT: a smaller number of these structures in BSA–containing complexes from sterilized milk were found when compared with both complexes of UHT–milk ($p = 0.005$) and the ones isolated from dry milk ($p = 0.03$). Such an observation may be caused by the specificity of this technological process, as sterilization is not only high–temperature, but also the most long–term of the processes under consideration. Apparently, this alters the protein globules much stronger. The difference in the number of β – sheets in the complexes of dry and UHT milk was not of statistical significance.

3.3 α – helices were more characteristic for protein complexes from UHT–milk, rather than for complexes of dry milk.

Considering the content of α – helices, it was found that the largest number of such components was characteristic to UHT–milk (Fig. 5). It should be noted, that the content difference was statistically significant for complexes of dry and UHT–milk ($p = 0.012$), but insignificant for the aggregates of UHT– and SHT–milk. Thus, the mobility of such structures is affected by the dehydration taking place during the spray–drying of milk to a greater extent, rather than high temperature and exposure duration.

Table 5 The contribution of structural components in samples of milk proteins complexes obtained from the sources various heat treatment (mean ± SD, %)

Treatment	β – sheet	Random coil	α – helix
UHT	24.40 ± 6.65	42.48 ± 4.18	40.36 ± 6.41
SHT	16.66 ± 3.01	41.46 ± 5.03	28.51 ± 3.88
DRY	21.84 ± 6.02	37.04 ± 7.52	28.92 ± 6.73



(a) (b) (c)

Fig. 5 Comparison of quantitative distribution of secondary structure in protein complexes depending on the type of processing used. Outliers are marked with a red asterisk, Mann–Whitney test significance levels are black: "ns" – $p > 0.05$; "*" – $p \le 0.05$; "**" – $p \le 0.01$; "***" –$p \le 0.001$; "****" – $p \le 0.0001$.

3.4 Mutual conversion of secondary structure in protein complexes is affected by the type of heat treatment

Among the major structural components, the presence of β – sheets were detected in all complexes, but their number varied in the samples as mentioned above. Fig. 6 shows the mutual correlations of structural components in BSA–containing complexes of variously processed milk relative to the content of β – sheets in it.

Although in some cases the dependencies are expressed implicitly (high p – value, Spearman), it is noticeable that samples from dry milk containing more β – sheets in the Amide I region also contained more α – helices (excluding α – 3_{10}). Controversially, such samples were shown to possess reduced the content of random coils. This observation could be explained as the mutual conversion of structural components in such samples.

An opposite situation was observed in the study of the structure contributions in complexes of sterilized and UHT milk. Random coils in such samples were found in greater amount, although they varied in the frequency of occurrence, which was mentioned above. Simultaneously, a decrease in the content of α – helices was observed in samples along with an increase in the content of β – sheets.

During UHT processing, the protein complexes showed a decrease in the number of α – helices, which correlates with an increase in the β – sheet content (R = –0.82). When considering the mutual correlation of the secondary structure components in complexes of sterilized milk, this tendency can be clearly seen. Thus, it can be concluded that α – helices are converted into random coils in these two processing types.

Although the two methods, SHT– and UHT–processing, vary greatly in their implementation, spray–drying causes an additional effect of dehydration, which obviously affects the profile of the secondary structure in protein complexes.

Conclusion

The study has found that the components of the secondary structure in BSA–containing protein complexes isolated from milk of various technological processing are unevenly distributed. All complexes studied were shown to contain β – sheets, but their quantitative contribution in all cases was small relative to the other secondary structures. The lowest content

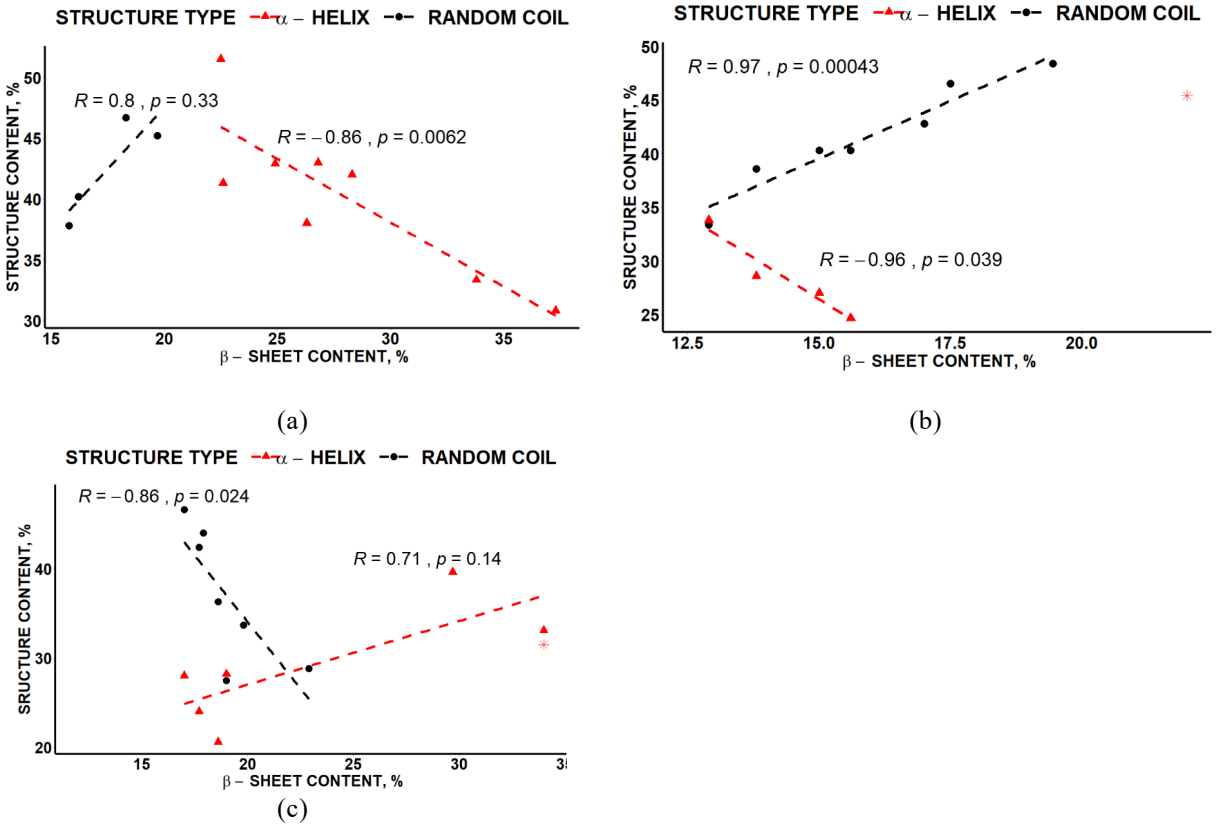


Fig. 6 Mutual correlation of secondary structure in complexes isolated from milk of various technological processing: (a) UHT–milk, (b) SHT–milk, (c) spray–dried milk. Triangle and circle depict α – helices and random coil content, respectively. R reflects the Spearman correlation coefficient, p – the significance of correlation. The data marked with red asterisk were not considered.

of β – sheets was found in SHT–milk, thus it can be concluded that it is the exposure time to high temperature that leads to a decrease in their content. For UHT– milk complexes, the smallest frequency in occurrence of random coils was also noted. This observation could be explained with the shortest incubation time at a high temperature in the process among those considered, preventing the formation of such structures. When comparing complexes of dry and UHT–milk, the presence of α – 3_{10} – helices was more characteristic than α – helices for the complexes of the first treatment type. This fact also confirmed when comparing the quantitative contribution of α – helices to the secondary structure of these complexes. Thus, dehydration during spray–drying could be concluded to promote the shift at this region towards large wave numbers.

The study of mutual correlation of the secondary structures quantitative contribution established similar models for UHT– and SHT–processes, differing from those, which occur during the spray–drying. Thus, in the samples of SHT– and UHT– treated milk samples, an increase in the number of random coils occurs with a decrease in the number of α – helices, while during spray–drying the increase in random structures correlates with a decrease in the number of β – sheets.

Based on the data described, the alteration of milk proteins' secondary structure during heat treatment is greatly defined by the certain type of technological processing. With further investigations this finding could be used for the improvement of identity control methods applied for dairy products.

Abbreviations

UHT: ultra–high–temperature; SHT: sterilization; DRY: spray drying; BSA: bovine serum albumin; TCO: trans–cycloocten–PEG4–NHS ester; 2ME: 2 – mercaptoethanol; Tz: methyltetrazine–PEG4–NHS ester; DMSO: dimethyl sulfoxide; SDS: sodium dodecyl sulfate; ATR: attenuated total reflectance; FT–IR–spectroscopy: Fourier-transform infrared spectroscopy.

Disclosures

All authors declare that there is no conflict of interests in this paper.

Acknowledgements

We thank Olga Poleshchuk (EPAM Systems) for assistance with data processing and statistical analysis.

References

1. S. N. Moejes, A. J. B. van Boxtel, "Energy saving potential of emerging technologies in milk powder production," Trends in Food Science & Technology 60, 31–42 (2017).
2. L. Malafronte, L. Ahrné, E. Schuster, F. Innings, and A. Rasmuson, "Exploring drying kinetics and morphology of commercial dairy powders," Journal of Food Engineering 158, 58–65 (2015).
3. Y. Lin, Y. Liu, L. Wang, Y. Xie, Z. Gao, and S. Wang, "Optimization of drying conditions and components to reduce wall sticking during spray drying of infant formula milk," International Journal of Agricultural and Biological Engineering 11(2), 214–218 (2018).
4. E. A. Permyakov, α-Lactalbumin, Nova, New York (2005). ISBN 1-59454-107-8.
5. P. E. Morgan, T. M. Treweek, R. A. Lindner, W. E. Price, and J. A. Carver, "Casein proteins as molecular chaperones," Journal of Agricultural and Food Chemistry 53(7), 2670–2683 (2005).
6. V. A. Borzova, K. A. Markossian, N. A. Chebotareva, S. Y. Kleymenov, N. B. Poliansky, K. O. Muranov, V. A. Stein-Margolina, V. V. Shubin, D. I. Markov, and B. I. Kurganov, "Kinetics of Thermal Denaturation and Aggregation of Bovine Serum Albumin," PLoS One 11(4), e0153495 (2016).
7. K. Murayama, M. Tomida, "Heat-Induced Secondary Structure and Conformation Change of Bovine Serum Albumin Investigated by Fourier Transform Infrared Spectroscopy," Biochemistry 43(36), 11526–11532 (2004).
8. S. Verruck, S. Sartor, F. B. Marenda, E. L. da Silva Barros, C. Camelo-Silva, M. H. Machado Canella, and E. S. Prudencio, "Influence of Heat Treatment and Microfiltration on the Milk Proteins Properties," Advances in Food Technology and Nutritional Sciences 5(2), 54–66 (2019).
9. S. K. Baier, E. A. Decker, and D. J. McClements, "Impact of glycerol on thermostability and heat-induced gelation of bovine serum albumin," Food Hydrocolloids 18(1), 91–100 (2004).
10. H. B. Wijayanti, N. Bansal, and H. C. Deeth, "Stability of Whey Proteins during Thermal Processing: A Review," Comprehensive Reviews in Food Science and Food Safety 13(6), 1235–1251 (2014).
11. G. B. Jameson, J. J. Adams, and L. K. Creamer, "Flexibility, functionality and hydrophobicity of bovine β-lactoglobulin," International Dairy Journal 12(4), 319–329 (2002).
12. K. Ponniah, T. S. Loo, P. J. B. Edwards, S. M. Pascal, G. B. Jameson, and G. E. Norris, "The production of soluble and correctly folded recombinant bovine beta-lactoglobulin variants A and B in Escherichia coli for NMR studies," Protein Expression and Purification 70(2), 283–289 (2010).

13. R. N. W. Zeiler, P. G. Bolhuis, "Exposure of thiol groups in the heat-induced denaturation of β-lactoglobulin," Molecular Simulation 41(10–12), 1006–1014 (2015).
14. E. N. C. Mills, A. S. Tatham, "Allergenes," in Encyclopedia of Food Sciences and Nutrition, B. Caballero, P. M. Finglas, and F. Toldrá (eds.), 2nd ed., Academic Press, New York, 143–150 (2003). ISBN: 978-0-12-227055-0.
15. D. Mercadante, L. D. Melton, G. E. Norris, T. S. Loo, M. A. K. Williams, R. C. J. Dobson, and G. B. Jameson, "Bovine β-Lactoglobulin Is Dimeric Under Imitative Physiological Conditions: Dissociation Equilibrium and Rate Constants over the pH Range of 2.5–7.5," Biophysical Journal 103(2), 303–312 (2012).
16. P. Havea, H. Singh, and L. K. Creamer, "Characterization of heat-induced aggregates of β-lactoglobulin, α-lactalbumin and bovine serum albumin in a whey protein concentrate environment," Journal of Dairy Research 68(3), 483–497 (2001).
17. A. M. Gil, "Nuclear Magnetic Resonance," in Encyclopedia of Food and Health, F. T. B. Caballero, P. M. Finglas (Eds.), Academic Press, New York (2003). ISBN: 978-0-12-384953-3.
18. P. Havea, H. Singh, and L. K. Creamer, "Formation of New Protein Structures in Heated Mixtures of BSA and α-Lactalbumin," Journal of Agricultural and Food Chemistry 48(5), 1548–1556 (2000).
19. L. Donato, F. Guyomarc'h, "Formation and properties of the whey protein/κ-casein complexes in heated skim milk – A review," Dairy Science and Technology 89(1), 3–29 (2009).
20. F. Chevalier, A. L. Kelly, "Proteomic Quantification of Disulfide-Linked Polymers in Raw and Heated Bovine Milk," Journal of Agricultural and Food Chemistry 58(12), 7437–7444 (2010).
21. M. S. Mahomud, N. Katsuno, and T. Nishizu, "Formation of soluble protein complexes and yoghurt properties influenced by the addition of whey protein concentrate," Innovative Food Science & Emerging Technologies 44, 173–180 (2017).
22. A. K. Dunker, C. J. Brown, J. D. Lawson, L. M. Iakoucheva, and Z. Obradović, "Intrinsic disorder and protein function," Biochemistry 41(21), 6573–6582 (2002).
23. T. F. Kumosinski, E. M. Brown, and H. M. Farrell, "Three-Dimensional Molecular Modeling of Bovine Caseins: An Energy-Minimized β-Casein Structure," Journal of Dairy Science 76(4), 931–945 (1993).
24. T. K. Głąb, J. Boratyński, "Potential of Casein as a Carrier for Biologically Active Agents," Topics in Current Chemistry 375(4), 1–20 (2017).
25. T. M. Treweek, D. C. Thorn, W. E. Price, and J. A. Carver, "The chaperone action of bovine milk αS1- and αS2-caseins and their associated form αS-casein," Archives of Biochemistry and Biophysics 510(1), 42–52 (2011).
26. M. Ehrnsperger, S. Gräber, M. Gaestel, and J. Buchner, "Binding of non-native protein to Hsp25 during heat shock creates a reservoir of folding intermediates for reactivation," The EMBO Journal 16(2), 221–229 (1997).
27. A. M. Andreeva, A. S. Vasiliev, I. Y. Toropygin, D. V. Garina, N. Lamash, and A. Filippova, "Involvement of apolipoprotein A in maintaining tissue fluid balance in goldfish Carassius auratus," Fish physiology and biochemistry 45(5), 1717–1730 (2019).
28. J. R. Powell, F. M. Wasacz, and R. J. Jakobsen, "An Algorithm for the Reproducible Spectral Subtraction of Water from the FT-IR Spectra of Proteins in Dilute Solutions and Adsorbed Monolayers," Applied Spectroscopy 40(3), 339–344 (1986).
29. J. Kong, S. Yu, "Fourier Transform Infrared Spectroscopic Analysis of Protein Secondary Structures," Acta Biochimica et Biophysica Sinica 39(8), 549–559 (2007).
30. P. Garidel, H. Schott, "Fourier-Transform Midinfrared Spectroscopy for Analysis and Screening of Liquid Protein Formulations Part 2: Detailed Analysis and Applications," Bioprocess International 1, 48–55 (2006).
31. A. Barth, C. Zscherp, "What vibrations tell about proteins," Quarterly Reviews of Biophysics 35(4), 369-430 (2002).
32. R. Khurana, A. L. Fink, "Do parallel beta-helix proteins have a unique fourier transform infrared spectrum?" Biophysical Journal 78(2), 994–1000 (2000).
33. A. Dong, W. S. Caughey, "Infrared methods for study of hemoglobin reactions and structures," Methods in Enzymology 232, 139–175 (1994).
34. R. I. Litvinov, D. A. Faizullin, Y. F. Zuev, and J. W. Weisel, "The α-helix to β-sheet transition in stretched and compressed hydrated fibrin clots," Biophysical Journal 103, 1020–1027 (2012).
35. A. Roque, I. Iloro, I. Ponte, J. L. R. Arrondo, and P. Suau, "DNA-induced secondary structure of the carboxyl-terminal domain of histone H1," Journal of Biological Chemistry 280(37), 32141–32147 (2005).
36. S. Venkataramani, J. Truntzer, and D. R. Coleman, "Thermal stability of high concentration lysozyme across varying pH: A Fourier Transform Infrared study," Journal of Pharmacy & Bioallied Sciences 5(2), 148–153 (2013).
37. C.-Y. Lin, M.-C. Yang, "Improved p-Value Tests for Comparing Two Independent Binomial Proportions," Communications in Statistics-Simulation and Computation 38(1), 78–91 (2008).
38. M. D. C. Martínez-Ballesta, P. García-Gomez, L. Yepes-Molina, A. L. Guarnizo, J. A. Teruel, and M. Carvajal, "Plasma membrane aquaporins mediates vesicle stability in broccoli," PLoS One 13(2), e0192422 (2018).
39. L. M. Miller, M. W. Bourassa, and R. J. Smith, "FTIR spectroscopic imaging of protein aggregation in living cells," Biochimica et Biophysica Acta (BBA) – Biomembranes 1828(10), 2339–2346 (2013).
40. M. Svensson, J. Fast, A.-K. Mossberg, C. Düringer, L. Gustafsson, O. Hallgren, C. L. Brooks, L. Berliner, S. Linse, and C. Svanborg, "Alpha-lactalbumin unfolding is not sufficient to cause apoptosis, but is required for the conversion to HAMLET (human alpha-lactalbumin made lethal to tumor cells)," Protein Science 12(12), 2794–2804 (2003).

Optical Biopsy of Amelanotic Melanoma with Raman and Autofluorescence Spectra Stimulated by 785 nm Laser Excitation

Ivan A. Bratchenko[1†], Yulia A. Khristoforova[1*], Lyudmila A. Bratchenko[1], Alexander A. Moryatov[2], Sergey V. Kozlov[2], Ekaterina G. Borisova[3], and Valery P. Zakharov[1]

[1] Samara National Research University, 34 Moskovskoe shosse, Samara 443086, Russia
[2] Samara State Medical University, 89 Chapaevskaya str., Samara 443099, Russia
[3] Bulgarian Academy of Sciences, 72 Tsarigradsko Chaussee Blvd, Sofia 1784, Bulgaria

† **e-mail:** iabratchenko@gmail.com

* **e-mail:** khristoforovajulia@gmail.com

I. A. Bratchenko and Y. A. Khristoforova should be considered joined first author

Abstract. In this work, Raman and autofluorescence spectroscopy in the near-infrared region has been used for examining amelanotic melanoma as the most dangerous type of malignant melanoma. There were 9 patients with amelanotic melanoma, 60 with pigmented melanoma and 120 with basal cell carcinoma enrolled in this study. We studied 9 amelanotic melanoma cases to differentiate them from basal cell carcinoma (n = 120) and pigmented malignant melanoma (n = 60) using portable spectroscopy setup with laser excitation source at 785 nm and low-cost spectrometer. The spectra of the different tumor type were classified using projection on the latent structure analysis with 10-Fold cross-validation. The results of the tumor classification were presented using box-plot diagrams and ROC analysis. We obtained 0.53 and 0.88 ROC AUCs for distinguishing amelanotic melanoma versus (1) pigmented melanoma and (2) basal cell carcinoma respectively based on the joint autofluorescence and Raman spectroscopy analysis that allowed one to diagnose amelanotic melanoma as true melanoma but no basal cell carcinoma. © 2021 Journal of Biomedical Photonics & Engineering.

Keywords: Raman spectroscopy; autofluorescence; optical biopsy; projection on the latent structure analysis; PLS; amelanotic melanoma; basal cell carcinoma; skin cancer.

Paper #3415 received 13 Apr 2021; revised manuscript received 22 Jun 2021; accepted for publication 25 Jun 2021; published online 30 Jun 2021. doi: 10.18287/JBPE21.07.020308.

1 Introduction

Melanoma is one of the most aggressive skin malignancies that caused the highest number of deaths of the all cases of skin cancer due to its metastatic character. In 2020, 324 635 new cases of melanoma incidence and 57 043 deaths from melanoma were registered worldwide that is significantly higher in comparison with the last years [1]. Moreover, a high incidence of melanoma is observed among young individuals in comparison with other skin tumors.

The ABCD algorithm is basic diagnostic method for melanoma detection at the preliminary stage worldwide based on the following features: asymmetry (A), border irregularity (B), color (C) variation and diameter (D). However, atypical morphological features of malignant melanoma (MM) complicate the detecting melanoma at the early stages that leads to the untimely treatment. Amelanotic melanoma (AMM) is one of the most dangerous melanoma types accounted for about 2–8% of all melanomas [2, 3]. AMM has a variety of clinical appearances and partial or complete pigment absence

simulating nonmelanocytic skin lesions (basal cell carcinoma (BCC), keratoacanthoma, seborrheic keratosis, Bowen's disease, etc.), that may not be so dangerous to the patient's survival as MM. Dermoscopy analysis is not effective to diagnose AMM as true MM, as no specific clinical features and histopathologic standards [3] correspond to the AMM. This greatly complicates the detecting of AMM at the early stages even for the most experienced oncologists.

Today, optical biopsy is one of the promising methods to detect tumors based on their spectral features caused by the contribution of the different chemical components. Different optical methods including terahertz spectroscopy [4], ultraviolet and visible fluorescence spectroscopy [5], Raman spectroscopy [6, 7], diffuse reflectance spectroscopy [9] demonstrated possibility to diagnose cancer of the different body sites and in particular skin cancer. However, to improve the efficiency of the optical biopsy to detect skin cancer the combination of the different methods may be used [9]. Some initial efforts in this direction are presented more than ten years ago, using combination of UV-excited autofluorescence and diffuse reflectance spectroscopy of pigmented skin disorders, including AMM lesions. However, the authors utilized 337 nm nitrogen laser as an excitation source, which is suboptimal for clinical applications, due to complex support of this type of laser systems and UV irradiation application [10].

When using long wavelength spectral range, namely 785 nm laser excitation for tissue analysis, one has a unique possibility to register simultaneously both autofluorescence in the near-infrared region (NIR) and Raman signals that carries information about biochemical composition of tissue [7]. In this context, combination of Raman and autofluorescence could be an appropriate method for recognizing AMM as a true MM at the preliminary step based on the specific spectral features.

Recent studies [6–8] have performed optical biopsy based on the Raman spectroscopy and/or autofluorescence analysis to classify melanoma versus seborrheic keratosis, pigmented nevus and other type of malignant tumors (BCC, squamous cell carcinoma). Zeng et al. [11] focused on the detection of the spectral differences between cancer and benign lesions using 785 nm Raman spectroscopy. Borisova et al. [12, 13] have studied pigmented melanoma and different types of malignant and benign pigmented tumors based on the ultraviolet, visible and NIR autofluorescence spectroscopy. Puppels et al. [14] demonstrated the power of Raman spectroscopy to differentiate melanoma from different type of pigmented nevi. These results are very valuable for the detecting of true pigmented MM, however, there is a lack of studies involving optical biopsy in AMM detection. Therefore, the aim of this work is the application of Raman and autofluorescence combination in the detection of AMM among other malignant tumors.

2 Materials and methods

2.1 Experimental setup

In vivo tumors spectra were registered using portable spectroscopic setup using NIR excitation source (785 nm laser diode), spectrometer QE 65Pro (Ocean Optics Inc.) and Raman optical probe InPhotonics [6]. Laser radiation 785 nm is delivered to the optical detector by excitation fibers (100 μm diameter, 0.22 NA) and collimating lenses. NIR (785 nm) laser radiation passes through the bandpass filter (BPF), which cuts off the Raman component of the optical fiber. The dichroic mirror transmits 785 nm laser radiation to lens, which focuses exciting radiation onto the sample (7 mm focal length). The same lens collects Raman signal, autofluorescence and backscattered radiation. The same dichroic mirror transmits the collected radiation to NIR channels, which include an appropriate longpass filter to cut off exciting NIR laser radiation, matching lens, and collection fibers (200 μm diameter, 0.22 NA), connected to spectrometer QE 65Pro.

The spectra were registered in the 780–1000 nm region in SpectraSuite program with 0.2 nm spectral resolution that was obtained using 200 μm slit in the spectrometer. The integration time of each spectrum was 20 s with triple accumulation. The silicon tip on the optical probe allowed one to fix the 7 mm distance between probe and the skin surface to obtain the collection of the scattered radiation from the upper skin layer of 1 to 2 mm from the different anatomical sites. The laser power density on the skin was about 0.3 W/cm^2 and did not caused any damage to the skin or discomfort in patients.

2.2 Materials

The protocols of the *in vivo* tissue diagnostics were approved by the ethical committee of Samara State Medical University (Samara Region, Samara, Russia, protocol No 132, 29 May 2013, clinical studies fall within The Code of Ethics of a Doctor of Russia, approved at the 4th conference of the Russian Medical Association, and within the World Medical Association Declaration of Helsinki). All patients were at least 18 years old. Informed consents were acquired from all patients before the *in vivo* study.

In total, 189 spectra skin neoplasms were registered *in vivo* using spectroscopic system from 189 patients (60 pigmented MM (PMM), 9 AMM and 120 BCC). Type of each tumor was identified using histopathological analysis.

2.3 Spectra preprocessing and data analysis

In vivo spectra statistical analysis was performed in 800–914 nm region that corresponds to the 237–1800 cm^{-1}. All spectra were smoothing by Savitzky-Golay filter (0 derivative order, 15 window width,

2 polynomial order), normalized on the standard deviation of the whole spectrum to reduce dispersion of experimental data and centered for further analysis.

The analyzed spectral region 237–1800 cm^{-1} contains both broadband autofluorescence signal and weak Raman peaks. However, autofluorescence overlaps weak Raman signal in the 237 to 1200 cm^{-1} region due to low signal-to-noise ratio (SNR) and only fluorescent skin features may be analyzed in this part of spectral region. In the 1200 to 1800 cm^{-1} range a smaller autofluorescence contribution is observed, which allows one extracting tissue Raman peaks from the registered signal. Thus, tissue Raman peaks are important features of the 1200 to 1800 cm^{-1} spectral range. Analysis of the entire spectrum of skin in the 237–1800 cm^{-1} takes into account both autofluorescence and Raman spectral features of analyzed tissues [6].

The entire spectra in the 800–914 nm area contain hidden links between different spectrum bands, due to the contribution of the same chemical components to these bands that causes multiple correlations of the spectral data. To analyze the highly correlated spectral data of the large dimension the regression analysis using the partial least square discriminant analysis (PLS–DA) was used [15]. PLS–DA method allows constructing the regression model for identifying spectra to the neoplasm classes based on the significant spectral differences by decomposing the original spectral data and the predictor matrix into a new space of lower dimension.

Four regression models were built in accordance with aim of this work:

(1) discrimination of PMM versus BCC;
(2) discrimination of PMM versus AMM;
(3) discrimination of all MM versus BCC;
(4) discrimination of AMM versus BCC.

The stability of the obtained classification PLS–DA models was checked by means of 10-fold cross-validation. The number of Latent Variables (LV) was chosen by the criterion of the minimum of the root mean square error (RMSE) for the applied of 10-Fold cross validation. We selected the first 4 (LVs) in (1) “PMM versus BCC” regression model, the first 3 LVs in (2) “PMM versus AMM” model, the first 2 LVs in both (3) “all MM versus BCC” and (4) “AMM versus BCC” models. The selected LVs describe 95% of the total variances of the spectral differences between analyzed tumor classes in (1) “PMM versus BCC” model, 94% in (2) “PMM versus AMM” model, 89% in (3) “all MM versus BCC” model and 86% in (4) “AMM versus BCC” model.

To determine the discriminant analysis of the analyzed neoplasm types, the PLS predictors were calculated to present the numeric value of the neoplasm diagnosis in the built model. PLS predictors were calculated in “R studio” software to implement the SIMPLS algorithm for PLS part of PLS–DA method using mdatools packages [16]. The PLS prediction algorithm is presented in Ref. [15]. Results of tumor classification based on the PLS analysis were presented using box-plot diagram and ROC curve. To quantify of the model’s efficiency, the area under the ROC curve (ROC AUC) was calculated.

3 Results and Discussion

Fig. 1 shows the mean spectra of PMM, AMM and BCC including Raman and autofluorescence signals with dispersion. The spectrum stimulated with 785 nm laser is a nonlinear decreasing autofluorescence curve with broadband maxima (near 870 nm) and narrow Raman peaks in 850–900 nm area. The broadband autofluorescence maxima that are contributed by the endogenous skin fluorophores (mainly melanin, lipids, lipofuscins and others [17]) overlap weak Raman bands especially near 866 nm (1200 cm^{-1}) that makes it difficult to register Raman signal in this spectral region, especially in MM analysis. Therefore, Raman bands can be visualized at wavenumbers between 1200 and 1800 cm^{-1}.

MM and BCC are skin malignancies with different biochemical and clinical features. According to the Fig. 1 the spectra of BCC and MM have distinguishable spectral differences both in the autofluorescence shape and in the intensity of the Raman signal. This allows one to perform classification of PMM (n = 60) and BCC (n = 120) with 0.95 accuracy (0.95 sensitivity and 0.96 specificity) and 0.98 ROC AUC (see Fig. 2 a, e). For BCC (n = 120) vs all MM (n = 69; including AMM and PMM) discriminating accuracy is 0.90 (0.86 sensitivity and 0.93 specificity) and AUC ROC is 0.86 (Fig. 2 b, f). Thus, addition of AMM to the analysis of MM and BCC lead to the decrease of the classification model performance. This fact may be explained by the low content of melanin both in AMM and BCC tissues.

As we can see from Fig. 1a, mean spectra of AMM and PMM have similar shape features of autofluorescence curve. Broadband maxima may be observed near 810, 840 and 865 nm. The spectral differences in the 800–870 nm region not exceed 5.9%. Both mean AMM and PMM spectra have spectral maxima at 840 and 865 nm in comparison with normal skin and other skin tumors such as BCC [12]. In our previous studies, we have mentioned that local maxima at 840 and 865 nm are observed in the spectra of tumors with high melanin concentration [12]. These peaks are shifted to longer wavenumber region that causes overlapping of Raman peaks at 1086 (υ_s (PO_2^-) in phospholipids), 1285–1305 cm^{-1} (υ_{as} (PO_2^-) in phospholipids and $\tau(CH_2)$ in collagen/phospholipids) in both PMM and AMM spectra.

The similar autofluorescence of PMM and AMM with different pigmentation level may be explained by contribution of multiple skin components. At the same time, high autofluorescence and broadband emission maxima in both PMM and nevi spectra are due to the high melanin concentration in these neoplasms [12]. Therefore, it is not clear which skin components besides melanin cause high autofluorescence during 785 nm laser stimulation of skin tissues. Darvin et al. [18] have examined the changes of the NIR autofluorescence and

Raman spectra for the different fraction of melanin at different depths in human skin using depth-resolved confocal microspectroscopy system. They found that NIR autofluorescence spectral characteristics are changed not rapidly while the melanin fraction changes. The main achievement of their study is that NIR autofluorescence in the skin is caused by the melanin, keratin and possible impact of proteins/lipids oxidation products. Thus, further studies are required in order to determine specific skin components that mostly contribute to AMM autofluorescence.

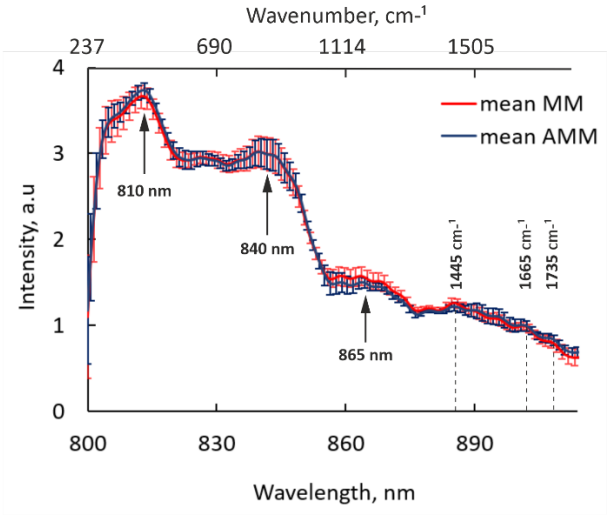


Fig. 1 The registered spectra of the skin neoplasms stimulated with 785 nm laser: (a) comparison of PMM and AMM spectra, (b) comparison of BCC and AMM.

AMM and BCC spectra are distinguished significantly with differences up to 54%. In comparison to AMM, BCC spectrum has decreasing curve with maximum values at 800–810 nm without broadband maxima at 840 and 865 nm. BCC mean spectrum are more smoothed in the region near 866 nm and allows one to register Raman peaks at 1285–1305 cm^{-1} ($\upsilon_{as}(PO_2^-)$ in phospholipids and $\tau(CH_2)$) in collagen/phospholipids, 1445 cm^{-1} ($\delta(CH_2)$ in lipids), 1665 cm^{-1} ($\upsilon(C=C)$ in unsaturated lipids, Amide I). Also, weak autofluorescence allows one to register Raman peak near 1086 cm^{-1} for some studied BCC.

Let us consider regression models based on spectral differences and similarities to separate AMM versus PMM and BCC. Table 1 and Fig. 2 (c–d, g–h) demonstrates the results for the built regression models. Fig. 2 (c, g) shows box-plot diagrams and ROC curve for the classification of PMM (n = 60) versus AMM (n = 9). The Fig. 2 (d, h) shows box-plot diagrams and ROC curve for the classification of AMM (n = 120) vs BCC (n = 9).

Table 1 Results of the tumor classification using PLS regression models.

Model		Accuracy	ROC AUC
PMM (n = 60) vs BCC (n = 120)		0.95	0.98
all MM (n = 69) vs BCC (n = 120)		0.90	0.86
PMM (n = 60) vs AMM (n = 9)	for 300–1800 cm^{-1}	0.75	0.53
	for 1200–1800 cm^{-1}	0.82	0.72
AMM (n = 9) vs BCC (n = 120)		0.90	0.88

The discrimination model of AMM vs PMM shows very poor result. The PLS predictors are equally concentrated in the narrow range of 0.10–0.16 relative units for both PMM and AMM spectra, and this fact significantly complicates AMM and PMM discrimination. The small variance of the PLS predictors for PMM and AMM spectra is caused by the small spectral differences. The ROC AUC of this model is only 0.53. The equivalent PLS predictors for PMM and AMM are caused by the similar biochemical compositions because any clinical subtype of cutaneous melanoma may be amelanotic [19]. In the case of AMM vs BCC we observe better results. The dispersion of the PLS predictors are in a wide range from 0.01 to 0.6 relative units. The obtained model allowed us to achieve 0.90 discrimination accuracy (0.89 sensitivity and 0.90 specificity) based on the joint Raman and autofluorescence analysis. The proposed optical biopsy approach demonstrates 0.88 ROC AUC for AMM and BCC separation.

The low discrimination of AMM and PMM is caused by similar broadband intensive autofluorescence, which mask low-intense Raman bands in the range of 237–1800 cm^{-1}. For typical MM, high autofluorescence is usually associated with increased melanin content in the tumor. In the case of AMM, there is a lack of accurate biochemical interpretation of studied tissues and

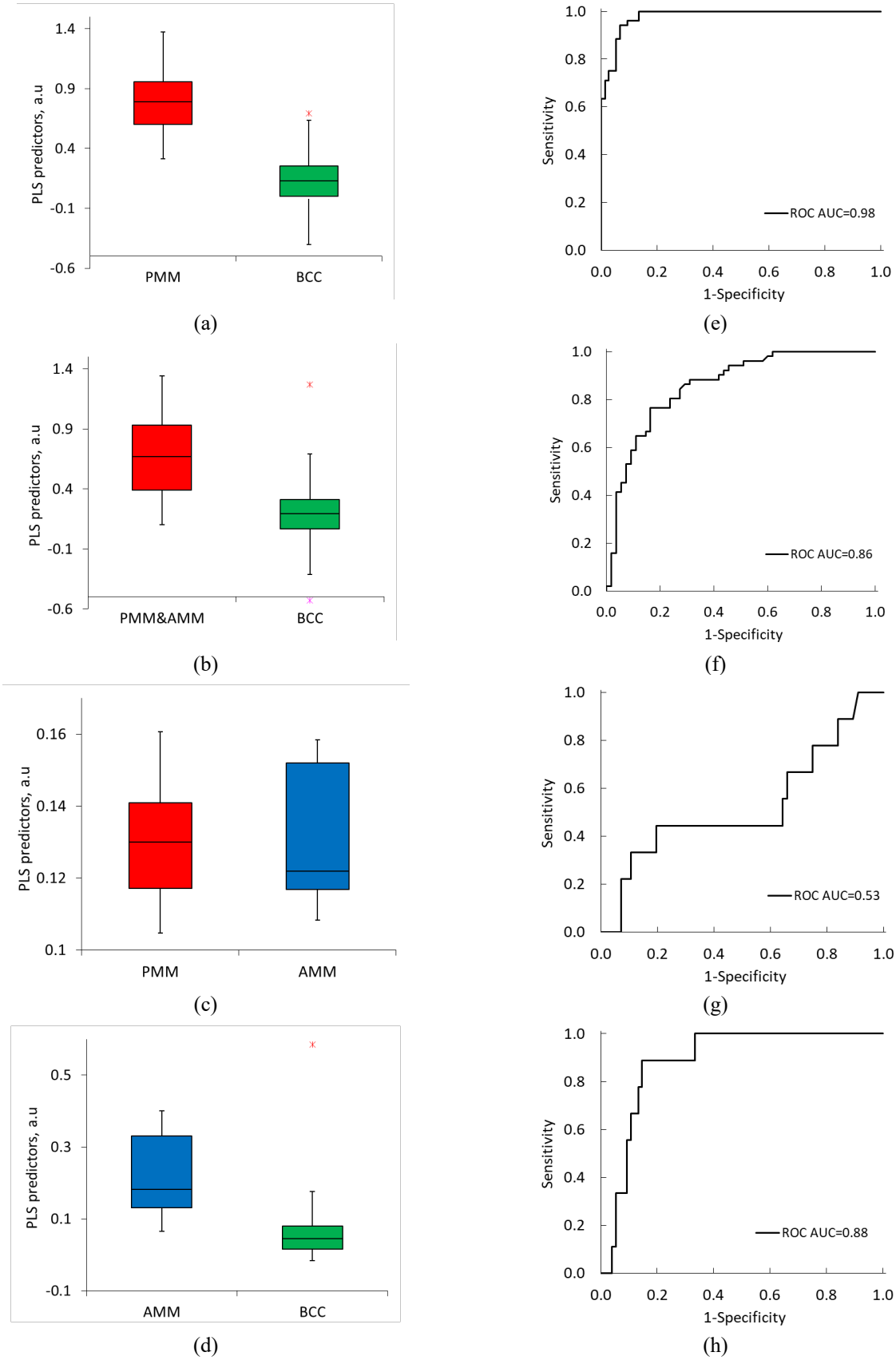


Fig. 2 Neoplasm classification by Raman and autofluorescence spectroscopy based on PLS-DA analysis: a–d Box-plots of PLS-predictors for discriminating skin lesions: (a) PMM vs BCC; (b) PMM & AMM vs BCC; (c) AMM vs PMM; (d) AMM vs BCC; e–h Corresponding ROC curves are derived from spreading PLS-predictors. Asterisks indicate outliers.

consequently along with the contribution of the melanin we may only assume the impact of other tissue components, such as proteins/lipids oxidation products [18]. This assumption may be partially confirmed by Meehan et al [3]. Their group had performed detailed morphologic analysis of 75 AMM cases and found that melanin might not be presented in AMM on visual inspection but it was detected on histopathological examination. In fact, PMM and AMM are subtypes of the same tumor type with similar composition of fluorophores but different relative concentrations, the total fluorescence spectrum of which is noninformative due to the overlap of the maxima. Therefore, for differentiation of PMM and AMM we completely removed fluorescence from registered spectra using baseline correction by asymmetric least squares method. This way allows us to perform classification of various melanoma types based only on Raman bands in the region 1200–1800 cm^{-1} with 0.82 accuracy (0.71 sensitivity and 0.85 specificity) and 0.72 ROC AUC. In accordance with Fig. 3 (a) PLS predictors medians for the PMM and AMM cohorts in box plot diagrams for this model are more differed in comparison with PLS predictors calculated when analyzing full tumor spectra in 237–1800 cm^{-1} region (Fig. 2 (c)) that results in improving classification accuracy to the 0.82. Therefore, we can assume that analysis of the Raman spectra is more effective for classification of different subtypes of melanoma in comparison with analysis of the full spectra containing both fluorescence and Raman signals because similar fluorescence features of AMM and PMM spectra do not allow to identify their Raman differences due to high overlap of their spectra.

In studies of skin cancer by Raman and autofluorescence spectroscopy several works have demonstrated promising results to classify MM versus other skin tumors. In such studies all cases of melanoma are considered as joint class without subtyping. Despite the importance of the AMM detection among all MM cases lack of works with AMM studying using optical methods is observed. Only in several medical studies selected cases of AMM were examined in details to demonstrate the difficulty of diagnosing AMM on the basis of only clinical or dermoscopic features [20, 21]. In different studies the misdiagnosed rate of AMM reaches a high value of 89% [21]. Cheung et al have investigated 75 AMM cases and only 2 cases demonstrated distinctive clinical features of AMM [3]. In study by Gualandri et al. only 2 cases of AMM (from 36 studied AMM cases in total) were suspected as true MM [2]. In study by Detrixhe et al. [22], it was shown that all 7 studied cases of AMM were incorrectly diagnosed by clinicians.

The obtained results show that spectral analysis in the NIR region allows one to define AMM as true MM. This finding is based on the similarity of AMM and PMM spectral properties. At the same time, it seems like AMM and MM differentiation is impossible based on the similar analysis of the full spectral region 237–1800 cm^{-1} and only Raman spectra in the 1200–1800 cm^{-1} can contain useful information to differ them. On the other hand, the real problem in clinical diagnosis is to differentiate AMM from other malignant tumors. In this study we achieved 0.90 accuracy and 0.88 ROC AUC in AMM and BCC separation. Such values of diagnostic performance are very promising and the proposed optical biopsy method may be helpful in clinical evaluation of AMM among nonmelanoma tumors. However, further large trials are required to prove this assumption.

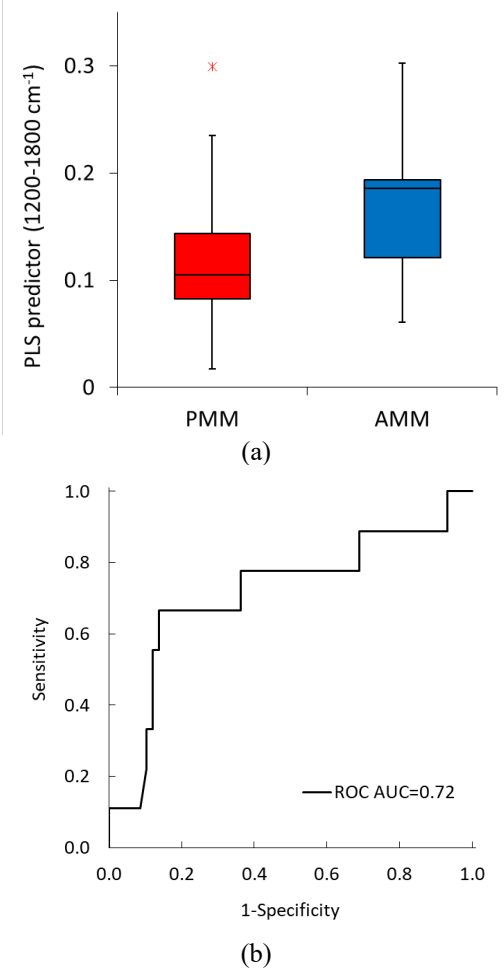


Fig. 3 PMM and AMM classification by Raman spectra in the 1200–1800 cm^{-1} based on PLS-DA analysis: (a) box-plots of PLS-predictors for discriminating skin lesions; (b) corresponding ROC curve is derived from spreading PLS-predictors. Asterisk indicates outlier.

4 Conclusions

AMM is the most dangerous type of MM because it either has been misdiagnosed frequently as BCC and other nonmelanotic benign lesions or not attract attention due to the absence of the clinical melanoma features. In result, AMM are progressed and detected at the advanced stages that is harmful to the patient's survival. In this work, we performed the classification of the AMM versus PMM and BCC cases. Spectral analysis on the basis of the near-infrared Raman and autofluorescence features allowed us to distinguish AMM and BCC with 0.90 accuracy while AMM and MM showed almost equal fluorescence spectral properties and only Raman signal

can contain useful spectral differences that can be proved by increase of the AMM cases. Achieved ROC AUC of AMM and BCC differentiation was 0.88 that proves the proposed technique of skin tumors optical biopsy may be useful in clinical practice. The obtained results show the power of spectral analysis to correctly define AMM as MM and avoid AMM treatment as other nonmelanoma tumors.

Disclosures

All authors declare that there is no conflict of interests in this paper.

Acknowledgments

This study is supported by joint program of Russian Foundation of Basic Research and Bulgarian Science Fund respectively under contracts № 19-52-18001 Bolg_a and № KP06-Russia/19/28.09.2019 "Multivariative Raman and fluorescence diagnosis of cutaneous tumors".

References

1. Global Cancer Observatory, Cancer Fact Sheets: Skin, 2020 (accessed 11 January 2021) [https://gco.iarc.fr/today/fact-sheets-cancers].
2. L. Gualandri, R. Betti, and C. Crosti, "Clinical features of 36 cases of amelanotic melanomas and considerations about the relationship between histologic subtypes and diagnostic delay," Journal of the European Academy of Dermatology and Venereology 23(3), 283–287 (2009).
3. W. L. Cheung, R. R. Patel, A. Leonard, B. Firoz, and S. A. Meehan, "Amelanotic melanoma: a detailed morphologic analysis with clinicopathologic correlation of 75 cases," Journal of Cutaneous Pathology 39(1), 33–39 (2012).
4. K. I. Zaytsev, K. G. Kudrin, V. E. Karasik, I. V. Reshetov, and S. O. Yurchenko, "In vivo terahertz spectroscopy of pigmentary skin nevi: Pilot study of non-invasive early diagnosis of dysplasia," Applied Physics Letters 106(5), 053702 (2015).
5. E. Borisova, T. Genova, V. Mircheva, P. Troyanova, I. Bratchenko, L. Bratchenko, Y. Khristoforova, V. Zakharov, I. Lihacova, A. Lihacovs, and J. Spigulis, "Multispectral fluorescence detection of pigmented cutaneous tumours," SPIE Proceedings 11585, 1158504 (2020).
6. I. A. Bratchenko, L. A. Bratchenko, A. A. Moryatov, Y. A. Khristoforova, D. N. Artemyev, O. O. Myakinin, A. E. Orlov, S. V. Kozlov, and V. P. Zakharov, "In vivo diagnosis of skin cancer with a portable Raman spectroscopic device," Experimental Dermatology 30(5), 652–663 (2021).
7. E. Cordero, I. Latka, C. Matthäus, I. W. Schie, and J. Popp, "In-vivo Raman spectroscopy: from basics to applications," Journal of Biomedical Optics 23(7), 071210 (2018).
8. L. A. Bratchenko, Y. A. Khristoforova, A. A. Morytatov, and I. A. Bratchenko, "Raman spectroscopy based diagnosis of dermatofibrosarcoma protuberans: Case report," Photodiagnosis and Photodynamic Therapy 35, 102351 (2021).
9. B. W. Murphy, R. J. Webster, B. A. Turlach, C. J. Quirk, C. D. Clay, P. J. Heenan, and D. D. Sampson, "Toward the discrimination of early melanoma from common and dysplastic nevus using fiber optic diffuse reflectance spectroscopy," Journal of Biomedical Optics 10(6), 064020 (2005).
10. E. Borisova, E. Nikolova, P. Troyanova, and L. Avramov, "Autofluorescence and diffuse reflectance spectroscopy of pigment disorders in human skin", Journal of Optoelectronics and Advanced Materials 10(3), 717–722 (2008).
11. H. Lui, J. Zhao, D. McLean, and H. Zeng, "Real-time Raman Spectroscopy for In Vivo Skin Cancer Diagnosis," Cancer Research 72(10), 2491–2500 (2012).
12. E. G. Borisova, I. A. Bratchenko, Y. A. Khristoforova, L. A. Bratchenko, T. I. Genova, A. I. Gisbrecht, A. A. Moryatov, S. V. Kozlov, P. P. Troyanova, and V. P. Zakharov, "Near-infrared autofluorescence spectroscopy of pigmented benign and malignant skin lesions," Optical Engineering 59(6), 061616 (2020)
13. E. Borisova, A. Gisbrecht, T. Genova-Hristova, P. Troyanova, E. Pavlova, N. Penkov, I. Bratchenko, V. Zakharov, I. Lihachova, I. Kuzmina, and J. Spigulis, "Multispectral autoflourescence detection of skin neoplasia using steady-state techniques," SPIE Proceeding 11047, 1104704 (2019).
14. I. P. Santos, R. van Doorn, P. J. Caspers, T. C. B. Schut, E. M. Barroso, T. E. Nijsten, V. N. Hegt, S. Koljenovic, and G. J. Puppels, "Improving clinical diagnosis of early-stage cutaneous melanoma based on Raman spectroscopy," British Journal of Cancer 119(11), 1339–1346 (2018).
15. D. M. Haaland, E. V. Thomas, "Partial least-squares methods for spectral analyses. 1. Relation to other quantitative calibration methods and the extraction of qualitative information," Analytical chemistry 60(11), 1193–1202 (1988).
16. S. Kucheryavskiy, "Mdatools: Multivariate Data Analysis for Chemometrics," R Package, version 0.9.4 (2019) [https://mdatools.com/].

17. I. Giovannacci, C. Magnoni, P. Vescovi, A. Painelli, E. Tarentini, and M. Meleti, "Which are the main fluorophores in skin and oral mucosa? A review with emphasis on clinical applications of tissue autofluorescence," Archives of Oral Biology 105, 89–98 (2019).
18. B. P. Yakimov, E. A. Shirshin, J. Schleusener, A. S. Allenova, V. V. Fadeev, and M. E. Darvin, "Melanin distribution from the dermal–epidermal junction to the stratum corneum: non-invasive in vivo assessment by fluorescence and Raman microspectroscopy," Scientific Reports 10(1), 14374 (2020).
19. M. Beyeler, R. Dummer, "Cutaneous melanoma: uncommon presentations," Clinics in Dermatology 23(6), 587–592 (2005).
20. M. Mascolo, D. Russo, M. Scalvenzi, S. Varricchio, and S. Staibano, "Pitfalls in the dermoscopic diagnosis of amelanotic melanoma," Journal of the American Academy of Dermatology 72(1), S2–S3 (2015).
21. H. Z. Gong, H. Y. Zheng, and J. Li, "Amelanotic melanoma," Melanoma Research 29(3), 221–230 (2019).
22. A. Detrixhe, F. Libon, M. Mansuy, N. Nikkels-Tassoudji, A. Rorive, J. E. Arrese, P. Quatresooz, M.-A. Reginster, and A. F. Nikkels, "Melanoma masquerading as nonmelanocytic lesions," Melanoma Research 26(6), 631–634 (2016).

The Effect of Noise in Raman Spectra on the Reconstruction of the Concentration of Amino Acids in the Mixture by Multivariate Curve Resolution (MCR) Analysis

Irina A. Matveeva*, Lyudmila A. Bratchenko, Oleg O. Myakinin, Elena N. Tupikova, and Valery P. Zakharov

Samara National Research University, 34 Moskovskoe shosse, Samara 443086, Russia

*** e-mail:** m-irene-a@yandex.ru

Abstract. Changes in the concentration of free amino acids in biological tissues is a sign of impaired protein metabolism in patients with cancer. Recently, Raman spectroscopy has been used for early diagnostics of oncological diseases. The concentrations of individual components of biological tissue (for instance, the concentrations of amino acids) can be obtained by decomposing the tissue Raman spectrum. This study was designed to evaluate the effect of noise in the Raman spectra of individual amino acids on the result of the decomposition of the spectra of an amino acid mixture. As a decomposition method, we used Multivariate Curve Resolution-Alternating Least Squares (MCR–ALS) analysis and investigate experimental Raman spectra of amino acids and mathematically simulated Raman spectra of amino acid mixtures. Noise with different signal-to-noise ratios (SNR) was artificially added to both the experimental spectra of pure amino acids and the spectra of the mixtures. Concentration values for each amino acid obtained as a result of applying the MCR–ALS analysis have been compared with the corresponding true values and the correlation coefficients have been calculated. The results show a less pronounced negative effect of noise in the case when the spectra of pure amino acids (which were used as a basis for the MCR–ALS analysis) are noisy, and a more pronounced negative effect when the spectrum of the mixture is noisy. The accuracy of reconstruction of an amino acid is also negatively affected by strong background fluorescence in the amino acid spectrum. Moreover, the results indicate that using the basis spectra with a high SNR (SNR = 5) makes it possible to successfully estimate the amino acid concentrations in a mixture even when the Raman spectrum of the mixture is noisy and has a low SNR (SNR < 5). © 2021 Journal of Biomedical Photonics & Engineering.

Keywords: Signal-to-noise ratio; Raman spectrum; Raman scattering; multivariate curve resolution; free amino acids.

Paper #3424 received 23 May 2021; revised manuscript received 25 Jun 2021; accepted for publication 26 Jun 2021; published online 30 Jun 2021. doi: 10.18287/JBPE21.07.020309.

1 Introduction

Cancer is the second leading cause of death worldwide. The most common type of cancer was lung cancer. According to the World Health Organization, there was about 2.21 million new cases in 2020. Moreover, lung cancer was the most common cause of cancer death in 2020 (1.80 million deaths). It is well known that lung cancer risk and mortality can be reduced by early detection of cases [1].

It is also known that during the malignant tumor development, changes in protein metabolism occur in the

patient's body. Many researchers have described changes in plasma free amino acid (PFAA) profiles in patients with cancer. Kubota, Meguid, and Hitch [2] analyzing PFAA in venous blood of patients with breast cancer, gastrointestinal tract cancer, and head and neck cancer suggested that PFAA profiles correlate diagnostically with the organ-site origin of three different kinds of malignant tumors. Miyagi et al. [3] determined the characteristics of the PFAA profiles in cancer patients with one of five types of cancer: lung, gastric, colorectal, breast, or prostate cancer. PFAA profiling for detecting lung cancer was also studied by Shingyoji et al. [4], Zhao et al. [5], and Proenza et al. [6]. These findings suggest that PFAA profiling has great potential for improving early detection of lung cancer.

It makes us look for new methods to analyze PFAA profiles. Recently, Raman spectroscopy has been used for early diagnostics of oncological diseases. Bratchenko et al. [7] have shown that this method can be used in the diagnosis of cancer, such as skin neoplasms. Moreover, Raman spectroscopy is an optical method that is relevant for the analysis of liquid media. So, we believe that Raman spectroscopy can be used for non-invasive analysis of blood plasma. The Raman spectra of PFAAs are specific and can be used to successfully evaluate PFAAs' concentration in a mixture of different substances by the Raman spectrum of this mixture.

In this study, we use Multivariate Curve Resolution–Alternating Least Squares (MCR–ALS) method to analyze the Raman spectra of amino acid mixtures. This method is widely used to reconstruct the concentration profiles of chemicals analysis [8, 9]. Recently, MCR–ALS method has found wide biological and medical applications [8, 10] and has been used for the analysis of spectral data when it is required to determine the concentrations of complex mixture components from spectra. For example, Xu and Rice [11] used a MCR spectral unmixing in fluorescence imaging. Chen et al. [12] used Raman spectroscopic detection of keratin with MCR analysis for automatic oral cancer diagnosis. Iwasaki et al. [13] investigated the possibilities of discrimination of breast cancer cells from normal mammary epithelial cells by Raman microspectroscopy and MCR analysis. It should be noted that the use of MCR–ALS analysis makes it possible not only to estimate the concentrations of components, but also to obtain their "pure" Raman spectra [14].

However, the MCR–ALS analysis can be sensitive to noise in the Raman spectra analyzed. In the practical application, the efficiency of evaluation of PFAAs' concentration in a mixture may decrease due to the fact that the Raman spectra contain a noise signal. We also suppose that, if MCR–ALS uses a known predetermined basis of amino acids, the result can be affected by noise in both the pure amino acid Raman spectra of the basis and Raman spectra of the mixtures. On the one hand, we can provide high-quality registration of basis Raman spectra (that is, the spectra of pure amino acids that are used in the MCR–ALS analysis) with high signal-to-noise ratio (SNR) using a spectroscopic setup with high spectral resolution and increasing integration time. In addition, pure amino acids may be available for registration (or Raman microscopy of the samples may be used). And finally, it is enough to record the spectra (which are used as the basis) only once – then one can use them when analyzing other samples of mixtures. On the other hand, in a clinical setting, high-quality recording of Raman spectra can be difficult due to the large patient flow and limited time to examine a patient. Therefore, it can be assumed that the Raman spectra, which are subject to analysis by the MCR–ALS method, will have a lower SNR than the previously obtained Raman spectra of amino acids used as a basis for the MCR–ALS analysis.

This study was designed to evaluate an effect of the noise in Raman basis spectra of amino acids and Raman spectra of a mixture on their reconstruction from the mixture.

2 Materials and Methods

The experimental Raman spectra used in our study are recorded using a portable spectroscopic setup which includes a thermally stabilized LML-785.0RB-04 laser diode module as an excitation source (785 ± 0.1 nm central wavelength, 200 mW laser power) and a QE 65 Pro spectrometer (OceanOptics, Inc., USA) with CCD detector operating at –15 °C [15].

We used 20 standard proteinogenic amino acids (see Table 1 and Fig. 1). Amino acids are presented in crystalline powder form. The amino acids in the crystal form were placed onto the metal-coated slide. All spectra were registered at the room temperature. The registration of spectra using this system was carried out in 800–1000 nm with 0.2 nm spectral resolution that corresponds to the 240–2236 cm^{-1}. The Raman signal of amino acids was acquired from 3 accumulations each of 5 sec integration time. The mean Raman spectrum for each amino acid was averaged over three registered spectra.

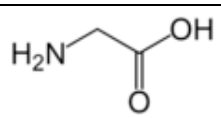
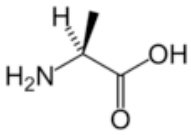
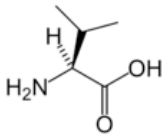
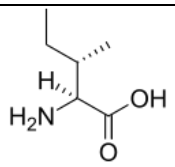
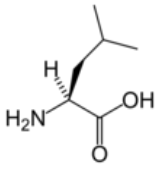
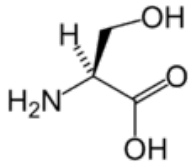
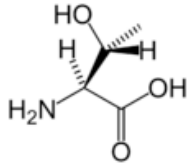
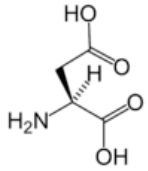
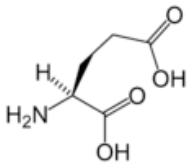
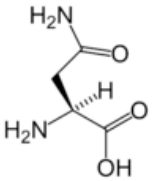
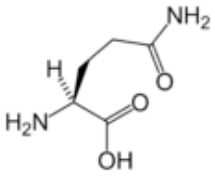
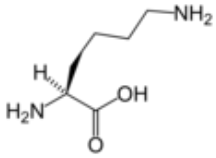
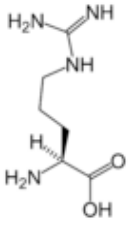
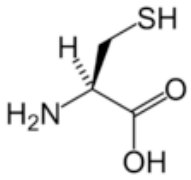
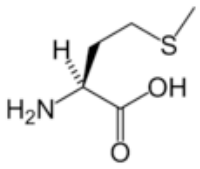
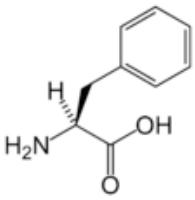
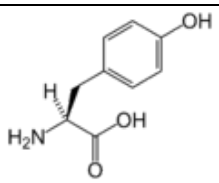
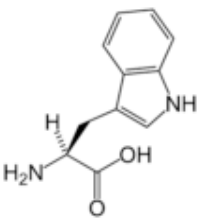
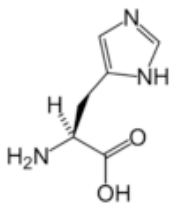
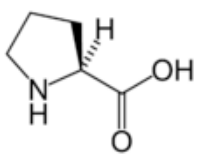
The preprocessing of the registered data includes only cosmic ray and dark noise removal that are automatically applied in the "Spectra Suite" software package (OceanOptics, Inc., USA) [16]. Examples of recorded and preprocessed spectra is shown in Fig. 1.

Then we have modeled amino acid mixtures. The "mixture" means the sum of 20 standard proteinogenic amino acids (see Table 1), taken in different quantities, that is, with different concentrations. The concentration of amino acids in the mixtures is chosen so that the mixtures correspond to real PFAA profiles of blood plasma samples studied by other researchers [3–6].

We define a Raman spectrum of an amino acid mixture as a mathematical sum of the products of the pure amino acid spectra of and its concentrations in the mixture:

$$S_M(\lambda) = c_{A1} \times s_{A1}(\lambda) + \cdots + c_{AN} \times s_{AN}(\lambda), \quad (1)$$

Table 1 The standard proteinogenic amino acids.

Amino acid	Glycine	Alanine	Valine	Isoleucine
Letter code	Gly	Ala	Val	Ile
Formula	C_2H_3NO	C_3H_5NO	C_5H_9NO	$C_6H_{11}NO$
Skeleton formula				
Amino acid	Leucine	Serine	Threonine	Aspartic acid
Letter code	Leu	Ser	Thr	Asp
Formula	$C_6H_{11}NO$	$C_3H_5NO_2$	$C_4H_7NO_2$	$C_4H_5NO_3$
Skeleton formula				
Amino acid	Glutamic acid	Asparagine	Glutamine	Lysine
Letter code	Glu	Asn	Gln	Lys
Formula	$C_5H_7NO_3$	$C_4H_6N_2O_2$	$C_5H_8N_2O_2$	$C_6H_{12}N_2O$
Skeleton formula				
Amino acid	Arginine	Cysteine	Methionine	Phenylalanine
Letter code	Arg	Cys	Met	Phe
Formula	$C_6H_{12}N_4O$	C_3H_5NOS	C_5H_9NOS	C_9H_9NO
Skeleton formula				
Amino acid	Tyrosine	Tryptophan	Histidine	Proline
Letter code	Tyr	Trp	His	Pro
Formula	$C_9H_9NO_2$	$C_{11}H_{10}N_2O$	$C_6H_7N_3O$	C_5H_7NO
Skeleton formula				

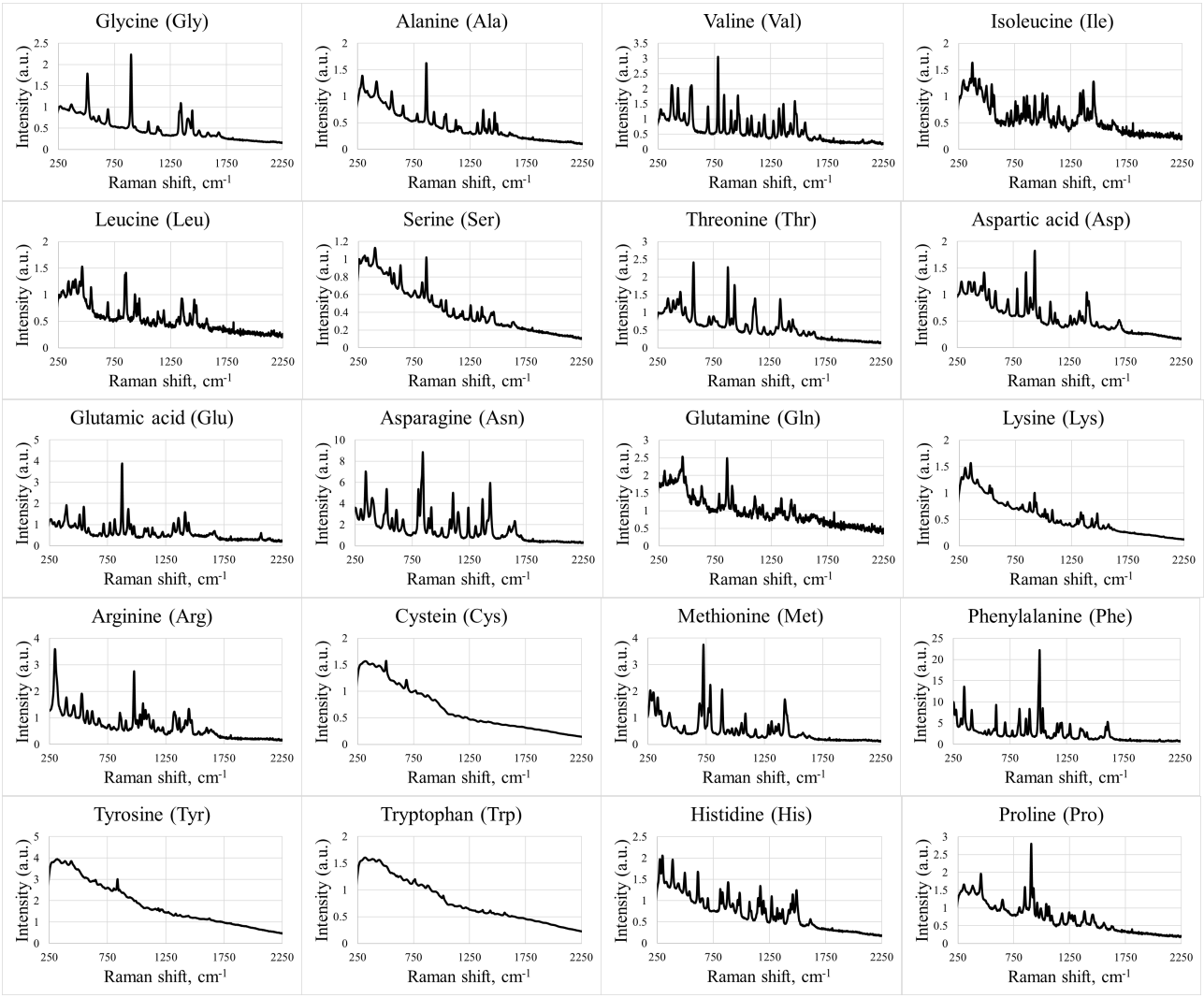


Fig. 1 Recorded and preprocessed Raman spectra of the amino acids.

where $c_{A1},...,c_{AN}$ – are the concentrations of pure amino acids in the mixture, $s_{A1}(\lambda),...,s_{AN}(\lambda)$ – are the pure amino acid spectra.

Using information on PFAA profiles in lung cancer patients [3–6], we have artificially modelled 10 Raman spectra: 5 spectra of lung cancer patient PFAA profiles and 5 spectra of control group PFAA profiles. Concentrations of amino acids in the mixtures are presented in Table 2.

The next step in our study was the simulation of a noise in the Raman spectra. It should be noted that the spectra recorded have a noise signal due to the spectroscopic setup. However, in this study, we investigate the effect of additively added noise. Therefore, the noise contained in the Raman spectra initially is not taken into account.

We added the noise as the random value process with hypothetically normal distribution, zero mean value and various standard deviations. In this case, the formula for a Raman spectrum looks like this:

$$S'(\lambda) = S(\lambda) + s_E(\lambda), \quad (2)$$

where $S(\lambda)$ is an original Raman spectrum, $s_E(\lambda)$ is the a noise spectrum.

To simulate different noise levels, we evaluated an additive noise level from a signal-to-noise ratio (SNR) metric proposed in [15]:

$$SNR = \frac{S}{6 \times \sigma_{s_E}}, \quad (3)$$

where S is the Raman signal level (intensity of Raman peak in 980–1025 cm^{-1} band); σ_{s_E} is the noise standard deviation.

To investigate the effect of the noise, it is necessary to compare different combinations of a noisy mixture and noisy basis spectra. For this purpose, we simulated Raman spectra of pure amino acids with SNRs equal to 1, 5, and 10 and Raman spectra of mixtures with SNRs equal to 2, 3, 4, and 5. Examples of the noisy spectra are shown in Fig. 2.

Table 2 Concentrations of amino acids in the mixtures.

Amino acids	Concentrations of amino acids, μM									
	Lung cancer patients					Control patients				
	№1 [4]	№2 [4]	№3 [5]	№4 [3]	№5 [6]	№1 [4]	№2 [4]	№3 [5]	№4 [3]	№5 [6]
Gly	214.3	208	298	220.7	133	209.7	203.5	454	207.2	120
Ala	324.2	366.5	643	356.1	213	343.1	353.5	611	348.1	231
Val	215.1	242.1	241	225.8	140	220.5	230	281	222.4	152
Ile	64.7	73.9	158	66.6	35.3	60.8	64.4	190	61.6	36.1
Leu	117.6	135.2	188	123.8	83.5	118.8	125.2	166	120.1	87.6
Ser	107.8	110.7	253	113.6	68.1	108.8	106.7	258	108.5	60.8
Thr	115.8	122.6	270	122.8	68.8	118.5	121.8	214	119.8	74.7
Asp	0	0	105	0	8.6	0	0	54	0	5.8
Glu	0	0	211	0	39.7	0	0	210	0	37.1
Asn	42.6	47.9	0	44.7	31.6	45.2	46.1	0	45.7	24
Gln	547.4	577.5	0	555.3	355	586.9	587.1	0	585.3	360
Lys	183.9	195.7	325	192.9	78.2	189.1	191.6	279	189.8	83.1
Arg	93.1	100.4	101	96.4	0	95.1	96.4	96	95.4	0
Cys	0	0	84	0	0	0	0	68	0	0
Met	24.2	26.9	57	25.6	16.1	25.8	26.8	61	26.1	14.8
Phe	59.5	66.5	139	61.3	40.3	59.6	61.3	109	59.5	35.4
Tyr	65.9	71.9	74	67.4	45.3	65.2	67.3	71	65.5	43.2
Trp	51.3	56.4	53	54.2	0	57	59.6	298	57.3	0
His	69.7	74.1	238	74.1	34.7	69.7	81.2	184	80.3	38.4
Pro	141.6	157.3	129	151.1	99.3	132.3	138.6	339	135.1	121

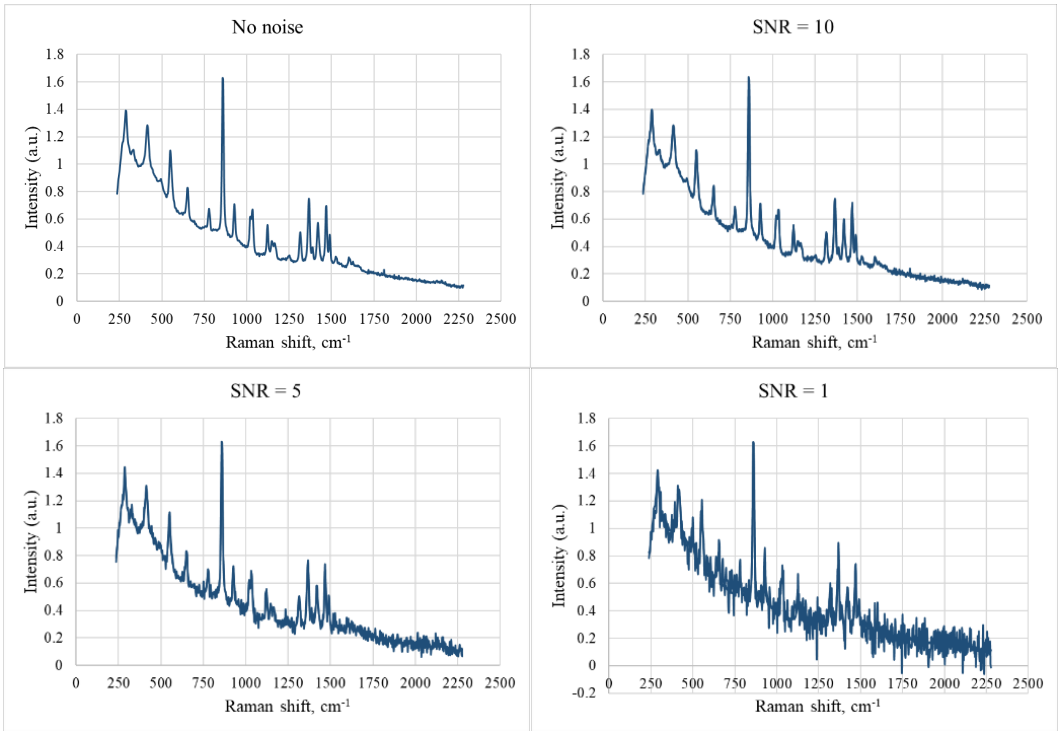


Fig. 2 Raman spectrum of alanine with different SNRs.

For unmixing spectra by MCR–ALS analysis we used a protocol by Felten et al. [14]. The main idea of MCR–ALS is to decompose the Raman spectra matrix D into smaller matrices C and S^T:

$$D = C \times S^T + E, \quad (4)$$

where C represents the concentration profiles for each of the amino acids, S^T is the pure amino acid spectra matrix, and E is the error matrix.

As a basis (S^T), we used the noisy amino acid spectra of 20 standard proteinogenic amino acids (see Table 1) to which we added noise in the previous step. After initial estimation is given for C, it is optimized iteratively using an alternative least squares algorithm (ALS) until convergence is reached [14].

3 Results and Discussion

In this study, we investigated the following combinations of a mixture and basis spectra:

- no noise in mixture spectra, no noise in basis spectra;
- no noise in mixture spectra, SNR = 10 for basis spectra;
- no noise in mixture spectra, SNR = 5 for basis spectra;
- no noise in mixture spectra, SNR = 1 for basis spectra;
- SNR = 10 for mixture spectra, no noise in basis spectra [17];
- SNR = 5 for mixture spectra, no noise in basis spectra [17];
- SNR = 1 for mixture spectra, no noise in basis spectra [17];
- SNR = 5 for mixture spectra, SNR = 5 for basis spectra;
- SNR = 4 for mixture spectra, SNR = 5 for basis spectra;
- SNR = 3 for mixture spectra, SNR = 5 for basis spectra;
- SNR = 2 for mixture spectra, SNR = 5 for basis spectra.

As a result of the MCR–ALS analysis, we have obtained a matrix of amino acid concentrations in the mixture spectra. Concentrations for each amino acid have been compared with the corresponding true values and the correlation coefficients have been calculated between the true concentration array and the obtained concentration array (see Tables 3, 4, 5).

Each concentration array corresponds to one of the amino acids and different mixtures (all the mixtures which we investigated). That is, each element of the array is a concentration of an amino acid in a mixture spectrum (a spectrum of one of the mixtures we used). The correlation coefficient indicates the degree of linear relation of the arrays and varies in the range between –1 and +1, where zero value corresponds to completely uncorrelated arrays.

Table 3 Correlation coefficients between obtained and true amino acid concentration values for the case of the noise added to basis spectra only.

Amino acids	SNR			
	∞ (no noise)	10	5	1
Gly	1.000	1.000	1.000	0.996
Ala	1.000	1.000	1.000	0.999
Val	1.000	1.000	1.000	0.998
Ile	1.000	0.999	1.000	0.988
Leu	1.000	0.997	0.999	0.908
Ser	1.000	0.999	1.000	0.994
Thr	1.000	1.000	1.000	0.999
Asp	1.000	0.997	1.000	0.996
Glu	1.000	1.000	1.000	1.000
Asn	1.000	1.000	1.000	0.999
Gln	1.000	1.000	1.000	1.000
Lys	1.000	1.000	0.999	0.982
Arg	1.000	1.000	1.000	0.994
Cys	1.000	0.987	0.999	0.998
Met	1.000	1.000	1.000	0.998
Phe	1.000	1.000	1.000	1.000
Tyr	1.000	0.988	0.979	0.989
Trp	1.000	0.999	0.999	0.996
His	1.000	1.000	1.000	0.998
Pro	1.000	0.999	1.000	1.000

Table 4 Correlation coefficients between obtained and true amino acid concentration values for the case of the noise added to mixture spectra only [17].

Amino acids	SNR			
	∞ (no noise)	10	5	1
Gly	1.000	0.999	0.991	0.966
Ala	1.000	0.999	0.995	0.959
Val	1.000	0.997	0.989	0.934
Ile	1.000	0.991	0.977	0.760
Leu	1.000	0.983	0.883	0.139
Ser	1.000	0.987	0.773	0.547
Thr	1.000	0.998	0.997	0.988
Asp	1.000	0.992	0.988	0.661
Glu	1.000	1.000	0.999	0.943
Asn	1.000	0.999	0.998	0.984
Gln	1.000	1.000	0.999	0.979
Lys	1.000	0.998	0.964	0.703
Arg	1.000	0.998	0.982	0.846
Cys	1.000	0.968	0.948	0.599
Met	1.000	0.997	0.953	-0.005
Phe	1.000	1.000	1.000	0.994
Tyr	1.000	0.923	0.448	0.344
Trp	1.000	0.991	0.966	0.641
His	1.000	0.999	0.990	0.901
Pro	1.000	0.998	0.992	0.899

Table 3 shows the correlation coefficients for the case when the basis spectra are noisy with a different SNR, and the mixtures have no noise. For comparison, Table 4 shows the results that we obtained in the previous study, when we investigated the effect of noise in the mixture Raman spectra on the quality of unmixing spectra [17].

As one can see from Table 3, the correlation coefficient between true and reconstructed concentrations of amino acids equals 1 for the case without noise. In the case of noisy Raman spectra, the quality of reconstruction of amino acid concentrations is expected to decrease. Nevertheless, in the cases of SNR from 10 to 1, the correlation coefficients are high for all amino acids and ranges from 0.90 to 1.

Paying attention to the comparison of these results with those obtained in the previous study (see Table 4), one can see the following. While in the case of a noise in the basis spectra, amino acids were reconstructed successfully with any of the considered SNRs, in the case of a noise in the mixture spectrum we failed to reconstruct all amino acids when SNR is less than 10. So, when SNR = 5, three out of 20 amino acids are reconstructed with an accuracy of less than 90%, and in the case of SNR = 1 there are already 11 such amino acids.

The results of our previous study [17] show that the concentrations of amino acids are restored with lower correlation coefficients if their Raman spectra have no intense peaks. That is, the ratio between Raman peaks and background, apparently caused by fluorescence, is not high (compare the Raman spectra of cysteine, tyrosine, tryptophan with weak background fluorescence and the Raman spectra of glutamic acid, methionine, phenylalanine with strong background fluorescence in Fig. 1).

It can be concluded that a noise in the Raman spectrum of an amino acid mixture decreases the quality of reconstruction more than a noise in the basis, which is used in MCR–ALS. This may be due to the random nature of the noise we added to the spectra. It has zero mean value; therefore, during MCR–ALS analysis (see Eq. 4), the noise components compensate each other.

Table 5 demonstrates the correlation coefficients of reconstruction of mixture Raman spectra with different SNR using noisy basis Raman spectra of amino acids (SNR = 5). As expected, at higher mixture SNR (SNR > 4) the correlation coefficients are in a range from 0.9 to 1 for almost all amino acids except cysteine and tyrosine, which are characterized by low Raman peaks in all spectral range (see Fig. 1). For noisier mixture Raman spectra with SNR = 3 and SNR = 2 MCR–ALS method failed to reconstruct 5 and 6 amino acids with high quality, respectively. It should be noted that one of the failed components is cysteine, which either is absent in mixtures analyzed or its concentration is low.

As in our previous study [17], the concentrations of leucine, serine, cysteine, tyrosine, tryptophan are restored with lower correlation coefficients because random noise overlaps their spectra (which have a low ratio between Raman peaks and background fluorescence).

Table 5 Correlation coefficients between obtained and true amino acid concentration values for the case of the noise added to both basis spectra (SNR = 5 for all the cases) and mixture spectra.

Amino acids	SNR of mixture Raman spectra			
	5	4	3	2
Gly	0.996	0.995	0.988	0.991
Ala	0.994	0.990	0.988	0.956
Val	0.986	0.991	0.985	0.968
Ile	0.996	0.991	0.961	0.906
Leu	0.863	0.821	0.798	-0.085
Ser	0.876	0.869	0.628	0.571
Thr	0.992	0.986	0.985	0.949
Asp	0.983	0.947	0.941	0.964
Glu	0.998	0.999	0.997	0.996
Asn	0.997	0.983	0.991	0.971
Gln	0.999	1.000	0.997	0.995
Lys	0.969	0.939	0.928	0.776
Arg	0.992	0.993	0.987	0.941
Cys	0.555	0.650	0.727	0.403
Met	0.982	0.984	0.964	0.929
Phe	1.000	0.999	0.999	0.999
Tyr	0.451	0.666	0.214	0.589
Trp	0.907	0.903	0.876	0.829
His	0.991	0.992	0.966	0.978
Pro	0.991	0.992	0.984	0.947

It should be noted that the correlation coefficients for the cases of the basis spectra with noise and without noise are comparable. Thus, the approach proposed makes it possible to estimate amino acid concentrations from noisy Raman spectra of the mixture using basis spectra with noise, and this can be done almost as efficiently as if using pure basis spectra without noise.

Nevertheless, the presence of fluorescence in the spectra is not the only problem. The form of the spectrum, that is, the presence of Raman peaks in certain wavelength ranges, has a strong influence on the result of the decomposition of the mixture spectrum. For example, in the cases of SNR = 1 and SNR = 2, one can see extremely low negative correlation values for leucine (Leu) and methionine (Met) (see Tables 4 and 5). It can be explained by the fact that the Raman spectra of these amino acids do not contain peaks that are unique to only these amino acids; moreover, the spectra are noisy. Thus, the MCR method is not efficient enough in this case.

Having studied the effect of noise in Raman spectra on the reconstruction of the concentration of amino acids in the artificially modelled mixtures, we should check the obtained relations for real mixtures, when the noise is of different nature. It is very clear that the real mixture samples (i.e., biological tissue samples) may contain other components such as lipids and proteins. In this case, the resolved spectra of the components may have some background contribution incorporated, a final estimation of component concentrations should be performed by fixing the pure spectra of the amino acids and leaving free the background contribution, which requires the correction of the protocol settings. In addition, the efficiency of reconstruction may be affected by removing background fluorescence and normalization of the basis spectra in order to equalize their intensities. Therefore, our future research will be devoted to experiments on real mixtures of amino acids and study of the influence of basis spectra preprocessing.

Disclosures

All authors declare that there is no conflict of interests in this paper.

Acknowledgments

This work was supported by the RFBR Grant № 19-52-18001 Bolg_a.

References

1. Cancer, World Health Organisation, 3 March 2021 (accessed 5 April 2021). [https://www.who.int/news-room/fact-sheets/detail/cancer].
2. A. Kubota, M. M. Meguid, and D. C. Hitch, "Amino acid profiles correlate diagnostically with organ site in three kinds of malignant tumors," Cancer 69(9), 2343–2348 (1992).
3. Y. Miyagi, M. Higashiyama, A. Gochi, M. Akaike, T. Ishikawa, T. Miura, and M. Moriyama, "Plasma free amino acid profiling of five types of cancer patients and its application for early detection," PloS One 6(9), e24143 (2011).
4. M. Shingyoji, T. Iizasa, M. Higashiyama, F. Imamura, N. Saruki, A. Imaizumi, and M. Yamakado, "The significance and robustness of a plasma free amino acid (PFAA) profile-based multiplex function for detecting lung cancer," BMC Cancer 13(1), 77 (2013).
5. Q. H. Zhao, Y. Cao, Y. Wang, C. L. Hu, A. L. Hu, L. Ruan, and M. Ren, "Plasma and tissue free amino acid profiles and their concentration correlation in patients with lung cancer," Asia Pacific journal of clinical nutrition 23(3), 429–436 (2014).
6. A. M. Proenza, J. Oliver, A. Palou, and P. Roca, "Breast and lung cancer are associated with a decrease in blood cell amino acid content," The Journal of Nutritional Biochemistry 14(3), 133–138 (2003).
7. I. A. Bratchenko, L. A. Bratchenko, A. A., Moryatov, Y. A., Khristoforova, D. N. Artemyev, O. O. Myakinin, A. E. Orlov, S. V. Kozlov, and V. P. Zakharov, "In vivo diagnosis of skin cancer with a portable Raman spectroscopic device," Experimental Dermatology 30(5), 652–663 (2021).
8. A. de Juan, R. Tauler, "Multivariate Curve Resolution: 50 years addressing the mixture analysis problem – A review," Analytica Chimica Acta 1145(8), 59–78 (2020).
9. M. Garrido, F. X. Rius, and M. S. Larrechi, "Multivariate curve resolution–alternating least squares (MCR-ALS) applied to spectroscopic data from monitoring chemical reactions processes," Analytical and Bioanalytical Chemistry 390(8), 2059–2066 (2008).
10. H. Noothalapati, K. Iwasaki, and T. Yamamoto, "Biological and medical applications of multivariate curve resolution assisted Raman spectroscopy," Analytical Sciences 33(1), 15–22 (2017).
11. H. Xu, B. W. Rice, "In-vivo fluorescence imaging with a multivariate curve resolution spectral unmixing technique," Journal of Biomedical Optics 14(6), 064011 (2009).
12. P. H. Chen, R. Shimada, S. Yabumoto, H. Okajima, M. Ando, C. T. Chang, L. T. Lee, Y. K. Wong, A. Chiou, and H. O. Hamaguchi, "Automatic and objective oral cancer diagnosis by Raman spectroscopic detection of keratin with multivariate curve resolution analysis," Scientific Reports 6(1), 1–9 (2016).
13. K. Iwasaki, A. Araki, C. M. Krishna, R. Maruyama, T. Yamamoto, and H. Noothalapati, "Identification of Molecular Basis for Objective Discrimination of Breast Cancer Cells (MCF-7) from Normal Human Mammary Epithelial Cells by Raman Microspectroscopy and Multivariate Curve Resolution Analysis," International Journal of Molecular Sciences 22(2), 800 (2021).
14. J. Felten, H. Hall, J. Jaumot, R. Tauler, A. De Juan, and A. Gorzsás, "Vibrational spectroscopic image analysis of biological material using multivariate curve resolution–alternating least squares (MCR-ALS)," Nature protocols 10(2), 217–240 (2015).
15. L. A. Bratchenko, I. A. Bratchenko, A. A. Lykina, M. V. Komarova, D. N. Artemyev, O. O. Myakinin, A. A. Moryatov, I. L. Davydkin, S. V. Kozlov, and V. P. Zakharov, "Comparative study of multivariative analysis methods of blood Raman spectra classification," Journal of Raman Spectroscopy 51(2), 279–292 (2020).
16. SpectraSuite, Ocean Insight (accessed 29 July 2020). [https://oceanoptics.ru/spectrometers/59-spectrasuite.html].
17. I. A. Matveeva, O. O. Myakinin, Y. A. Khristoforova, I. A. Bratchenko, E. N. Tupikova, and V. P. Zakharov, "Possibilities for decomposing Raman spectra of amino acids mixture by Multivariate Curve Resolution (MCR) analysis," SPIE Proceedings 11582, 115821G (2020).